University of Maribor Press

ISSN 1854-0171

ACTA GEOTECHNICA SLOVENICA

2021/2
VOL.18

ACTA GEOTECHNICA SLOVENICA

ISSN: 1854-0171

Ustanovitelji	Founders

Univerza v Mariboru, Fakulteta za gradbeništvo, prometno inženirstvo in arhitekturo
University of Maribor, Faculty of Civil Engineering, Transportation Engineering and Architecture

Univerza v Ljubljani, Fakulteta za gradbeništvo in geodezijo
University of Ljubljana, Faculty of Civil and Geodetic Engineering

Univerza v Ljubljani, Naravoslovnotehniška fakulteta
University of Ljubljana, Faculty of Natural Sciences and Engineering

Slovensko geotehniško društvo
Slovenian Geotechnical Society

Društvo za podzemne in geotehniške konstrukcije
Society for Underground and Geotechnical Constructions

Izdajatelj	Publisher

Univerza v Mariboru, Fakulteta za gradbeništvo, prometno inženirstvo in arhitekturo
Faculty of Civil Engineering, Transportation Engineering and Architecture

Odgovorni urednik	Editor–in–Chief
Borut Macuh	University of Maribor

Tehnična urednica	Technical Editor
Tamara Bračko	University of Maribor

Uredniki	Co–Editors
Jakob Likar	Geoportal d.o.o.
Janko Logar	University of Ljubljana
Primož Jelušič	University of Maribor
Stanislav Škrabl	University of Maribor
Goran Vižintin	University of Ljubljana
Bojan Žlender	University of Maribor

Posvetovalni uredniki	Advisory Editors
Heinz Brandl	Vienna University of Technology
Chandrakant. S. Desai	University of Arizona
Bojan Majes	University of Ljubljana
Pedro Seco e Pinto	National Laboratory of Civil Eng.

Lektor	Proof–Reader
Paul McGuiness	

Naklada	Circulation
200 izvodov - issues	

Cena	Price

25 EUR/letnik - 25 EUR/vol.; (50 EUR for institutions/za institucije)

Tisk	Print
Design Studio d.o.o.	

Revija redno izhaja dvakrat letno. Članki v reviji so recenzirani s strani priznanih mednarodnih strokovnjakov. Baze podatkov v katerih je revija indeksirana: SCIE - Science Citation Index Expanded, JCR – Journal Citation Reports / Science Edition, ICONDA - The international Construction database, GeoRef. Izid publikacije je finančno podprla Javna agencija za raziskovalno dejavnost Republike Slovenije iz naslova razpisa za sofinanciranje domačih periodičnih publikacij.

Založnik	Published by
Univerzitetna založba Univerze v Mariboru	University of Maribor Press
Slomškov trg 15, 2000 Maribor, Slovenija	Slomškov trg 15, 2000 Maribor, Slovenia
e-pošta: zalozba@um.si, http://press.um.si/, http://journals.um.si/	e-mail: zalozba@um.si, http://press.um.si/, http://journals.um.si/

Naslov uredništva	Address

ACTA GEOTECHNICA SLOVENICA
Univerza v Mariboru, Fakulteta za gradbeništvo, prometno inženirstvo in arhitekturo
Smetanova ulica 17, 2000 Maribor, Slovenija
Telefon / Telephone: +386 (0)2 22 94 300
Faks / Fax: +386 (0)2 25 24 179
E-pošta / E-mail: ags@um.si

Spletni naslov	web Address

http://www.fg.uni-mb.si/journal-ags/

The journal is published twice a year. Papers are peer reviewed by renowned international experts. Indexation data bases of the journal: SCIE - Science Citation Index Expanded, JCR – Journal Citation Reports / Science Edition, ICONDA- The international Construction database, GeoRef. The publication was financially supported by Slovenian Research Agency according to the Tender for co-financing of domestic periodicals.

EXPERIMENTAL INVESTIGATION OF THE MECHANICAL PROPERTIES OF MUDSTONE IN SOUTHWESTERN CHINA

EKSPERIMENTALNA RAZISKAVA MEHANSKIH LASTNOSTI MELJEVCA NA JUGOZAHODU KITAJSKE

Qijian Zhou
Southwest Jiaotong University,
School of Civil Engineering
No.111 North Section 2, Erhuan Road, Chengdu 610031, P.R. China

China Southwest Architectural Design & Research Institute Co., Ltd,
No.866 of northern section of Tianfu Avenue, Chengdu 610052, P.R. China

Ronggui Deng
Southwest Jiaotong University,
School of Civil Engineering
No.111 North Section 2, Erhuan Road, Chengdu 610031, P.R. China

Lining Zheng
China Southwest Architectural Design & Research Institute Co., Ltd,
No.866 of northern section of Tianfu Avenue, Chengdu 610052, P.R. China

Quanbing Zhu
PowerChina Railway Construction Co., Ltd, Chengdu 610041, P.R. China

Qiang Xie
PowerChina Railway Construction Co., Ltd, Chengdu 610041, P.R. China

Xinhua Xue *(corresponding author)*
Sichuan University,
College of Water Resource and Hydropower
No.24 South Section 1, Yihuan Road, Chengdu 610065, P.R. China
E-mail: scuxxh@163.com

DOI https://doi.org/10.18690/actageotechslov.18.2.2-14.2022

Keywords

cretaceous mudstone, uniaxial compression tests, triaxial compression tests, scanning electron microscopy

Abstract

In this paper the mechanical properties of mudstone with different immersion durations (e.g., immersion in water for 0, 7 and 14 days), at different temperatures (20, 35 and 50 °C) and in different confining pressures (0.6 and 1.2 MPa) were investigated using uniaxial compression tests, conventional triaxial compression tests and scanning electron microscopy. The test results indicate that in the temperature range from 20 °C to 50 °C the water content can significantly reduce the mechanical parameters, including the strength and elastic modulus of the mudstone samples. In contrast, the Poisson ratio of the mudstone samples increases with the increase in the water content. In addition, there is little difference between the effects of an immersion time of 7 days and 14 days on the mudstone samples, indicating that the confining pressure plays a protective role on the mudstone samples.

Ključne besede

kredast meljevec, enoosni tlačni preizkusi, triosni tlačni preizkusi, elektronsko mikroskopsko skeniranje

Izvleček

V tem prispevku so bile z uporabo enoosnih tlačnih preizkusov, konvencionalnih triaksialnih tlačnih preizkusov in elektronskih mikroskopskih skenerjev raziskane mehanske lastnosti meljevca z različnim trajanjem potopitve (npr. potopitev v vodo za 0, 7 in 14 dni), pri različnih temperaturah (20, 35 in 50 °C) in pri različnih tlakih (0,6 in 1,2 MPa). Rezultati preizkusov kažejo, da lahko v temperaturnem območju od 20 °C do 50 °C vsebnost vode znatno zmanjša mehanske parametre, vključno s trdnostjo in modulom elastičnosti vzorcev meljevca. Nasprotno pa se Poissonov količnik v vzorcih meljevca povečuje s povečanjem vsebnosti vode. Dodatno je ugotovljeno, da je majhna razlika na vzorce meljevca med učinki časa potopitve 7 dni in 14 dni, kar kaže, da ima bočni tlak zaščitno vlogo na vzorce meljevca.

Nomenclature

T	=	Temperature
t	=	Immersion time
σ	=	Peak strength
E_{50}	=	Elastic modulus
μ_{50}	=	Poisson ratio
σ_1	=	Major principal stress
ε_1	=	Major principal strain
ε_3	=	Minor principal strain
ε_v	=	Volumetric strain

1 INTRODUCTION

With the development of urban underground engineering construction, the environment of urban rail-transit engineering is becoming more and more complex [1]. As the new national growth of economic development in western China, the Chengdu area has seen an increasing number of super-high-rise buildings in recent years. The main surface in Chengdu area is expansive clay or pebble bed. When the building is low-rise, the foundation is mainly in the covering layer. However, with the increase in the number of the super-high-rise buildings, the foundations need to penetrate into the red mudstone to guarantee the safety of these projects. Thus, the soil is required to have a very high bearing capacity.

The cretaceous mudstone is widely distributed in the Chengdu area, which is mainly composed of clay minerals with a small amount of sandstone. According to the degree of weathering, the cretaceous mudstone can be classified as strong, moderate and weakly weathering. The mechanical properties and water sensitivity of cretaceous mudstone with different weathering degrees are different [2]. Meanwhile, the cretaceous mudstone has some weak expansibility, disintegration, local corrosion and dissolution [3, 4], as shown in Figure 1. Therefore, in order to guarantee the safety of these super-high-rise buildings, it is necessary to study the mechanical properties of the cretaceous mudstone.

Figure 1. Corroded cavity in mudstone.

Significant efforts have been made to study the influence of water and temperature on the mechanical properties of mudstone, including numerical simulations, model testing and experimental tests [5, 6]. For instance, Han et al. [7] investigated the mechanical characteristics and energy properties of mudstone by use of experimental methods. Nahazanan et al. [8] studied the effect of inundation on the shear strength characteristics of mudstone backfill. Zhang et al. [9, 10] analyzed the meso-structure and fracture mechanism of mudstone at high temperature by X-ray diffraction (XRD) and scanning electron microscopy (SEM). Zhang et al. [11] investigated the effect of temperature on mudstone decay during the wetting-drying processes. Qi et al. [12] studied the slaking process and mechanisms under static wetting and drying cycles in a red strata mudstone. Adams et al. [13] investigated the permeability anisotropy and resistivity anisotropy of mechanically compressed mudrocks. Li et al. [14] studied the softening characteristics of sandstone and mudstone in relation to moisture content, which can provide a useful reference for the design of underground roadways. Mohammad et al. [15] investigated the petrophysical and acoustic properties of reconstituted shale and mudstone aggregates, and they believed their results could provide insights for hydrocarbon prospect discovery in a pre-mature sedimentary basin. Hu et al. [16, 17] established a constitutive model and damage evolution of mudstone under the action of dry-wet cycles. Lu et al. [18, 19] investigated the effect of water and temperature on the short-term and creep mechanical behaviors of coal measure rocks. Ma and Liu [20] predicted the peak strength of sandstone and mudstone joints infilled with high water-cement ratio grouts. Huang et al. [21] investigated the effects of cyclic wetting-drying conditions on the elastic modulus and compressive strength of sandstone and mudstone.

Previous studies have confirmed that the mechanical properties of rocks including the elastic modulus and strength can be weakened by the water content, which can be called the water-weakening effect [22]. According to a recent study conducted by Poulsen et al. [23], the water-weakening effect is greater in clay-rich rocks than in quartz-rich rocks. After absorbing water, the mechanical strength of clay-rich rocks can decrease by more than 60 %. Meanwhile, the water-weakening effect is closely connected with the water content. The experimental studies have indicated that the uniaxial compressive strength of rocks generally decreases with an increase in the water content. On the other hand, the mechanical parameters of rocks including, uniaxial the compressive strength and elastic modulus, are also affected by the temperature. In general, the uniaxial compressive strength and elastic modulus of rocks decrease with an increase in temperature, and these changes vary for different kinds of rocks.

However, most of the previous studies have only considered the individual effect of temperature or water on the mechanical properties of rocks, rather than the coupling effect of temperature and water. Therefore, in the present study, the mechanical properties of mudstone specimens under different immersion durations (e.g., immersion in water for 0, 7 and 14 days), different temperatures (20, 35 and 50 ℃) and different confining pressures (0.6 and 1.2 MPa) were investigated using uniaxial compression tests, conventional triaxial compression tests and scanning electron microscopy. The flowchart of the experimental study of the mechanical properties of mudstone is illustrated in Figure 2.

This paper is organized as follows. In Section 2, we introduce the uniaxial compression tests and results. In Section 3, we introduce the conventional triaxial compression tests and results. In Section 4, we introduce the scanning electron microscopy and results. The conclusions are drawn in Section 5.

2 UNIAXIAL COMPRESSION TESTS

2.1 Experimental Instruments and Testing Procedure

In this study the uniaxial compression tests were performed using an electrothermal blowing dry box (Figure 3) and an MTS815 electro-hydraulic servo system (Figure 4). The specific steps of the uniaxial compression test are as follows:

1) Number the prepared samples according to the sampling position and measure the size and mass of each rock sample.
2) Take a certain number of rock samples for drying for 24h, and then weigh the rock samples.
3) Immerse the dried rock samples in water for 12h, 24h and 48h. Then, weigh the rock samples and calculate the water content of each sample.
4) Uniaxial compression tests were carried out on the rock samples with different water contents.

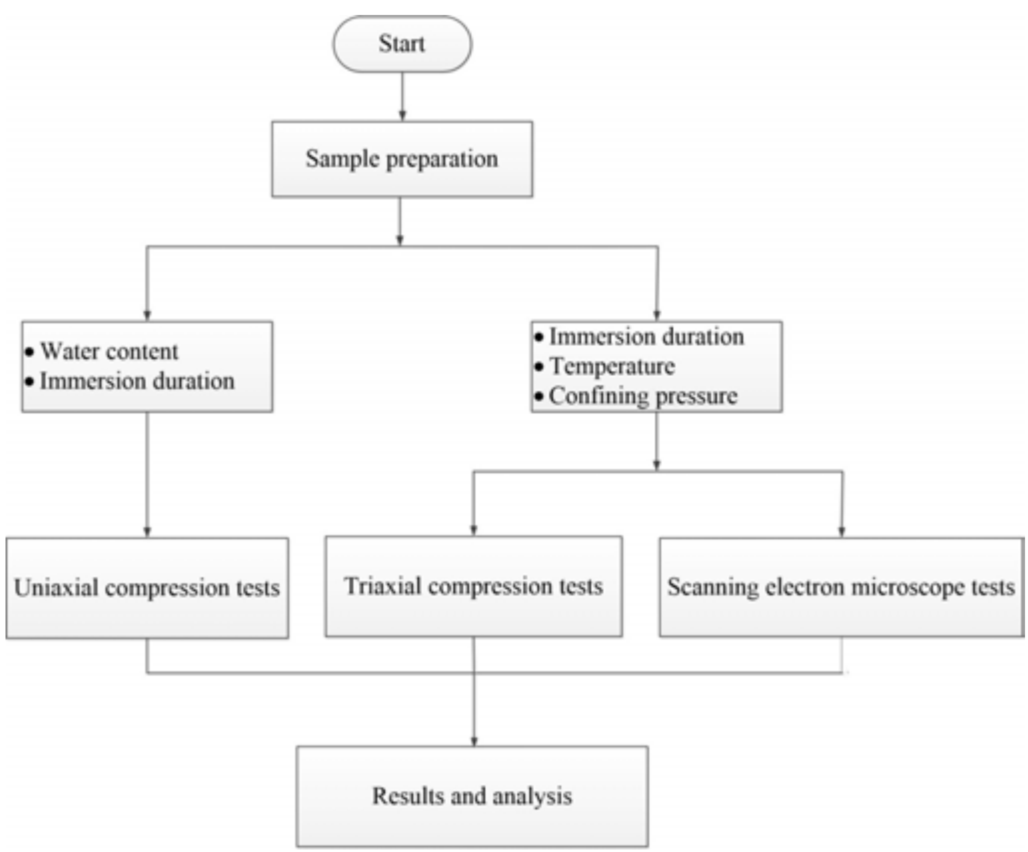

Figure 2. Flowchart of the experimental study on the mechanical properties of mudstone.

Figure 3. Electrothermal blowing dry box.

Figure 4. MTS815 electro-hydraulic servo system.

2.2 Results and Analysis

The mudstone samples for uniaxial compression tests are listed in Table 1. Figure 5 plots the stress-strain curves of the mudstone samples 21-3-1 to 21-3-3 under uniaxial compression. The photographs of mudstone samples 21-3-1 to 21-3-3 before and after the uniaxial compression tests are shown in Figure 6.

It is clear from Table 1 that the water content can significantly reduce the mechanical parameters, including the peak strength and the elastic modulus of the mudstone samples. For example, under dry conditions, the strength and elastic modulus of the mudstone samples are 4.92-43.01 MPa and 1.42-14.02 GPa, respectively. However, under natural conditions, the strength and elastic modulus of the mudstone samples are 3.61–3.63 MPa and 0.34–0.51 GPa, respectively. With an increase of the immersion time, the maximum water content of the mudstone can reach 30.49 %, and the strength and elastic modulus of the mudstone samples are only 0.07 MPa and 0.0006 GPa, respectively. In contrast, the Poisson ratio of the mudstone samples increases with an increase in the water content. For example, under dry conditions, the Poisson ratio of the 21-3-2 mudstone sample is equal to 0.29, while with an increase in the water content, the Poisson ratio of the 21-3-1 mudstone sample can reach 0.32. In addition, Figure 5 shows that the stress-strain curves of the mudstone under uniaxial compression exhibit typical elastoplastic failure modes. As the principal stress increases, the principal strain first increases and then decreases. The volumetric strain is positive at first and then becomes negative, showing a micro-expansibility. These results demonstrate that the water-weakening effect is very significant in mudstone. The main reason for this phenomenon is that the mudstone is rich in clay minerals; the clay minerals are strongly hydrophilic and are more prone to swelling, softening, and disintegration after absorbing water (as shown in Figure 6). Similar results have been reported in previous studies [18, 19]. For example, the decrease in the

Table 1. Summary of mudstone samples for uniaxial compression tests.

Sample No.	Sample depth (m)	Water content (%)	Peak strength, σ (MPa)	Elastic modulus, E_{50} (GPa)	Poisson ratio, μ_{50}	Condition
6-13	39.00	0.00	43.01	14.02	0.23	Dry
6-15	37.00	18.08	3.61	0.51	0.30	Natural
6-8	36.00	30.35	0.09	0.0026	--	Immersion in water for 48 h
16-15	37.00	0.00	14.93	1.65	0.28	Dry
16-10	35.00	8.61	3.63	0.34	0.33	Natural
16-14	37.00	30.49	0.07	0.0006	--	Immersion in water for 48 h
21-3-2	35.00	0.00	4.92	1.42	0.29	Dry
21-3-3	35.00	20.05	1.29	0.82	0.31	Immersion in water for 12 h
21-3-1	35.00	24.83	1.16	0.69	0.32	Immersion in water for 24 h

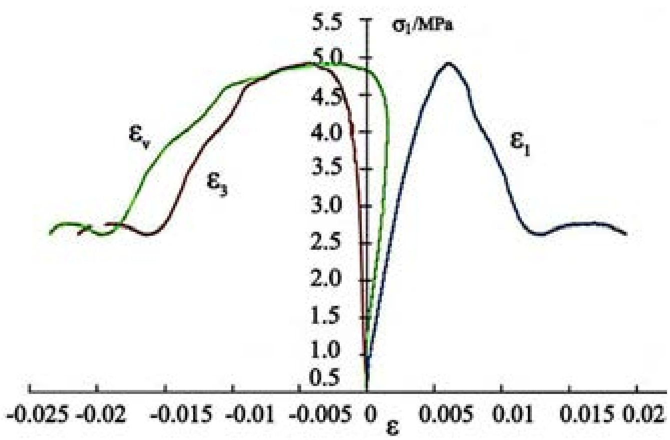

(a) 21-3-2

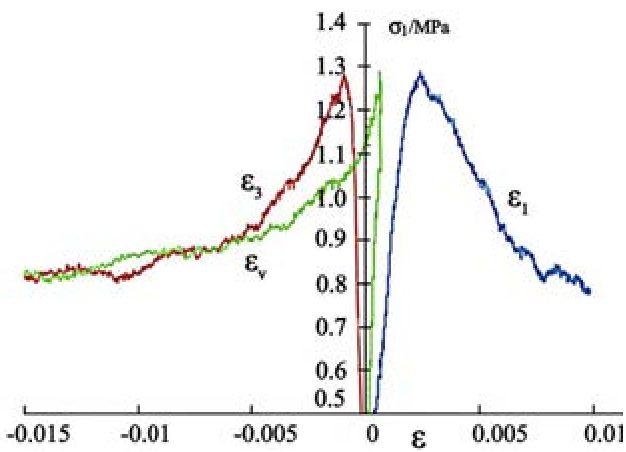

(b) 21-3-3

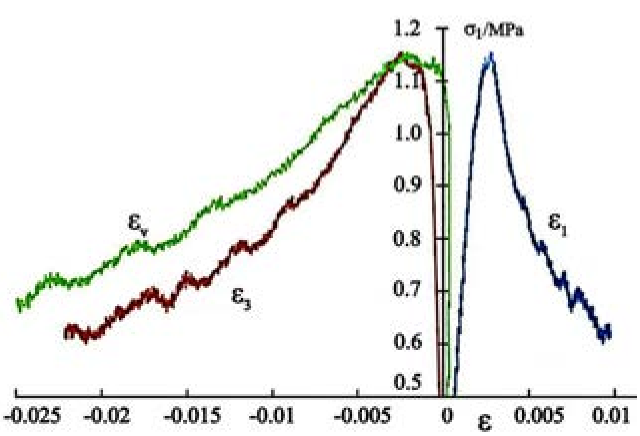

(c) 21-3-1

Figure 5. Stress-strain curves of mudstone samples under uniaxial compression.

uniaxial compressive strength and the elastic modulus of the mudstone with the increase in the water content were also observed in Ref. [19]. Thus, the rationality of the experimental results in this paper is proven.

(a) Before tests

(a) After tests

Figure 6. Photographs of mudstone samples.

3 CONVENTIONAL TRIAXIAL COMPRESSION TESTS

3.1 Effect of immersion time on the mudstone

To investigate the effect of the immersion time on the mudstone, the specimens were first immersed in water for 0, 7 and 14 days, respectively. Then, under the confining pressure of 0.6 MPa and at a temperature of 20, 35 and 50 °C, the conventional triaxial compression tests were conducted for one to two specimens under different immersion conditions. Table 2 lists the triaxial compression test results of the mudstone under different immersion times. Figure 7 plots the triaxial compression stress-strain curves of the mudstone sample under different immersion times at temperature T = 50 °C. The photographs of the mudstone samples before and after the triaxial compression tests are shown in Figure 8.

Table 2 shows that the immersion time has a significant effect on the strength and elastic modulus of the mudstone samples. It can be seen from Table 2 that the longer the immersion time, the smaller the peak strength and elastic modulus. For example, at temperature

Table 2. Triaxial compression test results for mudstone with different immersion times.

Immersion time t (day)	Sample No.	Temperature, T (℃)	Peak strength, σ (MPa)	Elastic modulus, E_{50} (GPa)	Poisson ratio, μ_{50}
0	6-7	20	2.35	0.52	0.31
7	16-7		1.49	0.45	0.33
	20-1		1.43	1.56	0.50
14	15-1		1.09	0.46	0.35
0	16-8-1	35	9.90	1.02	0.26
7	16-8-2		2.18	0.62	0.36
14	15-19-1		1.57	0.60	0.30
0	15-2-2	50	12.05	1.95	0.12
	20-2		10.09	1.57	0.15
	15-22		3.49	6.51	0.15
7	6-9		1.06	/	0.29
	15-24-2		2.78	1.23	0.23
	14-5		1.33	0.08	0.41
14	15-23		2.59	1.64	0.29

T = 35 ℃, when the immersion time is t = 0, the strength and elastic modulus of the mudstone samples are equal to 9.9 MPa and 1.02 GPa, respectively. However, when the immersion time is t = 14 days, the strength and elastic modulus of the mudstone samples are equal to 1.57 MPa and 0.6 GPa, respectively. In addition, there is little difference between the effects of the immersion time of 7 days and 14 days on the mudstone samples,

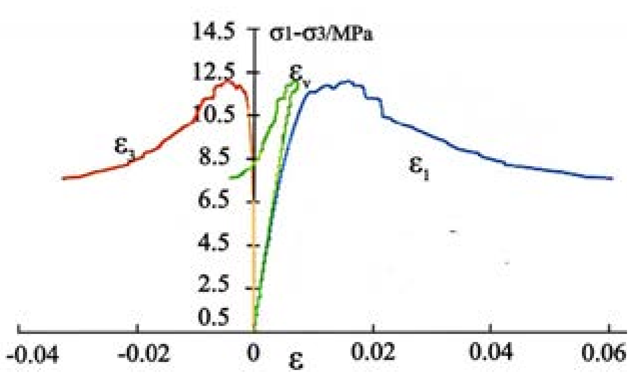

(a) t = 0, 15-2-2

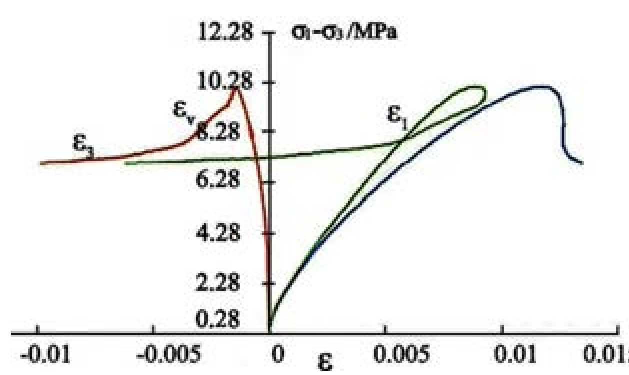

(b) t = 0, 20-2

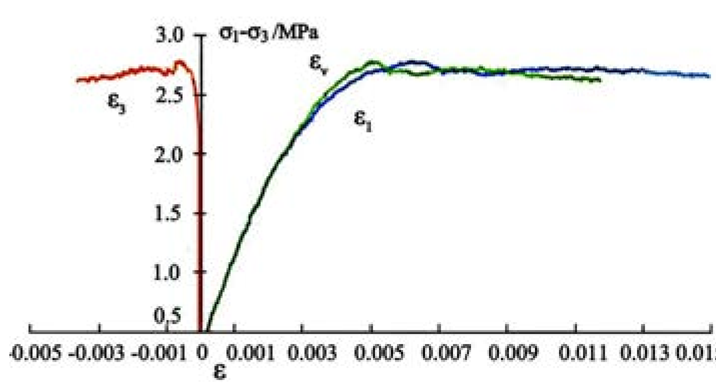

(c) t = 7 days, 15-24-2

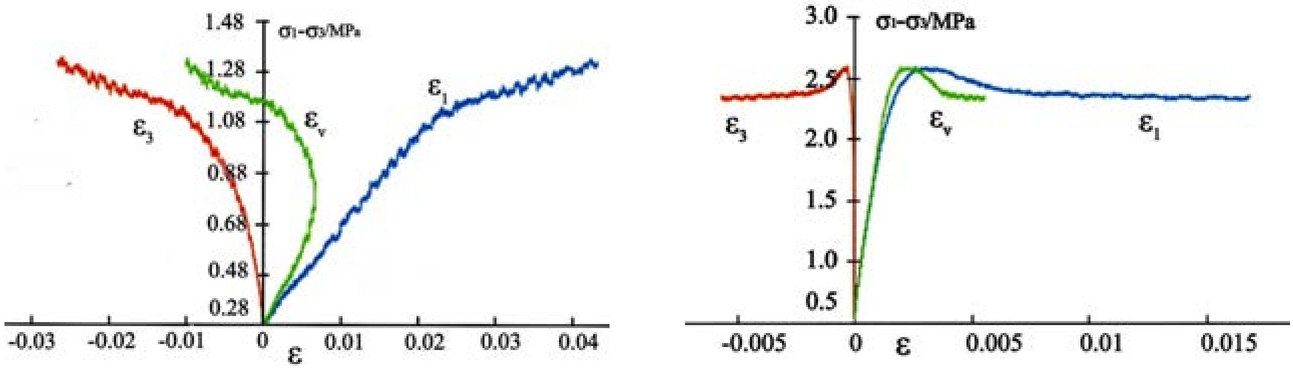

(d) t = 7 days, 14-5 (e) t = 7 days, 15-23

Figure 7. Triaxial compression stress-strain curves for mudstone with different immersion times at T = 50 °C.

(a) Before tests.

(b) After tests.

Figure 8. Photographs of mudstone samples.

indicating that the confining pressure has a protective effect on the mudstone samples.

3.2 Effect of temperature on the mudstone

To investigate the effect of temperature on mudstone, under the confining pressure of 1.2 MPa and immersion time t = 0, 7 and 14 days, the conventional triaxial compression tests were conducted for one to two specimens at temperatures of 20, 35 and 50 °C, respectively. Table 3 lists the triaxial compression test results for mudstone at different temperatures. Figure 9 plots the triaxial compression stress-strain curves of the mudstone sample with an immersion time t = 14 days at different temperatures. The photographs of the mudstone samples before and after the triaxial compression tests are shown in Figure 10.

Table 3 shows that the peak strength and elastic modulus generally increase with an increase in the temperature. For example, for the immersion time t = 0 condition, the strength and elastic modulus of the mudstone samples at temperature T = 20 °C are in the range of 2.86-12.51 MPa and 0.61-0.92 GPa, respectively. However, when the temperature is T = 50 °C, the

Table 3. Triaxial compression test results for mudstone with different temperatures.

Temperature, T (°C)	Sample No.	Immersion time, t (day)	Peak strength, σ (MPa)	Elastic modulus, E_{50} (GPa)	Poisson ratio, μ_{50}
20	16-9	0	2.86	0.61	0.34
	20-4		12.51	0.92	0.21
35	6-11-1		7.46	0.78	0.27
	20-3-1		6.83	0.69	0.25
50	6-11-2		8.40	0.78	0.21
	20-7		14.80	1.64	0.17
20	21-2	7	2.31	0.06	0.52
	15-4-1		3.53	1.14	0.28
35	14-4		1.70	0.23	0.44
	15-4-2		3.92	1.38	0.28
50	15-24-1		4.67	1.41	0.26
20	15-21-1	14	1.41	0.90	0.36
35	15-21-2		3.90	1.00	0.27
50	15-2-1		6.55	1.30	0.28

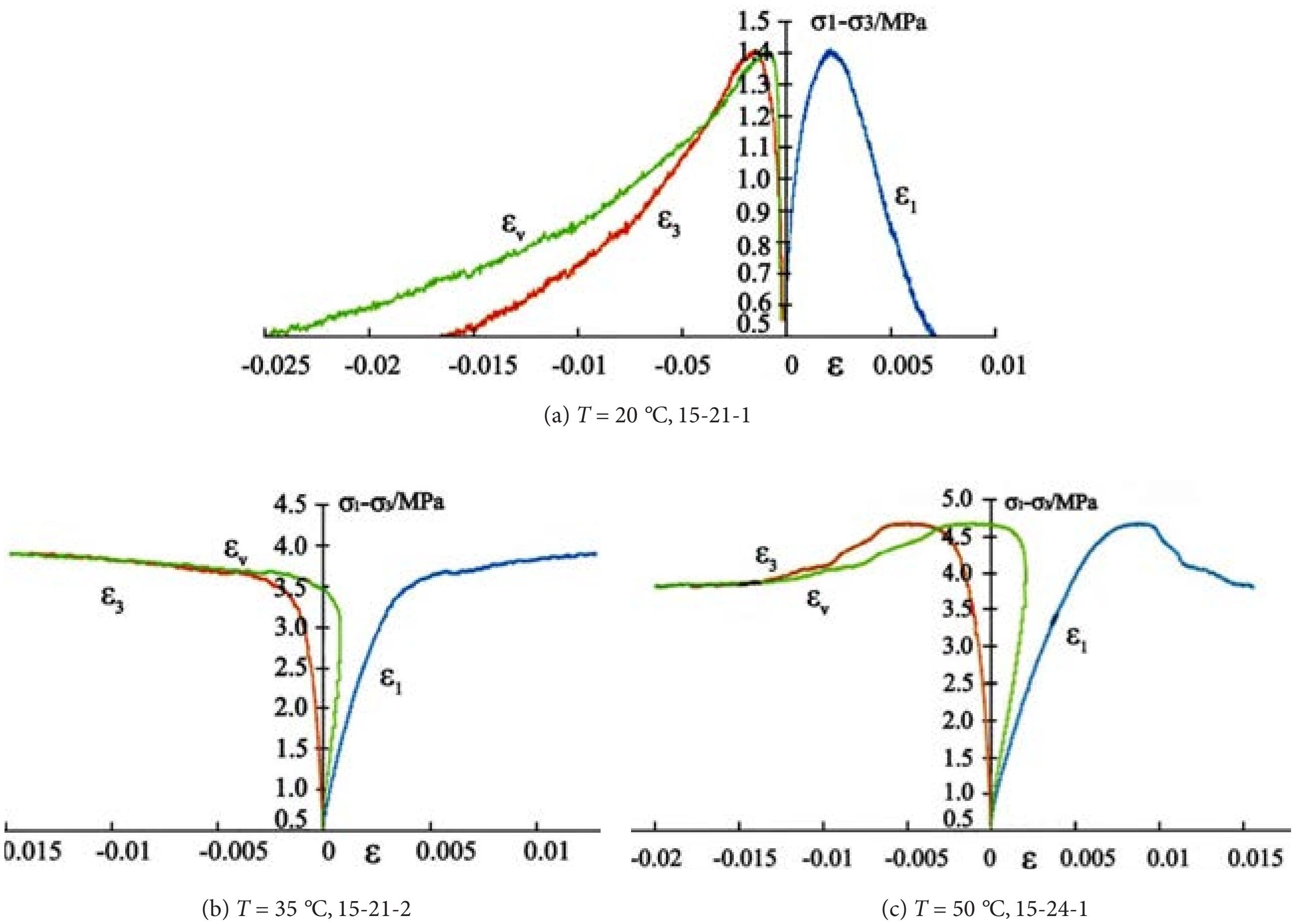

(a) T = 20 °C, 15-21-1

(b) T = 35 °C, 15-21-2

(c) T = 50 °C, 15-24-1

Figure 9. Triaxial compression stress-strain curves for mudstone after 14 days of immersion.

(a) Before tests. (b) After tests.

Figure 10. Photographs of mudstone samples.

strength and elastic modulus of the mudstone samples are in the range of 8.40-14.80 MPa and 0.78-1.64 GPa, respectively. In contrast, the Poisson ratio of the mudstone samples decreases with the increase in the temperature. For example, the Poisson ratio of the mudstone samples at temperature T = 20 ℃ is in the range 0.21-0.34, while the Poisson ratio of the mudstone samples at T = 50 ℃ is in the range 0.17-0.21. In addition, Figure 9 shows that the stress-strain curves of the mudstone samples in the temperature range 20 ℃ to 50 ℃ experience four typical stages, i.e., the phase of virgin consolidation, the linear elastic stage, the elastic-plastic stage, and the post-peak strain softening stage. The stress-strain curves are slightly different at different temperatures, which are mainly reflected in the difference of the peak strength and the residual strength. Similar results were reported in previous studies [18, 19].

Table 4. Summary of mudstone samples for SEM.

Sample No.	Immersion time, t (day)	Temperature, T (℃)	Confining pressure (MPa)
6-7	0		
16-7	7	20	
15-1	14		
16-8-1	0		
16-8-2	7	35	0.6
15-19-1	14		
15-2-2	0		
6-9	7	50	
15-23	14		
16-9		20	
6-11-1	0	35	
6-11-2		50	
15-4-1		20	
15-4-2	7	35	1.2
15-24-1		50	
15-21-1		20	
15-21-2	14	35	
15-2-1		50	

4 SCANNING ELECTRON MICROSCOPY (SEM)

4.1 Sample Preparation

The summary of mudstone samples for this scanning electron microscopy (SEM) is listed in Table 4.

4.2 Results and Analysis

4.2.1 The results for mudstone with different immersion times

Figures 11-13 show the SEM photomicrographs for the mudstone samples at T = 50 ℃ with different immersion times t = 0, 7 and 14 days, respectively.

As shown in Figures 11-13, the fracture morphology of the 15-2-2 mudstone sample exhibits grain boundary and inter-crystal fracture patterns; the fracture morphology of the 6-9 mudstone sample exhibits a grain-boundary pattern, and the fracture occurs on the grain interface; the fracture morphology of the 15-23 mudstone sample exhibits a striation pattern, showing the fracture form of cutting crystal and wiping flower. The experimental results show that under certain confining pressures (0.6 MPa) and temperatures (T = 50 ℃), the failure modes of the mudstone samples in triaxial compression tests are mainly tensile failure.

4.2.2 The results of mudstone under different temperatures

Figures 14-16 show the SEM photomicrographs of the mudstone samples under immersion time t = 14 days at different temperatures of 20, 35 and 50 ℃, respectively.

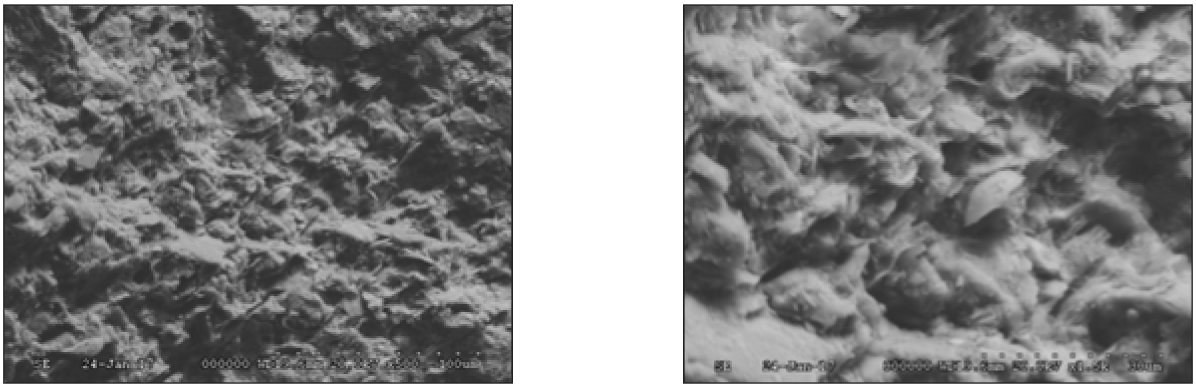

Figure 11. SEM photomicrographs of the 15-2-2 mudstone sample.

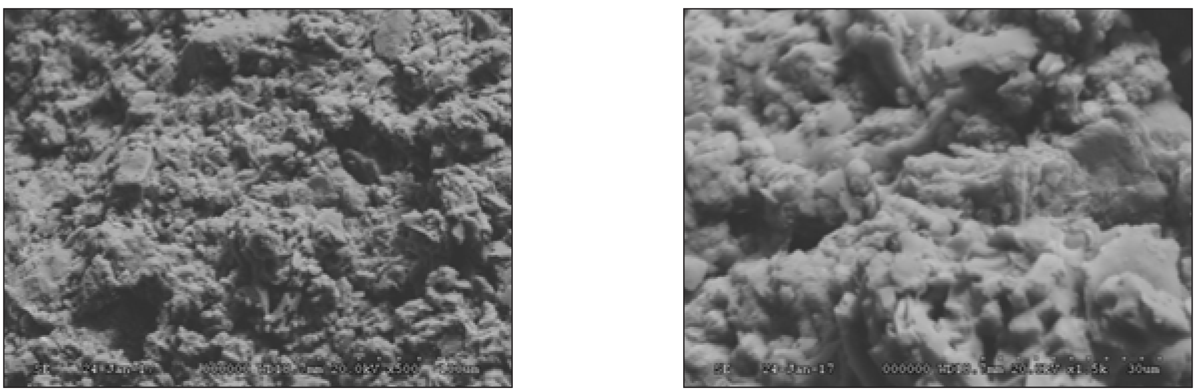

Figure 12. SEM photomicrographs of the 6-9 mudstone sample.

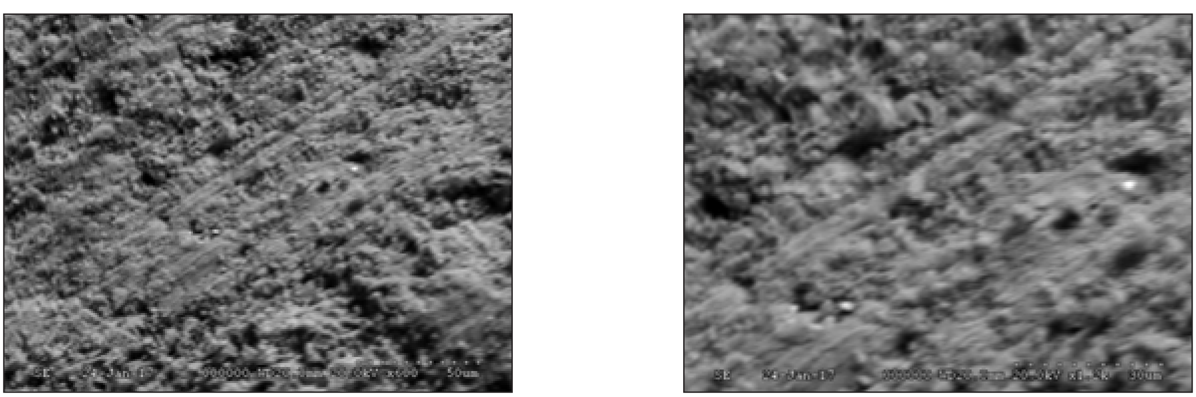

Figure 13. SEM photomicrographs of the 15-23 mudstone sample.

As shown in Figures 14-16, the fracture morphology of the 15-21-1 mudstone sample exhibits a triangular micro-pit fracture pattern, which might be caused by the brittle fracture of the mudstone sample under tensile stress. The fracture morphology of the 15-21-2 mudstone sample exhibits grain-boundary and intercrystal fracture patterns, and both grain interface and intercrystal surface have fracture, indicating the intercrystalline fracture pattern. The fracture morphology of the 15-2-1 mudstone sample exhibits a striation pattern, indicating the fracture pattern of cutting crystal and wiping flower. The experimental results show that under a certain confining pressure (1.2 MPa) and immersion time (t = 14 days), tensile failure occurs at 20 °C and 35 °C, while shear failure mainly occurs at 50 °C.

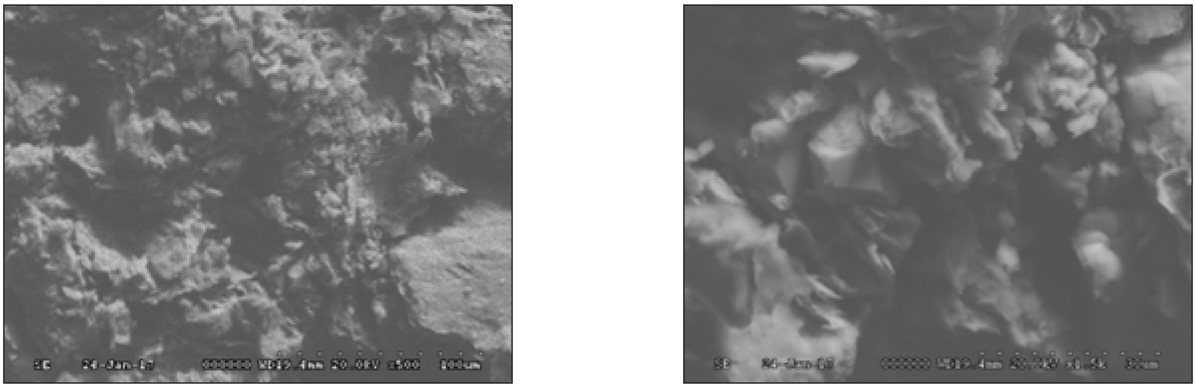

Figure 14. SEM photomicrographs of the 15-21-1 mudstone sample.

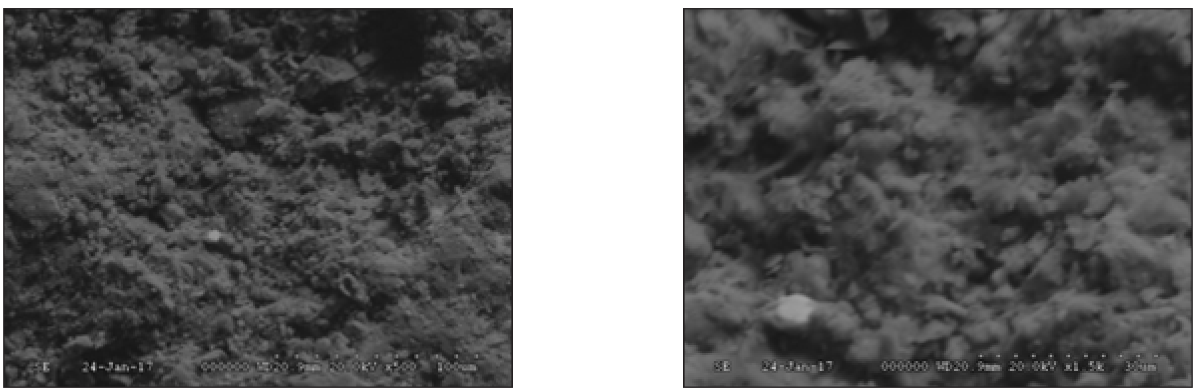

Figure 15. SEM photomicrographs of the 15-21-2 mudstone sample.

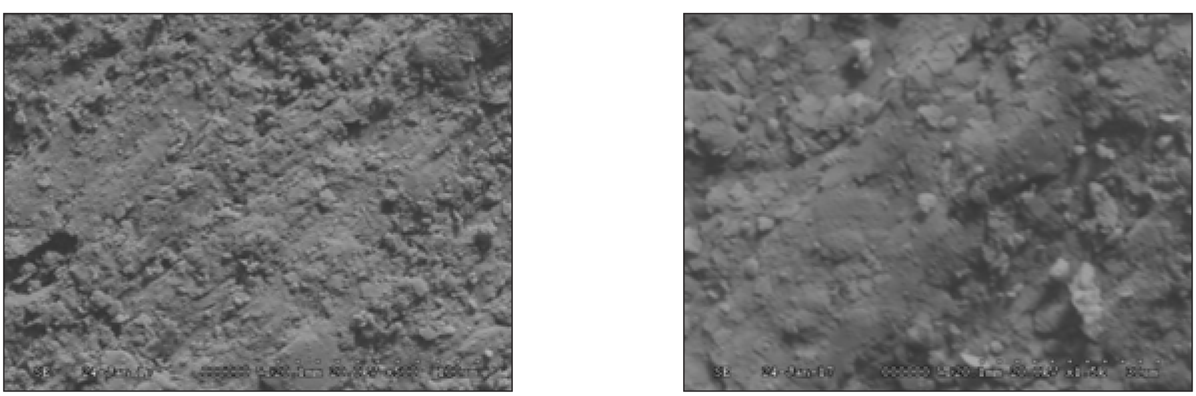

Figure 16. SEM photomicrographs of the 15-2-1 mudstone sample.

5 CONCLUSIONS

In this study a series of uniaxial compression tests, conventional triaxial compression tests and SEM tests were conducted on mudstone samples for different immersion times (0, 7 and 14 days), different temperatures (20, 35 and 50 ℃) and different confining pressures (0.6 and 1.2 MPa). The conclusions can be summarized as follows.

(1) The water content can significantly reduce the mechanical parameters including strength and elastic modulus of the mudstone samples. In contrast, the Poisson ratio of the mudstone samples increases with the increase in water content.

(2) Under the same confining pressure and temperature, the longer the immersion time, the smaller the strength and elastic modulus. However, there is little

difference between the effects of immersion time of 7 days and 14 days on the mudstone samples, indicating that the confining pressure has a protective effect on the mudstone samples.

(3) Under the same immersion time and confining pressure, and when the temperature is in the range 20 ℃ to 50 ℃, the strength and elastic modulus generally increase with an increase in the temperature, but the Poisson ratio decreases with the increase in temperature. In addition, the stress-strain curves of the mudstone samples in the temperature range from 20 ℃ to 50 ℃ experience four typical stages.

(4) Under a certain confining pressure (0.6 MPa) and temperature (T = 50 ℃), the failure modes of the mudstone samples in triaxial compression tests are mainly tensile failure. Under a certain confining pressure (1.2 MPa) and immersion time (t = 14 days), tensile failure occurs at 20 ℃ and 35 ℃, while shear failure mainly occurs at 50 ℃.

(5) In the present study, we only consider three lower-temperature cases (20, 35 and 50 ℃). However, higher temperatures are likely to be encountered in the process of exploiting deep ground resources. In addition to experiments, we also need to further establish relevant theoretical models to study the mechanism of water and temperature on the mechanical properties of mudstone. As such, there is still room for further improvement in future research work.

Conflicts of interest

The authors declare that they have no potential conflicts of interest regarding the publication of this paper.

Acknowledgments

This work was supported by the PowerChina Railway Construction Co., Ltd (Grant no.TK18352).

REFERENCES

[1] Wang, J.B., Liu, X.R., Zhao, B.Y., Song, Z.P., Lai, J.X. 2016. Experimental investigation and constitutive model for lime mudstone. SpringerPlus 5(1),1634. https://doi.org/10.1186/s40064-016-3297-8.

[2] Yu, C.Y., Tang, S.B., Tang, C.A., Duan, D., Zhang, Y.J., Liang, Z.Z., Ma,K., Ma, T.H. 2019. The effect of water on the creep behavior of red sandstone. Engineering Geology 253, 64-74. https://doi.org/10.1016/j.enggeo.2019.03.016

[3] Luo, Y. L., Luo, B., Xiao, M. 2020. Effect of deviator stress on the initiation of suffusion. Acta Geotechnica 15(6), 1607-1617. https://doi.org/10.1007/s11440-019-00859-x

[4] Zhang, Y.Y., Ye, W.J. 2018. Effect of dry-wet cycle on the formation of loess slope spalling hazards. Civil Engineering Journal 4 (4), 785-795. https://dx. doi.org/10.28991/cej-0309133

[5] Wang, Z.Q., Chen, X., Xue, X.H., Zhang, L., Zhu, W.K. 2019. Mechanical parameter inversion in sandstone diversion tunnel and stability analysis during operation period. Civil Engineering Journal 5 (9), 1917-1928. https://dx. doi.org/10.28991/cej-2019-03091382

[6] Gamil, Y., Bakar, I., Ahmed, K. 2017. Simulation and development of instrumental setup to be used for cement grouting of sand soil. Emerging Science Journal 1 (1), 16-27. https://doi.org/10.28991/esj-2017-01112

[7] Han, T.L., Chen, Y.S., Xie, T., Yu, Z., He, M.M. 2012. Experimental study on mechanics characteristic and energy properties of mudstone. Journal of Water Resources and Architectural Engineering 10(3), 116-120. (in Chinese)

[8] Nahazanan,H., Clarke,S., Asadi,A., Yusoff, Z., Huat,B.K. 2013. Effect of inundation on shear strength characteristics of mudstone backfill. Engineering Geology158, 48-56. https://doi.org/10.1016/j.enggeo.2013.03.003

[9] Zhang, L.Y., Mao, X.B., Liu, R.X., Li,Y., Yin, H.G. 2014a. Meso-structure and fracture mechanism of mudstone at high temperature. International Journal of Mining Science and Technology 24, 433-439. https://doi.org/10.1016/j.ijmst.2014.05.003

[10] Zhang, L.Y., Mao, X.B., Liu, R.X., Guo, X.Q., Ma, D. 2014b. The mechanical properties of mudstone at high temperatures: an experimental study. Rock Mechanics and Rock Engineering 47, 1479-1484. https://doi.org/10.1007/s00603-013-0435-2

[11] Zhang, D., Chen, A.Q., Wang, X.M., Liu, G.C. 2015. Quantitative determination of the effect of temperature on mudstone decay during wet-dry cycles: a case study of 'purple mudstone' from south-western China. Geomorphology 246, 1-6. https://doi.org/10.1016/j.geomorph.2015.06.011

[12] Qi, J., Sui, W., Liu, Y., Zhang, D. 2015. Slaking process and mechanisms under static wetting and drying cycles slaking tests in a red strata mudstone. Geotechnical and Geological Engineering 33(4), 959-972. https://doi.org/10.1007/s10706-015-9878-4

[13] Adams, A.L., Nordquist, T.J., Germaine, J.T., Flemings, P.B. 2016. Permeability anisotropy and resistivity anisotropy of mechanically compressed

mudrocks. Canadian Geotechnical Journal 53(9), 1474-1482. http://www.nrcresearchpress.com/doi/abs/10.1139/cgj-2015-0596

[14] Li, G.C., Qi, C.C., Sun, Y.T., Tang, X.L., Hou, B.Q. 2017. Experimental study on the softening characteristics of sandstone and mudstone in relation to moisture content. Shock and Vibration 1-14. https://doi.org/10.1155/2017/4010376

[15] Mohammad, N., Nazmul, H.M., Helge, H., Knut, B. 2017. Experimental mechanical compaction of reconstituted shale and mudstone aggregates: investigation of petrophysical and acoustic properties of SW Barents Sea cap rock sequences. Marine and Petroleum Geology 80, 265-292. https://doi.org/10.1016/j.marpetgeo.2016.12.003

[16] Hu, M., Liu, Y.X., Ren, J.B., Zhang,Y., Wu, R.Z. 2017. Temperature-induced deterioration mechanisms in mudstone during dry-wet cycles. Geotechnical and Geological Engineering 35, 2965-2976. https://doi.org/10.1007/s10706-017-0295-8

[17] Hu, M., Liu, Y.X., Song, L.B., Zhang, Y. 2018. Constitutive model and damage evolution of mudstone under the action of dry-wet cycles. Advances in Civil Engineering 1-10. https://doi.org/10.1155/2018/9787429

[18] Lu, Y.L., Wang, L.G. 2017a. Effect of water and temperature on short-term and creep mechanical behaviors of coal measures mudstone. Environmental Earth Sciences 76, 597. https://doi.org/10.1007/s12665-017-6941-x

[19] Lu, Y.L., Wang, L.G., Sun, X.K., Wang, J. 2017b. Experimental study of the influence of water and temperature on the mechanical behavior of mudstone and sandstone. Bulletin of Engineering Geology and the Environment 76(2), 645-660. https://doi.org/10.1007/s10064-016-0851-0

[20] Ma,H., Liu, Q.S. 2017. Prediction of the peak shear strength of sandstone and mudstone joints infilled with high water-cement ratio grouts. Rock Mechanics and Rock Engineering 50, 2021-2037. https://doi.org/10.1007/s00603-017-1225-z

[21] Huang, S.Y., Wang, J.J., Qiu, Z.F., Kang, K. 2018. Effects of cyclic wetting-drying conditions on elastic modulus and compressive strength of sandstone and mudstone. Processes 6, 234. https://doi.org/10.3390/pr6120234

[22] Wasantha, P.L.P., Ranjith, P.G. 2014. Water-weakening behavior of Hawkesbury sandstone in brittle regime. Engineering Geology 178, 91-101. https://doi.org/10.1016/j.enggeo.2014.05.015

[23] Poulsen, B.A., Shen, B., Williams, D.J., Huddlestone-Holmes C., Erarslan, N., Qin, J. 2014. Strength reduction on saturation of coal and coal measures rocks with implications for coal pillar strength. International Journal of Rock Mechanics and Mining Sciences 71, 41-52. https://doi.org/10.1016/j.ijrmms.2014.06.012

INVESTIGATING THE SHEAR PROPERTIES OF CEMENTED CLAYEY SAND WITH A NANO TiO_2 ADDITIVE

RAZISKOVANJE STRIŽNIH LASTNOSTI CEMENTIRANEGA GLINENEGA PESKA Z DODATKOM NANO TiO_2

Abbas Babaei
Islamic Azad University,
Department of Civil Engineering,
Science and Research Branch
Tehran, Iran
E-mail: a_babaei@iaunour.ac.ir

Mahmoud Ghazavi *(corresponding author)*
K. N. Toosi University of Technology,
Department of Civil Engineering,
Tehran, Iran
E-mail: ghazavi_ma@kntu.ac.ir

Navid Ganjian
Islamic Azad University,
Department of Civil Engineering,
Science and Research Branch
Tehran, Iran
E-mail: n.ganjian@srbiau.ac.ir

DOI https://doi.org/10.18690/actageotechslov.18.2.15-28.2022

Keywords

clayey sand, cement, nano TiO_2, RSM, CD triaxial test

Ključne besede

glinasti pesek, cement, nano TiO_2, metoda odzivne površine RSM, konsolidiran nedreniran triosni preizkus

Abstract

In this research a series of experimental tests were performed to investigate the effects of nano TiO_2 (NT) on the triaxial behavior of cemented clayey sand (with variable amounts of kaolinite). To reduce the number of experiments, time and cost of research, the design and assessment of the experiments were performed using the response surface method (RSM). The amount of used NT was 0–4 wt% of cement, and the amounts of cement and kaolinite were 3–9 wt% and 10–30 wt% of soil respectively. The consolidated drained (CD) triaxial tests were performed for the confining pressures of 100, 300 and 600 kPa. The results of these tests showed that the amount of kaolinite clay at 20 % has the largest effect on the peak deviator stress and friction angle, but the soil cohesion has an ascending trend at 10–30 % kaolinite clay. The amount of cement in the range of 3–9 % causes an increase in the peak-deviator stress, shear strength parameters and the brittleness index. Also, the use of NT in a desirable amount (2 %) causes an increase in the peak deviator stress and the shear strength parameters.

Izvleček

V predstavljeni raziskavi je bila izvedena serija eksperimentalnih preizkusov za raziskovanje učinkov nano TiO_2 (NT) na triosno obnašanje cementiranega glinastega peska (s spremenljivimi količinami kaolinita). Za zmanjšanje števila poskusov, časa in stroškov raziskav smo načrtovanje in ocenjevanje poskusov izvedli z metodo odzivne površine (RSM). Količina uporabljenega NT je bila 0 do 4 utežnega % cementa, količine cementa oz. kaolinita pa 3 do 9 utežnega % oz. 10 do 30 utežnega % zemljine. Izvedeni so bili konsolidirani drenirani triosni preizkusi za bočne tlake 100, 300 in 600 kPa. Rezultati teh preizkusov so pokazali, da je pri vsebnosti 20 % kaolinitne gline največji vpliv na vrhnjo deviatorično napetost in strižni kot, medtem, ko ima kohezija naraščajoči trend pri vsebnosti 10 do 30 % kaolinitne gline. Vsebnost cementa v območju 3 do 9 % povzroči povečanje vrhnje deviatorične napetosti, parametrov strižne trdnosti in indeksa krhkosti. Tudi uporaba NT v primerni količini (2 %) povzroči povečanje vrhnje deviatorične napetosti in parametrov strižne trdnosti.

1 INTRODUCTION

Among the main challenges in geotechnics is the effect of governing conditions. Some project sites may lack the desirable bearing capacity and be susceptible to excessive settlements, and this requires soil-improvement measures. Among the available methods for soil stabilization and improvement is the addition of cement or cement derivatives at the site or outside of it [1-6]. Previous studies show that the addition of cement could increase the shear strength of the soil. Yao et al. evaluated the strength of cement-treated clay with a wide range of mix ratios and curing periods using unconfined compressive strength tests (UCSTs). The effect of the cement, total water content and curing period on the unconfined compressive strength of cemented clay was investigated. They showed that for a constant water content in all samples, the unconfined compressive strength increases with increasing cement content, while the increase in the water content has the opposite effect. They also showed that for a mixture with constant ratios, the unconfined compressive strength of cemented clay has a semi-log increase with increasing curing [7]. Schnaid et al. investigated the stress-strain and strength behavior of artificially cemented sand using the drained triaxial test to examine the effects of the amount of cement and the confined pressure [8]. The results showed that the addition of cement causes an increase in the initial stiffness and peak strength. Kutanaei and Choobbasti performed several drained triaxial tests to investigate the effects of cement and polypropylene fiber on the triaxial behavior of sand. They demonstrated that by adding cement, both the initial stiffness and peak strength of cemented soil increase [9].

With advancements in nanotechnology, nanomaterials have been introduced as one of the promising materials in the modern era and have attracted the attention of geotechnical researchers for the improvement of cemented soils. Among them is the experimental study of Bahmani et al. in determining the effect of nanosilica particles on the compressive strength of residual soil stabilized by cement, where the addition of 0.4 % nanosilica to a soil treated by cement increased the compressive strength by 80 % [10]. Choobbasti et al. investigated the effect of nano silica on the unconfined compressive strength of cement-stabilized sand. The results of this study showed that the presence of nanosilica at the optimal percentage (10 wt% of cement), could considerably increase the unconfined compressive strength of cement-stabilized sand [11]. Ghasabkolaee et al. investigated the effect of nanosilica on the geotechnical properties of the cemented clay. The results showed that the addition of 1.5 % nanosilica increased the unconfined compressive strength of cemented clay up to 38 % after 28 days of curing [12]. Tao Meng et al. investigated the effect of adding nano calcium carbonate on the increase of the strength and improvement of the microstructure of a soil stabilized with cement in the marine environment. They showed that adding nano calcium carbonate increases the compressive strength [13]. The increased compressive strength in the initial time and with age contributes to the nucleation effect and nano filling. In another study, Yao et al. investigated the efficiency of nano magnesium oxide on the strength and microstructure characteristics of cement-stabilized soft soil. According to the performed unconfined compressive strength tests, it was found that the amount of nano magnesium oxide has an important role in the increased strength of the cement-stabilized soil. For 13 % cement content, 15 % nano magnesium oxide yielded the best response [14]. Yao et al. performed a series of direct shear tests to investigate the effect of the cement and nano magnesium oxide (MgO) contents on the shear-strength properties of silty clay. With an increase in the amount of cement and the normal stress, the shear stress increased. Both the cohesion and the friction angle of the cemented soil increased with increasing the amount of cement, and the exponential performance was obtained for the correlation of both factors with the amount of cement. For the 10 % cement content, the optimal amount of nano-MgO is 10 %, where the shear strength reaches its peak value [15]. Wang et al. examined the characteristics of nano-MgO admixed with cement for clay improvement using the direct shear test. The optimal amount of nano-MgO to reach the highest shear strength was 5 %. In this research, they also examined the effect of wetting the samples in a sulfuric acid solution, which shows that, in general, the shear strength of the mixture decreases with increasing the concentration of sulfuric acid. However, the shear strength of the mixture increases with increasing the wetting period, even in the sulfuric acid medium [16]. In another research, Wang et al. presented a mathematical model based on the reinforced exponential and power (REP) function to simulate different stress-strain behaviors of a nano-MgO–cement–soft coastal soil (NMCS) mixture under different conditions. A comparison was made between the conventional and REP-based models, which confirms the feasibility of the proposed models [17]. Kulanthaivel et al. examined the effect of white cement and nano-silica on clay using the permeability and California bearing ratio (CBR) tests. The optimal composition was formed at 2 % nano silica and 3 % white cement in terms of soil weight. In addition, the soil permeability was reduced by 45 % with this composition [18]. Li et al. studied the mechanical performance ofiron tailings powder (ITP) by combining cement and nano clay using the unconfined compressive strength (UCS) test, scanning electron microscopy (SEM), and energy-dispersive spectroscopy (EDS) with curing times of 7 and 28 days. The results showed that the combination of cement and nano clay increases the unconfined compressive strength of ITP. When 5-10 % nano clay is added to 10 % cement, the increase in unconfined compressive strength was almost identical. The results of the microstructural studies showed that the main function of nano clay is attributed to its small particle size, which makes the structure more compact [19].

Researchers have recently used non-pozzolanic and inactive nano-oxides due to the nucleation and filling effects in cementitious materials and have shown that due to the inherent effects on the C-S-H gel formation because of the increase in CH in early hydration, the inactive nanoparticles prevent the formation of large crystals and modify the orientation index of the CH crystal. Therefore, the hardness of the C-S-H gel is improved and the structural defect is reduced [20-21]. NT is an inactive and non-pozzolanic nanomaterial with anti-bacterial, self-cleaning, anti-aging, and photocatalytic effects. The researchers of the nanomaterial sector in the field of civil engineering currently study the photocatalytic and self-cleaning effects, improved mechanical properties and the electrical conductivity of building materials [22-28].

Some studies have examined the effect of modifying the mechanical properties of cementitious materials, including Zhang et al., by adding NT to the cementitious materials to investigate the strength-modification effect. The results showed that NT increases the compressive strength of cementitious materials by improving the hydration degree of the cement and reducing the porosity of the composites [29]. Li et al. also examined the effect of NT on the mechanical and microstructural properties of reactive concrete powder (RCP). The results showed that NT can accelerate the RCP hydration in the early stages due to the nucleation effect. The XRD analysis of powder and the observations of SEM confirm that the nucleation effect of NT cannot only reduce the degree of orientation of calcium hydroxide (CH), but can also limit the size of CH. Hence, NT can increase the strength, even for longer times. The 28-day increase in compressive strength with the addition of NT in the RCP is 18.05 %. Li et al. also examined the compressibility model in a study and showed that NT can modify the RCP compressibility and reduce the RCP porosity from 9.04 to 6.9 %. With SEM observations, they showed that NT can modify the effect of RCP holes and micro-cracks through the filling effect, which is consistent with the result of the compressibility model [30].

As seen in previous studies, the effect of NT on the mechanical properties of cemented clayey sand has not yet been investigated. Hence, in the current research several CD compression triaxial tests were performed using the RSM design method to determine this effect. Here, the effects of NT, cement, kaolinite and confining pressure on the behavior of clayey sand are assessed in terms of the peak-deviator stress, shear-strength parameters, and brittleness index.

2 MATERIALS AND METHOD

2.1 Used materials

In this research the material is made of clayey sand prepared in the laboratory (sand with 10% kaolinite, K10, sand with 20 % kaolinite, K20, and sand with 30 % kaolinite, K30). Fine sand is prepared from the banks of Mazandaran Sea located in northern Iran with the grain size distribution curve shown in Figure 1, according to ASTM D422-63 [31]. The technical properties of the sand are given in Table 1. Based on the results of the grading test and according to the unified soil classification system this sand is classified as poorly graded sand (SP). For the clayey soil, use is made of kaolinite mineral where its grain size distribution curve is shown in Figure 1. The technical properties of the clay are given in Table 2. The used cement is Portland cement Type I produced in Mazandaran Province and its chemical compound is given in Table 3. Also, its physical and mechanical properties are given in Table 4. NT is prepared from US

Table 1. Physical properties of sand.

Standard test	Value	Parameters
Maximum void ratio, e_{max}	0.80	ASTM D 4254
Minimum void ratio, e_{min}	0.526	ASTM D 4253
Specific gravity, G_S	2.75	ASTM D 854
Uniformity coefficient, C_U	2.128	-
Coefficient of curvature, C_C	1.322	-
Mean grain size, D_{50} (mm)	0.195	-

Table 2. Physical and index properties of kaolinite clay minerals.

Parameters	Value
Specific gravity, G_S	2.6
Liquid limit, w_L (%)	45
Plastic limit, w_P (%)	25
Plasticity index, I_P (%)	20
Activity, A (%)	46

Table 3. Chemical Compositions of Portland Cement type I.

Oxide	Percentage by weight (%)
SiO_2	21.75
Al_2O_3	5.15
Fe_2O_3	3.23
CaO	63.75
MgO	1.15
SO_3	1.95
Na_2O	0.33
K_2O	0.56

Table 4. Mechanical and physical characteristics of Portland cement type I.

Mechanical and physical properties	Value
Blaine specific surface (cm^2/gr)	3150
Specific gravity, G_S	3.15
Expansion (autoclave) (%)	0.13
Compressive strength (MPa)	
2 days	15
3 days	23
7 days	38.6
28 days	48.5

Table 5. Physical properties of NT.

Mechanical and physical properties	Value
Diameter (nm)	10–25
Surface volume ratio (m^2/g)	200–240
Density (g/cm^3)	0.24
Purity (%)	> 99%
Color	White

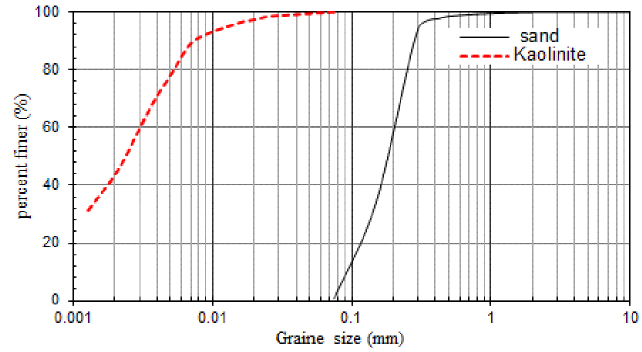

Figure 1. Grain size distribution of the soils.

Research Nanomaterials Co. and its physical properties are given in Table 5. The FESEM images of sand particles, kaolinite clay and NT are shown in Figure 2.

Figure 2 shows a FESEM image of sand, kaolinite, and NT prepared by a high-resolution MIRA3 TESCAN SEM. Figure 2 (a) shows the FESEM image of the used sand, which indicates its round corner structure. Figure 2 (b) shows the FESEM image of kaolinite, which indicates the plane structure. Figure 2 (c) shows the FESEM image of NT, which indicates an almost spherical structure with an average diameter of 20 nm.

2.2 Experimental Design Method

In this research to extract the model and find the largest effect, the response-surface method is incorporated. In this method the experiment matrix is designed by considering the number of variables and the maximum and minimum limits determined per each variable. In this way the number of tests and surfaces of each variable in each test are determined. Where the number of variables

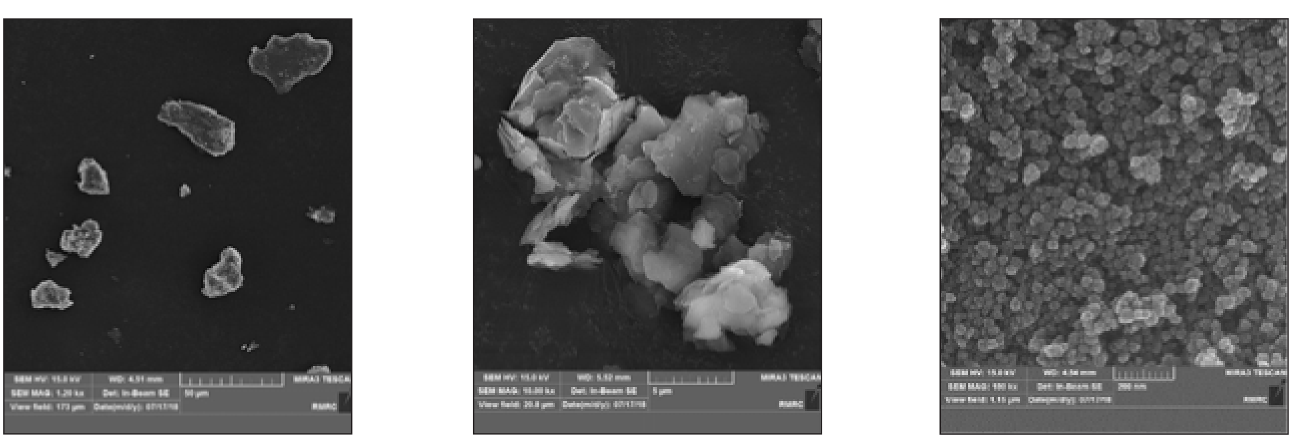
(a) (b) (c)

Figure 2. FESEM images: (a) sand (1.2 k×); (b) kaolinite (10 k×); (c) NT (10 k×).

is high, this method is preferred over other time-consuming methods such as the full factorial methods. The experiment design method provides good and reliable statistical results even without repeating the experiment. Thus, this method facilitates the research procedure and reduces the time and cost. In the RSM the face-centered central composite design (CCD) scheme was selected. In the face centered scheme, the maximum and minimum limits are designated with +1 and -1 surface codes. In fact, these are the only information that should be given to the statistical software with respect to the studies and the research idea per surfaces of each variable. So, the third surface, as the zero or central surface (0), has a value between the maximum and minimum values.

Table 6. Experimental range and levels of independent variables.

Variables	Range and levels		
	Low level (-1)	Center level (0)	High level (+1)
NT (A:%)	0	2	4
Cement (B:%)	3	6	9
Kaolinite (C:%)	10	20	30

Albeit where some other surfaces are defined, which may lie between theses surfaces, they could be easily coded [32]. In the present research, Design-Expert 7 software was used for the design, mathematical modelling, statistical analysis and assessment of the process variables. The three independent variables including the NT content which changes within the range 0–4 wt% of dry cement weight, Portland cement content which changes within the range 3–9 wt% of soil and kaolinite clay, which changes within the range 10–30 % of soil, are converted into the coded values (Table 6) and are designed according to CCD after performing a number of tests, which are shown in Table 7.

As shown in Table 7, a total of 18 tests were considered in this study, including 15 tests by the CCD method and three tests that are the laboratory soil samples (K10, K20 and K30). Each test also included three samples. A total of 54 samples were used in this study.

The quadratic regression equation is then obtained to forecast the responses. In this research the quadratic equation was appropriate, and thus the system behavior is expressed with the following quadratic equation (1) [32-35].

Table 7. Design of experiments and corresponding results obtained from laboratory tests.

No	ID of samples	Variation			Peak deviator stress (kPa)			Mechanical parameters		Brittleness index		
		NT (A:%)	Cement (B:%)	Kaolinite (C:%)	$\sigma_3 =$ 100 kPa	$\sigma_3 =$ 300 kPa	$\sigma_3 =$ 600 kPa	Cohesion (kPa)	Friction angle (degree)	$\sigma_3 =$ 100 kPa	$\sigma_3 =$ 300 kPa	$\sigma_3 =$ 600 kPa
1	K10C3NT0	0	3	10	1648	2279	3258	323	38	0.48	0.40	0.34
2	K10C3NT4	4	3	10	1885	2566	3577	367.5	39.10	0.49	0.41	0.35
3	K10C6NT2	2	6	10	2584	3526	4932	442	44.60	0.58	0.48	0.43
4	K10C9NT0	0	9	10	2391	3278	4610	418	43.56	0.70	0.52	0.44
5	K10C9NT4	4	9	10	2921	4182	6076	424	49.36	0.71	0.53	0.45
6	K20C3NT2	2	3	20	2593	3654	5254	413	46.60	0.48	0.40	0.34
7	K20C6NT0	0	6	20	2328	3274	4707	386	44.76	0.50	0.44	0.38
8	K20C6NT2	2	6	20	3316	4675	6713	470	50.60	0.55	0.46	0.40
9	K20C6NT4	4	6	20	2682	3717	5176	450	45.42	0.52	0.45	0.39
10	K20C9NT2	2	9	20	4277	6085	9013	510	55.80	0.67	0.50	0.43
11	K30C3NT0	0	3	30	2024	2750	3871	384	40.32	0.42	0.37	0.31
12	K30C3NT4	4	3	30	2313	3062	4209	442.5	40.86	0.44	0.38	0.312
13	K30C6NT2	2	6	30	3167	4227	5841	522	46.72	0.53	0.43	0.38
14	K30C9NT0	0	9	30	2821	3934	5354	480	45.42	0.62	0.46	0.38
15	K30C9NT4	4	9	30	3585	5000	7134	507	51.20	0.63	0.48	0.41
16	K10*	-	-	10	207	606	1206	2.00	29.94	0.45	0.38	0.32
17	K20*	-	-	20	286	804	1580	7.00	34.90	0.40	0.35	0.3
18	K30*	-	-	30	272	727	1410	12.00	32.16	0.36	0.31	0.28

* No design

$$Y = \beta_0 + \sum_{i=1}^{n} \beta_i X_i + \sum_{i=1}^{n} \beta_{ii} X_i^2 + \sum_{i=1}^{n} \sum_{j=1}^{n} \beta_{ij} X_i X_j + e \quad (1)$$

where Y is the predicted response, β_0 is the intercept term, β_i are the linear coefficients, and β_{ii} and β_{ij} are the quadratic and interaction coefficients, respectively. X_i and X_j are independent variables and e is the residual error between the predicted and real experimental values.

Furthermore, variance analysis (ANOVA) is incorporated for assessing the interaction between the various parameters and also the impact of an individual parameter. Also, it is used for assessing the statistical precision and importance of the used model.

2.3 Method of testing

In this study, a CD triaxial test was performed according to ASTM D7181-11 [36]. Figure 3 indicates the tri-axial test apparatus used in this research in the laboratory scale. The specimens considered for the triaxial tests were prepared in a mold with a 38 mm internal diameter and height of 76 mm. The materials needed for each experiment are determined based on the maximum dry unit weight and optimum moisture content of the compound obtained from the standard proctor test, and the internal volume of the triaxial test mold. The mix design is such that, first, the NT suspension is fully mixed with distilled water and cement to make a mortar, then a mixture of sand and clay is added to the cement mortar and is well blended [13]. Figure 4 shows the NT (a); Suspension NT and distilled water (b). Then this volume of compound is laid in five equal layers within the cylinder and is statically compacted according to AASHTO–T307-99 [37]. After the preparation period, the specimen is removed from the mold. To preserve the moisture of the specimens for the 28-days curing period, after being removed from the molds, they are wrapped in cellophane sheets and kept at 20 °C in the laboratory. The CD triaxial tests are performed in the fully saturated condition and under pressure values of 100, 300 and 600 kPa. Then carbon dioxide gas is passed through the specimens for 3 hours. This procedure causes removal of the air enclosed between the particles. Also due to higher rate of CO_2 solution in water, the saturation of the specimen is rapid and complete. Next, water is run through the specimen from bottom to top with a low pressure for one hour. At the final stage, to ensure a value greater than 0.98 for the Skempton's pore pressure parameter (B), the specimens are saturated under 300 kPa back pressure. The specimens were consolidated under the intended confining pressure and then axial loading was applied with an axial strain rate equal to 0.01 mm/min.

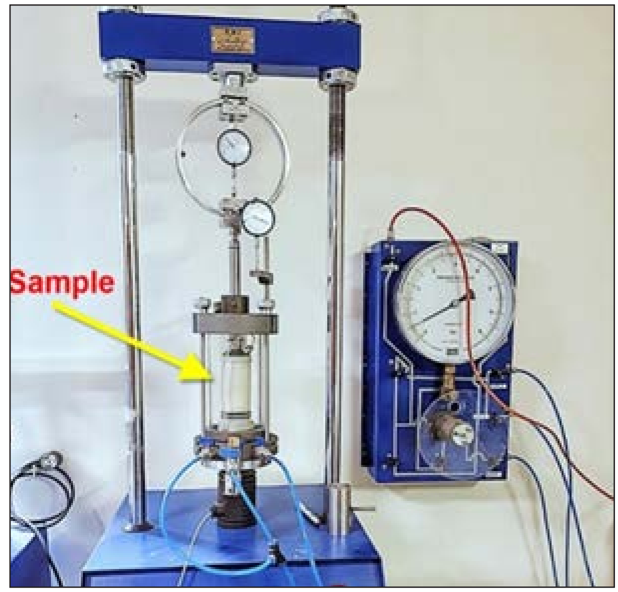

Figure 3. Tri-axial test apparatus.

(a) (b)

Figure 4. (a) NT; (b) Suspension NT and distilled water.

3 RESULTS

3.1 Statistical analyses

The results of the experimental tests obtained from the CD triaxial tests are given in Table 7 and are analyzed by RSM. The consistency and importance of the model are investigated using the coefficient of determination and the adjusted coefficient of determination (R^2 and Adj R^2), respectively (Table 8). The presented statistical models have a high coefficient of determination, which shows that the models have well fitted the data. The minimum p value which is less than 0.05 highlights the high significance of the model (Table 8). The low coefficient of variation (C.V) given in Table 8, shows the high precision of presented models. Therefore, the quadratic regression

Table 8. ANOVA for the quadratic models.

Statistical Measure	Responses models							
	Peak deviator stress (kPa)			Mechanical parameters		Brittleness index		
	σ_3=100 kPa	σ_3=300 kPa	σ_3=600 kPa	Cohesion (kPa)	Friction angle (degree)	σ_3=100 kPa	σ_3=300 kPa	σ_3=600 kPa
R^2	0.9684	0.9694	0.9613	0.9888	0.9841	0.9960	0.9959	0.9956
Adj R^2	0.9400	0.9400	0.9264	0.9787	0.9697	0.9925	0.9922	0.9917
CV	5.56	5.75	6.84	1.67	1.77	1.25	0.84	0.93
p value	<0.0001	<0.0001	<0.0001	<0.0001	<0.0001	<0.0001	<0.0001	<0.0001
F value	34.06	35.16	27.57	97.90	68.67	279.91	269.42	252.65

Table 9. Proposed model for the mechanical parameters, peak deviator stress and brittleness index using ANOVA.

Source	Models							
	Peak deviator stress (kPa)			Mechanical parameters		Brittleness index		
	σ_3=100 kPa	σ_3=300 kPa	σ_3=600 kPa	Cohesion (kPa)	Friction angle (degree)	σ_3=100 kPa	σ_3=300 kPa	σ_3=600 kPa
Intercept	3277.45	4603.75	6607.45	470.47	50.2	0.550	0.46	0.40
A	217.40	301.20	437.20	20.00	1.39	0.007	0.006	0.0062
B	553.20	816.80	1201.8	40.90	4.05	0.10	0.053	0.046
C	248.10	314.20	395.60	36.10	0.99	-0.032	-0.022	-0.022
AB	96.00	171.38	323.63	-8.75	1.24	-0.00125	0.00125	0.0035
AC	35.75	23.38	41.63	4.38	-0.072	0.00125	0.00125	0.0015
BC	36.25	63.38	69.63	1.13	-0.047	-0.00625	-0.00625	-0.004
A^2	-714.64	-1001.36	-1507.64	-53.18	-4.52	-0.032	-0.001	-0.015
B^2	215.36	372.64	684.36	-9.68	1.59	0.033	-0.005	-0.015
C^2	-344.14	-620.36	-1062.64	10.82	-3.95	0.013	0.00	0.00464

Table 10. ANOVA for the response parameters and significance of the components in quadratic models.

Source	*p* value							
	Peak deviator stress (kPa)			Mechanical parameters		Brittleness index		
	σ_3=100 kPa	σ_3=300 kPa	σ_3=600 kPa	Cohesion (kPa)	Friction angle (degree)	σ_3=100 kPa	σ_3=300 kPa	σ_3=600 kPa
A	0.0015	0.0019	0.0051	< 0.0001	0.0003	0.0094	0.0005	0.0003
B	< 0.0001	< 0.0001	<0.0001	< 0.0001	< 0.0001	< 0.0001	< 0.0001	< 0.0001
C	0.0006	0.0015	0.0090	< 0.0001	0.0036	< 0.0001	< 0.0001	< 0.0001
AB	0.118	0.0602	0.0397	0.0076	0.0017	0.6198	0.371	0.0203
AC	0.5385	0.7785	0.7674	0.1271	0.8095	0.6198	0.371	0.2652
BC	0.533	0.4516	0.6222	0.6778	0.8744	0.0284	0.0009	0.0104
A2	< 0.0001	< 0.0001	<0.0001	< 0.0001	< 0.0001	< 0.0001	0.0013	< 0.0001
B2	0.0482	0.0223	0.0150	0.0562	0.0097	< 0.0001	0.0528	< 0.0001
C2	0.0049	0.0012	0.0011	0.0366	< 0.0001	0.0121	1	0.0582

modelling based on the assumed statistical parameters is coded as the most consistent model among the three variables and the eight corresponding responses are given in Table 9. The *p* value obtained from the ANOVA is given in Table 10 to investigate the significance of each term in each model. The *p* values less than 0.05 demonstrate the significance of the term and values greater than 0.1 indicate a lack of significance of that term.

3.2 Peak-deviator stress

The peak-deviator-stress values for improved specimens are given in Table 7, per three confining pressures of 100, 300 and 600 kPa. The percentage of independent variables in the specimens is determined based on the central composite design method. The effect of independent variables percentage at peak-deviator-stress values and per confining pressure of 100 kPa is shown in Figures 5(a), 5(b) and 5(c). Examining Figure 5 (a) shows the interaction between NT and cement in terms of peak-deviator stress at a constant kaolinite value (20 %) and also it shows that the cement contents of 3–9 % cause an increase in the peak-deviator stress. Also, the NT values from low to high amounts of cement increase in the peak deviator stress so that the ascending trend takes the form of a concave downward parabola. It means that with an increase of NT from 0 to 2 % the peak-deviator stress also increases, and at 2 % reaches its peak value and from 2 to 4 % it begins to decrease. For example, the peak deviator stress value for three specimens of K20C6NT0, K20C6NT2 and K20C6NT4 is 2328, 3316 and 2682 kPa, respectively. As the amount of cement increases from low to high values, the effectiveness of NT increases, which shows that the interaction between the amount of cement and NT in the optimal value has a positive effect on the peak-deviator stress. Figure 5 (b) shows the interaction between NT and kaolinite in terms of peak deviator stress at a constant cement content (6 %). It is also observed that the highest peak-deviator stress occurs in the optimal value of NT, namely 2 %. However, regarding the interaction between kaolinite and NT, their effects seem to be independent of each other. This is because kaolinite fills the sand pores with its filling effect and increases the density and specific gravity of the sand and subsequently increases the peak-deviator stress. NT also affects the hydration properties of the cement slurry matrix through its nucleation and filling effect, meaning that it reduces the degree of orientation of calcium hydroxide (CH) and limits the size of the crystals. These effects can be seen in the studies of Li et al. [29]. Observing the effect of kaolinite, the peak-deviator stress in three samples K10C6NT2, K20C6NT2 and K30C6NT2 are 2584, 3316 and 3167 kPa, respectively.

Figure 5(c) also shows the diagram of the interaction between cement and kaolinite at a constant NT value (2 %). It is observed that with increasing the cement content from 3 to 9 % in all kaolinite values from low to high, the peak-deviator stress increases. The peak deviator stress value in three samples K20C3NT2, K20C6NT2 and K20C9NT2 is 2593, 3316 and 4277 kPa, respectively. In fact, regarding the interaction between cement and kaolinite, a very positive interactive effect can be observed. Despite the chemical properties with the filling effect and high specific gravity (G_s) (3.15) compared to kaolinite and sand (2.60 and 2.75, respectively), cement causes the maximum dry unit weight of the sample to increase.

In addition, the corresponding analyses of the interactive effect of the variables on the peak-deviator stress values are conducted for the confining pressure values of 300 and 600 kPa, respectively. The results are qualitatively similar to the case of 100-kPa confining pressure.

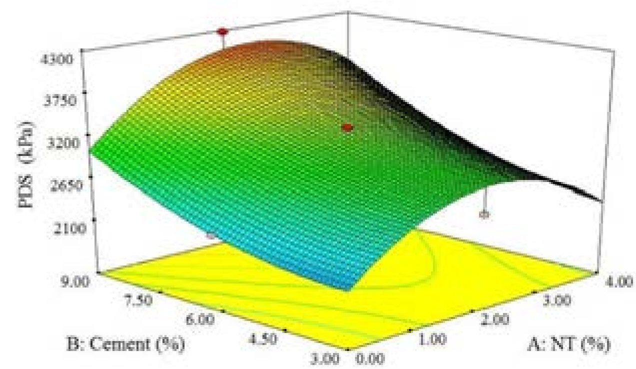

(a)

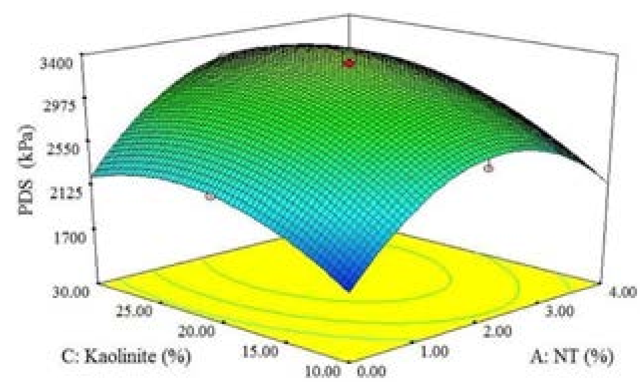

(b)

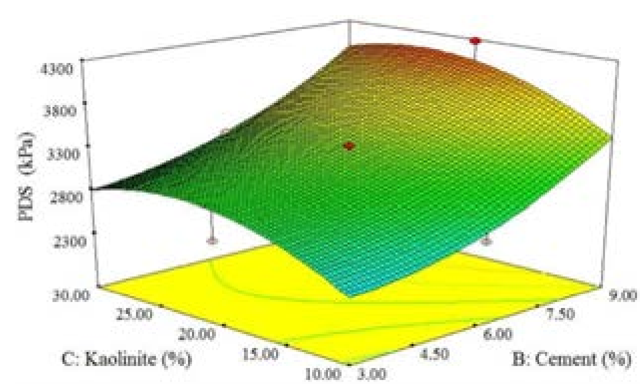

(c)

Figure 5. 3D response surface plots for interactive effects of variables on peak deviator stress per confining pressure equal to 100kPa at the constant amount of (a) kaolinite = 20 %; (b) cement = 6 %; (c) NT= 2 %.

3.3 Cohesion

Figure 6(a) shows the interactive effect of both cement and NT amounts on the cohesion at a constant kaolinite value (20 %). It is observed that cement from low to high amounts (3–9 %) causes an increase in cohesion. The effect of cement amount on cohesion for three specimens of K20C3NT2, K20C6NT2 and K20C9NT2 is 413, 470 and 510 kPa, respectively. Also, the cohesion increases with an increase in the NT amount in the form of a concave downward parabola, so that cohesion reaches its peak value at 2 % NT. The effect of NT amount on cohesion for three specimens of K20C6NT0, K20C6NT2 and K20C6NT4 is 386, 470 and 450 kPa, respectively. Regarding the effect of the interaction between cement and NT on the cohesion, it is observed that the amount of NT has a positive effect, especially for the optimal value. Figure 6 (b) shows the effect of interaction between kaolinite and NT values on the cohesion at a constant cement content (6 %). It is observed that increasing the amount of kaolinite from low to high (10 to 30 %) in all NT values increases the cohesion. The cohesion in three samples K10C6NT2, K20C6NT2 and K30C6NT2 is 418, 470 and 522 kPa, respectively. Figure 6(c) shows the interactive effect of both cement and kaolinite amounts on the cohesion at a constant amount of NT (2 %). It is seen that both cement and kaolinite from low to high amounts (3–9 % for cement and 10–30 % for kaolinite) cause an increase in the cohesion value. The combined effect of cement and kaolinite to increase the cohesion is very positive, as by increasing the amount of cement and kaolinite in their highest values, 9 and 30 %, the cohesion reaches its maximum value, namely 522 kPa. The research of Tang et al. shows that the cohesion increases with increasing the cement content [38]. Yao et al. also showed that the cohesion grows exponentially with increasing cement content [14].

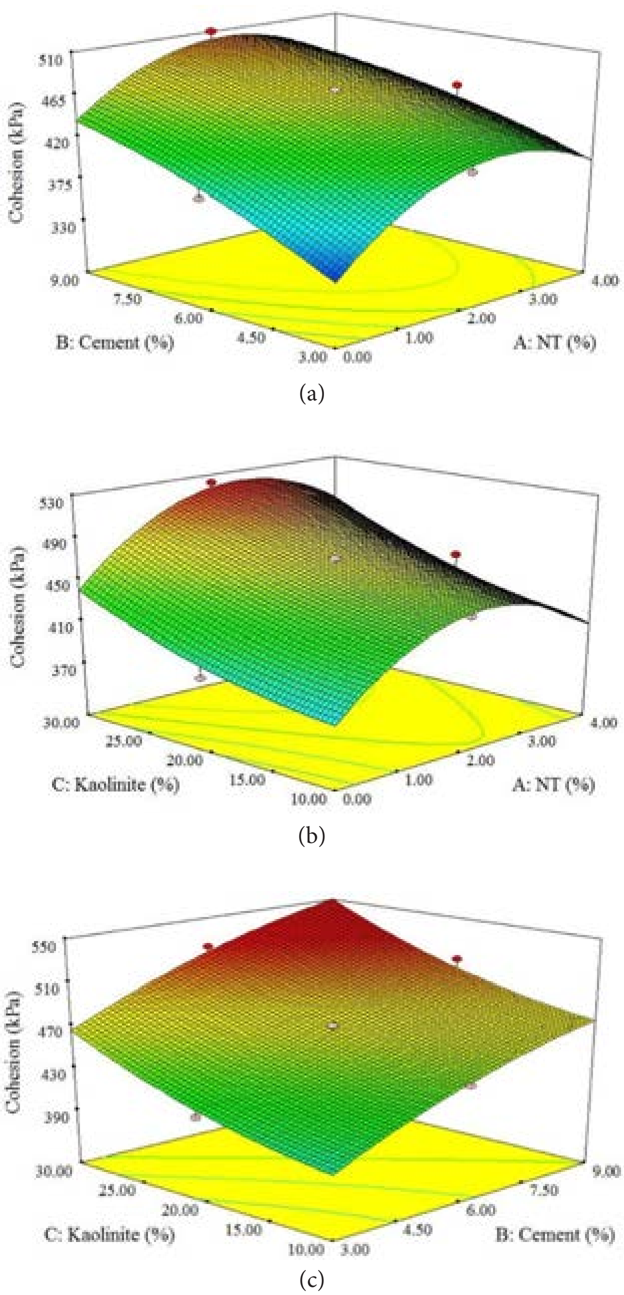

Figure 6. 3D response-surface plots for interactive effects of variables on cohesion at a constant amount of (a) kaolinite = 20 %; (b) cement = 6 %; (c) NT= 2 %.

3.4 Friction angle

Figure 7(a) shows the interactive effect of both NT and cement amounts at a constant kaolinite value (20 %). The results show that cement amounts of 3–9 % cause an increase in the friction angle. Also, the NT amounts cause an increase in the friction angle so that the ascending trend is in the form of a concave downward parabola. It means that the friction angle has an ascending trend with an increase in NT from 0 to 2 % and then from 2 to 4 % turns into a descending trend. The effect of NT on the friction angle for three specimens of K20C6NT0, K20C6NT2 and K20C6NT4 is 44.76, 50.60 and 45.42 degrees, respectively. Due to the interaction between cement and NT, NT has the greatest effect on the friction angle in the optimal percentage of 2 %, and this trend is increasing with the increase in the cement content. In fact, the combination of cement with NT in the optimal state is a positive and significant combination.

Figure 7(b) shows the interactive effect of both NT and kaolinite amounts for a constant amount of cement (6 %). The results show that the friction angle increases per 10–30 % kaolinite clay, so that the friction angle reaches its peak value at 20 % kaolinite clay. For example,

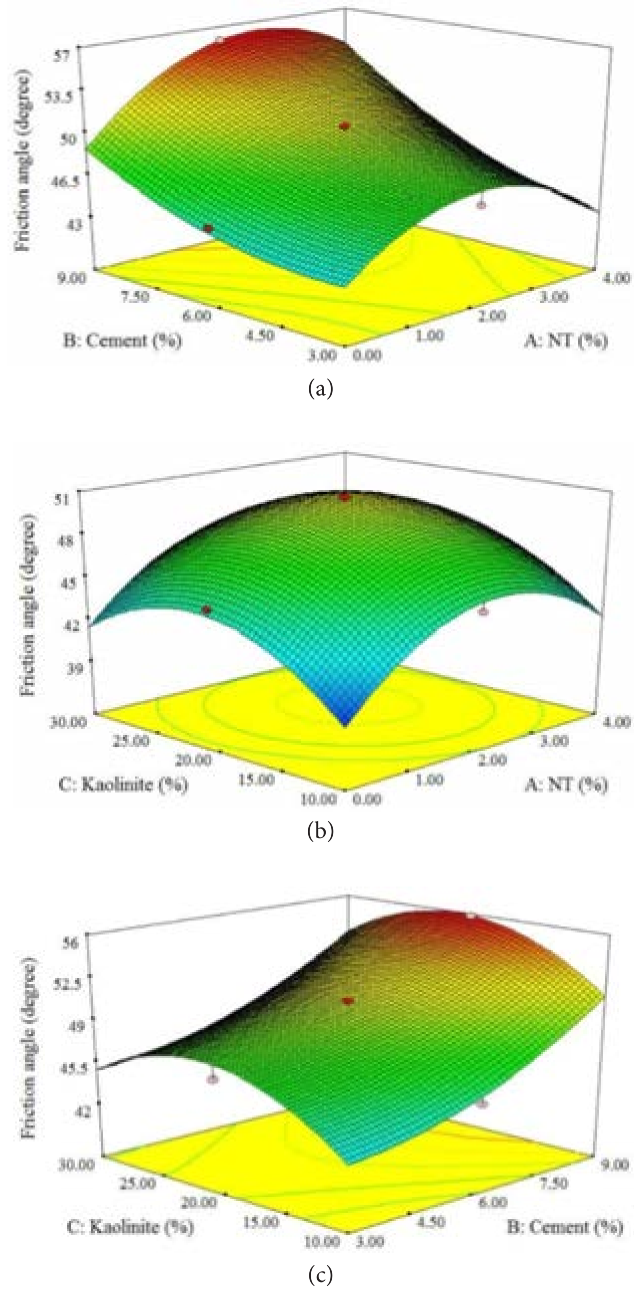

Figure 7. 3D response-surface plots for interactive effects of variables on cohesion at the constant amount of (a) kaolinite = 20 %; (b) cement = 6 %; (c) NT= 2 %.

the friction angle for three specimens of K10C6NT2, K20C6NT2 and K30C6NT2 is 43.56, 50.60 and 46.72 degrees, respectively. It is observed that kaolinite and NT in their optimal state, 20 % kaolinite and 2 % NT, will have the greatest effect on the friction angle and their effects are independent of each other. In fact, kaolinite fills the sand pores and causes the best state of sample density and interlocking to its optimal value. The effect of NT on cement is due to the nucleation and filling effects and its effect is independent of kaolinite.

Figure 7(c) also shows the interactive diagram of both cement and kaolinite for a constant amount of NT (2 %). It is observed that with an increase in the cement amount from 3 to 9 %, the friction angle increases. So, for three specimens of K20C3NT2, K20C6NT2 and K20C9NT2 the friction angle equals 46.60, 50.60 and 55.80 degrees, respectively. As can be seen, increasing the cement content in the optimal amount of kaolinite increases the friction angle of the samples. The studies of Tang et al. [38] and Yao et al. [7] can be cited to confirm the effect of cement on increasing the friction angle.

3.5 Brittleness Index

Consoli et al. [39] introduced the brittleness index as a measure for the brittle behavior of the soil:

$$I_B = \frac{q_{max}}{q_{min}} - 1 \qquad (2)$$

where q_{max} and q_{min} denote the peak-deviator stress and the residual-deviator stress, respectively, and I_B represents the brittleness index. The variation of the brittleness index as a function of cement, NT and kaolinite percentages is shown in Figure 8 for a confining pressure of 100 kPa. It is seen that with an increase in the cement content from 3 to 9 %, the brittleness index increases considerably. With an increase in the NT percentage from 0 to 4 %, the changes are in this way that from 0 to 2 % the brittleness index increases slightly (reaching a maximum at 2 %) and from 2 to 4 % has a descending trend. With an increase in the kaolinite percentage from 10 to 30 %, it is seen that the brittleness index decreases. It should be noted that the obtained results are qualitatively similar to the case of 100-kPa confining pressure. Table 7 represents the values of the brittleness index per three stress levels of 100, 300 and 600 kPa. This indicates that with an increase in the confining pressure, the brittleness index decreases. Kutanaei and Choobbasti [9] during their studies on the triaxial behavior of cemented soils observed that with an increase in the confining pressure, the brittle behavior of cemented soils turns into a flexible behavior.

For example, in specimen K10C6NT2, where its drained triaxial behavior is depicted in Figure 9, the brittleness index is equal to 0.58, 0.48 and 0.43 at confining pressures of 100, 300 and 600 kPa, respectively. This indicates that at larger depths (with respect to the smaller depths), the loss in the deviator residual stress is smaller with respect to the peak value.

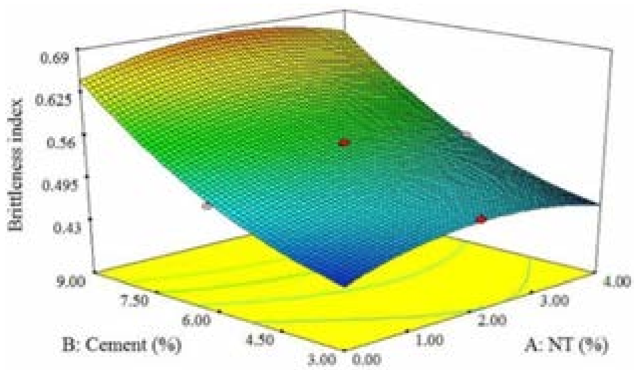

(a)

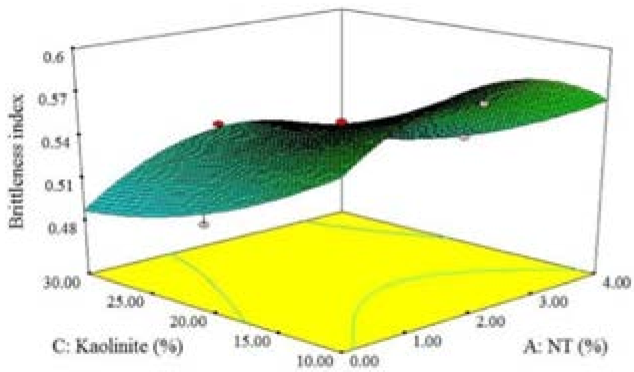

(b)

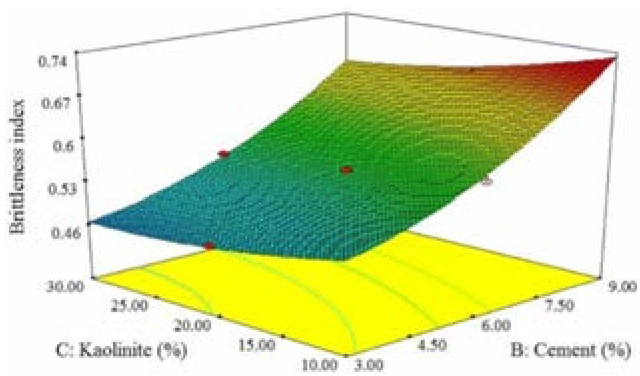

(c)

Figure 8. 3D response-surface plots for interactive effects of variables on the brittleness index per confining pressure equal to 100 kPa at the constant amount of (a) kaolinite = 20 %; (b) cement = 6%; (c) NT= 2 %.

4 PERFORMANCE OF KAOLINITE, CEMENT AND NT IN THE CEMENTED CLAYEY SAND BEHAVIOR

With an increase in the cement content from 3 to 9 %, the amounts of peak deviator stress, cohesion and friction angle increase. Considering that the density of solid grains in the cement is 3.15, that of sand is 2.75,

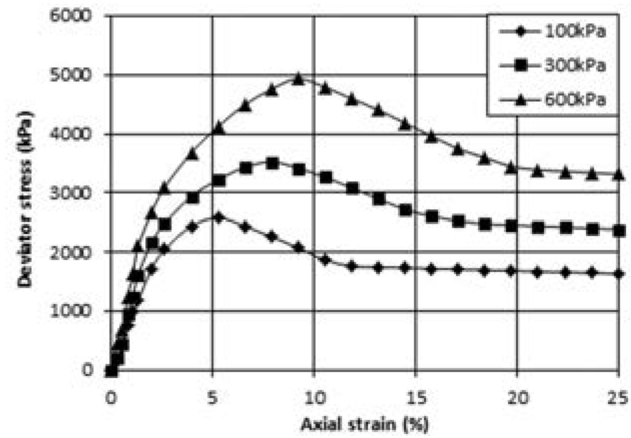

(a)

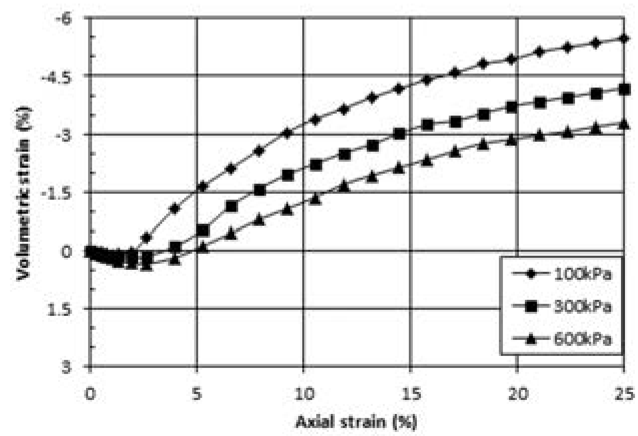

(b)

Figure 9. Drained triaxial behavior of K10C6NT2, (a) Variation of deviator stress versus the axial strain, (b) Variation of volumetric strain versus the axial strain.

and that of kaolinite clay mineral is 2.6, therefore the cement particles cause an increase in the maximum dry density of the clayey sand in all three states of basic soil (K10, K20 and K30). On the other hand, the cement particles are finer than the clayey sand and by filling the void space between them cause increased compaction of the soil, leading to increased coherence and maximum density of the cemented soil. In fact, two factors cause increased compaction and coherence in the soil: one is the higher density of solid particles in cement with respect to the soil and second is the finer particles of cement with respect to the soil and these two factors lead to an increase in the peak deviator stress, cohesion and friction angle of the cemented clayey sand [40]. Also, considering the cohesion rate, by change in the kaolinite amount, it could be seen that from low to high amounts of kaolinite (10–30 %) that the cohesion is increased, which is also compatible with the behavior and nature of the clay soil. The friction angle at first increases with low to medium amounts (10–20 %) of kaolinite. Then from medium to high amounts (20–30 %) its ascending trend slows down. The change in the behavior of the friction angle with kaolinite could be justified in this way that from 10 to 20 % kaolinite, as its particles are finer than those of sand, they fill the void space between them and cause increased compaction and coherence in the sand and clay mixture. Whereas the density of solid particles in the clay is 2.60 and when kaolinite content exceeds 20 % it surpasses the void space in sand and occupies the place of sand solid particles with 2.75 density, leading to a reduced friction angle in the range of 20–30 % kaolinite. One important issue is the role of NT in the cement matrix of a soil processed with cement. It is seen that with an increase in NT content from 0 to 2 %, both cohesion and friction angle increase and from 2 to 4 % the ascending trend slows down so it takes a concave down form. Han et al. have stated that if a uniform distribution of nanoparticles is created in the cement mortar with a proper distance between the core and shell (nano and the cover made by the hydration products around nano), then with an increase in the nano percentage its modifying effect would increase [41]. Among the reasons for enhanced mechanical properties of the cemented clayey sand containing NT is its nucleation effect, which absorbs water and hydration products. Therefore: 1) the hydration rate of the specimens is modified at the first stage. 2) NT not only reduces orientation degree of calcium hydroxide (CH) but also restricts its size. Therefore, the interface structure is optimized and its properties are modified, which both help with thenhanced mechanical properties. 3) NT also could modify the compactability and reduce the porosity of the specimen. 4) NT has the effect of filling the micro-holes and micro-cracks in the cement mortar. A reduction in the mechanical properties due to an increase of NT content from 2 to 4 % could be attributed to its high surface energy, which causes an accumulation of the core-shell nanoparticles and a reduction in the modifying effect of the NT [30][41].

5 CONCLUSION

This research investigated the combined effect of cement and NT with a confining pressure on the clayey sand (with variable amounts of clay). The variables in this research (amount of kaolinite, cement and NT) were adjusted based on the RSM, with the aim of investigating their effect on the mechanical properties of clayey sand. The examined parameters were the peak-deviator stress at three confining pressure (100, 300 and 600 kPa), the cohesion, the effective friction angle and the brittleness index at three confining pressure (100, 300 and 600 kPa). Eight models were presented considering the experimental results with small p values, negligible incompatibility in terms of R^2 and Adj R^2 and low CV values. According to the findings in the present study the following conclusions could be derived concerning the mechanical properties and triaxial behavior of the specimens:

- An increase in the amount of cement from low to high (3 to 9 %) causes an increase in the peak-deviator stress, cohesion, friction angle and brittleness index.
- An increase in the amount of kaolinite from low to high (10 to 30 %) causes an increase in cohesion. The peak-deviator stress and friction-angle values increase in the range 10 to 20 % kaolinite. So that at 20 % kaolinite they reach their peak values and then, i.e., at 20 to 30 % kaolinite, the ascending trend reverses. The brittleness index takes a descending trend at 10 to 30 % kaolinite.
- The peak-deviator stress, cohesion, effective friction angle and brittleness index increase with an increase of NT. These values increase from 0 to 2 % of NT, and reach their peak values at 2 % and from 2 to 4 % they take a descending trend.

REFERENCES

[1] Lorenzo, A. L., Bergado, D. T. 2004. Fundamental parameters of cement-admixed clay new approach, J GEOTECH GEOENVIRON, 130(10), 1042–1050. https://doi.org/10.1061/(ASCE)1090-0241(2004)130:10(1042).

[2] Sariosseiri, F., Muhunthan, B. 2009. Effect of cement treatment on geotechnical properties of some Washington State soils, Eng Geol, 104, 119–125. https://doi.org/10.1016/j.enggeo.2008.09.003.

[3] Ismail, M. A., Joer, H. A., Sim, W. H., Randolph, M. F. 2002. Effect of cement type on shear behaviour of cemented calcareous soil", J GEOTECH GEOENVIRON, 128(6) 520-529. https://doi.org/10.1061/(ASCE)1090-0241(2002)128:6(520).

[4] Garzón, E., Cano, M., O'Kelly, B. C., Sánchez-Soto, P. 2015. Phyllite clay-cement composites having improved engineering properties and material applications, Appl. Clay Sci, 114 229–233. https://doi.org/10.1016/j.clay.2015.06.006.

[5] Jin, L., Song, W., Shu, X., Huang, B. 2018. Use of water reducer to enhance the mechanical and durability properties of cement-treated soil, Constr Build Mater, 159 690-694. https://doi.org/10.1016/j.

conbuildmat.2017.10.120.
[6] Lo, S. C. R., Lade, P. V., Wardani, S. P. R., 2002.An experimental study of the mechanics of two weakly cemented soils. GEOTECH TEST J, 26(3), 328-341. https://doi.org/10.1520/GTJ11301J.
[7] Yao, K., Pan, Y., Jia, L., Yi, J. T., Hu, J., & Wu, C. (2019). Strength evaluation of marine clay stabilized by cementitious binder. Marine Georesources & Geotechnology, 38(6), 730-743. https://doi.org/10.1080/1064119X.2019.1615583.
[8] Schnaid, F., Prietto, P. D. M., Consoli, N.C. 2001. Characterization of cemented sand in triaxial compression, J GEOTECH GEOENVIRON, 127(10) 492-499. https://doi.org/10.1061/(ASCE)1090-0241(2001)127:10(857).
[9] Kutanaei, S. S., Choobbasti, A. J. 2016. Triaxial behavior of fiber-reinforced cemented sand, J ADHES SCI TECHNOL, 30 (6) 579-593. https://doi.org/10.1080/01694243.2015.1110073.
[10] Bahmani, S. H., Huat B. B. K., Asadi, A., Farzadnia, N. 2014. Stabilization of residual soil using SiO2 nanoparticles and cement, Constr Build Mater, 64 350–359. https://doi.org/10.1016/j.conbuildmat.2014.04.086.
[11] Choobbasti, A. J., Vafaei, A., Kutanaei, S. S. 2015. Mechanical Properties of Sandy Soil Improved with Cement and Nanosilica, Open Eng, 5 111–116. https://doi.org/10.1515/eng-2015-0011.
[12] Ghasabkolaei, N., Janalizadeh, A., Jahanshahi, M., Roshan, N., Ghasemi, S. E. 2016. Physical and geotechnical properties of cement-treated clayey soil using silica nanoparticles: An experimental study, Eur. Phys. J. Plus, 131(5) 1–11. https://doi.org/10.1140/epjp/i2016-16134-3.
[13] Meng, T., Qiang, Y., Hu, A., Xu, C. H., Lin, L. 2017. Effect of compound nano-CaCO3 addition on strength development and microstructure of cement-stabilized soil in the marine environment, Constr Build Mater, 151, 775–781. https://doi.org/10.1016/j.conbuildmat.2017.06.016.
[14] Yao, K., An, D., Wang, W., Li, N., Zhang, C., & Zhou, A. 2020. Effect of nano-MgO on mechanical performance of cement stabilized silty clay. Marine Georesources & Geotechnology, 38(2), 250-255. https://doi.org/10.1080/1064119X.2018.1564406.
[15] Yao, K., Wang, W., Li, N., Zhang, Ch., Wang, L. 2019. Investigation on strength and microstructure characteristics of nano-MgO admixed with cemented soft soil. Constr Build Mater. 206 160–168. https://doi.org/10.1016/j.conbuildmat.2019.01.221.
[16] Wang, W., Li, Y., Yao, K., Li, N., Zhou, A., & Zhang, C. 2019. Strength properties of nano-MgO and cement stabilized coastal silty clay subjected to sulfuric acid attack. Marine Georesources & Geotechnology, 1-10. https://doi.org/10.1080/1064119X.2019.1656313.
[17] Wang, W., Fu, Y., Zhang, C., Li, N., & Zhou, A. 2020. Mathematical Models for Stress–strain Behavior of Nano Magnesia-Cement-Reinforced Seashore Soft Soil. Mathematics, 8(3), 456. https://doi.org/10.3390/math8030456.
[18] Kulanthaivel, P., Soundara, B., Velmurugan, S., & Naveenraj, V. 2020. Experimental investigation on stabilization of clay soil using nano-materials and white cement. Materials Today: Proceedings. https://doi.org/10.1016/j.matpr.2020.02.107.
[19] Li, N., Lv, S., Wang, W., Guo, J., Jiang, P., & Liu, Y. 2020. Experimental investigations on the mechanical behavior of iron tailings powder with compound admixture of cement and nano-clay. Construction and Building Materials, 254, 119259. https://doi.org/10.1016/j.conbuildmat.2020.119259.
[20] Jalal, M., Ramezanianpour, A. A., & Pool, M. K. (2013). Split tensile strength of binary blended self compacting concrete containing low volume fly ash and TiO2 nanoparticles. Composites Part B: Engineering, 55, 324-337. https://doi.org/10.1016/j.compositesb.2013.05.050.
[21] Meng, T., Yu, Y., Qian, X., Zhan, S., Qian, K. 2012. Effect of nano-TiO2 on mechanical properties of cement mortar. Constr Build Mater. 29, 241-245. https://doi.org/10.1016/j.conbuildmat.2011.10.047.
[22] Chen, P., Wei, B., Zhu, Xi., Gao, D., Gao, Y., Cheng, J., Liu, Y., 2019. Fabrication and characterization of highly hydrophobic rutile TiO2-based coatings for self-cleaning. Ceram. Int. 45 (5). 6111-6118. https://doi.org/10.1016/j.ceramint.2018.12.085.
[23] Chen, J., Poon, C.S., 2009. Photocatalytic construction and building materials: from fundamentals to applications. Build Environ. 44(9). 1899-906. https://doi.org/10.1016/j.buildenv.2009.01.002.
[24] Hassan, M. M., Dylla, H., Mohammad, L.N., Rupnow, T., 2010. Evaluation of the durability of titanium dioxide photocatalyst coating for concrete pavement. Constr Build Mater. 24(14). 56-61. https://doi.org/10.1016/j.conbuildmat.2010.01.009.
[25] Shen, S., Burton, M., Jobson, B., Haselbach, L., 2012. Pervious concrete with titanium dioxide as a photocatalyst compound for a greener urban road environment. Constr Build Mater. 35(8), 74-83. https://doi.org/10.1016/j.conbuildmat.2012.04.097.
[26] Ngoh, Y.S., Nawi, M.A., 2016. Fabrication and properties of an immobilized P25 TiO_2- montmorillonite bilayer system for the synergistic photocatalytic-adsorption removal of methylene blue.

Mater. Res. Bull. 76, 8–21. https://doi.org/10.1016/j.materresbull.2015.11.060.
[27] Jalal, M., Fathi, M., Farzad, M., 2013. Effects of fly ash and TiO2 nano particles on rheological, mechanical, microstructural and thermal properties of high strength self-compacting concrete. Mech Mater. 61, 11-27. https://doi.org/10.1016/j.mechmat.2013.01.010.
[28] Gopalakrishnan, R., Vignesh, B., Jeyalakshmi, R. 2020. Mechanical, electrical and microstructural studies on nano-TiO2 admixtured cement mortar cured with industrial wastewater. Eng. Res. Express. 2, 025010. https://doi.org/10.1088/2631-8695/ab899c.
[29] Zhang, R., Cheng, X., Hau, P., Ye, Z. 2015. Influence of nano-TiO2 on the properties of cement based material: hydration and drying shrinkage. Constr Build Mater. 81, 35-41. https://doi.org/10.1016/j.conbuildmat.2015.02.003.
[30] Li, Zh., Han, B., Yu, X., Dong, S., Zhang, L., Dong, X., Ou, J., 2017. Effect of nano-titanium dioxide on mechanical and electrical properties and microstructure of reactive powder concrete. Mater. Res. Express. 4(9),1-23. https://doi.org/10.1088/2053-1591/aa87db.
[31] ASTM D422-63(2007)e2. 2007. Standard Test Method for Particle-Size Analysis of Soils (Withdrawn 2016), ASTM International, West Conshohocken, PA. https://doi.org/10.1520/D0422-63R07E02.
[32] Montgomery, D. C. 2012. Design and Analysis of Experiments, 8th Edition, John Wiley & Sons, Inc.
[33] Yetilmezsoy, K., Demirel, S., Vanderbei, R. J. 2009. Response surface modeling of Pb(II) removal from aqueous solution by Pistacia vera L.: Box–Behnken experimental design, J. Hazard. Mater, 171 551–562. https://doi.org/10.1016/j.jhazmat.2009.06.035
[34] Singh, K. P., Gupta, S., Singh, A. K., Sinha, S. 2011. Optimizing adsorption of crystal violet dye from water by magnetic nanocomposite using response surface modeling approach, J. Hazard. Mater, 186 1462–1473. https://doi.org/10.1016/j.jhazmat.2010.12.032.
[35] Shahbazi, M., Rowshanzamir, M., Abtahi, S. M., Hejazi, S. M. 2017. Optimization of carpet waste fibers and steel slag particles to reinforce expansive soil using response surface methodology, Appl. Clay Sci, 142 185–192. https://doi.org/10.1016/j.clay.2016.11.027
[36] ASTM D7181-11. 2011. Method for Consolidated Drained Triaxial Compression Test for Soils, ASTM International, West Conshohocken, PA. https://doi.org/10.1520/D7181-11.
[37] Groeger, J., Rada, G., Lopez, A. AASHTO T307 — Background and Discussion, in Resilient Modulus Testing for Pavement Components, ed. Durham, G., DeGroff, W., Marr, W (West Conshohocken, PA: ASTM International, 2003), (2003) 16-29. https://doi.org/10.1520/STP12519S.
[38] Tang, C., Shi, B., Gao, W., Chen, F., & Cai, Y. (2007). Strength and mechanical behavior of short polypropylene fiber reinforced and cement stabilized clayey soil. Geotextiles and Geomembranes, 25(3), 194-202. https://doi.org/10.1016/j.geotexmem.2006.11.002.
[39] Consoli, N. C., Prietto, P. D. M., Ulbrich, L. A,. 1998. Influence of fiber and cement addition on behavior of sandy soils, . J. Geotech. Eng, 124 1211–1214. https://doi.org/10.1061/(ASCE)1090-0241(1998)124:12(1211).
[40] Kutanaei, S. S., Choobbasti, A. J. 2017. Effects of nanosilica particles and randomly distributed fibers on the ultrasonic pulse velocity and mechanical properties of cemented sand, Mater Civil Eng, 29(3) 1-9. https://doi.org/10.1061/(ASCE)MT.1943-5533.0001761.
[41] Han, B., Zhang, L., Zeng, S., Dong, S., Yu, X., Yang, R., Ou, J. 2017. Nano-core effect in nano engineered cementitious composites", COMPOS PART A-APPL S, 95 100-109. https://doi.org/10.1016/j.compositesa.2017.01.008.

ELECTROKINETIC TREATMENT OF SOFT SOILS: EXPERIMENTAL STUDY AND NUMERICAL MODELS

ELEKTROKINETIČNI POSTOPEK ZA MEHKE ZEMLJINE: EKSPERIMENTALNA ŠTUDIJA IN NUMERIČNI MODELI

Abiola Ayopo Abiodun *(corresponding author)*
Eastern Mediterranean University,
Department of Civil Engineering
Famagusta, North Cyprus via Mersin 10, Turkey
E-mail: abiola.abiodun@emu.edu.tr

Zalihe Nalbantoglu
Eastern Mediterranean University,
Department of Civil Engineering
Famagusta, North Cyprus via Mersin 10, Turkey
E-mail: zalihe.nalbantoglu@emu.edu.tr

DOI https://doi.org/10.18690/actageotechslov.18.2.29-43.2022

Keywords

electrokinetic technique, ground improvement, ionic solutions, numerical analyses, soft soils, strengthening

Abstract

Soft soils have a high compressibility, and low shear strength, and constructions on such soils often require the use of ground-improvement techniques. This paper compares the use of an electrokinetic (EK) treatment of soft soils using the ionic solutions calcium chloride and sodium carbonate. The effects of the ionic-solution type, the EK-treatment duration, the cation exchange capacity (CEC), the specific surface area (S_a), the pH, the electrical conductivity (σ), and the ionic strength (I_s) were considered in this study. Examining the parameters and evaluating their effects on soil behavior are difficult and complex. The design of experiments (DOE) software program was used to evaluate the effects of the parameters and determine the significant input factors for the EK treatment on soft soils. The analysis and optimization of the data produced the threshold values using the design-expert® software. In this study, the EK-treated soil with CEC = 4.9 meq 100/g, S_a = 4.5 m^2/g , pH = 9.5, σ = 6.0 S/m, $I_s = 1.55 \cdot 10^{-4}$ mol/L, and electrolyte-type setup of $CaCl_2$-Na_2CO_3 gave better soil strengthening. The gain in strength is attributed to the flocculation and aggregation of the EK-treated soil particles. The analysis of the data by DOE indicated that it could be used to assess the significant effects of the input factors on the unconfined compressive strength, q_u of the EK-treated soft soils.

Ključne besede

elektrokinetični postopek, izboljšava temeljnih tal, ionska raztopina, numerična analiza, mehke zemljine, ojačitev

Izvleček

Mehke zemljine imajo visoko stisljivost in nizko strižno trdnost, zato konstrukcije na takšnih tleh pogosto zahtevajo uporabo tehnik za izboljšavo temeljnih tal. Prispevek primerja uporabo elektrokinetične (EK) obdelave mehkih zemljin z uporabo ionskih raztopin kalcijevega klorida in natrijevega karbonata. V tej študiji so bili upoštevani učinki vrste ionske raztopine, trajanja EK obdelave, kapacitete kationske izmenjave (CEC), specifične površine (S_a), pH, električne prevodnosti (σ) in ionske jakosti (I_s). Preučevanje parametrov in vrednotenje njihovih učinkov na obnašanje zemljine predstavljata težki in zapleteni nalogi. Računalniški program za načrtovanje eksperimentov (DOE) je bil uporabljen za oceno učinkov parametrov in določitev pomembnih vhodnih faktorjev za EK obdelavo mehkih zemljin. Z analizo in optimizacijo podatkov so bile pridobljene mejne vrednosti s programsko opremo design-expert®. V tej študiji je zemljina EK obdelana s CEC = 4,9 meq 100/g, S_a = 4,5 m^2/g, pH = 9,5, σ = 6,0 S/m, $I_s = 1{,}55 \cdot 10^{-4}$ mol/L, in elektrolitsko nastavitvijo $CaCl_2$-Na_2CO_3 , ki je omogočila boljšo utrjevanje zemljine. Povečanje moči se pripiše flokulaciji in agregaciji delcev EK obdelane zemljine. Analiza podatkov s pomočjo DOE, je pokazala, da bi jo lahko uporabili za oceno pomembnih učinkov vhodnih faktorjev na enoosno tlačno trdnost q_u EK obdelanih mehkih zemljin.

1 INTRODUCTION

The investigation of the strengthening properties of soft soils for higher compressive strength has resulted in the use of an innovative electrokinetic (EK) soil-treatment technique. The use of a low direct current via electrodes placed into the soft soils to transport charged stabilizing ions from ionic solutions under the influence of an electric field is widely reported in the literature [1, 2, 3, 4]. As such, the efficacy of EK soil treatment depends on the soil and material-dependent factors [5, 6]. The soil factors were noted as the electrical conductivity (σ) and resistivity (ρ), ionic concentration, ionic strength (I_s), pH, salinity, total dissolved solids (TDS), temperature, water content (w), and zeta-potential (ζ) [7, 8]. Also, the soil-index properties such as density, porosity, and the void ratio [9, 10, 11] can affect the efficacy of the EK treatment. The material factors are the electrodes, ionic solutions, energy supply, and the entire EK setup [12, 13]. References [14] and [15] reported that the EK processes depend on the pH variations resulting from the interactions of soil-ionic solutions during the EK soil treatment. Therefore, to maximize the efficacy of the EK processes, a suitable pH level in the soil is required [16, 17]. A more basic environment often increased the ion exchange and precipitation, electrical conductivity, σ, and soil strength during the EK soil treatment [18]. According to [8], initial σ values of 0.5 S/m to 5.0 S/m are suitable for cost-effective results in EK soil treatment. References [19, 20] reported the electrical conductivity values of fine-grained soils to be ≤ 10 S/m or ≥ 2.5 S/m for an effective EK process. References [11, 21] stated that the EK process is more effective in active soils with potential pH variations, high σ, high CEC, and high S_a suitable for exchangeable ions, within the soil-ionic solutions system. Also, it has been reported that an effective EK process during the EK soil treatment often guarantees effective soft-soil strengthening [22].

The EK treatment has a robust advantage as a cost- and time-effective technique with no pollution or soil disturbance. It is used for in-situ or ex-situ soils and poses no threat to structures on, or adjacent to the EK-treated soils [22, 23, 24]. It finds application in deficient soils for the environmental remediation of unwanted metals, detoxification of toxic substances, dewatering, desalination, decontamination, and ground stabilization [25, 26, 27, 28, 29, 30]. Despite its potentials, the EK soil treatment is complex due to the huge data generated by its controlling factors during its application. Therefore, analyzing and interpreting such a huge amount of data is very crucial. In many studies, the performance of EK techniques was analyzed using conventional experimental methods (CEMs) to examine the outcome of the huge experimental data [31, 32, 33, 34]. However, there was a limitation in using CEM to analyze significant input factors to navigate robust design models for effective soft-ground strengthening [35, 36]. In such studies, the CEM could only analyze the effects of individual factors, and no possible interactions with other input factors were achievable. The CEM could not depict significant factors to navigate accurate design models for large-scale in-situ geotechnical applications.

This study focuses on the application of the design of experiment (DOE) software program to determine whether the input and observed factors were suitable and significant to achieve better strength properties in the EK-treated soft soils. References [11, 37] reported the efficacy of DOE interpretations of selected controlling factors to examine their performance on the outcome of the results. This study aims to define the significance of the selected controlling factors and their interactions in EK treatment to navigate robust design models for soft-soil strengthening. In this study, the DOE ascertains the threshold values of the selected factors for optimum soil strengthening during the EK soil treatment. Therefore, these factors were analyzed at minimum, medium, and maximum levels to observe their effects on the output results. The findings of the analyses showed that DOE could provide numerical formulations and robust design models in large-scale geotechnical EK soil-treatment applications.

2 EXPERIMENTAL MATERIALS AND SETUP

2.1 Materials

The soil used in this electrokinetic study is a marine alluvial deposit along the coastline terrain of the Medi-

Table 1. Physical and index properties of the natural soil.

Soil index properties	Quantities
In-situ dry density, ρ_d (g/cm^3)	1.31
In-situ bulk density, ρ_b (g/cm^3)	1.94
In-situ water content, w (%)	48
Clay size fraction, < 2 μm (%)[a]	61
Silt size fraction, 2–74 μm (%)[a]	36
Sand size fraction, > 74 μm (%)[a]	3
Specific gravity, G_S[b]	2.75
Maximum dry density, $\rho_{d(max)}$ (g/cm^3)[c]	1.61
Optimum moisture content, w_{opt} (%)[c]	20
Liquid limit, LL (%)[d]	60
Plastic limit, PL (%)[d]	33
Plasticity Index, PI (%)[d]	27
Liquidity index, LI[d]	0.88
Activity[d]	0.51
USCS Classification[e]	CH
Unconfined compressive strength, q_u (kPa)[f]	21

According to [41[a], 42[b], 43[c], 44[d], 45[e], 53[f]].

Table 2. Physicochemical properties of the ionic (electrolytes) solutions.

Properties	$CaCl_2$ at 1.0 mole	Na_2CO_3 at 1.0 mole	Deionized water (DW)
Molecular formula	$CaCl_2 \cdot 2H_2O$	Na_2CO_3	H_2O
Molecular weight, M (g/mol)	110.98	105.99	18.02
Electrical conductivity, σ (mS/cm)	10.87	18.58	0.055
Ionic strength, I_s (mol/L)	$1.3650\ 10^{-4}$	$2.3325\ 10^{-4}$	---
pH	8.65	11.75	7.00
Solubility in water, s (g/L) at 20 °C	147.10	105.99	---
Specific gravity, G_S at 20 °C	1.85	2.15	1.00
Total dissolved solids, T_{ds} (mg/L)	5.46	9.33	---

terranean Sea in the Tuzla region of North Cyprus. It is depicted having a low shear strength and high-volume instability [38, 39, 40]. Table 1 presents the index properties of the natural soil.

The chemical solutions used to supply the stabilizing ions needed to initiate electrochemical reactions in the soil were calcium chloride ($CaCl_2 \cdot 2H_2O$) and sodium carbonate (Na_2CO_3). Table 2 provides the physicochemical properties of the ionic solutions. The electrodes used were perforated aluminum and stainless-steel plates as the anode and cathode, respectively. The EK testing model was conducted in a non-conductive, transparent, fluid-leakage-proof rectangular glass test tank.

Figure 1 shows the test setup. The test tank had three cells: the ionic solutions, which occupied the two adjacent cells in the test tank, and the soft soil placed in the middle of the adjacent perforated electrodes in the test tank. Electric wires were used to connect the electrodes to the electrical power supply. The power device provided the direct current required in the test set up at a constant voltage gradient of 30 V/m along an anode-cathode distance within the EK-treated soils.

2.2 Experimental Procedure

Figure 1 presents the schematic diagram of the test tank setup and its dimensions. In this study, the middle cell of the glass tank test setup encased the natural soft soil, and the two outside cells housed the ionic solutions and the perforated electrodes. Different setups of ionic solutions: $CaCl_2$-DW, Na_2CO_3-DW, and $CaCl_2$-Na_2CO_3 occupied the outside cells of the test tank. The locations of the ionic solutions in the anolyte and catholyte cells are listed in Table 3. The ionic solutions were maintained at a constant level by continuously feeding the cells during the experimental test setups.

The perforated electrodes were connected to a controllable DC power supply using electrical wires, sealed with epoxy resin to prevent corrosion at their contacts. These ionic solutions flowed freely from their cells into the soil chamber via the perforated electrodes fitted with a filtering system. The filtering system was to prevent the clogging of the perforated holes of the electrodes, and the movement of soil fines from the soil chamber into the storing cells for the ionic solutions. The EK process is initiated by supplying a constant voltage gradient of 30 V/m across the soil blocks for selected days for the three test setups to enhance the interaction of the soil and the ionic solution. Then, the EK-treated soil samples were extracted from the test tanks at the predetermined points A to E, within the anode-to-cathode distances, as shown in Figure 1. The soil samples to be tested were extracted carefully using the standard cylindrical steel tubes of internal diameter, D, of 3.8 cm, and a height, H, of 7.6 cm for the unconfined compression tests. At each point of extraction, three soil samples were obtained along the vertical direction to determine the average outcome of each test result.

Table 3. Locations of ionic (electrolyte) solutions in the electrode chambers of the test setups.

#	Ionic solution test setups	Ionic solutions in anode cell	Ionic solutions in cathode cell
1	$CaCl_2$-DW	$CaCl_2$	Deionized water (DW)
2	Na_2CO_3-DW	Deionized water (DW)	Na_2CO_3
3	$CaCl_2$-Na_2CO_3	$CaCl_2$	Na_2CO_3

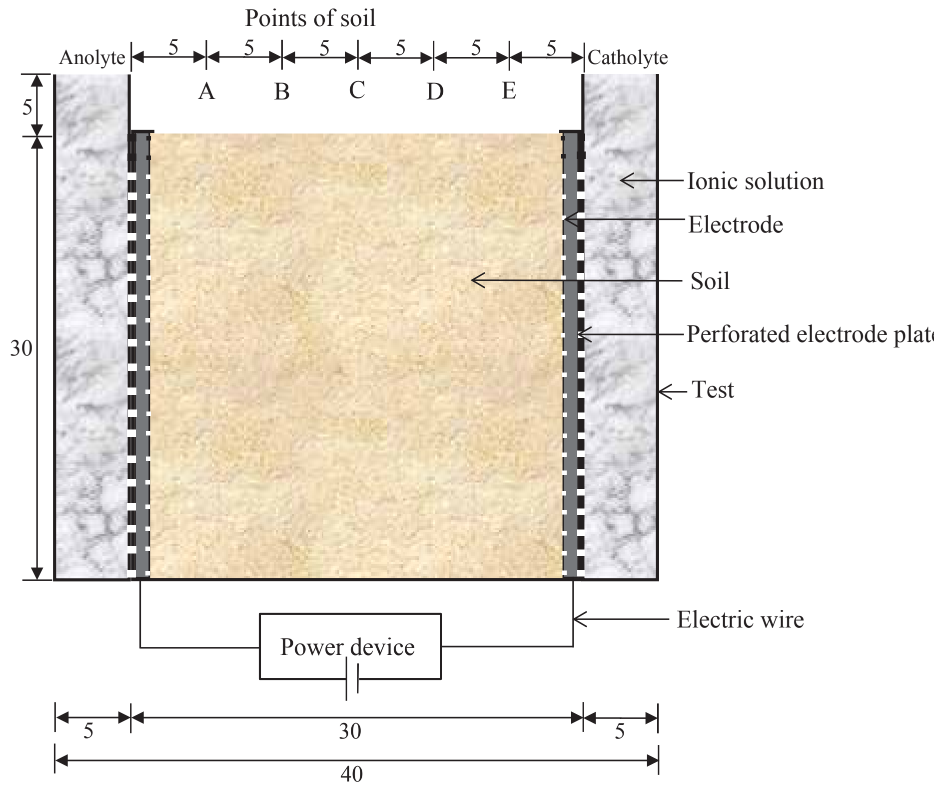

Figure 1. Cross-sectional view of the rectangular test tank set up (all dimensions are in cm).

2.3 Experimental Methods

To monitor the EK-treated soils, the values of the pH, CEC, S_a, σ, and I_s from the soil-ionic solutions interactions were measured for different EK-treatment durations. The EK-treatment durations of 7, 15, and 28 days were selected based on previous studies [3] [11] [30] [46], for the experimental test setups. Figure 2 presents the calibrated linear curves for the initial pH, TDS, σ, and I_s values of the $CaCl_2$ and Na_2CO_3 ionic solutions at different molar concentrations. The initial calibration of the chemical properties of the ionic solutions was to determine the accurate and precise measurements at different molar concentrations before being placed within their cells during the EK soil treatment. The observed R^2 values and equations were used to carefully monitor the validity and consistency of the measurements taken at different molar concentrations during the EK soil treatment. A calibrated, multi-parameter device probe measured the pH, TDS, and σ values of the EK-treated soils. The TDS values measured the total sum of ions present in a standard aqueous solution. The I_s of an aqueous substance is a function of its concentration of ions. The TDS, σ, and I_s values of given ionic solutions have empirical linear relationships, as in Eqs. (1)-(6) [47, 48, 49].

$$\text{TDS} = \Sigma \text{ cations} + \Sigma \text{ anions of the ionic (electrolyte) solutions} \tag{1}$$

$$\text{TDS (mg/L)} = \text{conversion factor} \times \sigma \text{ (S/m)} \quad (\text{conversion factor} = 0.65 \pm 0.01) \tag{2}$$

$$I_s = \frac{1}{2} \sum_i z_i^2 c_i \tag{3}$$

where, c_i and z_i represent the molar concentration and the charge of ion, i.

$$I_s \text{ (mol/L)} \approx 2.50 \cdot 10^{-5} \times \text{TDS (mg/L)} \quad (\text{conversion factor} = 2.50 \cdot 10^{-5} \pm 0.000001) \tag{4}$$

$$\sigma \text{ (μS/cm)} = 6.25 \cdot 10^{4} \times I_s \text{ (mol/L)} \tag{5}$$

$$I_s \text{ (mol/L)} = 1.60 \cdot 10^{-5} \times \sigma \text{ (μS/cm)} \tag{6}$$

The cation exchange capacity (CEC) and specific surface area (S_a) values were considered to evaluate the effects of the EK-treatment technique on the soil's behavior and the unconfined compressive strength (q_u) of the EK-treated soils. The use of the methylene-blue adsorption test method [50] determined the CEC values of the EK-treated soils. The use of the method proposed by [51] determined the S_a of the EK-treated soils. The extraction of insitu soft soil and EK-treated soils from

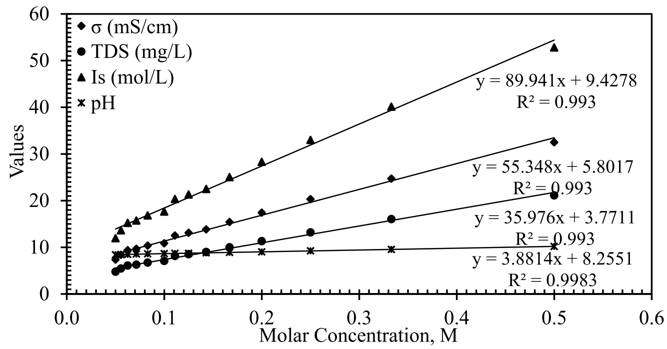

(a)

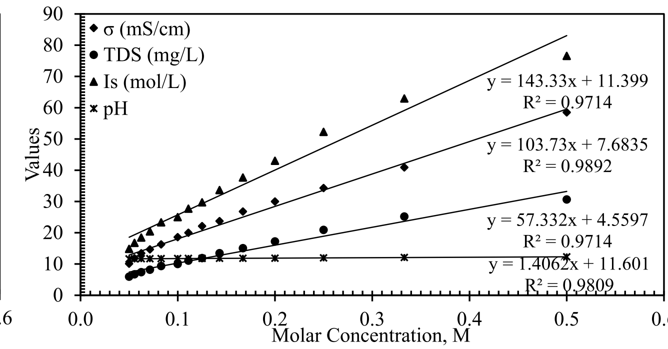

(b)

Figure 2. Electrical conductivity (σ), total dissolved solids (TDS), ionic strength (I_s), and pH calibration curves at different molar concentrations for (a) $CaCl_2$ and (b) Na_2CO_3 electrolytes.

the test tank setups after the EK treatment, which were used for unconfined compression tests were conducted following the method proposed by [52]. The unconfined compression test was performed in conformity with the ASTM standard [53] to determine the unconfined compressive strength, q_u of the natural soft soil and the EK-treated soils. In this study, a total of eighteen test setups were used. In all, two repetitive tests of the ionic-solution combinations of $CaCl_2$-DW, Na_2CO_3-DW, and $CaCl_2$-Na_2CO_3 test setups were conducted at the specified EK-treatment durations of 7, 15 and 28 days. Three successive test readings were taken for pH, CEC, S_a, σ, and I_s values of the EK-treated soils to affirm their accuracy and consistency during the EK soil treatment.

Anode region

Cathode region

Figure 3. Experimental observations showing cementitious gels within the EK-treated soils.

3 EXPERIMENTAL OBSERVATION

Figure 3 shows the aftermath of the EK treatment in the EK-treated soils close to the soil-electrode contacts. The continuous flow of ionic solutions into the soil mass aided the soil-ionic solution physico-chemical reactions. The formation of white cementitious precipitates was observed in the EK-treated soils over time. Such a formation caused the cementation and flocculation of clay fines of the EK-treated soils [54] [55]. The EK-treated soils were then tested for the changes in their q_u and analyzed in a completely randomized design. The DOE runs the numerical analytical formulation for the selected input factors and their interactions with the obtained q_u values of the EK-treated soils.

4 MATHEMATICAL MODELING USING A DESIGN OF EXPERIMENTS (DOE)

In this study, the strength properties were the targeted response in the numerical and optimization analyses. Table 4 shows the selected factors and their levels in the DOE. Each factor was coded at three different levels: maximum, medium, and minimum as +1, 0, and -1, respectively, consistent with the response end-use data; thus, the average values of the data obtained were analyzed.

The DOE used a multilevel categoric methodology (MCM) to analyze the selected categoric factors. The factors include the electrolyte type, EK-treatment duration, CEC, and S_a. The DOE used a response-surface methodology (RSM) design to study the effects of three numeric factors, pH, σ, and I_s, and their interaction on the response, q_u. There was a replication of unconfined compressive strength, q_u values at the two-factor combinations for three different EK-treatment durations of 7, 15, and 28 days, to produce the required numbers of runs in a completely randomized design.

Table 4. Factors and their levels using the design of experiment, DOE.

Factors name	Units	Type	Min.	Med.	Max.
Electrolyte type	---	Categoric	A1	A2	A3
EK-treatment duration	days	Categoric	7	15	28
CEC	meq/100g	Categoric	5.00	9.00	15.00
S_a	m^2/g	Categoric	5.00	11.00	18.00
pH	---	Numeric	8.00	9.50	11.00
σ	S/m	Numeric	4.00	6.00	10.00
I_s	mol/L	Numeric	0.500	1.50	2.00
Level coded			-1	0	+1

Min. = minimum, Med. = medium, Max. = maximum

4.1 Statistical data analysis (SDA)

The Statease statistical software version 11 trial 2018 (SAS Institute Inc., Cary, NC) [56] provided the numerical and statistical analyses. To consider the selected factors as significant and to examine their effect on the outcome of the results, such factors should satisfy some statistical conditions. The calculated probability values should satisfy P-values ≤ 0.0500 or 0.0500 < P < 0.1000 or "Prob. > F" < 0.0500, which indicates that the model term is significant [57]. The P-values > 0.1000 indicate the model terms are not significant. Also, there should be a reasonable agreement in the fit statistics when the experimental (observed) R-squared (R^2) is high and the difference between the adjusted R^2 and predicted R^2 is ≤ 0.2 [58, 59]. There should be adequate precision; a fit statistic tool measures the signal-to-noise ratio. According to [60, 61], an adequate precision ratio > 4 is more desirable in analysis of variance (ANOVA) analysis. The high F-value indicates that the model is significant statistically. The ANOVA produced the prediction model, interaction effects, and 3D plots of model terms. The observed values of the output results were obtained from the experimental test, while the ANOVA generated the predicted values from the selected input factors.

5 RESULTS AND DISCUSSION

5.1 EK effects on the unconfined compressive strength

Figure 4 presents the unconfined compressive strengths, q_u values of the EK-treated soils measured along different anode-to-cathode distances, at different EK-treatment durations using the ionic solutions. These values obtained for q_u in the EK-treated soils were in the range 25 to 92 kPa, which indicated that the soil properties changed from being very soft to soft and medium soils. The observation was that the q_u values of the EK-treated soils increased as the EK-treatment periods increased using the different ionic solutions along the

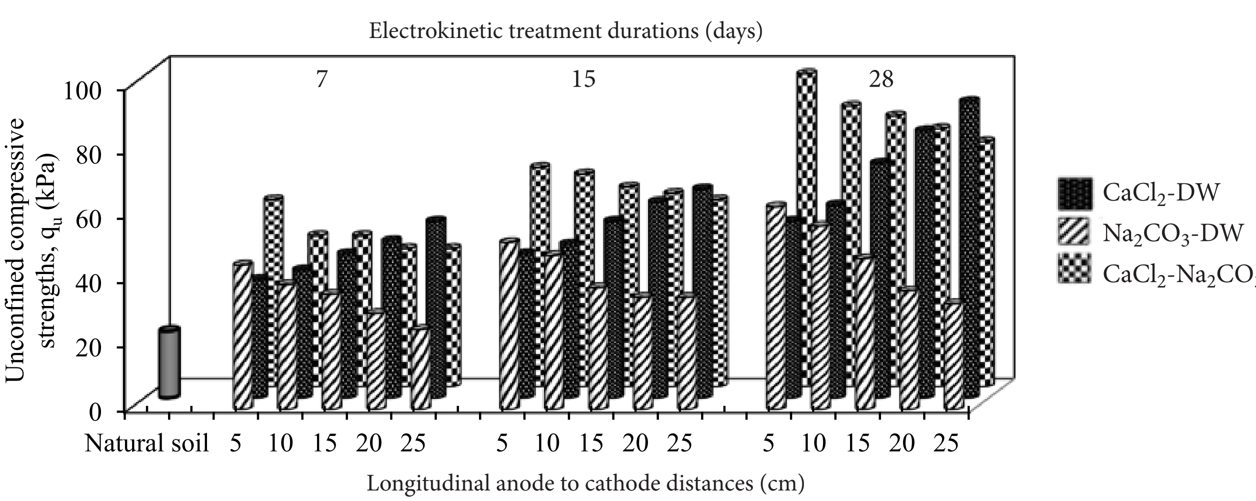

Figure 4. Unconfined compressive strengths, qu values of EK treated soils along different anode to cathode distances at different EK treatment durations using different ionic solution combinations.

anode-to-cathode distances. The increasing trend for varied tendencies of q_u values was due to the different exchange of ions such as Ca^{2+}, Na^{+}, and CO_3^{2-} ions from the $CaCl_2$-DW, Na_2CO_3-DW, and $CaCl_2$-Na_2CO_3 ionic solutions reacting with the EK-treated soils [62, 63, 64]. As reported in the literature, [65, 66], there was a sharp increase in q_u values for the EK-treated soils due to the exchange of ions during the EK-soil treatment. Unlike other studies, the numerical analyses in this study, using DOE developed the threshold values for the selected input factors and navigated the design model for strengthening the soft soils.

5.2 EK effects of factors on the unconfined compressive strength

To indicate the effects of the ionic solutions on the soil behavior, the CEC, S_a, pH, σ, and I_s values for the natural soil and EK-treated soils at 28 days were compared in Table 5. The test results of the EK-treated soils were measured at different EK-treatment durations using the $CaCl_2$-DW, Na_2CO_3-DW, and $CaCl_2$-Na_2CO_3 ionic solutions, respectively. The findings in Table 5 indicated that the EK soil treatment caused the largest reduction in the cation exchange capacity (CEC) and the specific surface area (S_a) values of the EK-treated soils in the $CaCl_2$-Na_2CO_3 test setup. Thus, increased the pH, σ, and I_s values of the EK-treated soils due to the chemical reaction of the $CaCl_2$ and Na_2CO_3 ionic solutions with the EK-treated soil. The increase in the alkaline nature, the pH of the EK-treated soil, aided the cementation, aggregation, and flocculation of the soil fines (Figure 3), thus improved the strengthening properties of the soft soils and was consistent with the findings reported by [4, 6, 65].

In this study, the DOE analyzed the input factors on the unconfined compressive strength; q_u values of EK-treated soils. Table 6a presents the analysis of variance (ANOVA) for the input factors of electrolyte types and EK-treatment durations to evaluate their effects on the measured q_u values.

The observed and predicted R^2 values were in reasonable agreement with the adjusted R^2 values. The adequate precision ratio indicated an adequate signal. Thus, the P-value and F-value implied that the model term was significant. The statistical analysis suggested that the electrolyte type and EK-treatment duration were substantial factors, that had a considerable effect on the performance of the EK treatment of the soft soil. But, the interaction effect of the electrolyte type and EK-treatment duration were insignificant. Figure 5 shows the plots for the prediction model and 3D graphical plots of the electrolyte type and EK-treatment duration versus q_u response.

Table 5. Measured factor values of EK-treated soils using ionic solutions in 28 days.

Test set up with	EK duration (days)	Anode to cathode distances (cm)	Measured factors of the EK-treated soil				
			CEC (meq 100/g)	S_a (m^2/g)	pH (---)	σ (S/m)	I_s (10^{-4} mol/L)
Natural soil	-	-	14.7	17.5	8.38	4.08	0.65
$CaCl_2$-DW ionic solution	28	5	4.90	5.31	8.37	8.18	1.31
		10	5.71	5.35	8.85	7.78	1.25
		15	5.83	6.01	8.97	6.71	1.07
		20	5.99	6.55	9.01	6.51	1.04
		25	6.27	6.89	9.15	5.54	8.86
Na_2CO_3-DW ionic solution	28	5	11.12	11.30	8.74	4.45	0.71
		10	10.87	11.26	9.08	6.78	1.09
		15	10.87	11.23	10.13	7.28	1.17
		20	9.11	10.80	10.24	8.91	1.43
		25	9.12	10.78	10.41	8.91	1.43
$CaCl_2$-Na_2CO_3 ionic solution	28	5	3.52	4.51	9.91	9.85	1.58
		10	3.62	4.63	10.18	9.38	1.50
		15	3.49	4.51	10.52	8.99	1.44
		20	3.50	4.53	10.88	9.41	1.51
		25	3.52	4.56	10.97	9.62	1.50

Table 6a. ANOVA model fit for q_u in terms of electrolyte type and EK-treatment duration.

Source	Sum of squares	df, degree of freedom	Mean square	F-value	P-value	
Model	9686.00	8	1210.75	12.24	< 0.0001	significant
A-Electrolyte type	3242.17	2	1621.08	16.39	< 0.0001	significant
B-EK duration	5703.17	2	2851.58	28.83	< 0.0001	significant
AB	740.67	4	185.17	1.87	0.1444	insignificant
Pure Error	2670.75	27	98.92			
Cor Total	12356.75	35				
Std. Dev.	9.95			R^2	0.7839	
Mean	51.58			Adjusted R^2	0.7198	
C.V. %	19.28			Predicted R^2	0.6158	
				Adeq. Precision	10.4568	

The Model F-value of 12.24 implies the model is significant. There is only a 0.01 % chance that a "Model F-value" this large could occur due to noise. Values of "Prob. > F" less than 0.0500 indicates model terms are significant. In this case, A and B are significant model terms.

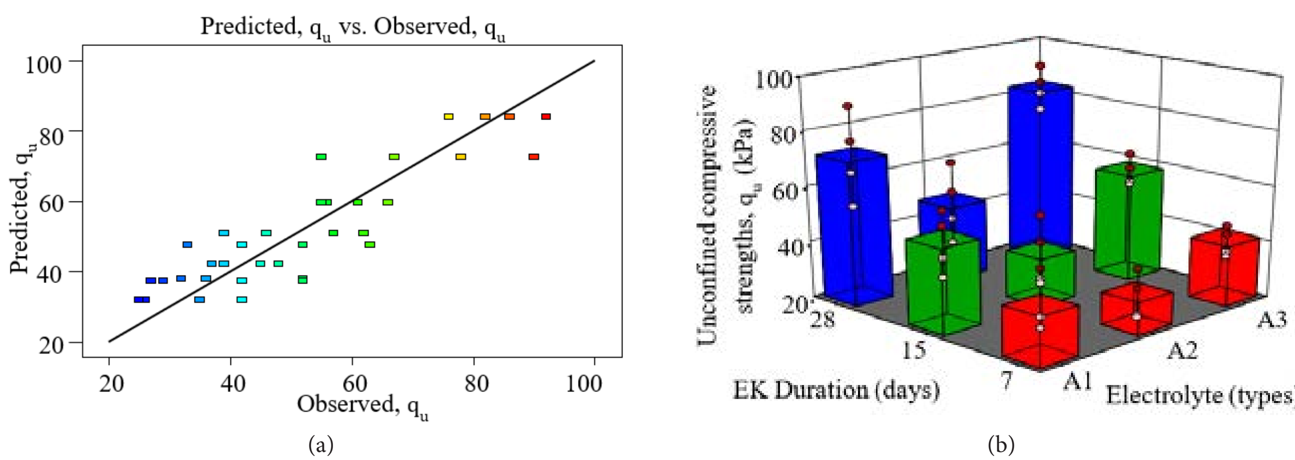

Figure 5. (a) Prediction model and (b) 3D plots for electrolyte types A1: $CaCl_2$–DW, A2: Na_2CO_3–DW, A3: $CaCl_2$–Na_2CO_3, and EK-treatment duration with respect to q_u response.

The prediction model supports the ANOVA analysis, which showed the observed and predicted R^2 values were in agreement. According to the statistical interpretation of the 3D plots, the electrolyte type had a significant effect on the EK-treated soils in the order $CaCl_2$-Na_2CO_3 > $CaCl_2$-DW > Na_2CO_3-DW and produced better soil strength for a longer EK treatment duration. It showed the chemical reaction between the $CaCl_2$-Na_2CO_3 and the clay particles produced a significant result in the formation of cementitious gels within the tiny pores of the soft clay soils, thus increasing their strength. The considerable effect of these factors on the q_u values is in the order EK-treatment duration > electrolyte type > interaction effect of electrolyte type and EK-treatment duration.

In this case, the electrolyte type and EK-treatment duration factors were significant model terms. Therefore, the analysis showed that the soil strength properties were significantly affected by electrolyte type and EK-treatment duration more than the interaction effect between them.

Table 6b shows the ANOVA analysis for the input factors of electrolyte types, CEC, and S_a. The P-value and F-value indicated that the model was significant. The observed R^2 and the predicted R^2 values were in reasonable agreement with the adjusted R^2 values in the ANOVA model fit for q_u.

The adequate precision ratio indicated a sufficient signal. The model terms were all significant. The analysis showed that the factors and their interaction had a considerable effect on the performance of the EK soil treatment. The prediction model also validated the obtained R^2 values.

Figures 6 and 7 show the prediction model, and 3D plots between the factor's electrolyte type and CEC; and electrolyte type and S_a to ascertain their effects on q_u, respectively. The analysis showed that the soil strength

Table 6b. ANOVA model fit for q_u in terms of electrolyte type and CEC.

Source	Sum of squares	df, degree of freedom	Mean square	F-value	P-value	
Model	2361.78	4	590.44	149.69	0.0001	significant
A-Electrolyte type	1761.56	2	880.78	223.30	< 0.0001	significant
B-EK duration	600.22	2	300.11	76.08	0.0007	significant
AB	600.22	2	300.11	76.08	0.0007	significant
Pure Error	15.78	4	3.94			
Cor Total	2377.56	8				
Std. Dev.	1.99			R^2	0.9934	
Mean	71.78			Adjusted R^2	0.9867	
C.V. %	2.77			Predicted R^2	0.9664	
				Adeq. Precision	35.3526	

The Model F-value of 149.69 implies the model is significant. There is only a 0.01 % chance that a "Model F-value" this large could occur due to noise. Values of "Prob. > F" less than 0.0500 indicates model terms are significant. In this case, A and B are significant model terms.

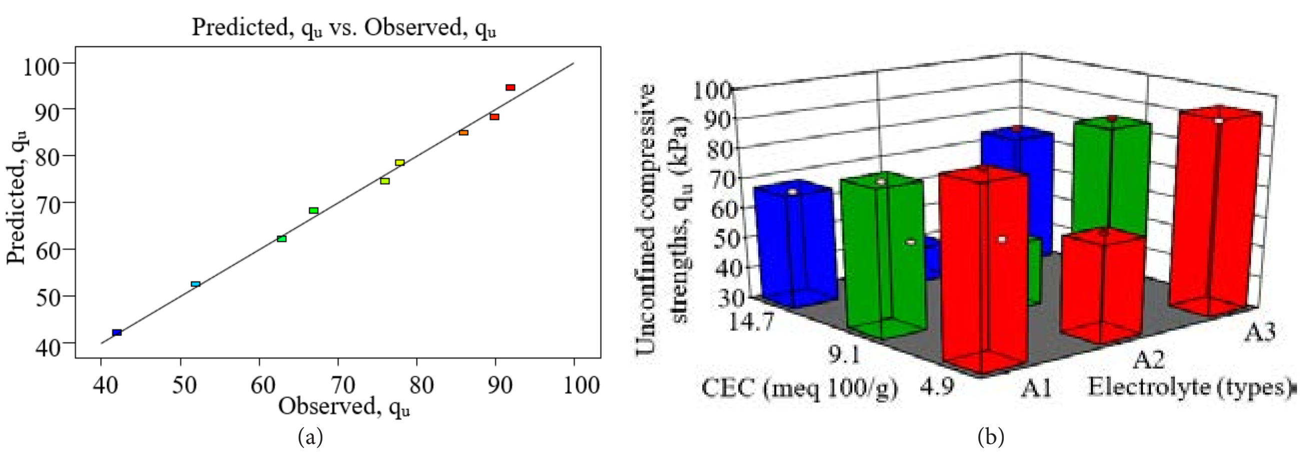

Figure 6. (a) Prediction model and (b) 3D plots for electrolyte types A1: $CaCl_2$–DW, A2: Na_2CO_3–DW, A3: $CaCl_2$–Na_2CO_3, and CEC variables to q_u response.

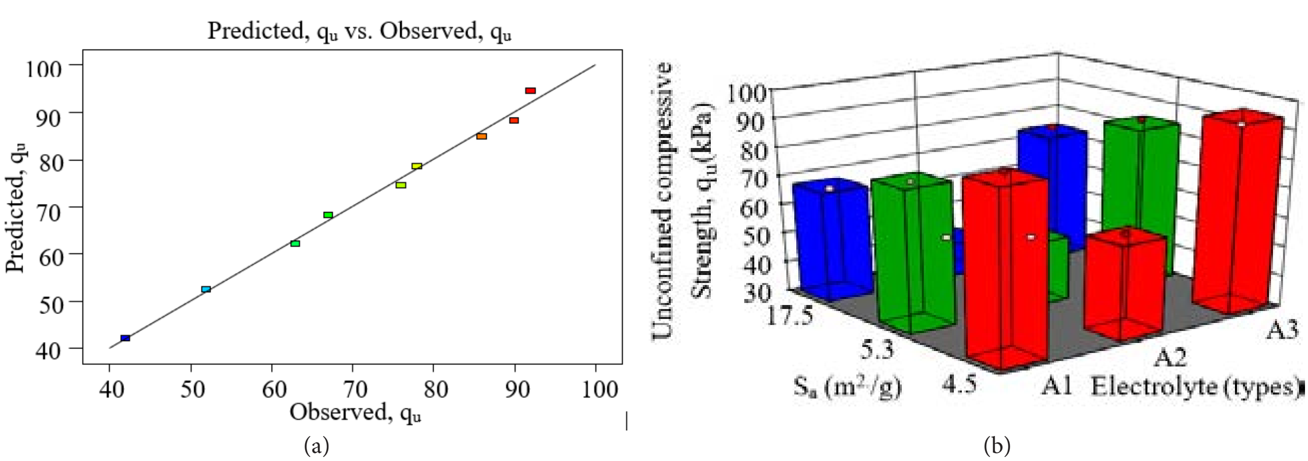

Figure 7. (a) Prediction model and (b) 3D plots for electrolyte types A1: $CaCl_2$–DW, A2: Na_2CO_3–DW, A3: $CaCl_2$–Na_2CO_3, and S_a variables to q_u response.

properties were more significantly affected by electrolyte type, CEC, and S_a more than their interactions. The factors had significant effects on q_u, but their interaction effects were insignificant on q_u.

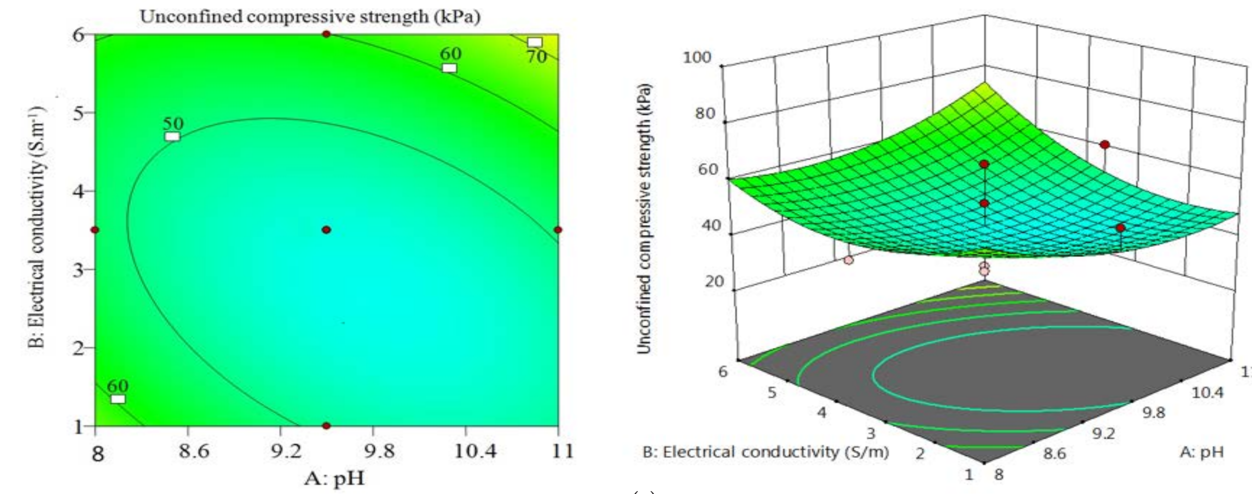

(a)

Figure 8a. Contour and 3D plots showing effects of the interaction of factors A: pH and B: electrical conductivity, σ, factors to q_u response.

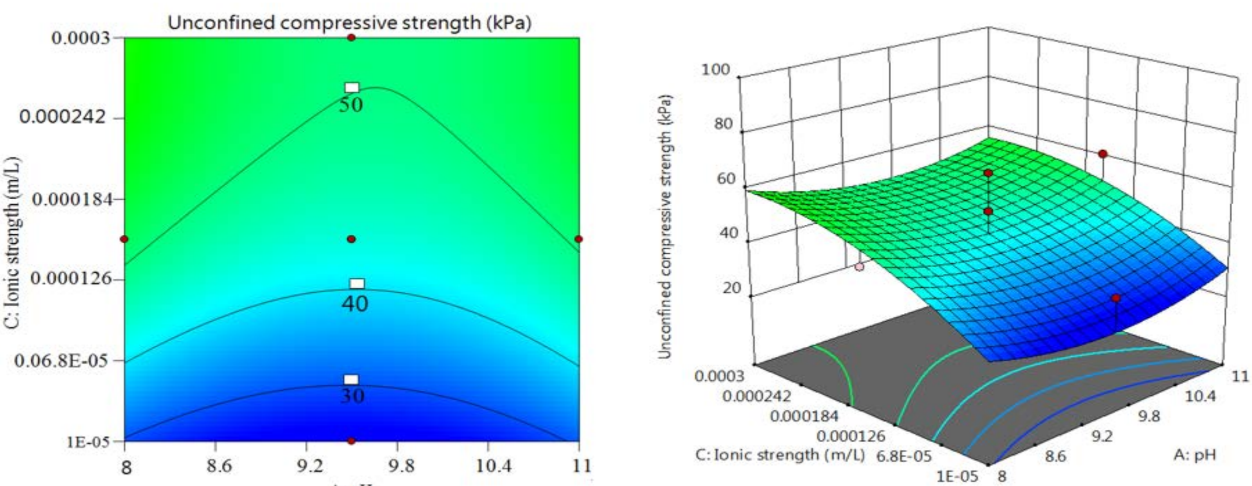

(b)

Figure 8b. Contour and 3D plots showing effects of the interaction of factors A: pH and C: ionic strength, I_s factors for q_u response.

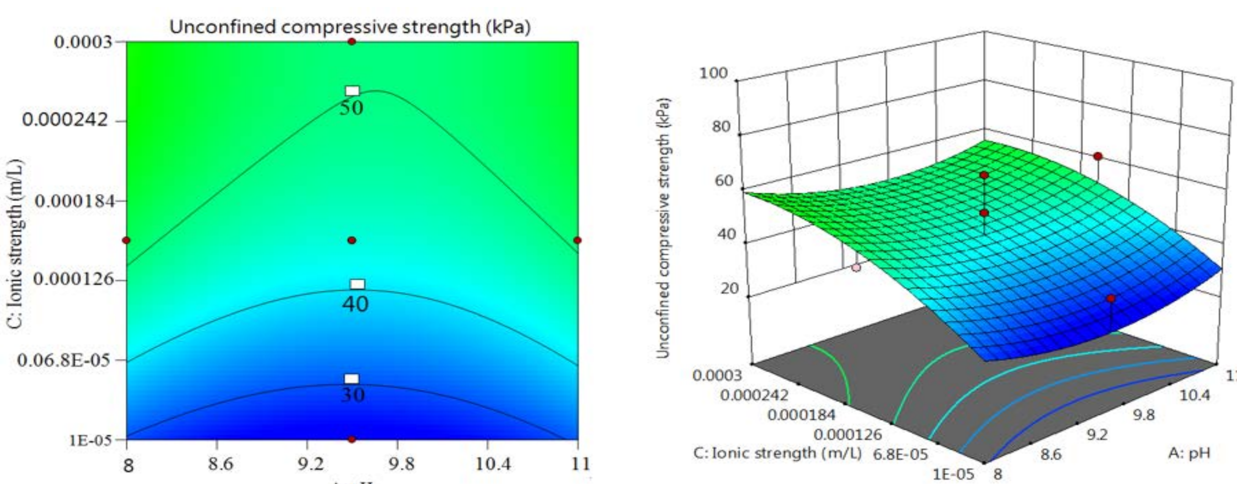

(c)

Figure 8c. Contour and 3D plots showing effects of the interaction of factors B: electrical conductivity, σ, and C: ionic strength, I_s factors for q_u response.

The observation was that the EK-treated soils at the lowest CEC = 4.9 meq 100/g, and Sa = 4.5 m^2/g had a considerable effect on the performance of the EK-treated soils. An indication that the EK-treated soil became more effectively strengthened at low CEC and S_a values. The 3D plots indicated that the types of the electrolyte setups had a more significant effect in the order $CaCl_2$-Na_2CO_3 > $CaCl_2$-DW > Na_2CO_3-DW, respectively. The significant factors were in the order electrolyte type > CEC > S_a > interaction effects of electrolyte type, CEC and S_a, and confirmed by the ANOVA analyses.

Table 7 provided the analysis of variance (ANOVA) employed by the RSM. The input factors considered were the pH, σ, and I_s . The P-value and F-value showed that the model term for electrical conductivity (σ) and ionic strength (I_s) were significant. Thus, the model term for pH and σ interaction had a significant effect. The prediction model for the observed and predicted R^2 values was in reasonable agreement with the adjusted R^2 value. The adequate precision ratio indicated an appropriate analysis. The interaction effect showed that the interaction of the factors pH and σ had a more significant effect on q_u than the interaction of the factors pH and I_s, or σ and I_s.

Figure 8 presents the contour and 3D plots showing the effect of the interaction of the factors pH, σ, and I_s on the q_u response. Figures 8a, 8b, and 8c show that high pH alkaline font at high σ and high I_s yielded effective q_u in the EK-treated soils, while acidic pH font at low σ and low I_s had a less remarkable effect on the q_u. The contour plots validated the significant effect of the model terms. In Figure 8a, the contour lines for the interaction factors pH and σ were curved, which indicated that the model term was significant for the performance of the EK treatment of the soft soils.

Whereas the model terms of interaction factors in Figures 8b and 8c, for the interaction factors of pH and I_s ; and σ and I_s had semi curves and parallel lines, respectively. Thus, they had only the substantial effects of the individual factor and no significant effect on the interaction factors. The considerable effect of the factors analyzed in this section was in the order I_s > σ > interaction effect of pH and σ > pH > σ and I_s > interaction effect of pH and I_s . The DOE produced the threshold values obtained as CEC = 4.9 meq 100/g, S_a = 4.5 m^2/g, pH = 9.5, ionic strength, electrical conductivity, σ = 6.0 S/m and I_s = $1.55 \cdot 10^{-4}$ mol/L, with a substantial performance for the optimum effective strengthening of the EK-treated soft soil used in this study.

Table 7. Summary of ANOVA for q_u model fit with electrolytes and pH, σ, and I_s.

Source	Sum of squares	df, degree of freedom	Mean square	F-value	P-value	
Model	8187.88	9	909.76	5.67	0.0002	significant
A-pH	9.85	1	9.85	0.0614	0.8062	insignificant
B-Electrical conductivity, σ	775.54	1	775.54	4.84	0.0370	significant
C-Ionic strength, I_s	4984.62	1	4984.62	31.09	< 0.0001	significant
AB	1335.04	1	1335.04	8.33	0.0078	significant
AC	40.04	1	40.04	0.2497	0.6215	insignificant
BC	0.3750	1	0.3750	0.0023	0.9618	insignificant
A^2	162.13	1	162.13	1.01	0.3239	insignificant
B^2	316.42	1	316.42	1.97	0.1719	insignificant
C^2	157.31	1	157.31	0.9811	0.3311	insignificant
Residual	4168.87	26	160.34			
Lack of Fit	529.37	5	105.87	0.6109	0.6926	
Pure Error	3639.50	21	173.31			
Cor Total	12356.75	35				
Std. Dev.	12.66			R^2	0.6626	
Mean	51.58			Adjusted R^2	0.5458	
C.V. %	24.55			Predicted R^2	0.3655	
				Adeq. Precision	8.5324	

The Model F-value of 5.67 implies the model is significant. There is only a 0.01 % chance that a "Model F-value" this large could occur due to noise. Values of "Prob. > F" less than 0.0500 indicates model terms are significant. In this case, B, C, and AB are significant model terms.

6 CONCLUSIONS

A numerical analysis of the design-of-experiment methodology for examining the significant factors in the electrokinetic application for strengthening the soft soils used in this study has been proposed.

- The results presented have highlighted the significant performance of the selected factors on the unconfined compressive strength, q_u values obtained from the EK-treated soils used in this study.
- The threshold values and relative order of the significant effects of the selected factors were developed using the numerical analyses of the DOE to validate better strengthening of the EK-treated soft soils.
- The prediction models and ANOVA analyses validated the strong agreement between the observed and predicted, q_u values obtained using the DOE of the selected factors and result outputs.
- The numerical model validated the experimental results that the electrolyte type $CaCl_2$-Na_2CO_3 in an alkaline font depicted better soil strengthening due to the clay-electrolyte reaction, ions exchange, precipitates formation, and strong inter-particles bond strength of soil particles of EK-treated soil.
- As a recommendation, the numerical analyses of the DOE can be used to navigate a robust design model for a wide range of problematic soils for large-scale in-situ EK geotechnical applications.

List of Notation

ASTM = the American Society for Testing and Materials
CEC = the cation exchange capacity, meq 100/g
DC = direct current, A
EK = Elastic modulus
Gs = the electrokinetic
kPa = the kilopascal
OMC = the optimum moisture content, %
ρ_b = the bulk density, g/cm^3
ρ_d = the dry density, g/cm^3
$\rho_{d(max)}$ = the maximum dry density, g/cm^3
q_u = the unconfined compressive strength, kPa
V = the voltage, V
w = the water content, %
σ = the electrical conductivity, μS/cm
s = the solubility in water, kg/L
S_a = the specific surface area, m^2 100/g
V = the volume, m^3
w_{opt} = the optimum moisture content, %
ΔV = the potential difference, V

Disclosure statement

No potential conflict of interest was reported by the authors.

REFERENCES

[1] Lefebvre, G., Burnotte, F. 2002. Improvements of electroosmotic consolidation of soft clays by minimizing power loss at electrodes. Canadian Geotechnical Journal 39(2), 399-408. https://doi.org/10.1139/t01-102.
[2] Bergado, D.T., Sasanakul, I., Horpibulsuk, S. 2003. Electro-osmotic consolidation of soft Bangkok clay using copper and carbon electrodes with PVD. Geotechnical testing journal 26 (3), 277-288. https://doi.org/10.1520/GTJ11309J.
[3] Barker, J.E., Rogers, C.D.F., Boardman, D.I., Peterson, J. 2004. Electrokinetic stabilisation: an overview and case study. Proceeding of the Institute of Civil Engineering Ground Improvement 8(2), 47-58. https://doi.org/10.1007/s10706-014-9753-8.
[4] Jayasekera, S. 2015. Electrokinetics to modify strength characteristics of soft clayey soils: a laboratory based investigation. Electrochimica Acta, 181, 39-47. http://dx.doi.org/10.1016/j.electacta.2015.06.064.
[5] Ng, Y.S., Gupta, B.S., Hashim, M.A. 2014. Stability and performance enhancements of Electrokinetic-Fenton soil remediation. Reviews in Environmental Science and Bio/Technology, 13(3), 251-263. https://doi.org/10.1007/s11157-014-9335-5.
[6] Moayedi, H., Kassim, K.A., Kazemian, S., Raftari, M., Mokhberi, M. 2014. Improvement of peat using Portland cement and electrokinetic injection technique. Arabian Journal for Science and Engineering, 39(10), 6851-6862. https://doi.org/10.1007/s13369-014-1245-x.
[7] Jayasekera, S., Hall, S. 2007. A Modification of the properties of salt affected soils using electrochemical treatments. Geotechnical and Geological Engineering 25(1), 1. https://doi.org/10.1007/s10706-006-0001-8.
[8] Malekzadeh, M., Lovisa, J., Sivakugan, N. 2016. An overview of electrokinetic consolidation of soils. Geotechnical and Geological Engineering 34(3), 759-776. https://doi.org/10.1007/s10706-016-0002-1.
[9] Abdullah, W.S., Al-Abadi, A.M. 2010. Cationic–electrokinetic improvement of an expansive soil. Applied Clay Science, 47 (3-4), 343-350. https://doi.org/10.1016/j.clay.2009.11.046.
[10] Wang, D., Kang, T., Han, W., Liu, Z., Chai, Z. 2010. Electrochemical modification of the porosity and zeta potential of montmorillonitic soft rock.

Geomechanics and Engineering 2(3), 191-202. https://doi.org/10.1016/j.egypro.2012.01.265.
[11] Yan, S., Singh, A.N., Fu, S., Liao, C., Wang, S., Li, Y., Hu, L. 2012. A soil fauna index for assessing soil quality. Soil Biology and Biochemistry 47, 158-165. https://doi.org/10.1016/j.soilbio.2011.11.014.
[12] Asadollahfardi, G., Rezaee, M. 2019. Electrokinetic remediation of diesel-contaminated silty sand under continuous and periodic voltage application. Environmental Engineering Research, 24(3), 456-462. https://doi.org/10.4491/eer.2018.301.
[13] Jayasekera, S. 2004. Electroosmotic and hydraulic flow rates through kaolinite and bentonite clays. Australian Geomechanics, 39(2), 79-86.
[14] Li, Y., Gong, X., Lu, M., Tao, Y. 2012. Non-mechanical behaviors of soft clay in two-dimensional electro-osmotic consolidation. Journal of rock mechanics and geotechnical engineering, 4(3), 282-288. https://doi.org/10.3724/SP.J.1235.2012.00282.
[15] Cameselle, C., Gouveia, S., Akretche, D. E., Belhadj, B. 2013. Advances in electrokinetic remediation for the removal of organic contaminants in soils. Organic Pollutants-Monitoring, Risk and Treatment, 209-229. https://doi.org/10.5772/54334.
[16] Airoldi, F., Jommi, C., Musso, G., Paglino, E. 2009. Influence of calcite on the electrokinetic treatment of a natural clay. Journal of Applied Electrochemistry, 39(11), 2227. https://doi.org/10.1007/s10800-009-9840-3.
[17] Liaki, C., Rogers, C.D.F., Boardman, D.I. 2010. Physico-chemical effects on clay due to electromigration using stainless steel electrodes. Journal of applied electrochemistry 40(6), 1225-1237. https://doi.org/10.1007/s10800-010-0096-8.
[18] Askin, T., Turer, D. 2016. Effect of electrode configuration on electrokinetic stabilization of soft clays. Quarterly Journal of Engineering Geology and Hydrogeology, 49(4), 322-326. https://doi.org/10.1144/qjegh2015-074.
[19] Loch, J.G., Lima, A.T., Kleingeld, P.J. 2010. Geochemical effects of electro-osmosis in clays. Journal of Applied Electrochemistry, 40(6), 1249-1254. https://doi.org/10.1007/s10800-010-0098-6.
[20] Mitchell, J.K., Soga, K. 2005. Fundamentals of soil behavior (Vol. 3). New York: John Wiley & Sons.
[21] Schmidt, C.A., Barbosa, M.C., de Almeida, M.D.S. 2007. A laboratory feasibility study on electrokinetic injection of nutrients on an organic, tropical, clayey soil. Journal of Hazardous Materials, 143(3), 655-661. https://doi.org/10.1016/j.jhazmat.2007.01.009.
[22] Jeyakanthan, V., Gnanendran, C.T., Lo, S.C. 2011. Laboratory assessment of electro-osmotic stabilization of soft clay. Canadian Geotechnical Journal 48(12), 788-1802. https://doi.org/10.1139/t11-073.
[23] Kaniraj, S.R., Yee, J.H.S. 2011. Electro-osmotic consolidation experiments on an organic soil, Geotechnical and Geological Engineering 29(4), 505-518. https://doi.org/10.1007/s10706-011-9399-8.
[24] Mosavat, N., Oh, E., Chai, G. 2014. Laboratory evaluation of physico-chemical variations in bentonite under electrokinetic enhancement, International Journal of Geomate: Geotechnique, Construction Materials and Environment 6(1), 817-823. https://doi.org/10.21660/2014.11.3347.
[25] Kim, K.J., Kim, D.H., Yoo, J.C., Baek, K. 2011. Electrokinetic extraction of heavy metals from dredged marine sediment. Separation and Purification Technology 79(2), 164-169. https://doi.org/10.1016/j.seppur.2011.02.010.
[26] Lukman, S., Mu'azu, N.D., Essa, M.H. 2015. Optimal Removal of Cadmium from Heavily Contaminated Saline–Sodic Soil Using Integrated Electrokinetic-Adsorption Technique. Arab Journal Science and Engineering 40(5), 1289-1297. https://doi.org/10.1007/s13369-015-1605-1.
[27] Mu'azu, N.D., Essa, M.H., Lukman, S. 2016. Scale-up of hybrid electrokinetic–adsorption technique for removal of heavy metals from contaminated saline-sodic clay soil Journal of King Saud University-Engineering Sciences. https://doi.org/10.1016/j.jksues.2016.12.002.
[28] Mu'azu, N.D., Essa, M.H., Lukman, S. 2017. Response Surface Modeling of Rate of Replenishing Processing Fluids During Hybrid Electrokinetics-Adsorption Treatment of Saline-Sodic Soil. Arabian Journal for Science and Engineering 42(3).1117-1127. https://doi.org/10.1007/s13369-016-2310-4.
[29] Essa, M.H., Mu'azu, N.D., Lukman, S., Bukhari, A. 2015. Application of Box-Behnken design to hybrid electrokinetic-adsorption removal of mercury from contaminated saline-sodic clay soil. Soil and Sediment Contamination: An International Journal 24(1), 30-48. https://doi.org/10.1080/15320383.2014.911720.
[30] Chai, Z., Zhang, Y., Scheuermann, A. 2016. Study of physical simulation of electrochemical modification of clayey rock. Geomechanics and Engineering 11(2), 197-209. https://doi.org/10.12989/gae.2016.11.2.197.
[31] Liaki, C., Rogers, C.D.F., Boardman, D.I. 2010. Physico-chemical effects on clay due to electromigration using stainless steel electrodes. Journal of applied electrochemistry 40(6), 1225-1237. https://doi.org/10.1007/s10800-010-0096-8.
[32] Mosavat, N., Oh, E. and Chai, G. 2012. A review

of electrokinetic treatment technique for improving the engineering characteristics of low permeable problematic soils. International Journal of Geomate 2(2), 266-272. https://doi.org/10.21660/2012.4.3i.

[33] Mohanty, S.K., Pradhan, P.K., Mohanty, C.R. 2017. Stabilization of expansive soil using industrial wastes. Geomechanics and Engineering 12(1), 111-125. https://doi.org/10.12989/gae.2017.12.1.111.

[34] Alrubaye, A.J., Muzamir, H., Fattah, M.Y. 2018. Effects of using silica fume and lime in the treatment of kaolin soft clay. Geomechanics and Engineering 14(3), 247-255. https://doi.org/10.12989/gae.2018.14.3.247.

[35] Bezerra, M.A., Santelli, R.E., Oliveira, E.P., Villar, L.S., Escaleira, L.A. 2008. Response surface methodology (RSM) as a tool for optimization in analytical chemistry. Talanta 76(5), 965-977. https://doi.org/10.1016/j.talanta.2008.05.019.

[36] Myers, R.H., Montgomery, D.C., Anderson-Cook, C.M. 2009. Response Surface Methodology, John Wiley and Sons, Inc, New Jersey, NJ, USA, 20, 38-44.

[37] Kamani, H., Safari, G.H., Asgari, G., Ashrafi, S. D. 2018. Data on modeling of enzymatic elimination of direct red 81 using response surface methodology. Data in brief, 18, 80-86. https://doi.org/10.1016/j.dib.2018.03.012.

[38] Nalbantoğlu, Z. 2004. Effectiveness of class C fly ash as an expansive soil stabilizer. Construction and Building Materials 18(6), 377-381. https://doi.org/10.1007/s12205-014-0137-7.

[39] Sridharan, A., Gurtug, Y. 2005. Compressibility characteristics of soils. Geotechnical and Geological Engineering 23(5), 615-634. https://doi.org/10.1007/s10706-004-9112-2.

[40] Danial, L., Huriye, B. 2012. A comprehensive soil characteristics study and finite element modeling of soil-structure behavior in Tuzla Area, 3rd International Conference on New Developments in Soil Mechanics and Geotechnical Engineering, Nicosia, Northern Cyprus.

[41] ASTM D 422. 1998. Standard test method for particle-size analysis of soils. ASTM International, West Conshohocken, PA, USA. https://doi.org/10.1520/D0422-63R98.

[42] ASTM D 854 - 06e1. 2006. Standard test methods for specific gravity of soil solids by water pycnometer. ASTM International, West Conshohocken, PA, USA. https://doi.org/10.1520/D0854-06E01.

[43] ASTM D698. 2007. Standard Test Methods for Laboratory Compaction Characteristics of Soil Using Standard Effort (12 400 ft-lbf ft-3 (600 kN-m/m3)), ASTM International, West Conshohocken, PA, USA. https://doi.org/10.1520/D698-07.

[44] ASTM D 4318. 2000. Standard test methods for the liquid limit, plastic limit, and plasticity index of soils. ASTM International, West Conshohocken, PA, USA. https://doi.org/10.1520/D4318-00.

[45] ASTM D 2487. 2000. Standard practice for classification of soils for engineering purposes (Unified Soil Classification System). ASTM International, West Conshohocken, PA, USA. https://doi.org/10.1520/D2487-00.

[46] Ahmad Tajudin, S.A., Jefferson, I., Madun, A., Abidin, M.H.Z., Baharuddin, M.F.T., Mohammad Razi, M.A. 2015. Monitoring of electric current during electrokinetic stabilisation test for soft clay using EKG electrode. In Applied Mechanics and Materials (Vol. 773, pp. 1560-1564). Trans Tech Publications Ltd. https://doi.org/10.4028/www.scientific.net/AMM.773-774.1560.

[47] Appelo, C.A.J. 2010. Specific conductance-how to calculate the specific conductance with PHREEQC.

[48] McCleskey, R.B., Nordstrom, D.K., Ryan, J.N. 2012. Comparison of electrical conductivity calculation methods for natural waters. Limnology and Oceanography: Methods 10(11), 952–967. https://doi.org/10.4319/lom.2012.10.952.

[49] Aqion 2018. TDS - Electrical conductivity; ionic strength; total dissolved solids. http://www.http://www.aqion.de/site/69,130, 133, 130#fnref:1.

[50] AFNOR 1993. Mesure de la quantité et de l'activité de la fraction argileuse (Norme Française NF P 94-068). Assoc. française de Normalization (ANFOR), La Défense, Paris, France.

[51] Hequet, E., Abidi, N., Gourlot, J.P. 1998. Application of methylene blue adsorption to cotton fibre specific surface area measurement: Part 1 Methodology. J. Cotton Science 2, 164-173.

[52] Abiodun, A.A., Nalbantoglu, Z. 2015. Lime pile techniques for the improvement of clay soils. Canadian Geotechnical Journal, 52(6), 760-768. dx.doi.org/10.1139/cgj-2014-0073.

[53] ASTM D 2166. 2007. Standard test method for unconfined compressive strength of cohesive soil. ASTM International, West Conshohocken, PA, USA. https://doi.org/10.1520/D2166-07.

[54] STAT-EASE 2011. Design-Expert Reference Manual, STAT-EASE Corp., Minnesota, USA.

[55] Le CT, I. B., Biostatistics, P.M.I. 2003. John Wiley and Sons, Inc, New Jersey, NJ. Analysis of Experiments. John Wiley and Sons, New York, NY, USA.

[56] STAT-EASE 2011. Design-Expert Reference Manual, STAT-EASE Corp., Minnesota, USA.

[57] Le CT, I. B., Biostatistics, P. M. I. 2003. John Wiley and Sons, Inc, New Jersey, NJ.
[58] Wang, Q., Hou, Y., Xu, Z., Miao, J., Li, G. 2008. Optimization of cold-active protease production by the psychrophilic bacterium Colwellia sp. NJ341 with response surface methodology. Bioresource technology, 99(6), 1926-1931. https://doi.org/10.1016/j.biortech.2007.03.028.
[59] Montgomery, D.C., Runger, G.C., Hubele, N.F. 2009. Engineering Statistics, John Wiley and Sons, USA.
[60] Montgomery, D.C. 2017. Design and Analysis of Experiments. John Wiley and Sons, New York, NY, USA.
[61] Le CT, I. B., Biostatistics, P. M. I. 2003. John Wiley and Sons, Inc, New Jersey, NJ.
[62] Abiodun, A.A., Nalbantoglu, Z. 2020. Effect of ionic solutions on the performance of electrokinetic treatment of soft soils. European Journal of Environmental & Civil Engineering, 1-18. https://doi.org/10.1080/19648189.2020.1765201.
[63] Mosavat, N., Oh, E., Chai, G. 2013. Laboratory assessment of kaolinite and bentonite under chemical electrokinetic treatment. Journal of Civil & Environmental Engineering, 3(01), 1-7. https://doi.org/10.4172/2165-784X.1000125.
[64] Harris, A., Nosrati, A., Addai-Mensah, J. 2018. The influence of pulp and interfacial chemistry and mode of electrical power input on electroosmotic dewatering of Na-exchanged smectite dispersions. Applied Clay Science, 162, 214-222. https://doi.org/10.1016/j.clay.2018.06.017.
[65] Azhar, A.T.S., Azim, M.A.M., Syakeera, N. N., Jefferson, I. F., Rogers, C. D. F. 2017. Application of Electrokinetic Stabilisation (EKS) Method for Soft Soil: A Review. In IOP Conference Series: Materials Science and Engineering (Vol. 226, No. 1, p. 012075). IOP Publishing. https://doi.org/10.1088/1757-899X/226/1/012075.
[66] Thuy, T. T. T., Putra, D.P.E., Budianta, W., Hazarika, H. 2013. Improvement of expansive soil by electrokinetic method. Journal of Applied Geology, 5(1).

AN INSIGHT INTO THE LIQUEFACTION RESISTANCE OF SAND USING CYCLIC UNDRAINED TRIAXIAL TESTS: EFFECT OF THE RELATIVE DENSITY AND THE LOADING AMPLITUDE

VPOGLED V ODPORNOST PESKA NA LIKVEFAKCIJO Z UPORABO CIKLIČNIH NEDRENIRANIH TRIOSNIH PREIZKUSOV: VPLIV RELATIVNE GOSTOTE IN AMPLITUDE OBTEŽBE

El-Hadj Meziane
Univ. UHBC Hassiba Benbouali of Chlef,
FGC&A Faculty, Civil Engineering Department
02000 Chlef, Algeria
E-mail: hadjmeziane@yahoo.fr

Ismail Benessalah
Univ. UHBC Hassiba Benbouali of Chlef,
LsmE Laboratory of Materials Sciences and Environment
02091 Chlef, Algeria
E-mail: i.benessalah@univ-chlef.dz

Ahmed Arab
Univ. UHBC Hassiba Benbouali of Chlef,
LsmE Laboratory of Materials Sciences and Environment
02091 Chlef, Algeria
E-mail: ah_arab@yahoo.fr

DOI https://doi.org/10.18690/actageotechslov.18.2.44-55.2022

Keywords

sand, liquefaction, relative density, cyclic stress ratio, pore water pressure

Ključne besede

pesek, likvefakcija, relativna gostota, ciklično napetostno razmerje, porni vodni tlak

Abstract

A stability analysis of soils prone to liquefaction based on their undrained shear-strength characteristics is an indispensable challenge in earthquake geotechnical engineering. This paper presents a laboratory study of the influence of relative density on the cyclic behavior of Chlef sand. The experimental program includes undrained, triaxial cyclic tests that were carried out for three different relative densities (Dr = 15, 50 and to 65 %) with various cyclic stress ratios (CSR = 0.15, 0.25 and 0.35). All the samples were consolidated under one initial effective confining pressure σ'_c = 100 kPa. The main results show that the increases in the relative density led to significant increases in the shear strength established by an increase in the number of cycles and with an exponential rise. In contrast, it was demonstrated that the number of cycles was decreased when increasing the cyclic stress ratio due to the shearing frequency. The two main effects of the studied parameters did not have the same influence on the cyclic undrained response of the sandy soil submitted to

Izvleček

Analiza stabilnosti zemljin, ki bi se lahko utekočinila na podlagi njihovih lastnosti nedrenirane strižne trdnosti, je nepogrešljiv izziv v potresnem geotehničnem inženirstvu. V prispevku je predstavljena laboratorijska študija vpliva relativne gostote na ciklično obnašanje peska Chlef. Eksperimentalni program vključuje nedrenirane triosne ciklične preizkuse, ki so bili izvedeni za tri različne relativne gostote (Dr = 15, 50 in do 65 %) z različnimi razmerji cikličnih napetosti (CSR = 0,15, 0,25 in 0,35). Vsi preizkušanci so bili konsolidirani pri enakem začetnem efektivnem bočnem tlaku σ'_c = 100 kPa. Najvažnejši rezultati kažejo, da je povečanje relativne gostote povzročilo znatno povečanje strižne trdnosti z eksponentnim dvigom, ugotovljeno s povečanjem števila ciklov. Nasprotno pa je bilo dokazano, da se je število ciklov zmanjšalo s povečanjem razmerja ciklične napetosti zaradi frekvence striženja. Glavna učinka proučevanih parametrov nista imela enakega vpliva na ciklični nedreniran odziv peščene zemljine, izpostavljene seizmični obremenitvi: povečanje *seismic loading: an increase of the deviatoric stress due to the high relative density that participates in the increase of the loading capacity of the compacted soils by minimizing the void ratios, and an increase of the pore-water pressure that has a negative effect on the liquefaction of the soil. From the results obtained, it can be concluded that these two mechanisms led to a global increase of the maximum shearing stress.*

deviatorične napetosti zaradi visoke relativne gostote, ki prispeva k povečanju nosilnosti zgoščene zemljine z zmanjšanjem količnika por in povečanjem pornega vodnega tlaka, ki negativno vpliva na utekočinjanje zemljine. Iz rezultatov je mogoče sklepati, da sta ta dva mehanizma vodila do globalnega povečanja največje strižne napetosti.

Notation

The following symbols are used in this paper:

C_c = Coefficient of gradation $C_c = (D_{30})^2/(D_{10} \cdot D_{60})$
C_u = Uniformity coefficient $C_u = (D_{60}/D_{10})$
CSR = Cyclic stress ratio ($CSR = q_m/(2 \cdot p'_c)$)
D_{10} = Effective grain diameter
D_{30} = Grain size corresponding to 30 % finer
D_{60} = Grain size corresponding to 60 % finer
D_{50} = Mean grain size
D = Diameter of the sample
Dr = Relative density
ε_a = Axial strain
e_{max} = Maximum void ratio
e_{min} = Minimum void ratio
e = Initial void ratio
f_c = Fines content
H = Height of the sample
I_P = Plasticity index
N_c = Number of cycles
σ'_c = Initial effective confining pressure
p' = Effective mean pressure
q = Deviator stress
q_m = Cyclic loading amplitude
γ_s = Unit weight of solids
Δu = Excess pore-water pressure

1 INTRODUCTION

Liquefaction is a particular phenomenon of instability that is characterized by a significant loss of material resistance under a static or dynamic load. It is a phenomenon that can occur during earthquakes within granular soil (sand) due to the presence of water in confined spaces (i.e., there being no place where the water pressure can dissipate). As a result of the earthquake waves, the soil loses cohesion and friction between its particles and behaves like water. When seismic waves reach this type of soil, the soil loses cohesion and friction between its particles and behaves as water. When seismic waves reach this type of soil, a large compressive energy is transferred to both the soil and water between the grains, but affects more quickly the soil particles than the water (due to the vibrational and physical properties) creating tensile forces between the grains and thus decreasing the frictional forces within the granular network. So, the soil becomes non-resistant to the shear and water becomes the main carrier of the stresses transferred to the soil.

Several earthquakes occurred in the last century near Chlef located in northern Algeria. The most disastrous earthquake (El-Asnam 1980) with Richter Magnitude, ML = 7.2, corresponding to a Surface Wave Magnitude, Ms = 7.3 hit Chlef City and surrounding areas on October 10, 1980 (Belkhatir et al., [1]). The city lies in an expansive alluvial valley flanked toward the north and south by ranges of hills that rise to a height of roughly 1000 meters. Many failures occurred on heavily

Figure 1. Sliding of the Chlef river banks during the 1980 El Asnam earthquake.

populated regions, in this manner loss of life and a lot of damage occurred. Differential soil settlements were observed, especially in field areas, and large amounts of backfill behind bridge abutments collapsed. Numerous slope failures were observed in the mountains, some of them involving the whole side of hills in the typical region of fault movements (Figure 1). Some major slope failures were observed in the city of Chlef. Soil liquefaction occurred over widespread areas in the flood plain of the Chlef River, particularly in Chlef and the surrounding areas (Belkhatir et al., [2]).

The factors that have a major effect on the undrained shear strength (liquefaction resistance) of silty sands under monotonic and/or cyclic loading conditions have been extensively studied by Amini and Qi [3], Krim et al. [4]; Lade and Yamamuro [5]; Naeini and Baziar [6]; Sharafi and Baziar [7]; Thevanayagam [8]; Thevanayagam et al. [9]; Yamamuro and Lade [10]; Wang et al. [11]; and Zlatovic and Ishihara [12]. Tatsuoka et al. [13] made a study of Toyoura sand. Their results indicate that that the liquefaction resistance increases linearly with an increase of the relative density until a value of 70 %. After this value, they found that there is a significant increase of the liquefaction resistance. Polito and Martin [14] conducted a series of triaxial tests on Monterrey and Yatesville sand samples with different fines contents. They found a linear trend between the change in the liquefaction resistance and the increase in the relative density until a limit value of fines was reached. However, the resistance to liquefaction higher than this limit value is also controlled by the relative density of the sample. Mulilis et al. [15] conducted a series of stress-controlled cyclic triaxial tests and found that the sand prepared by moist tamping exhibited a liquefaction resistance far superior to their counterparts formed by air pluviation. Using cyclic undrained triaxial tests, Benghalia et al. [16] conducted a laboratory study prone to the liquefaction resistance, emphasizing the effects of the fines content on the mechanical behavior of Chlef, Rass and Zemmouri sands. They found that the effect of fines can lead to an increase of the liquefaction resistance for Zemmouri sand, and a decrease or stabilization for the Rass and Chlef sands, respectively. Arab and Belkhatir [17] conducted a series of undrained triaxial cyclic tests which were carried out for fines contents ranging from 0 to 40 %, emphasizing their study on the effect of low plastic fines on the cyclic behavior of the sand-silt mixtures and also the effect of the preloading on the soil liquefaction. Their test results indicated that the liquefaction potential of the mixtures decreases with increasing fines content until f_c = 20 %, after which the potential of the liquefaction increases moderately with the fines content f_c = 40 %. They concluded that the over-consolidation and the cyclic drained preloading of low stress amplitude improved the liquefaction resistance of the sand-silt mixtures. Shariatmadari et al. [18] investigated the stress/strain characteristics of sand/ground rubber mixtures in the Sandlike zone, at different confining pressures, using hollow cylinder specimens subjected to torsional monotonic and cyclic loading. Their test results under cyclic loading on mixtures with 10 % and 25 % ground rubber had a similar liquefaction resistance. They concluded that the addition of ground rubber to the sand would affect the shear strain variation and excess pore-water pressure trends, and this effect was further intensified with an increasing ground-rubber percentage.

By using conventional cyclic triaxial undrained tests, the objective of the present laboratory study was to concentrate on the cyclic mechanical behavior of sand in terms of the liquefaction resistance; emphasizing the effect of the relative density (*Dr*) and the cyclic stress ratio (*CSR*) on the variation of the deviatoric stress, change in the pore pressure and the (q, P') curves. The samples were consolidated under isotropic effective confining pressures of 100 kPa. Tests were conducted on three different relative densities, i.e., *Dr* = 15, 50 and 65 %, with three cyclic loading amplitudes (q_m = 30, 50 and 70 kPa). This leads to us having 0.15, 0.25 and 0.35 as the cyclic stress ratios ($CSR = q_m/(2 \cdot p'_c)$). Analyses of these results led to useful results concerning the influence of the above parameters on the liquefaction resistance of the sand. The paper presents the materials utilized as a part of the examination, the trial methodology and a parametric study.

2 MATERIALS, DEVICE AND TESTING PROGRAM

2.1 Tested materials

The soil used for this work (Figure 3) comes from the Chlef Valley in Algeria and contains a low silt content (f_c = 2.7 %). The soil is a medium sand whose average grain size is characterized by D_{50} = 0.61 mm. This material has been the subject of numerous research, in particular (Aouali et al. [19]; Arab et al., [20]; Belkhatir et al. [1] ; Benessalah, [21]; Benessalah et al., [22]; [23]; [24]; Boutouba et al. [25]; Della et al. [26]; Flitti et al. [27]; Merabet et al. [28]). The unit weight of the soil particles γ_s is 26.63 kN/m^3 according to the ASTM D854-83 [29] standard. The silt is non-plastic with a low plasticity index of 6 %. This sand was used as a base material for the sample preparation. The sand particles are isometric and have a round form, composed mainly of quartz with a certain proportion of limestone. All the samples were taken from a layer of liquefiable soil 6 to 8 m below the natural ground (Figure 2a). The samples taken from this layer were silty sand. But the study in this paper focused on the clean sand. The soil was cleaned before the

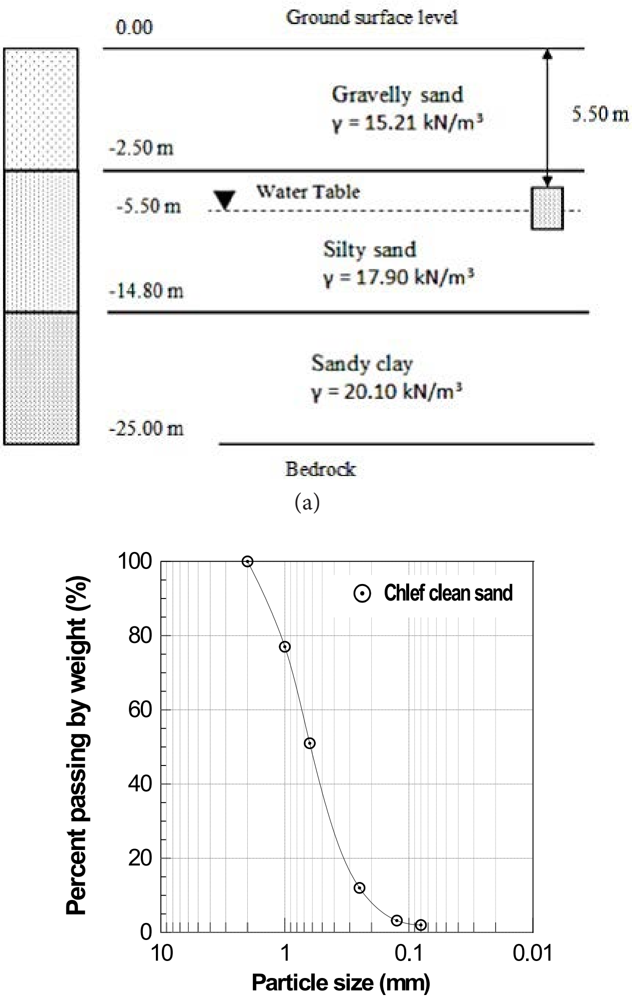

Figure 2. Sand used: (a) Geotechnical profile of the soil deposit at the site, (b) Grain size distribution curve of tested Chlef sand.

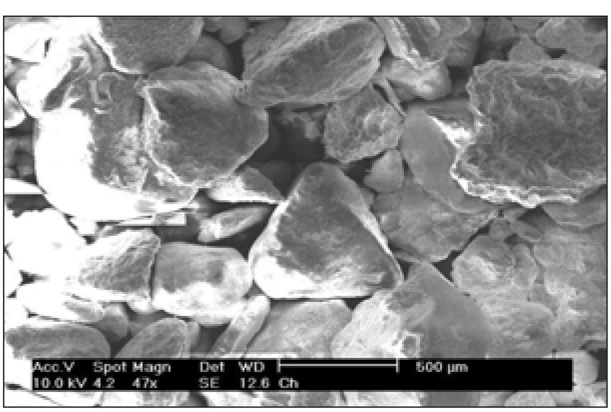

Figure 3. Scanning electron microscope (SEM) view of Chlef sand [31].

samples' preparation. The sizes of the solid grains vary between 0.08 and 2 millimeters, the grain size distribution was obtained on the basis of the ASTM D422-63 [30] standard and shown in Figure 2b. The basic physical properties of the sand are given in Table 1. The sand can be defined as poorly graduated with little or no fines with SP symbols according to USCS.

Table 1. Principal properties of Chlef sand.

Composition	Chlef sand
Mean grain size, D_{50} (mm)	0.61
D_{10} (mm)	0.225
Coefficient of uniformity, C_u (.)	3.38
Coefficient of curvature, C_c (.)	0.98
USCS classification	SP*
Unit weight of the solid grains, γ_s (kN/m^3)	26.63
Minimum void ratio, e_{min} (.)	0.854
Maximum void ratio, e_{max} (.)	0.535
Fine content, f_c (%)	0.5
Plasticity index of fines elements (%)	6

2.2 Device and testing program

2.2.1 Samples preparation

The care taken in the preparation of the soil samples of 70 mm in diameter and 70 mm in height is very important in the experimental procedure and will be described in this section. First, the dry soil samples are set up and compacted meticulously by successive layers (seven, in general); their masses being beforehand calculated to reach the desired height and density of the sample. A static process of compaction was applied, as reported by Unnikrishnan et al. [32]. The method of deposition that was utilized as a part of this investigation was dry funnel pluviation (DFP) (w = 0). Dry pluviation appeared to make the grain structure like that of naturally deposited sands. Thus, the dry pluviation mode was chosen as a reasonable deposition system for the specimens' preparation. The mass of sand used to reconstitute the sand test in the triaxial chamber was based on the initial relative density (Dr = 25 %) using Eq. 1. This formula has been used in the literature by Benessalah et al. [33]; Merabet et al. [28]; Aouali et al., [19]).

$$m_s = (V_T * \gamma_s)/(1 + e_{\max}(1 - Dr) + Dr * e_{\min}) \qquad (1)$$

The sample construction was carried out in a cylindrical mold; a latex membrane having a thickness of 0.3 mm is plated by the application of a vacuum between it and the mold. At both ends of the sample are placed two porous bases to allow the flow of water inside the sample. The mold is released by applying a slight negative pressure to the sample (about -15 kPa). Once the mold is removed, this pressure is reduced to -100 kPa to maintain the sample. Note that at this stage, the sample is already consolidated under 100 kPa confinement. If the desired consolidation pressure is less than 100 kPa, the vacuum pressure in the sample must not exceed this value. Subsequently, the confinement constraint is gradually applied to the desired value.

2.2.2 Consolidation and samples saturation

The samples are isotropically consolidated with an effective initial confining pressure (σ'_c) equal to 100 kPa. The degree of saturation is verified by the Skempton coefficient B after consolidation. To obtain a satisfactory degree of saturation, an upward flow of carbon dioxide is introduced into the sample at low pressure (about 16 kPa) for 8 to 10 minutes, which allows the air to circulate freely. Then, distilled water is introduced into the test cylinder for 15 to 20 minutes. After this step, the drainage lines are closed and the transducer is initialized to zero. After the consolidation step and evaluation of e_0 (i.e., the void ratio after consolidation), the axial load is applied at a constant rate (strain controlled). All of the undrained triaxial tests are conducted at a constant strain rate of 0.167 % per minute, which is slow enough to obtain a uniform pore pressure within the sample. This rate was successfully applied by several authors (Benessalah et al. [34]; Arab et al. [20]; Della et al. [26]).

3 RESULTS OF THE TESTS

A series of nine stress-controlled cyclic triaxial tests were carried out on samples of clean sand from the Oued Chlef region; under different cyclic stress ratios and different relative densities (*Dr* = 15, 50 and 65 %); with the same confining pressure of 100 kPa. The tested samples were subjected to symmetrically alternating modes of deviatoric stress under undrained conditions that simulate an essential undrained model similar to that of an earthquake to determine the potential liquefaction curves. A frequency of 0.3 Hz was used throughout the testing program. The Table 2 presents the experimental program of this laboratory study.

3.1 Effect of the cyclic loading amplitude (q_m) on the undrained response

3.1.1 Samples with a loose relative density

Figures 4, 5 and 6 show the results of the undrained cyclic tests carried out on samples with an initial relative density *Dr* = 15 % ; sheared under imposed shear stresses of 30, 50 and 70 kPa. The cyclic liquefaction was obtained after two loading cycles for the samples sheared under an imposed shear stress of 70 kPa, whereas for samples sheared under 50 and 30 kPa liquefaction was obtained after three and twenty-three cycles, respectively.

3.1.2 Samples with a medium relative density

Figures 7, 8 and 9 illustrate the results of the undrained cyclic tests performed on samples with an initial relative density *Dr* = 50 %, sheared under imposed shear stresses of 30, 50 and 70 kPa. The cyclic liquefaction was obtained after four loading cycles for the samples sheared under an imposed stress of 70 kPa. For samples sheared under 50 and 30 kPa, liquefaction was obtained after six and seventy cycles, respectively. The present results are in good agreement with those found by Benghalia et al. [17].

Table 2. Summary of undrained cyclic triaxial tests.

N°	Name of the test	Cycle stress ratio, *CSR*	Relative density, *Dr* (%)	Initial confining pressure, σ'_c (kPa)	Skempton coefficient, *B* (%)	Number of cycles, N_c
1	CU_30_LD	0.15	15	100	90	23
2	CU_50_LD	0.25	15	100	90	3
3	CU_70_LD	0.35	15	100	90	2
4	CU_30_MD	0.15	50	100	90	70
5	CU_50_MD	0.25	50	100	85	6
6	CU_70_MD	0.35	50	100	85	4
7	CU_30_HD	0.15	65	100	85	120
8	CU_50_HD	0.25	65	100	89	11
9	CU_70_HD	0.35	65	100	92	5

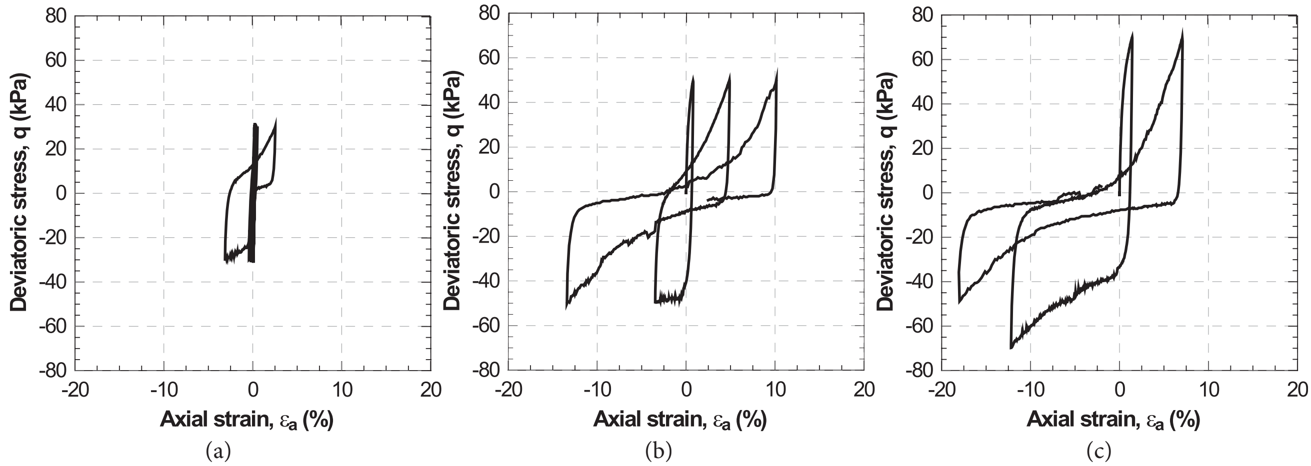

Figure 4. Undrained cyclic response, variation of the deviatoric stress versus axial strain (Dr = 15 %, σ'_c = 100 kPa): (a) CSR = 0.15, (b) CSR = 0.25, (c) CSR = 0.35.

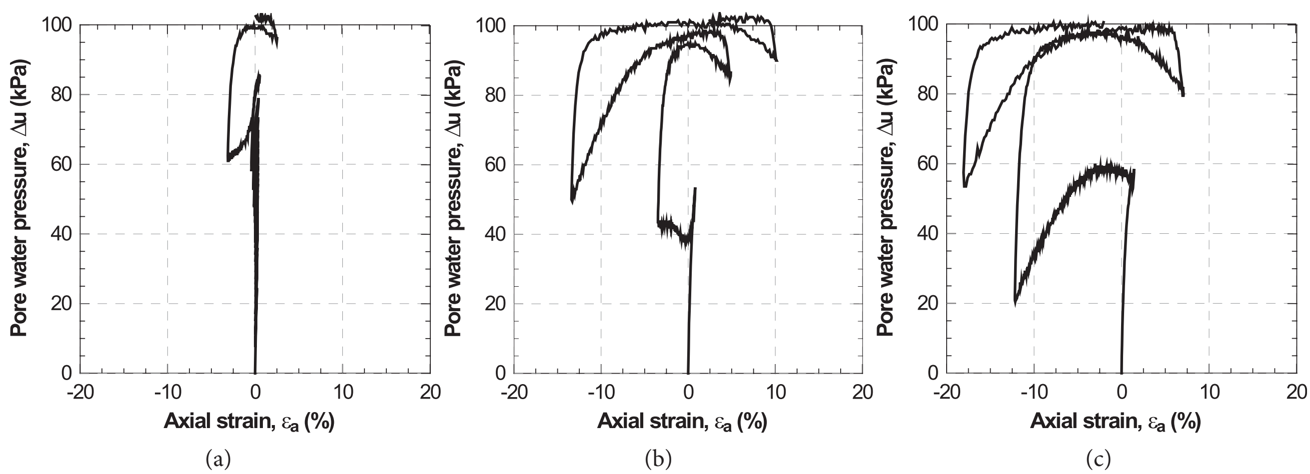

Figure 5. Undrained cyclic response, variation of the pore water pressure versus axial strain (Dr = 15 %, σ'_c = 100 kPa): (a) CSR = 0.15, (b) CSR = 0.25, (c) CSR = 0.35.

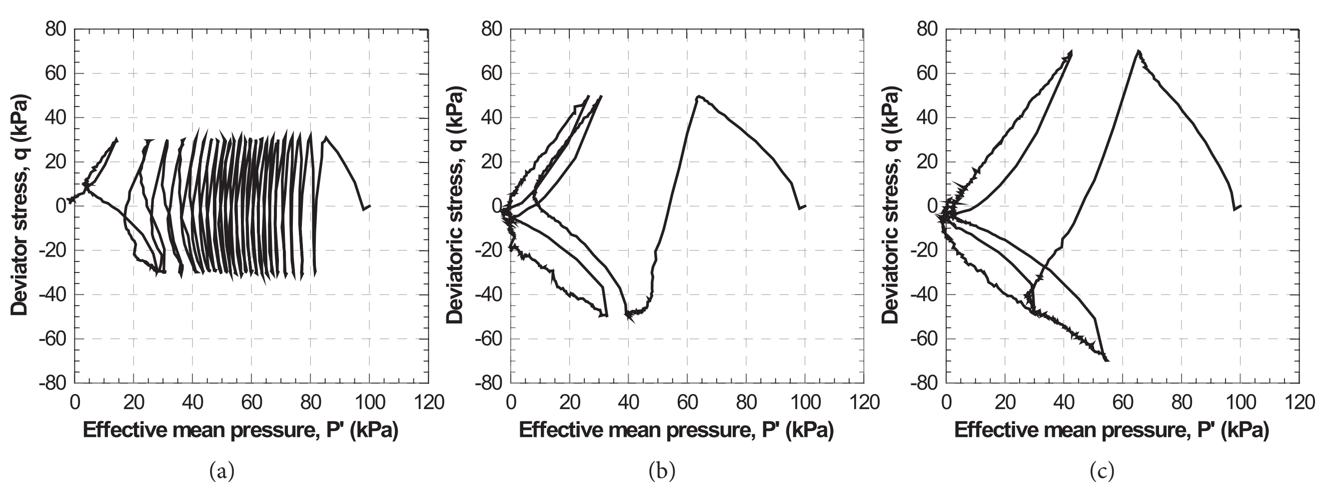

Figure 6. Undrained cyclic response, (q, P') curves (Dr = 15 %, σ'_c = 100 kPa): (a) CSR = 0.15, (b) CSR = 0.25, (c) CSR = 0.35.

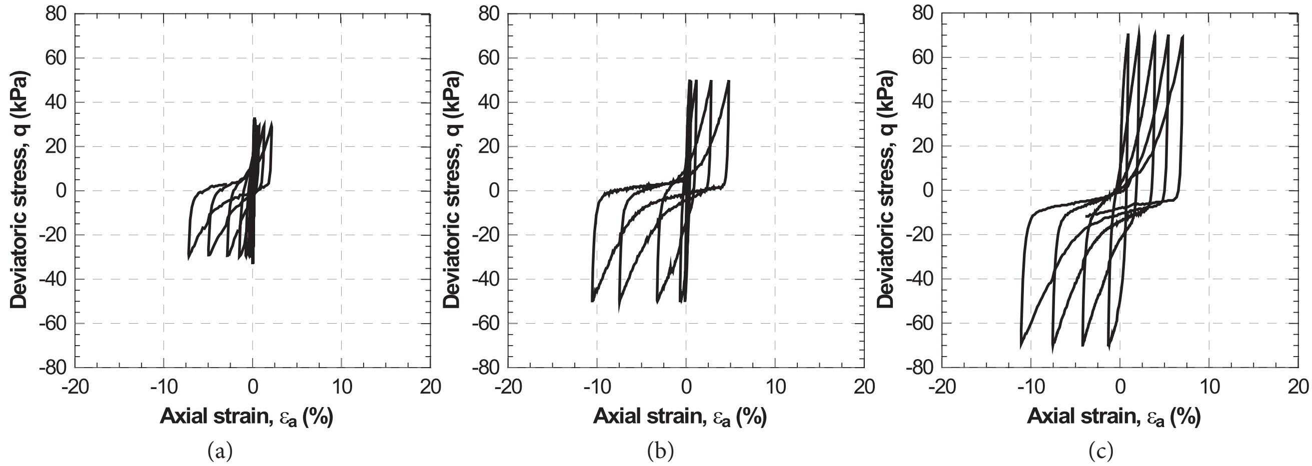

Figure 7. Undrained cyclic response, variation of the deviatoric stress versus axial strain (Dr = 50 %, σ'_c = 100 kPa): (a) CSR = 0.15, (b) CSR = 0.25, (c) CSR = 0.35.

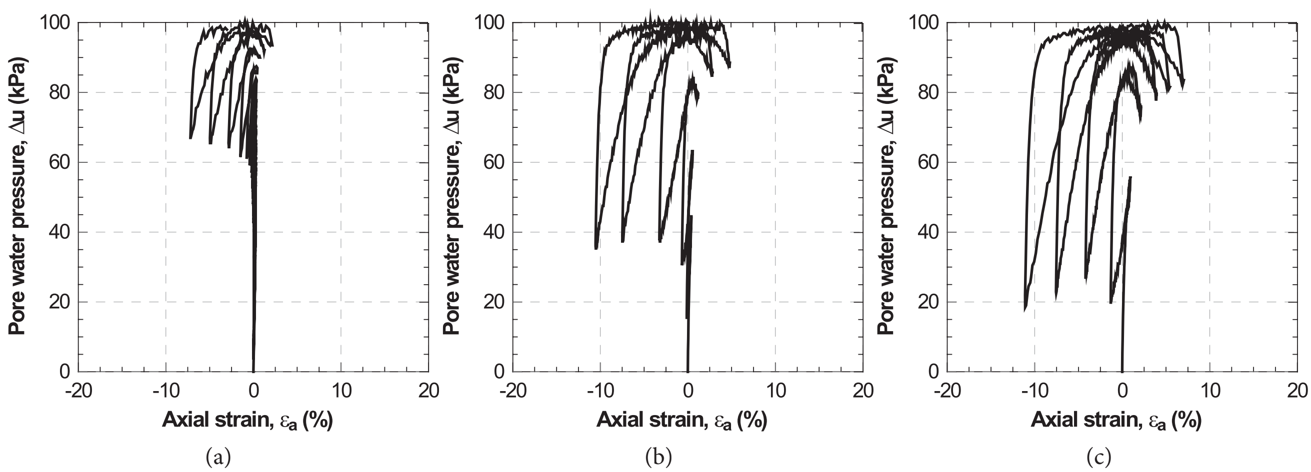

Figure 8. Undrained cyclic response, variation of the pore water pressure versus axial strain (Dr = 50 %, σ'_c = 100 kPa): (a) CSR = 0.15, (b) CSR = 0.25, (c) CSR = 0.35.

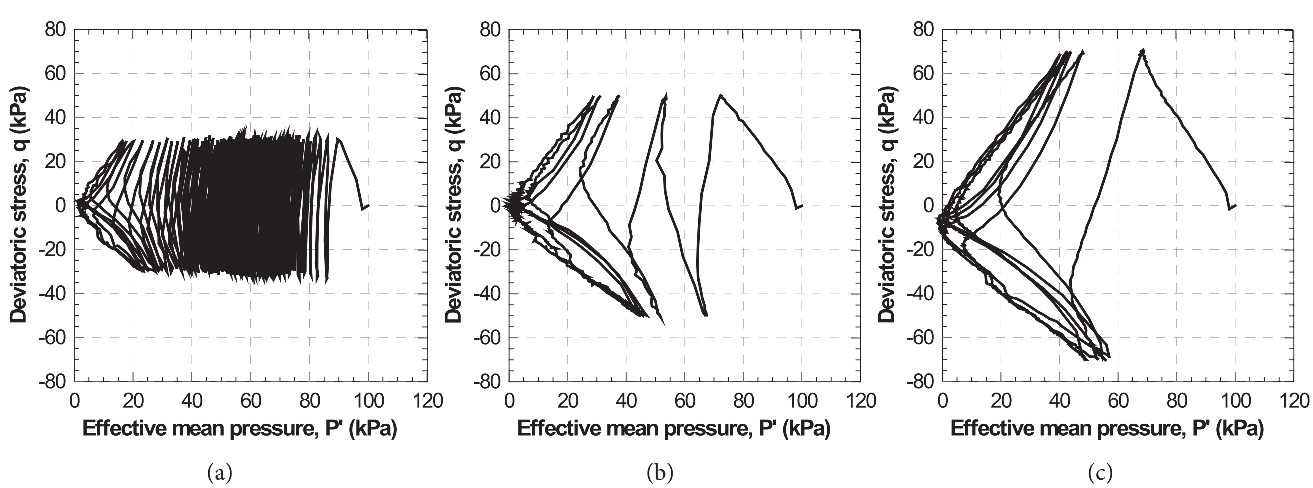

Figure 9. Undrained cyclic response, (q, P') curves (Dr = 50 %, σ'_c = 100 kPa): (a) CSR = 0.15, (b) CSR = 0.25, (c) CSR = 0.35.

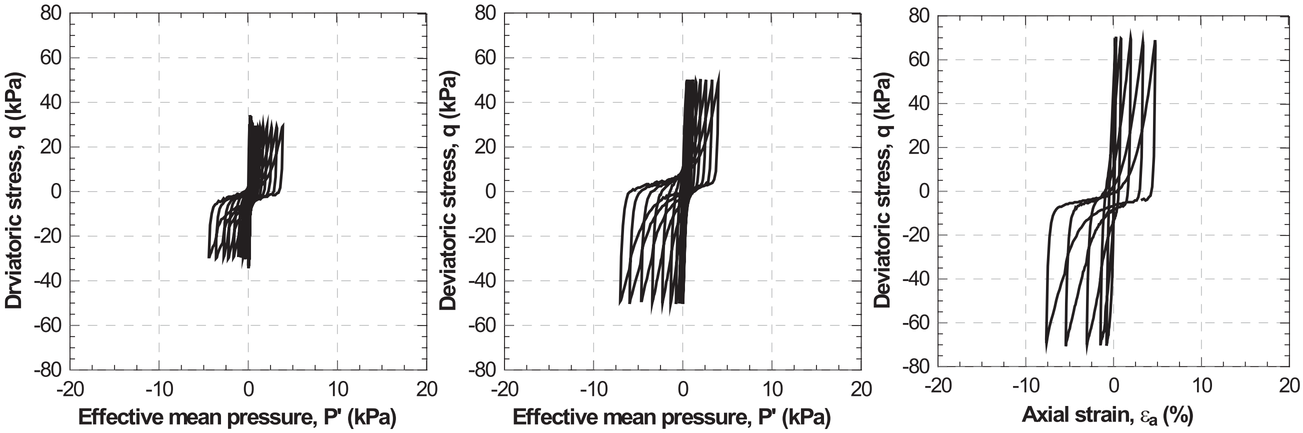

(a) (b) (c)

Figure 10. Undrained cyclic response, variation of the deviatoric stress versus axial strain (Dr = 65 %, σ'_c = 100 kPa): (a) CSR = 0.15, (b) CSR = 0.25, (c) CSR = 0.35.

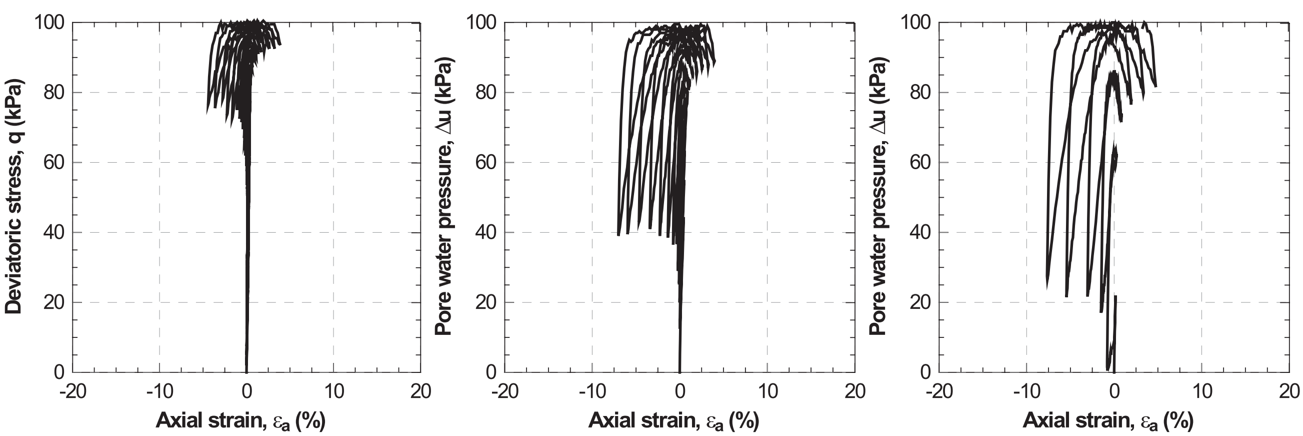

(a) (b) (c)

Figure 11. Undrained cyclic response, variation of the pore water pressure versus axial strain (Dr = 65 %, σ'_c = 100 kPa): (a) CSR = 0.15, (b) CSR = 0.25, (c) CSR = 0.35.

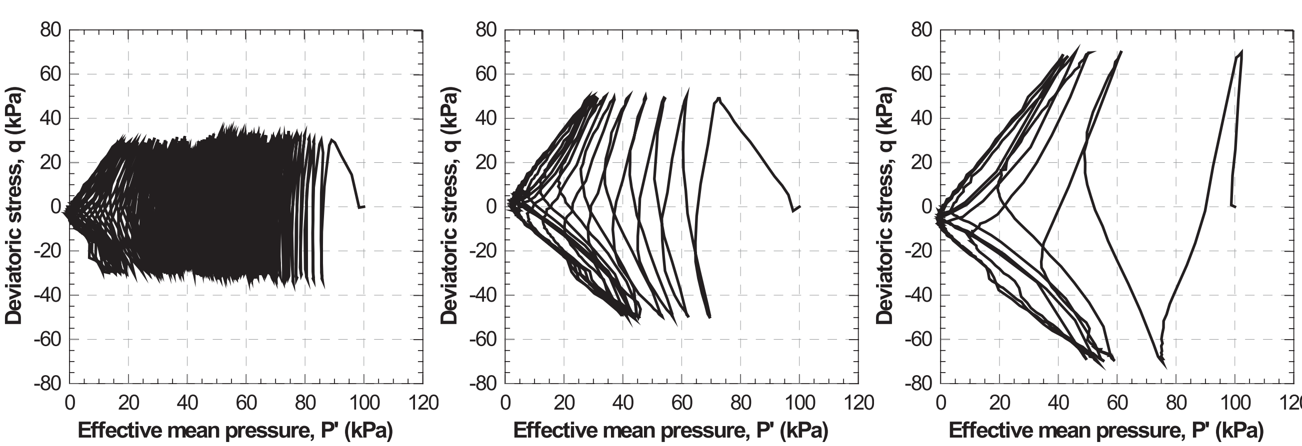

(a) (b) (c)

Figure 12. Undrained cyclic response, (q, P') curves (Dr = 65 %, σ'_c = 100 kPa): (a) CSR = 0.15, (b) CSR = 0.25, (c) CSR = 0.35.

3.1.3. Samples with a high relative density

The results of the undrained cyclic tests performed on samples with an initial relative density *Dr* = 65 %, sheared under imposed shear stresses of 70, 50 and 30 kPa are illustrated in Figure 10, 11 and 12. The results obtained show that the cyclic liquefaction was obtained after five loading cycles for the samples sheared under an imposed stress of 70 kPa, whereas for samples sheared under 50 and 30 kPa, liquefaction was obtained after eleven and one hundred and twenty cycles.

4 DISCUSSION

4.1 Variation of the number of cycles versus the relative density and cyclic stress ratio

It is noted here for the comparison that it takes 23 cycles to obtain total liquefaction for the sample sheared under a loading amplitude of 30 kPa and a relative density *Dr* = 15 %, while it takes 70 and 120 cycles for the same sample of relative density *Dr* = 50 and 65 %, respectively. The same observations are made for samples sheared under s of 70 and 50 kPa. Samples sheared under high loading amplitudes rapidly generate pore pressures (Figure 14).

The results of all these tests are summarized in Figure 13a. Figure 13a illustrates the influence of the relative density on the liquefaction resistance of the sand samples, and clearly shows that the increase in the relative density leads to an increase in the liquefaction resistance of this sand. Figure 13b illustrates the number of cycles evolution required for liquefaction as a function of the relative density (*Dr*). It should be noted here that the number of cycles increases almost exponentially with an increase of the relative density (*Dr*). This figure shows clearly that the liquefaction resistance increases with the increasing relative density and the decreasing of the loading amplitude. These results are in good agreement with those of Arab and Belkhatir [17].

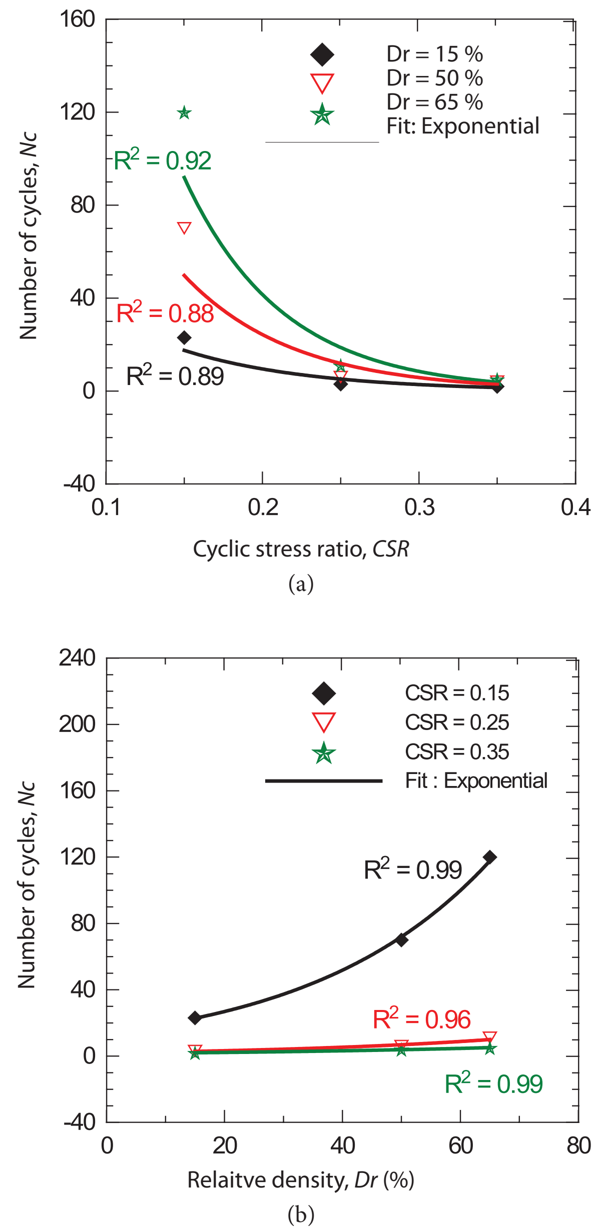

Figure 13. Variation in the number of cycles: (a) versus the cyclic stress ratio; (b) versus the relative density.

4.2 Variation of the pore-water pressure and axial strain versus the time

Figure 14 shows the evolution of the pore-water pressure and the axial strain during loading. Figure 14a illustrates the evolution of the pore-water pressure as a function of time. It is clearly noted that the samples with a relative density *Dr* = 15 % were liquefied faster (reaching the limit of 100 kPa after only 23 cycles) than the ones with *Dr* = 50 %, which were liquefied after 70 cyclesand compared to the samples with a relative density *Dr* = 65 % that were liquefied after 120 cycles. These results confirm those presented in Fig. 13a that explain the drop in values of the liquefaction resistance for the lower values of the relative density, which led us to conclude that the increase in the relative density led to improving the undrained cyclic behavior of the sand being studied. Note also that the test with an amplitude q_m = 0.35 (Figure 14b) rapidly generates the water pressure, reaching the value of the initial confining pressure (100 kPa) after only 5 cycles (cancellation of the effective stress). For the same value of the cyclic stress ration (*CSR* = 0.35), the axial deformation reaches 5 %

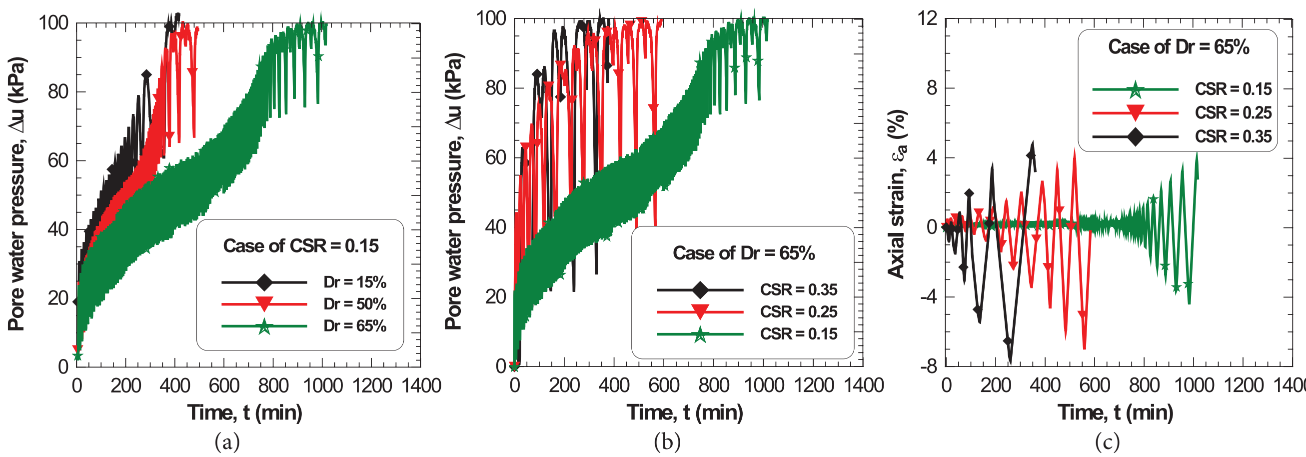

Figure 14. Evolution of pore pressure and axial strain during loading (versus time).

in compression and 8 % in extension after a period of around 375 min, which is less than the other values of cyclic stress ratio (around 580 and 1020 min for *CSR* = 0.25 and 0.15, respectively). These results mean that the greater cyclic stress ratio (or the greater amplitude) lead to faster liquefaction compared to a small amplitude, for an amplitude variation range between 30 and 70 kPa. Cyclic loading with an amplitude q_m = 50 kPa (or *CSR* = 0.25) leads to liquefaction after 11 cycles. The deformation reaches 4 % during compression and 7 % in extension. The test with q_m = 30 kPa leads to liquefaction after 120 cycles (Figure 14c).

5 CONCLUSION

A series of undrained cyclic triaxial tests were performed to investigate the performance of the relative density and the effect of the cyclic stress ratio (amplitude) on vulnerable sand (Chlef sand) in undrained conditions to the liquefaction phenomena. Tests were conducted on three different relative densities (*Dr* = 15, 50 and 65 %) for cases of three cyclic stress ratios (*CSR* = 0.15, 0.25 and 0.35) and under an initial confining pressure of 100 kPa. This study focused on the cyclic mechanical behavior of the samples under study in terms of the shear strength characterized by the deviatoric stress, pore-water pressure, number of cycles and the (*q*, *P*'). The results provide useful information about the influence of the relative density and the cyclic stress ratio on the enhancement of the cyclic mechanical behavior of the sand under study with respect to the liquefaction phenomena. The following conclusions can be deduced from this study:

- The increase in relative density leads to a significant translation of the liquefaction potential curves (Figure 13a) upwards. That is to say, the increase in the relative density improves the resistance to liquefaction of this sand. This result is consistent with the influence of the relative density on the increase in the expansion properties of the sand.
- Concerning the number of cycles of evolution required for liquefaction as a function of the relative density (*Dr*), our results indicate that the number of cycles increases almost exponentially with an increasing of the relative density, which means that the liquefaction resistance increases with increasing relative density and decreasing of the loading amplitude.
- For a giving value of the cyclic stress ratio (for example, *CSR* = 0.35), the axial deformation reaches 5 % in compression and 8 % in extension after a period of around 375 min, which is less than the other values of the cyclic stress ratio (around 580 and 1020 min for *CSR* = 0.25 and 0.15, respectively). These results mean that the greater cyclic stress ratio (or the greater amplitude) led to a faster liquefaction compared to the small amplitude, for an amplitude variation range between 30 and 70 kPa.

The behavior of the sand with respect to liquefaction by cyclic testing is recommended to obtain the most relevant information for the susceptible liquefied silty sand soils. The deductions of this study can be used in soil classification and to determine the liquefaction potential of seismic zones with higher values of relative density or the cyclic stress ratio.

Acknowledgment

The authors would like to thank the reviewers for their constructive and detailed comments. Tests were performed in the Laboratory of Material Sciences and

Environment (LsmE) at UHBC University of Chlef. The study was financially supported by the General Directorate for Scientific Research and Technological Development (DGRSDT). The authors express their gratitude to all who assist in the preparation of this paper.

REFERENCES

[1] Belkhatir M., Arab A., Schanz T., Missoum H., Della N., : Laboratory study on the liquefaction resistance of sand-silt mixtures: effect of grading characteristics. Granular Matter 13 (5), 599-609 (2011)

[2] Belkhatir M., Schanz T., Arab A. (2013). "Effect of fines content and void ratio on the saturated hydraulic conductivity and undrained shear strength of sand–silt mixtures". Environ Earth Sci. 2013, DOI 10.1007/s12665- 013-2289-z

[3] Amini, F., Qi, G.Z.: Liquefaction testing of stratified silty sands. J. Geotech. Geoenviron. Eng. Proc. ASCE 126(3), 208–217 (2000)

[4] Krim, A., Arab, A., Bouferra, R., Sadek, M. and Shahrour, I., (2016). «Characteristics of cyclic shear behaviour of sandy soils: A Laboratory study». Arabian Journal for Science and Engineering, 41(10), 3995-4005.

[5] Lade, P.V., Yamamuro, J.A.: Effects of non-plastic fines on static liquefaction of sands. Can. Geotech. J. 34, 918–928 (1997)

[6] Naeini, S.A., Baziar, M.H.: Effect of fines content on steady-state strength of mixed and layered samples of a sand. Soil Dyn. Earthq. Eng. 24, 181–187 (2004)

[7] Sharafi, H., Baziar, M.H.: A laboratory study on the liquefaction resistance of Firouzkooh silty sands using hollow torsional system. EJGE 15, 973–982 (2010)

[8] Thevanayagam, S.: Effect of fines and confining stress on undrained shear strength of silty sands. J. Geotech. Geoenviron. Eng. Div. ASCE 124(6), 479–491 (1998)

[9] Thevanayagam, S., Ravishankar, K., Mohan, S.: Effects of fines on monotonic undrained shear strength of sandy soils. ASTM Geotech. Test. J. 20(1), 394–406 (1997)

[10] Yamamuro, J.A., Lade, P.V.: Steady-state concepts and static liquefaction of silty sands. J. Geotech. Geoenviron. Eng. ASCE 124(9), 868–877 (1998)

[11] Wang, B., Chen, G. & Jin, D. (2010). Pore water pressure increment model for saturated Nanjing fine sand subject to cyclic loading. Earthq. Eng. Eng. Vib. 9: 569. https://doi.org/10.1007/s11803-010-0038-9

[12] Zlatovic, S., Ishihara, K.: On the influence of non-plastic fines on residual strength. In: Proceedings of the First International Conference on Earthquake Geotechnical Engineering. Tokyo, pp. 14–16 (1995)

[13] Tatsuoka, F.; Miura, S.; Yoshimi, Y.; Yasuda, S.; Makihara, Y.: Cyclic undrained triaxial strength of sand by a cooperative test program. Soils Found. 26, 117–128 (1986)

[14] Polito, C.P.; Martin, J.R.: Effects of non-plastic fines on the liquefaction resistance of sands. J. Geotech. Geoenviron. Eng. 127(5), 408–415 (2001)

[15] Mulilis, J. P., Seed, H. B., Chan, C. K., Mitchell, J. K., and Arulanandan, K. (1977). "Effects of sample preparation on sand liquefaction." J. Geotech. Engrg. Div., 103(GT2), 91–108.

[16] Benghalia Y., Bouafia A., Canou J., Dupla J. C. (2015). Liquefaction susceptibility study of sandy soils: effect of low plastic fines. Arab J Geosci (2015) 8: 605. https://doi.org/10.1007/s12517-013-1255-0

[17] Arab A., Belkhatir M. (2012) Fines content and cyclic preloading effect on liquefaction potential of silty sand: a laboratory study. Acta Polytechnica Hungarica 9(4):47–64

[18] Shariatmadari, N., Karimpour-Fard, M. & Shargh, A. (2018). Undrained monotonic and cyclic behavior of sand-ground rubber mixtures. Earthq. Eng. Eng. Vib. 17: 541. https://doi.org/10.1007/s11803-018-0461-x

[19] Aouali N., Benessalah I., Arab A., Ali B., Abed M. (2018). Shear Strength Response of Fibre Reinforced Chlef (Algeria) Silty Sand: Laboratory Study. Geotech Geol Eng. 2018. https://doi.org/10.1007/s10706-018-0641-5

[20] Arab A., Sadek M., Belkhatir M., Shahrour I. (2014). "Monotonic preloading Effect on the Liquefaction Resistance of Silty Sand: a Laboratory Study". Arabian Journal for Sciences Engineering. 2014. 39:685–694. DOI 10.1007/s13369-013-0700-4

[21] Benessalah I. (2017). "Comportement des interfaces géosynthétiques sous chargement dynamique due à l'impact". PhD thesis, Faculty of Civil engineering & Architecture. University of Chlef 2017.

[22] Benessalah, I., Arab, A., Sadek, M., Bouferra R. (2019): Laboratory study on the compressibility of sand–rubber mixtures under one dimensional consolidation loading conditions". Granular Matter (2019) 21: 7. https://doi.org/10.1007/s10035-018-0860-8

[23] Benessalah, I., Lambert, S., Villard, P., Arab, A. (2018). "Effect of dynamics on the Soil-geosynthetic interfaces used in reinforced rockfall embankments". Rock slope stability, Nov 2018, Chambéry, France. Rock slope stability, 2018. <hal-02000349>

[24] Benessalah I., Arab A., Villard P., Sadek M., Kadri A. (2015). "Laboratory Study on Shear Strength Behavior of Reinforced Sandy Soil: Effect of Glass-Fibers Content and Other Parameters". Arab J Sci Eng. 2015. 41 (4) : pp 1343-1353. doi:10.1007/s13369-015-1912-6
[25] Boutouba, K., Benessalah, I., Arab, A., Djafar Henni, A. (2019). Shear Strength Enhancement of Cemented Reinforced Sand: Role of Cement Content on the Macro-Mechanical Behavior. Studia Geotechnica et Mechanica. Volume 1 (ahead-of-print)
[26] Della, N., Arab, A., Belkhatir, M., Missoum, H., Bacconnet, C., and Boissier, D. (2010). "Effect of the initial structure on the behaviour of Chlef sand". Acta Geotechnica Slovenica. 2010. Vol. 5–15, no. 2, p. 5–15.
[27] Flitti, A., Della, N., De Kock, T., Cnudde, V., eras-tigui-Flores, D. R. (2019). Effect of initial fabric on the undrained response of clean Chlef sand. European Journal of Environmental and Civil Engineering. Doi : 10.1080/19648189.2019.1631217
[28] Merabet, K., Benessalah, I., Chemmam, M., Arab, A. (2019). Laboratory study of shear strength response of Chlef natural sand: Effect of saturation. Marine Georesources & Geotechnology. Online first: 11 May 2019. doi.org/10.1080/1064119X.2019.1595792
[29] ASTM D854-83. (1989). "Standard test method for specific gravity of soils". Annual Book of Standards, Vol. 04.08, West Conshohoken, pp. 162–164.
[30] ASTM D422-63. (1989). "Standard method for particle-size analysis of soils". Annual Book of Standards. Vol. 04.08, West Conshohoken, pp. 86–92.
[31] Djafar Henni A., Arab A., Belkhatir M., Hamoudi S. & Khelafi H. (2013). Undrained behavior of silty sand: effect of the overconsolidation ratio. Arab J Geosci 6, 297–307 (2013). https://doi.org/10.1007/s12517-011-0365-9
[32] Unnikrishnan N., Rajagopal K., Krishnaswamy N.R. (2002). "Behavior of reinforced clay under monotonic and cyclic loading". Geotxtiles and Geomembranes. 2002. 20, pp. 117-133
[33] Benessalah, I., Sadek, M., Villard, P. and Arab A. (2020). Undrained triaxial compression tests on three-dimensional reinforced sand: effect of the geocell height. European Journal of Environmental and Civil Engineering, 1-12
[34] Benessalah I., Arab A., Villard P., Merabet K., Bouferra R. (2016). "Shear Strength Response of a Geotextile-Reinforced Chlef Sand : A Laboratory Study". Geotech Geol Eng 2016. 34 (6) : pp 1775–1790. doi:10.1007/s10706-016-9988-7

A NEW APPROACH TO OPTIMIZING THE GEOGRID LAYOUT TO MAXIMIZE THE BEARING CAPACITY OF STRIP FOOTING

NOVI PRISTOP OPTIMIRANJA POSTAVITVE GEOTEKSTILA ZA POVEČANJE NOSILNOSTI TEMELJNIH TAL POD PASOVNIM TEMELJEM

Masoud Rabeti Moghadam *(corresponding author)*
Yasouj University,
Faculty of Engineering,
Department of Civil Engineering,
Yasouj, Iran
E-mail: rabeti@yu.ac.ir

Jahanpour Monfared
Yasouj University,
Faculty of Engineering,
Department of Civil Engineering
Yasouj, Iran
E-mail: jahan.m2011@gmail.com

Mansour Parvizi
Yasouj University,
Faculty of Engineering,
Department of Civil Engineering
Yasouj, Iran
E-mail: parvizi@yu.ac.ir

DOI https://doi.org/10.18690/actageotechslov.18.2.56-69.2022

Keywords

bearing capacity, strip footing, geogrid, optimum layout, finite element

Ključne besede

nosilnost temeljnih tal, pasovni temelj, geomreža, optimalna postavitev, končni element

Abstract

This study presents a new approach to optimizing the layout of the geogrid layers to achieve the maximum bearing capacity of the strip footing under different loading conditions (Vertical (V), Horizontal (H) and eccentric (M) loads) using a numerical method. To find the best location of the geogrid layers in the current method, the optimum depth of each layer is obtained separately, which was not considered in previous studies. The effects of parameters such as different loading combinations, numbers and layout of geogrid layers on the ultimate bearing capacity of the strip footing have been studied. The results of the analyses are plotted in the form of dimensionless graphs. For different loading combinations, the optimum layout and number of reinforcing layers have been determined. The results show that the presence of the reinforced layers, at the optimum layout, significantly increases the ultimate bearing capacity of the strip footing, especially in the V and VM loading conditions. The optimum number of geogrid layers was different for different loading conditions. Based on the analyses, 7, 4 and 4 geogrid layers were obtained as the optimum number of reinforcement layers for the V, VH and VM loading conditions, respectively. Also, it was found that the position of each layer depends on the number of

Izvleček

Študija predstavlja uporabo numeričnih metod za nov pristop k optimizaciji postavitve plasti geomreže za doseganje največje nosilnosti temeljnih tal pod pasovnim temeljem pri različnih obtežnih pogojih (vertikalna (V), horizontalna (H), in ekscentrična obtežba (M)). Pri iskanju najboljše lokacije plasti geomreže v predstavljeni metodi se optimalna globina vsake plasti določi posebej, kar v prejšnjih študijah ni bilo upoštevano. Proučevani so vplivi parametrov, kot so različne kombinacije obtežb, število in postavitev plasti geomreže na mejno nosilnost temeljnih tal pod pasovnim temeljem. Rezultati analiz so prikazani v obliki brezdimenzijskih grafov. Za različne kombinacije obtežb je bila določena optimalna postavitev in število armaturnih plasti. Rezultati kažejo, da prisotnost ojačanih slojev pri optimalni postavitvi bistveno poveča mejno nosilnost temeljnih tal pod pasovnim temeljem, zlasti v pogojih obtežb V in VM. Optimalno število plasti geomreže je bilo različno za različne pogoje obtežb. Na podlagi analiz smo dobili 7, 4 oz. 4 plasti geomreže kot optimalno število armaturnih plasti za obremenitve V, VH oz. VM. Prav tako je bilo ugotovljeno, da je položaj posamezne plasti odvisen od števila plasti. V tej študiji je bila lega prvega sloja od temelja (u/B) *layers. In this study, the position of the first layer from the foundation (u/B) was varied by increasing the number of reinforcement layers and the loading conditions. In the VM loading condition, the geogrid reinforcement effect on the bearing capacity is more prominent with respect to the VH loading conditions. The increase of the bearing capacity in the VM loading condition at the optimum layout of reinforcement (N = 4) is about 100 %, compared to the bearing capacity of the unreinforced soil.*

spreminjana s povečanjem števila armaturnih plasti in pogojev obremenjevanja. Pri obtežbi VM je učinek ojačitve geomreže na nosilnost bolj izrazit glede na pogoje obtežbe VH. Povečanje nosilnosti v stanju obtežbe VM pri optimalni postavitvi armature (N = 4) je približno 100 % v primerjavi z nosilnostjo nearmirane zemljine.

1 INTRODUCTION

Nowadays, geogrids are widely utilized in geotechnical engineering to enhance the mechanical properties of low bearing soils. Many experimental and numerical types of research have demonstrated the effectiveness of geogrid-reinforced soil foundations. Most previous researchers considered only vertically applied loads to obtain the effectiveness of the geogrid on the bearing capacity of the strip footing [1-12], however, other studies considered the effect of the eccentricity and inclination of loads on the bearing capacity of reinforced soils [13-18]. Previous studies show that the layout of the geogrid layers including the distance between the first layer and footing (u), the vertical spacing of the reinforced layers (h), the length of the reinforcements (L) and the number of the reinforcement layers (N), play an important role in increasing the foundation's bearing capacity. Previous researchers investigated the optimum layout of the reinforcement layers to maximize the bearing capacity of the foundations as the most important parameter. The optimum values for these parameters resulted from the previous researchers are demonstrated in Table 1. As can be seen, the optimum values are varying from one study to another, which depends on the soil properties, the loading condition, and the type of footing.

Gottardi and Butterfield [19] experimentally analyzed the bearing capacity of the shallow footing under both inclined and eccentric loads. In this research, the

Table 1. Optimum values for the geogrid's layout parameters, obtained by previous researchers [1-18].

Studies	Type of footing	Type of load	Type of soil	u/B*	h/B	N
Binquet and Lee [1]	Strip	V	Sand	0.33	0.33	6
Khing et al. [2]	Strip	V	Sand	0.25-0.4	0.375	6
Omar et al. [3]	Strip	V	Sand	0.4	0.33	6
Das et al. [4]	Strip	V	Sand	0.33	0.33	8
Shin et al. [6]	Strip	V	Sand	0.4	0.4	6
Patra et al. [7]	Strip	V	Sand	0.35	0.25	4
Patra et al. [13]	Strip	V-VM	Sand	0.35	0.25	4
Saran et al. [14]	Square	V-VM	Sand	0.25	0.25	4
Sadoglu et al. [15]	Strip	V-VM	Sand	0.5	-	1
El-Sawwaf [16]	Strip	V-VM	Sand	0.33	0.53	3
Zidan [23]	Circular	V	Sand	0.19	0.2	4
Chakraborty and Kumar [9]	Circular	V	Sand	0.2-0.4	0.0.25-0.4	2
Chen and Abu-Farsakh [10]	Strip	V	Sand	0.2-0.4	0.2-0.4	-
Badakhshan and Noorzad [17]	Circular	V-VM	Sand	0.42	0.42	3
Badakhshan and Noorzad [18]	Square-Circular	V-VM	Sand	0.42	0.42	3
Ziegler [11]	Circular	V	Sand	0.45	0.45	7
El-Saud and Belal [12]	Strip	V	Sand	0.25	-	1

*B= width of the foundation

interaction diagrams approach was used, and also the reasons for the models' failures were explained. Loukidis et al. [20] used the finite-element method to study the collapse of strip footings under the combined loadings of *V*, *VH* and *VM*. The ultimate bearing capacity in the *V*, *VH* and *VM* space was determined. Based on the numerical results, formulas were proposed for the inclination factor, the effective width, and the footing-failure envelope in the *V*, *VH*, and *VM* space. The behavior of circular footings over reinforced sand under static and dynamic loading conditions was numerically investigated by Zidan [21]. In this study, the optimum value of u/B and h/B was obtained as 0.2.

In the previous studies, to determine the optimum layout of the geogrid layers to maximize the bearing capacity, firstly the optimum distance between the first geogrid layer and the base of the footing (u/B) was determined. Then, the next reinforcement layers were placed just under the first layer at constant intervals (h/B), until the maximum bearing capacity is achieved. In this study, the optimum depth of the geogrid layers was determined using a new procedure, in which the optimum depth of each geogrid layer (h/B) is determined separately instead of taking it constantly for different numbers of the geogrid layers. The optimum depth of each geogrid layer is defined as the depth that results in the maximum bearing capacity of the foundation. The study was performed using a series of verified numerical modeling, considering the different loading conditions.

Table 2. Properties of materials used in the numerical analyses [20].

Material	Parameter	Notation	Unit	Value
Soil	Soil type	-		SAND
	Modulus of elasticity	E_S	kN/m^2	8×10^4
	Friction angle	φ	°	35
	Cohesion	c	kPa	0
	Poisson's ratio	ϑ	-	0.35
	Unit weight	γ	kN/m^3	20
	Dilatancy angle	ψ	°	6
	Interface coefficient	R_{int}	-	0.9
Foundation	Material	-	-	Concrete
	Footing width	B	m	1
	Footing thickness	t	m	0.5
	Modulus of elasticity	E_c	GPa	20
Geogrid	Geogrid type			22XT
	Axial stiffness	EA	kN	2000
	Geogrid Length	L	m	1
	Geogrid Width	W	m	6
	Mass per unit area	m	gr/m^2	956
	Ultimate tensile strength	F_u	kN/m	300
	Tensile strength (at 5 % strain)	$F_{u,5\%}$	kN/m	98

2 NUMERICAL MODELING

PLAXIS 2D finite-element software was used to assess the effects of the geogrid on the ultimate bearing capacity of strip footing under different loading conditions.

The results of the numerical model were verified against the results of previous studies. For this purpose, the two-dimensional plane-strain model was considered with 6 m height and 13 m width. Moreover, the strip footing was designed with 1 m of width ($B = 1$ m) and

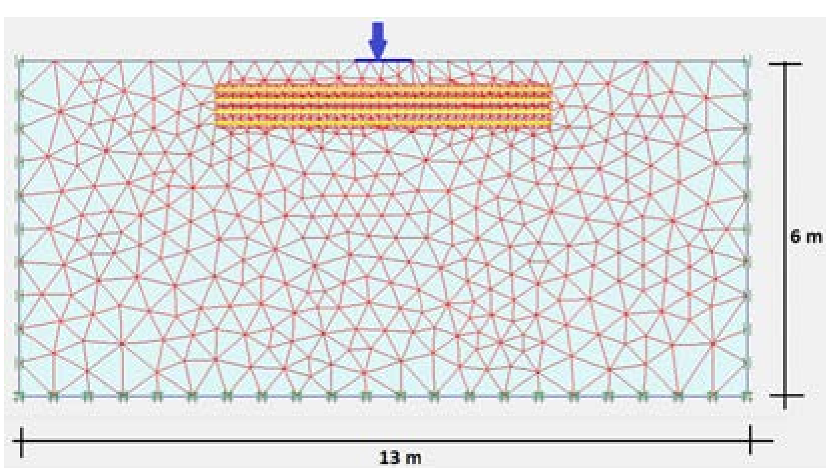

Figure 1. The general layout of the numerical model for the reinforced footing.

0.5 m of thickness using concrete material. 15-node triangular elements were used to mesh the finite-element model. The behavior of sandy soil was modeled with the Mohr-Coulomb failure criterion. To define the materials used in the modeling of the concrete footing, the PLATE element was used in PLAXIS software. Since the input parameters for the PLATE element are bending stiffness (EI) and normal stiffness (EA), the values were calculated based on $E = 20$ GPa, where E is the elasticity modulus of the concrete material. The geogrid elements were modeled by predefined GEOGRID elements in the software. Miragrid@22XT geogrid was used in the analyses [22]. The width of geogrids was considered to be 6 m (6B), according to Khing et al., Chen, and Abu-Farsakh [2,10]. The properties of the defined materials in the numerical model are given in Table 2. The geometry of the numerical model is also shown in Figure 1.

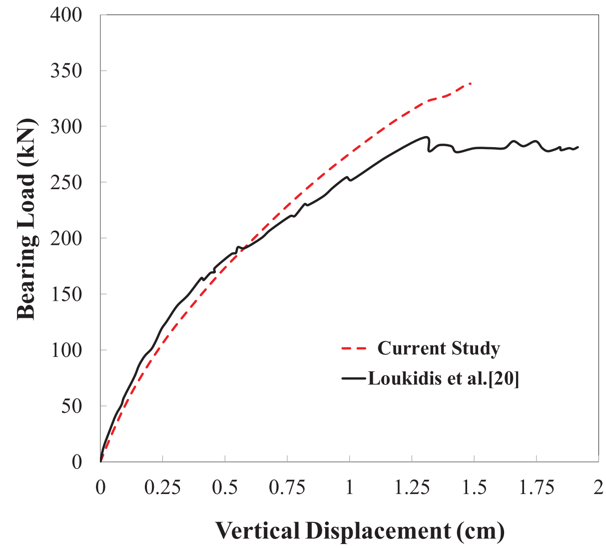

Figure 2. Load-displacement curve: current study vs Loukidis et al. [20].

3 VERIFICATION OF THE NUMERICAL MODEL

To verify the accuracy of the numerical model, the results of the models were compared with the results of Loukidis et al. and Gottardi and Butterfield [19-20]. Gottradi and Butterfield [19] performed a series of experimental tests and proposed equations for the bearing capacity of the strip footing under eccentric and inclined loads. Loukidis et al. [20] studied the bearing capacity of strip footings on sandy soil under eccentric and inclined loads using a numerical model.

The verification of the numerical model was performed for the loading combinations of V, VH and VM defined as follows:

- Comb I. Vertical load is applied at the center of footing (V)
- Comb II. Combinations of Vertical and Horizontal loads were applied to the footing (VH)
- Comb III. Vertical load with eccentricity is applied to the footing (VM)

3.1 Comb I. Vertical load is applied at the center of the footing (V)

Figure 2 indicates the load-displacement curve of the numerical analysis and the results of Loukidis et al. [20]. The model simulates the strip footing on the unreinforced sand under the vertical loading (V), applied at the center of the foundation. As shown in Figure 2, the results of the PLAXIS model and the results of Loukidis et al. [20] are in good agreement, both in the terms of the load-displacement curve and the ultimate bearing capacity. The ultimate bearing capacity of the unreinforced soil in the vertical loading condition (V_{max}) is equal to 286.6 kN and 338.1 kN, for Loukidis et al. [20] and the current study, respectively.

3.2 Comb II. Combination of Vertical and Horizontal loads (VH)

In the VH loading condition, combinations of vertical and horizontal loads were applied to the footing in two stages. In the first stage, the vertical load (V), as a fraction of $V_{max} = 338.1$ kN, was applied to the footing. In the next stage, the shear force (H) was increased until the model was collapsed. For the unreinforced model, combinations of the vertical (V) and horizontal (H) forces, which resulted in the shear failure of the soil, are tabulated in Table 3. The corresponding diagram is depicted in Figure 3 in the dimensionless form (H/V_{max} vs V/V_{max}).

Table 3. Combinations of the vertical (V) and horizontal (H) forces that resulted in shear failure of the soil for unreinforced footing ($V_{max} = 338.1$ kN).

V (kN)	H (kN)	V/V_{max}	H/V_{max}
338.1	0	1	0
300	17	0.887	0.050
250	26	0.739	0.077
200	29.8	0.591	0.088
150	38	0.436	0.112
100	34.8	0.295	0.102
50	23.5	0.148	0.070
25	14.4	0.074	0.042
0	0	0	0

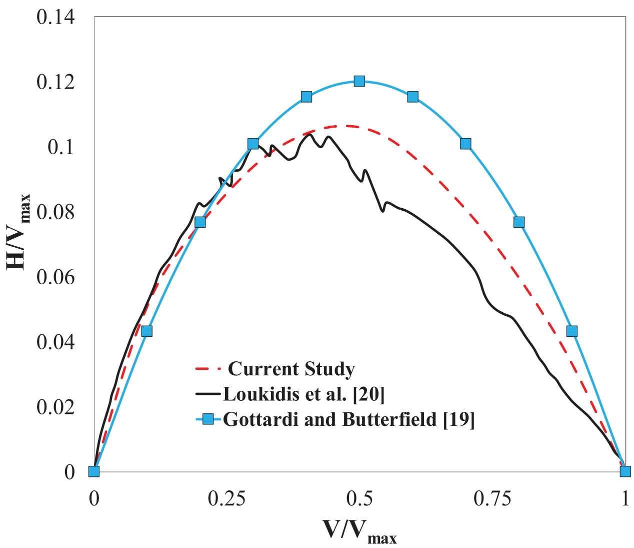

Figure 3. Dimensionless graph in *VH* loading condition: present study vs Gottardi and Butterfield [19] and Loukidis et al. [20].

Gottardi and Butterfield [19] proposed the following equation for the ultimate bearing capacity of strip footing under the *VH* loading condition, which presents a second-order parabola.

$$\frac{H}{V_{\max}} = 0.48\frac{V}{V_{\max}}(1-\frac{V}{V_{\max}}) \qquad (1)$$

In Figure 3 the dimensionless graphs that resulted from this study are compared with the Gottardi and Butterfield [19] and Loukidis et al. [20] in the *VH* loading condition. In this diagram the horizontal axis is V/V_{max} and the vertical axis is H/V_{max}, in a dimensionless space. As shown in Figure 3, the results of this study agree with the result of Gottardi and Butterfield [19] and Loukidis et al. [20].

3.3 Comb III. Vertical load with eccentricity is applied to the footing (*VM*)

For the unreinforced model, the vertical load with eccentricity (*VM*) that resulted in the shear failure of the soil is presented in Table 4. The corresponding diagram is depicted in Figure 4 in a dimensionless space (V/V_{max} vs $M/(B\times V_{max})$).

Gottardi and Butterfield [19] proposed the following equation for the ultimate bearing capacity of the strip footing, with the width of *B*, under the *VM* loading condition, which presents a second-order parabola.

$$\frac{M}{B\times V_{\max}} = 0.36\frac{V}{V_{\max}}(1-\frac{V}{V_{\max}}) \qquad (2)$$

Table 4. Combinations of the vertical load with eccentricity (*VM*) that resulted in shear failure of the unreinforced soil.

e/B	V	$M=V\times e$	$M/(B\times V_{max})$	V/V_{max}
0	338.1 (=V_{max})	0	0	1
$1/24$	296	12.33	0.04	0.88
$1/12$	247.4	20.62	0.06	0.73
$1/8$	210.2	26.28	0.08	0.62
$1/6$	178.3	29.72	0.09	0.53
$1/4$	111.4	27.85	0.08	0.33
$1/3$	48.3	16.1	0.05	0.14

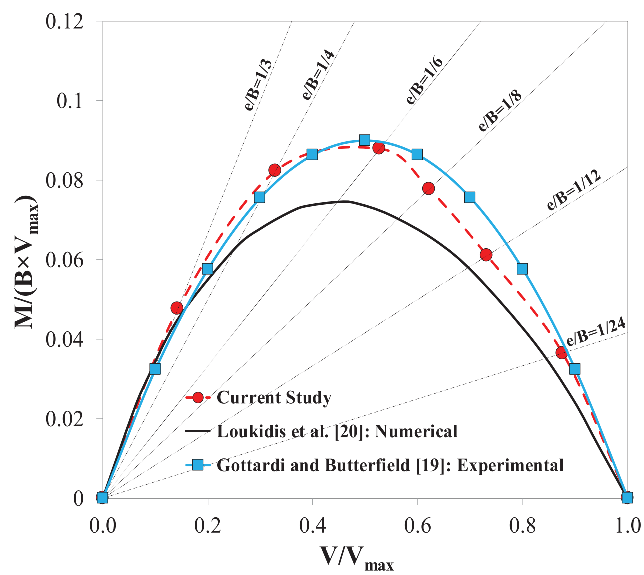

Figure 4. Dimensionless diagram in *VM* loading condition: this study vs Gottardi and Butterfield [19] and Loukidis et al. [20].

In Figure 4 the results of the numerical modeling in PLAXIS software are compared with the results of Loukidis et al. [20] and Gottardi and Butterfield [19], where the unreinforced footing is under the *VM* loading condition. The numerical model result is in good agreement with the previous studies, especially with the equation proposed by Gottardi and Butterfield [19].

3.4 The optimization procedure

In previous studies, to determine the optimum layout of the geogrid layers to maximize the bearing capacity, the optimum distance between the first layer and the base of the footing (u) was determined. Then, the next reinforcement layers were placed below the first layer at constant intervals (h). The added layer was placed at a deeper depth than previous layers.

In the current study, the optimum depth of the geogrid layers was determined using a new procedure. In this method, the optimum depths of the geogrid layers are determined separately for each layer, so that in each step the geogrid layer is added and placed at different depths from the foundation and its effect at different locations on the ultimate bearing capacity is surveyed. The depth that is related to the maximum bearing capacity is chosen as the optimum depth of the selected layer (Z_n). Subsequently, the number of layers was increased until the effects on the bearing capacity are significant. Therefore, in the current method, the optimum depth of each layer is obtained separately, something that was neglected by previous researchers. In this method, after determining the optimum depth of the first layer, the subsequent layer was placed above and below the first layer, and the effect of each layout was investigated on the ultimate bearing capacity. Based on this method, the optimum depth of the first layer from the foundation (u) was not constant and can vary with the number of geogrid layers.

Figure 5 illustrates that the parameters are defined in this study to optimize the layout of the geogrid layers. In this figure, V is a vertical force, applied on the footing, and B, L, and e are the width of the footing, the length of the geogrid layers and the eccentricity of the vertical load, respectively. Z_n is the optimum depth of the n^{th} layer of the geogrid from the base of the footing, which is obtained by placing the n^{th} layer at different depths and surveying its effect on the ultimate bearing capacity.

To determine the effect of a reinforced layer on the bearing capacity, the BCR_u parameter was used, which is defined by Eq. (3).

$$BCR_u = \frac{q_{u(R)}}{q_u} \qquad (3)$$

where BCR_u = ultimate bearing capacity ratio, $q_{u(R)}$ and q_u = ultimate bearing capacity with and without reinforcement, respectively [23].

4 ANALYSES, RESULTS AND DISCUSSIONS

4.1 Determination of the optimum reinforcement layout: V loading condition

4.1.1 Single-layer reinforcement

In Section 3.1 the maximum vertical load at failure for the strip footing on unreinforced soil was obtained to be 338.1 kN. To determine the optimum depth of the first layer from the foundation base, u (Z_1), a geogrid layer was placed at various depths from the footing. Then, the bearing capacity of the reinforced soil for each depth was

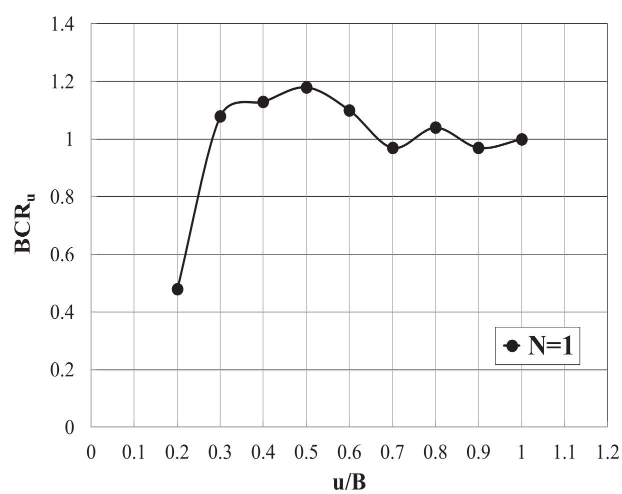

Figure 6. BCR_u versus u/B (Z_1/B) for single-layer geogrid.

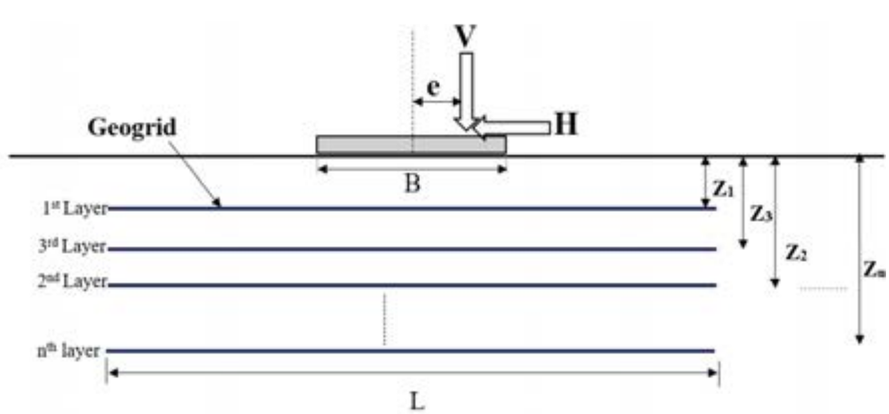

Figure 5. Parameters defined in the current study to investigate the effect of soil reinforcement on the bearing capacity.

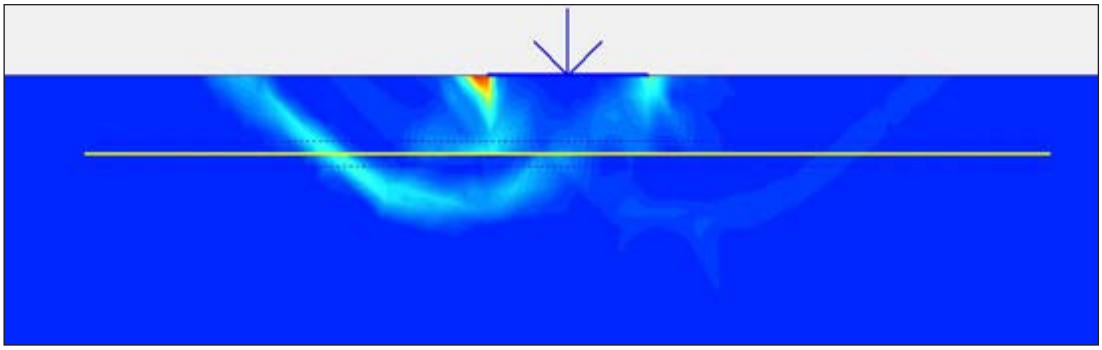

(a)

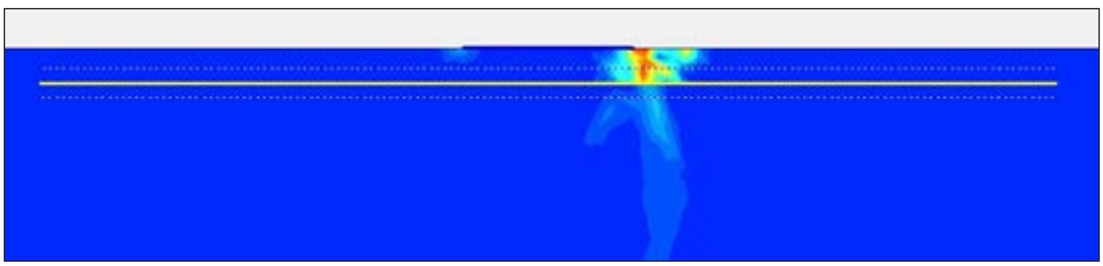

(b)

Figure 7. Developed failure wedges beneath the footing (a) geogrid at u/B = 0.5, (b) geogrid at u/B = 0.2.

calculated. The variation of the ultimate bearing capacity ratio versus the different values of u/B is shown in Figure 6. The optimum value of u/B is 0.5, where BCR_u is maximized. Figure 7 presents the failure wedge, developed beneath the footing, at u/B = 0.5 and u/B = 0.2. At u/B = 0.2 a rigid boundary is formed under the foundation, which prevents the failure wedges from developing.

4.1.2 Multi-layer reinforcement

The adopted procedure for finding the first layer's optimum depth was used to determine the optimum depth of the next layers of the geogrids (Z_i). Layers were added until the added layer had no significant effect on the ultimate bearing capacity. The maximum bearing-capacity ratio was achieved with 7 layers of reinforcement.

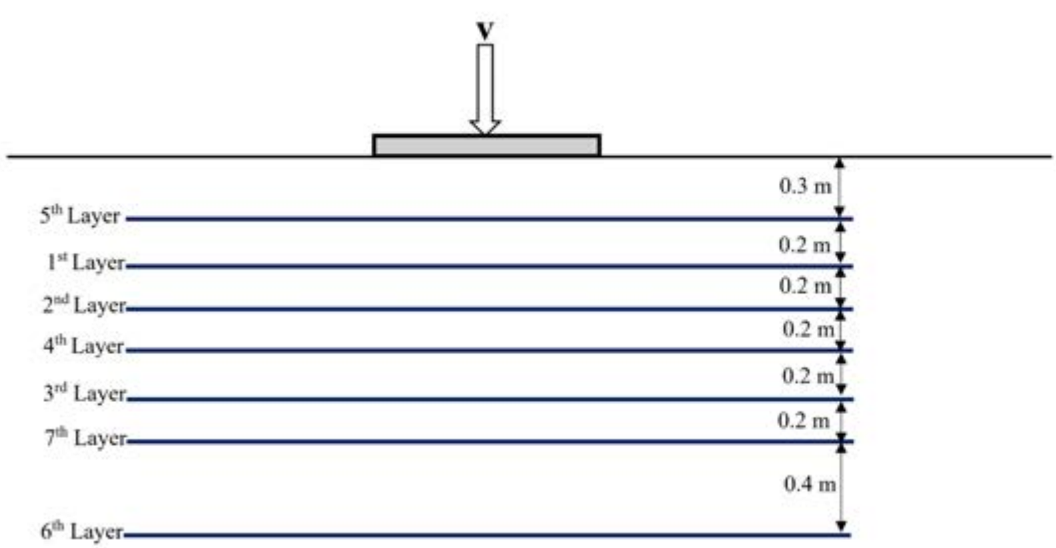

Figure 8. Optimum layout of the geogrid layers for the vertical loading condition (V).

Eventually, Figure 8 demonstrates the optimum configuration of the geogrid layers for the vertical loading (V). The figure shows the order of the placement of the layers to reach the maximum bearing capacity for the different numbers of geogrid layers. The optimum depth of the first layer from the footing base (u) is varied with the number of geogrid layers. For example, for the five layers $u/B = 0.3$, while for the two layers $u/B = 0.5$. Additionally, the spacing between the reinforced layers (h) is not identical to the optimum layout.

Table 5 demonstrates the variation of BCR_u for 8 layers of the reinforcements. Regarding the table, as the number of geogrid layers increases, the BCR_u increases until there are 7 layers of the geogrid. Also, the results of the BCR_u until the 4th geogrid layers were shown in Table 5 by using the classic approach and constant intervals between the geogrids. The proposed approach shows a 15 % rise in BCR_u until the 4th layer compared to the ordinary approach and Zidan [21] results. Zidan [21] suggested $h/B = 0.2$ to reach the best value for a bearing-capacity ratio that was obtained in the current study. Ghazavi and Lavasan [24] reported the ultimate bearing capacity is a maximum when u/B is between 0.25 and 0.35. Yetimoglu et al. [25] proposed the optimum u/B is approximately 0.3; they also recommended the optimum spacing for the reinforced sand (h/B) to be between 0.2B and 0.4B.

4.2 Determination of the optimum reinforcement layout: *VH* loading condition

We adopted the same scenario that was used for the V loading condition to determine the optimum depth of the geogrid layers in the VH loading condition. Adding the layers was continued until the added layer had no significant effect on the ultimate bearing capacity.

Table 5. Results of the numerical analyses for different numbers of the geogrid layers placed at the optimum layout.

Number of geogrid Layer	1	2	3	4	5	6	7	8
Depth of geogrid layer (u/B)	0.5	0.7	1.1	0.9	0.3	1.7	1.3	1.9
BCR_u using a new approach	1.18	1.36	1.4	2.13	2.39	2.38	3.04	1.59
BCR_u using a classic approach (h/B=0.2)	1.18	1.36	1.37	1.9	2.1	-	-	-

Figure 9 shows the effect of reinforcement on the bearing capacity of the foundation in the VH loading condition. For each number of the geogrid layer, some layouts of placement were considered and their effects on the bearing capacity were evaluated. The effect of using one layer of reinforcement ($N = 1$) was analyzed at different depths (Z_1), equal to 0.2, 0.3, 0.4, 0.5, 0.6 and 1 m. The obtained dimensionless diagrams are compared with the diagram of the unreinforced soil in Figure 9a. As is obvious from this figure, the bearing capacity of the foundation is increased by adding the geogrid layers. When the geogrid layer is placed at a depth of 0.5 m from the footing ($Z_1 = 0.5$), the reinforcement results in the highest bearing capacity. In Figure 9b, the effect of adding the second layer of the geogrid was investigated, considering $Z_2 = 0.3$, 0.7 and 0.9 m. It should be noted that the depth of the first layer (Z_1) is considered to be equal to 0.5 m, at the optimum depth. In this case, $Z_2 = 0.7$ m resulted in the highest bearing capacity and

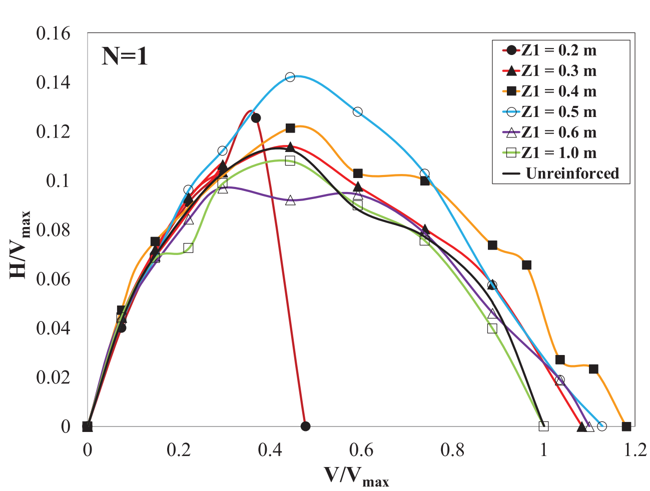

(a)

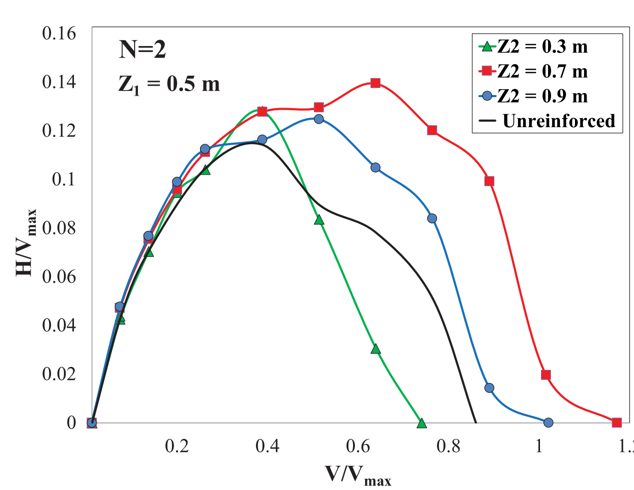

(b)

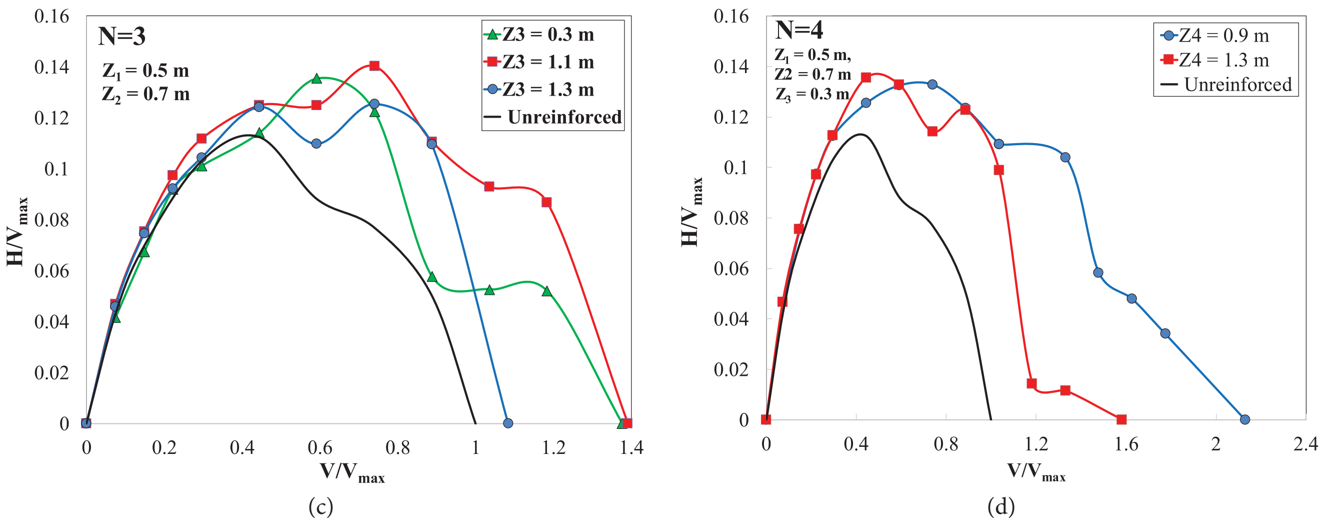

Figure 9. Dimensionless diagrams for the different numbers of geogrid layers in the *VH* loading condition (a) N = 1, (b) N = 2, (c) N = 3 and (d) N = 4.

was selected as the optimum depth for the second layer. Subsequently, the effects of the 3rd and 4th layers on the *VH* loading capacity were indicated in Figures 9c and 9d, respectively. From the diagrams, the optimum values for the depths of these layers are Z_3 = 1.1 m and Z_4 = 0.9 m, respectively.

To illustrate the effect of the geogrid reinforcement on the bearing capacity in the *VH* loading condition, the optimum cases from Figure 9 are collected and depicted in Figure 10. According to Figure 10, in the *VH* loading condition, adding one layer of the geogrid increases the *VH* bearing capacity of the soil up to 25 % relative to the unreinforced soil, although no significant enhancement can be seen in the horizontal bearing capacity for more layers. For the study performed here, four layers of geogrid resulted in the best improvement of the foundation bearing capacity for both the vertical and horizontal capacity.

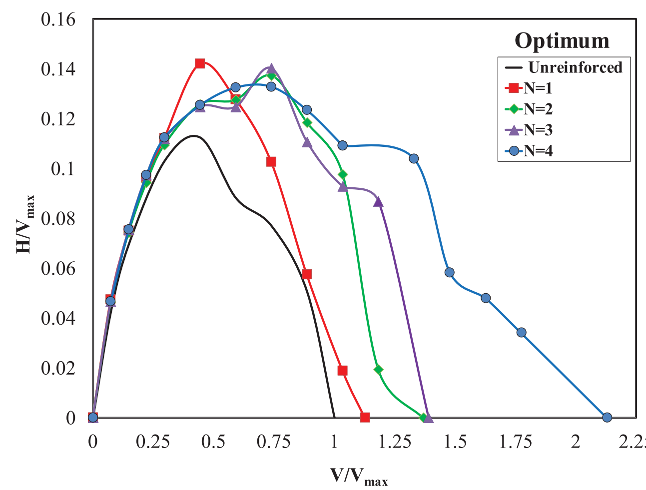

Figure 10. Dimensionless diagram for the optimum arrangement of geogrid layers in the *VH* loading condition.

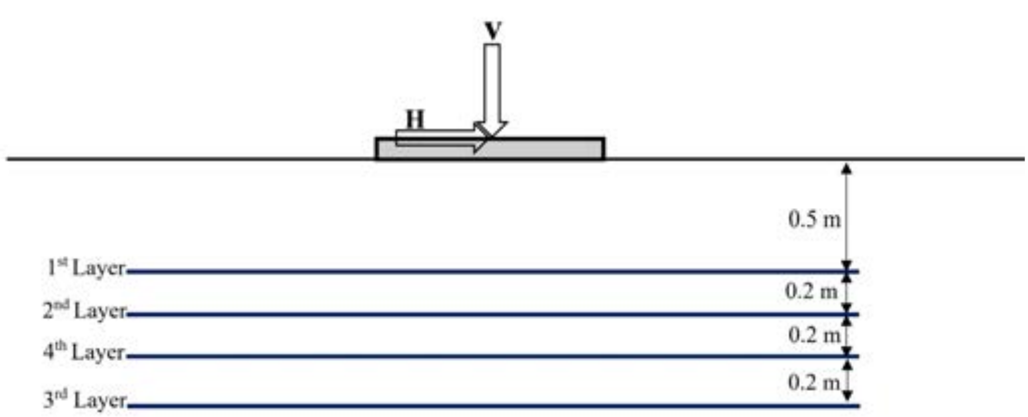

Figure 11. Optimum arrangement of the geogrid layers in the *VH* loading condition.

Figure 11 demonstrates the optimum configuration of the geogrid layers for the *VH* loading. This figure shows the order of placement of the layers to reach the maximum ultimate bearing capacity for a different number of geogrid layers.

4.3 Determination of the optimum reinforcement layout: *VM* loading condition

To investigate the effect of reinforced layers on the ultimate bearing capacity of the strip footing under the vertical eccentric loads (*VMs*), a vertical force is applied to the footing with different eccentricities (*e*). This eccentricity was presented as the *e/B* parameter and it was considered to be 0, 1/24, 1/12, 1/8, 1/6, 1/4 and 1/3 (*B* is the width of the foundation, equals 1 m in this study). So, for each *e/B*, the maximum amount of vertical force that caused the soil failure was obtained. According to the *V* and *VH* loading conditions, in Sections 4.1 and 4.2, the first layer of the geogrid was placed at a specific depth and then the ultimate bearing capacity of the foundation was calculated for different eccentricities. The combinations of *V* and *M* that caused the foundation to collapse were plotted in a dimensionless graph. This process was repeated for the next added layers of the geogrid. To find the optimum depth for each layer of geogrid, a different layout was considered, and the optimum layout was selected based on the maximum ultimate bearing capacity for the *VM* loading condition.

Figure 12 indicates the results of the numerical analyses for a different number of geogrid layers (*N*) in the *VM* loading condition. Each graph is related to the specific depth of layers (Z_i). The effect of using one layer to seven layers of reinforcement was investigated and compared with the unreinforced soil bearing capacity. Also, the lines with specific tangents are drawn in the figures. The tangent of these lines is related to a specific eccentricity

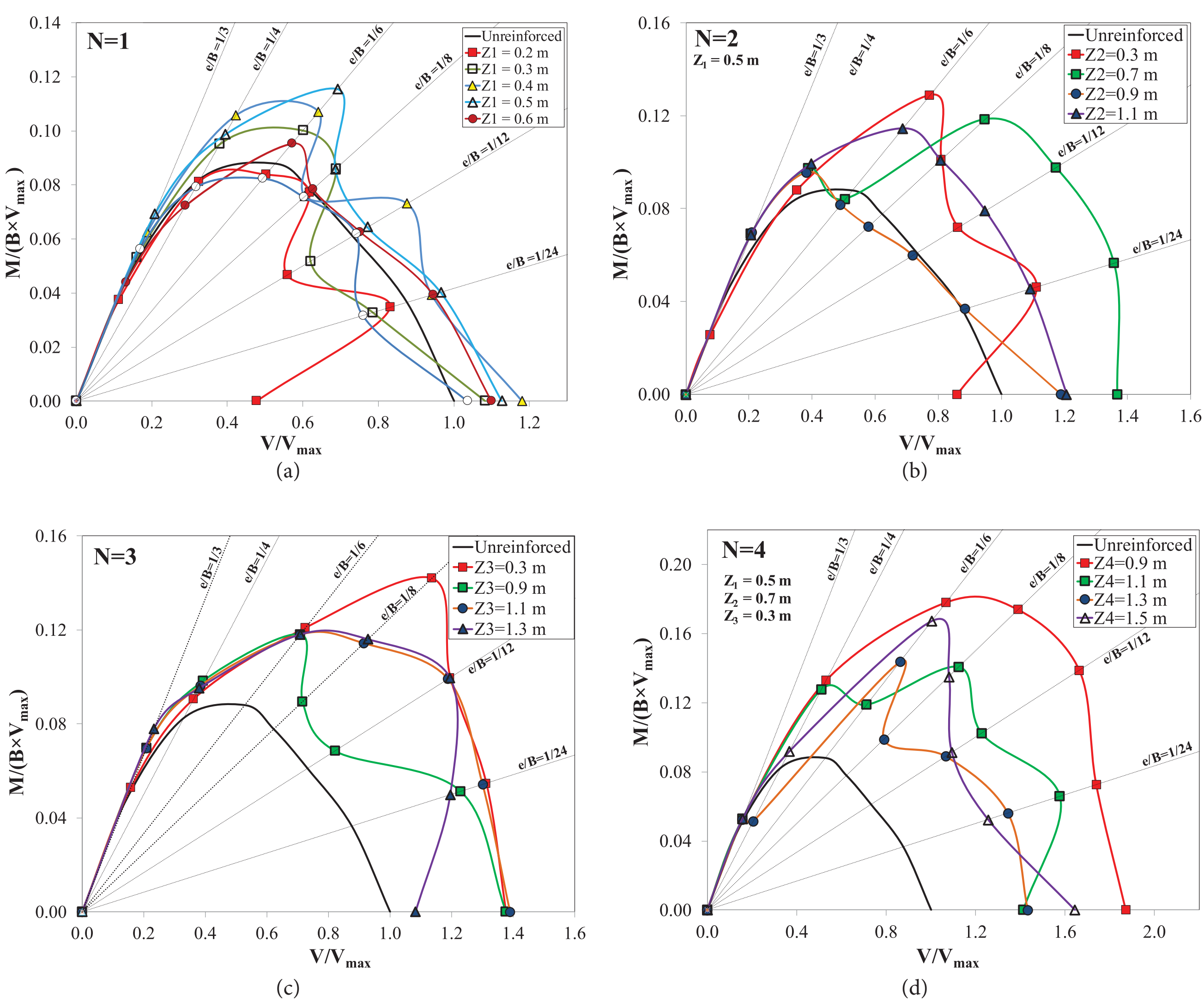

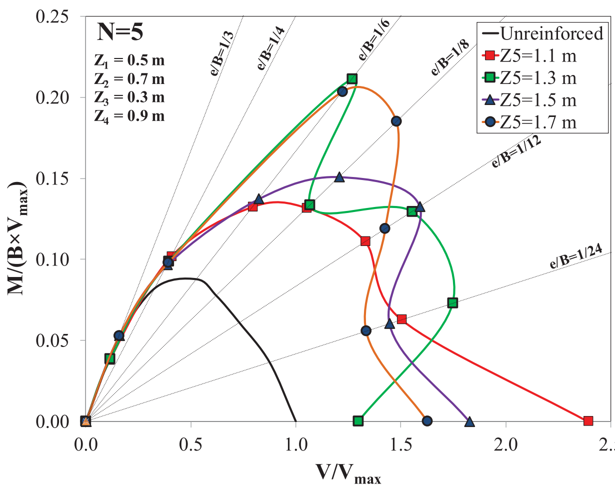

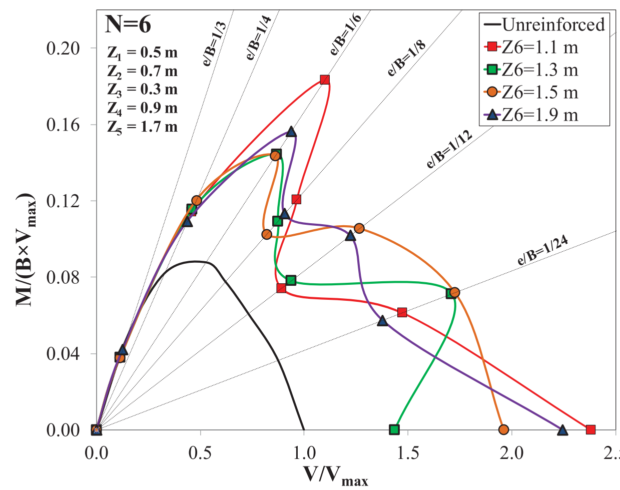

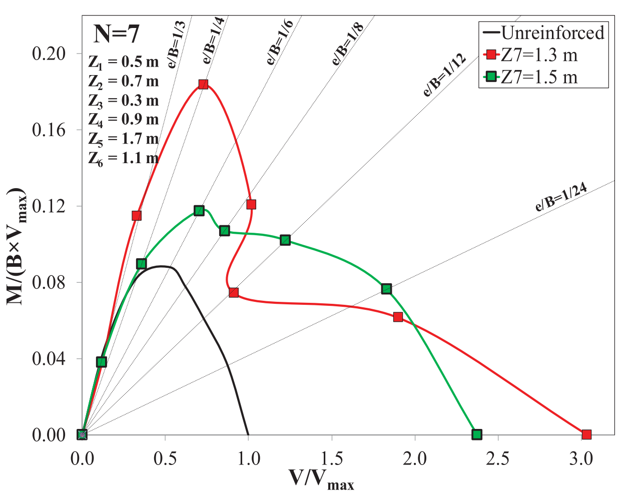

Figure 12. Dimensionless diagrams for the different numbers of geogrid layers in the *VM* loading condition: (a) *N*=1, (b) *N*=2, (c) *N*=3,(d) *N*=4 (e), *N*=5, (f) *N*=6, (g) *N*=7.

ratio, *e/B*. To obtain the optimum depth of each layer, the following approach was considered:

1. First, one layer of the geogrid was placed at different depths from the footing (Z_1) and the bearing capacity of the soil was obtained. The corresponding dimensionless curves were drawn for different positions of the geogrid layer. As seen from Figure 12a, Z_1 = 0.5 m can be chosen as the optimum depth for the first geogrid layer, because of the highest values obtained for the bearing capacity.
2. As the optimum location of the first layer was obtained, the second layer was placed at different depths from the footing and the bearing capacity of the soil was obtained. Corresponding dimensionless curves were drawn for different positions of the second layer. As seen from Figure 12b, Z_2 = 0.7 m can be selected as the optimum depth of the second geogrid layer. It should be noted that the position of the first layer is fixed, which was obtained from the first step (Z_1 = 0.5 m).
3. This procedure was continued to obtain the optimum depth for the next layers of the geogrids. It should be noted that the positions of the previous layers were considered to be at their optimum depths.

Using the above-mentioned procedure, dimensionless curves obtained in the optimum layout of the geogrid layers were collected and depicted in Figure 13. The dimensionless curves of the unreinforced soil, along with the diagrams corresponding to the one to seven layers of geogrid reinforced soil, are compared. It can be concluded from the figure that the geogrid reinforcement effect on the bearing capacity is prominent in

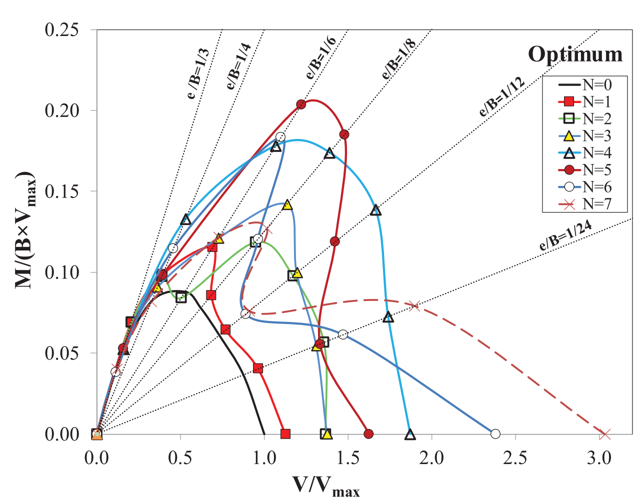

Figure 13. Dimensionless diagram for the optimum arrangement of the geogrid layers in the *VM* loading condition.

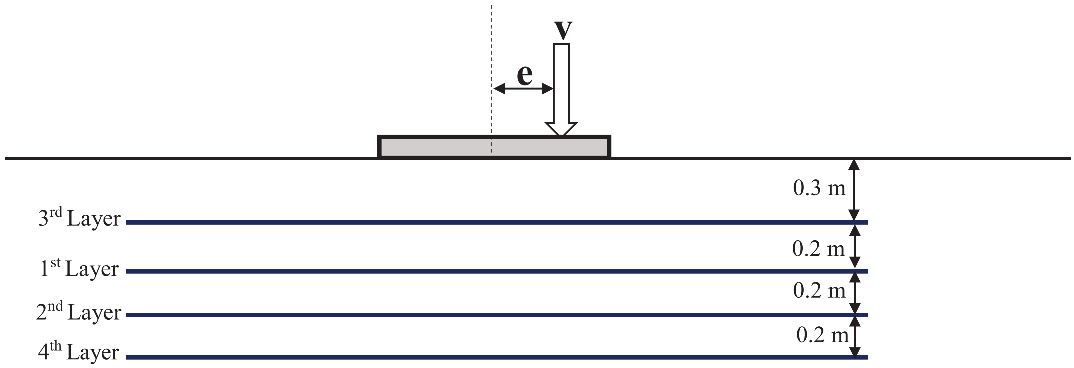

Figure 14. Optimum layout of the geogrid layers in *VM* loading condition.

the *VM* loading condition. The effect of the geogrid on the bearing capacity is increased by adding the geogrid layers up to five numbers, but for a larger number of the geogrid layers, the bearing capacity is declined. Based on the figure, the optimum number of the reinforced layers depends on the load eccentricity. $N = 4$ can be selected as the optimum number of geogrid layers in the *VM* loading condition. The increase of bearing capacity, in *VM* loading condition, for the best condition of reinforcement ($N = 4$), is equal to 100 %, compared to the bearing capacity of the unreinforced soil.

Figure 14 demonstrates the optimum configuration of the geogrid layers for the *VM* loading condition. The figure shows the order of the layers and the placement to reach the maximum bearing capacity. According to this figure, it can be observed that for $N = 4$ the depth of the first layer from the footing (u) is 0.3 m.

Saran et al. [14] obtained the best value for the ultimate bearing capacity using 4 layers of the geogrid in the *VM* condition. They also mentioned that the ultimate bearing capacity decreases with the increase in e/B.

5 CONCLUSIONS

In this study, a new approach was introduced to optimize the layout of the geogrid layers to achieve the maximum bearing capacity of the strip footing under different loading conditions (Vertical (V), Horizontal (H) and eccentric (M) loads). The interval of the geogrid layer can be changed by increasing the number of layers and the load combinations. The effects of parameters such as the different loading combinations, the number, and the layout of the geogrid layers on the ultimate bearing capacity of the strip footing were studied. The results of the analyses are plotted in the form of dimensionless graphs. Based on the results, the following conclusions can be drawn:

1. Adding the geogrid layers significantly increases the bearing capacity of the footing under the combined loads. The effect mainly depends on the layout of the geogrid layers and the load combinations.
2. The optimum depth of the first layer (u/B) is changed by increasing the number of layers beneath. In this study, for a single layer of reinforcement, $u/B = 0.5$; however, for five numbers of the reinforcement layers, it is equal to 0.3. This contradicts the previous results, in which the value of u/B is constant for any number of geogrid layers during their studies.
3. In the vertical loading condition (V), reinforcing the soil with seven layers of geogrid increases the ultimate bearing capacity up to three times relative to the unreinforced soil. Moreover, the new approach increases the BCR_u up to 15 % compared to the classic method and the Zidan [21] study.
4. In the *VH* loading condition, adding one layer of the geogrid increases the *VH* bearing capacity of the soil up to 25 % with respect to the unreinforced soil, although no significant enhancement can be seen in the horizontal bearing capacity for more layers. For the study performed here, four layers of geogrid resulted in the best improvement of the foundation bearing capacity in both the vertical and horizontal capacities. In this condition, there is no significant change between the classic and novel approaches.
5. In the *VM* loading condition, the geogrid reinforcement effect on the bearing capacity is more prominent with respect to the *VH* loading condition. The effect of the geogrid on the bearing capacity is increased by adding the geogrid layers up to four geogrid layers, but for the larger number of the geogrid layers, the bearing capacity is decreased. Based on the results, the optimum number of reinforced layers depends on the load eccentricity. The increase of the bearing capacity in *VM* loading condition for the best condition of reinforcement ($N = 4$) is about 100 % compared to the bearing capacity of the unreinforced soil.

Based on the results of this paper, adding the geogrid layers to the unreinforced soil greatly increases the ultimate bearing capacity under a vertical load with and without eccentricity (*V* and *VM* loading conditions), but it does not have a great influence on the bearing capacity of the footing under the *VH* loading condition. It should be noted that this study considered the ultimate bearing capacity of the soil without considering the allowable settlement criteria.

List of notations

E_s	=	Modulus of elasticity of soil
φ	=	Internal friction angle of soil
c	=	Cohesion of soil
ϑ	=	Poisson's ratio
γ	=	Unit weight
ψ	=	Dilatancy angle of soil
R_{int}	=	Interface coefficient
B	=	Footing width
t	=	Footing thickness
E_c	=	Modulus of elasticity of concrete material
EA	=	Axial stiffness of geogrid
L	=	Length of the geogrid layer
W	=	Width of the geogrid layer
m	=	Mass per unit area of geogrid
F_u	=	Ultimate tensile strength of geogrid
$F_{u,5\%}$	=	Tensile strength (at 5 % strain) of geogrid
e	=	Eccentricity of load from the footing center
M	=	Bending moment
V	=	Vertical load
H	=	Horizontal load
VH	=	Combination of vertical and horizontal loads
VM	=	Vertical load with eccentricity
V_{max}		Maximum bearing vertical load
H_{max}		Maximum bearing horizontal load
u		Distance of the first layer geogrid from the footing base
Z_i	=	Distance of i^{th} layer of geogrid from the footing base

REFERENCES

[1] Binquet, J. and Lee, K.L., (1975). Bearing capacity tests on reinforced earth slabs. Journal of Geotechnical and Geoenvironmental Engineering, 101(ASCE# 11792 Proceeding).

[2] Khing, K.H., Das, B.M., Puri, V.K., Cook, E.E. and Yen, S.C., (1993). The bearing-capacity of a strip foundation on geogrid-reinforced sand. Geotextiles and geomembranes, 12(4), pp.351-361.

[3] Omar, M.T., Das, B.M., Puri, V.K. and Yen, S.C., (1993). Ultimate bearing capacity of shallow foundations on sand with geogrid reinforcement. Canadian geotechnical journal, 30(3), pp.545-549.

[4] Das, B.M., Shin, E.C. and Omar, M.T., (1994). The bearing capacity of surface strip foundations on geogrid-reinforced sand and clay—A comparative study. Geotechnical and Geological Engineering, 12(1), pp.1-14.

[5] Adams, M.T. and Collin, J.G., (1997). Large model spread footing load tests on geosynthetic reinforced soil foundations. Journal of Geotechnical and Geoenvironmental Engineering, 123(1), pp.66-72.

[6] Shin, E.C., Das, B.M., Lee, E.S. and Atalar, C., (2002). Bearing capacity of strip foundation on geogrid-reinforced sand. Geotechnical and Geological Engineering, 20(2), pp.169-180.

[7] Patra, C.R., Das, B.M. and Atalar, C., (2005). Bearing capacity of embedded strip foundation on geogrid-reinforced sand. Geotextiles and Geomembranes, 23(5), pp.454-462.

[8] Ghazavi, M. and Lavasan, A.A., (2008). Interference effect of shallow foundations constructed on sand reinforced with geosynthetics. Geotextiles and Geomembranes, 26(5), pp.404-415.

[9] Chakraborty, M. and Kumar, J., (2014). Bearing capacity of circular foundations reinforced with geogrid sheets. Soils and Foundations, 54(4), pp.820-832.

[10] Chen, Q. and Abu-Farsakh, M., (2015). Ultimate bearing capacity analysis of strip footings on reinforced soil foundation. Soils and Foundations, 55(1), pp.74-85.

[11] Ziegler, M., (2017). Application of geogrid reinforced constructions: history, recent and future developments. Procedia Engineering, Modern Building Materials, Structures and Techniques, 172, pp.42-51.

[12] El-Soud, S.A. and Belal, A.M., (2018). Bearing capacity of rigid shallow footing on geogrid-reinforced fine sand—experimental modeling. Arabian Journal of Geosciences, 11(11), p.247.

[13] Patra, C.R., Das, B.M., Bhoi, M. and Shin, E.C., (2006). Eccentrically loaded strip foundation on geogrid-reinforced sand. Geotextiles and Geomembranes, 24(4), pp.254-259.

[14] Saran, S., Kumar, S., Garg, K. and Kumar, A., (2008). Model tests on eccentrically and obliquely loaded footings resting on reinforced sand. International Journal of Geotechnical Engineering, 2(3), pp.179-197.

[15] Sadoglu, E., Cure, E., Moroglu, B. and Uzuner, B.A., (2009). Ultimate loads for eccentrically loaded model shallow strip footings on geotextile-reinforced sand. Geotextiles and Geomembranes, 27(3), pp.176-182.
[16] El Sawwaf, M., (2009). Experimental and numerical study of eccentrically loaded strip footings resting on reinforced sand. Journal of geotechnical and geoenvironmental engineering, 135(10), pp.1509-1518.
[17] Badakhshan, E. and Noorzad, A., (2015). Load eccentricity effects on behavior of circular footings reinforced with geogrid sheets. Journal of Rock Mechanics and Geotechnical Engineering, 7(6), pp.691-699.
[18] Badakhshan, E. and Noorzad, A., (2017). A simplified method for prediction of ultimate bearing capacity of eccentrically loaded foundation on geogrid reinforced sand bed. International Journal of Geosynthetics and Ground Engineering, 3(2), pp.3-14.
[19] Gottardi, G. and Butterfield, R., (1993). On the bearing capacity of surface footings on sand under general planar loads. Soils and Foundations, 33(3), pp.68-79.
[20] Loukidis, D., Chakraborty, T. and Salgado, R., (2008). Bearing capacity of strip footings on purely frictional soil under eccentric and inclined loads. Canadian Geotechnical Journal, 45(6), pp.768-787.
[21] Zidan, A.F., (2012). Numerical study of behavior of circular footing on geogrid-reinforced sand under static and dynamic loading. Geotechnical and Geological Engineering, 30(2), pp.499-510.
[22] Tencate Geosynthetics, Miragrid@22XT, https://www.tencategeo.com.
[23] Shin, E.C., and Das, B.M., (2000). Experimental study of bearing capacity of a strip foundation on geogrid-reinforced sand. Geosynthetics International, 7(1), pp.59-71.
[24] Ghazavi, M., and Lavasan, A. A., (2008). Interference effect of shallow foundations constructed on sand reinforced with geosynthetics. Geotextiles and Geomembranes, 26(5), pp.404-415.
[25] Yetimoglu, T., Wu, J. T., and Saglamer, A. (1994). Bearing capacity of rectangular footings on geogrid-reinforced sand. Journal of Geotechnical Engineering, 120(12), pp.2083-2099.

SETTLEMENT OF SHALLOW STRIP FOOTING ON GRANULAR SOIL UNDER ECCENTRIC STATIC AND CYCLIC LOADS

POSEDEK PLITVEGA PASOVNEGA TEMELJA NA GROBO ZRNATIH ZEMLJINAH PRI EKSCENTRIČNIH STATIČNIH IN CIKLIČNIH OBTEŽBAH

Suvendu Kumar Sasmal
Department of Civil Engineering,
National Institute of Technology
Rourkela, India
E-mail: suvendukumarsasmal@gmail.com

Rabi Narayan Behera *(corresponding author)*
Department of Civil Engineering
National Institute of Technology
Rourkela, India
E-mail: rnbehera82@gmail.com

DOI https://doi.org/10.18690/actageotechslov.18.2.70-82.2022

Keywords

strip footing, settlement, beam on nonlinear Winkler foundation, load eccentricity, multivariate adaptive regression splines

Ključne besede

pasovni temelj, posedek, nosilec na nelinearnem Winklerjevem temelju, ekscentrična obtežba, multivariantni prilagodljivi regresijski zlepki

Abstract

The traditional way of analyzing the behavior of shallow foundations is based on applying the load to the center of the footing, but this is not always the case in practice. The settlement of a strip footing resting on dense sand under eccentrically applied static and cyclic loads is studied in this paper to find out the foundation's behavior in realistic conditions. During cyclic loading, the shear modulus of the soil is changed, due to which the stiffness of the soil and footing response are greatly affected. Under the influence of cyclic loading, in coarse-grained soil, the strain accumulates depending on the intensity of the cyclic loading. In low-intensity cyclic load conditions, the accumulated strain reaches a constant value after a finite number of load cycles. In this study, the analysis of settlement is carried out with the help of a numerical technique, based on Beam on Nonlinear Winkler Foundation (BNWF). The parameters, namely, static load, the intensity of the cyclic load ($q_{d(max)}$), the depth of embedment of footing (D_f) and the eccentricity ratio (e/B) are varied to observe the effect of the cyclic reversal of the load on the foundation's response. Using the simulation results of 144 model conditions, an empirical equation is proposed to estimate the total settlement of the footing using Multivariate Adaptive Regression Splines (MARS). The analysis of the numerical

Izvleček

Tradicionalni način analize obnašanja plitvih temeljev je za centrično obtežbo delujočo na osnovno ploskvo, ki pa ne zajema vse primere v geotehnični praksi. Da bi ugotovili obnašanje temeljev v realnih pogojih, v pričujočem prispevku preučujemo posedanje pasovnih temeljev na gostem pesku pod ekscentričnimi statičnimi in cikličnimi obtežbami. Med ciklično obtežbo se strižni modul zemljine spremeni, kar močno vpliva na togost zemljine in odziv temelja. Pod vplivom ciklične obtežbe se v grobozrnatih zemljinah specifična deformacija kopiči glede na intenzivnost ciklične obtežbe. V pogojih nizke intenzivnosti ciklične obtežbe nakopičena specifična deformacija doseže konstantno vrednost po omejenem številu ciklov obremenjevanja. V tej študiji je analiza posedkov izvedena s pomočjo numerične tehnike, ki temelji na nosilcu na nelinearnem Winklerjevem temelju (BNWF). V analizi se spreminjajo parametri, in sicer statična obtežba, intenzivnost ciklične obtežbe ($q_{d(max)}$), globina temeljenja (D_f) in razmerje ekscentričnosti (e/B) ter opazuje učinek cikličnega obrata obtežbe na odziv temelja. Z uporabo rezultatov simulacije 144 modelnih pogojev je predlagana empirična enačba za oceno totalnega posedka temelja z uporabo metode modeliranja z multivariantnimi prilagodljivimi regresijskimi zlepki (MARS). Analiza numeričnih rezultatov in *results and a parameter-sensitivity study suggest that the settlement under combined eccentric static and cyclic loads is mainly controlled by the existing static load.*

študija občutljivosti parametrov kažeta, da je posedanje pri kombiniranih ekscentričnih statičnih in cikličnih obtežbah v glavnem odvisno od dejanske statične obtežbe.

1 INTRODUCTION

Engineering constructions like railroad foundations and machine foundations are generally subjected to loads that change with time (repeated loads). The behavior of these foundations is controlled by the soil underneath. One of the key phenomena that takes place in a soil mass is a repeated change in the soil properties during cyclic stress reversal. This behavior of the underlying soil mass makes the analysis of the foundation response difficult. Yet, the study of these conditions is important as a proper understanding will be helpful in properly designing the structure to increase the lifetime. One of the key areas of studying the response of cyclically excited foundations is to observe the settlement due to an increasing number of load cycles. With an increase in the number of load cycles, the settlement of a plane-strain footing has been reported [1]. The authors observed the increase in settlement due to a large number of load cycles. Das et al. [2] observed the settlement of a square foundation under static and cyclic load. Apart from reporting the influence of static and cyclic loads, they reported a new outcome, i.e., the change in the settlement with a change in the number of load cycles is negligible after a particular instant of time. They referred to the settlement at this point as the ultimate permanent settlement. Das et al. [3] using the similar methodology, studied the response of a foundation on clay and observed that the settlement consists of two parts: primary (rapid) and secondary settlement. Sawicki et al. [4] studied the response of a cyclically loaded circular footing and concluded that the settlement is mainly controlled by cyclic stress levels and the number of load cycles. Tafreshi et al. [5] reported a plastic footing settlement under incremental cyclic loading. They found that the settlement is controlled by the soil properties as well as the footing size. Fatah et al. [6] studied the influence of the number of load cycles on the response of the foundation on sand and reported that a steady settlement occurs after 100–200 load cycles. A detailed analysis of the available literature describing the cyclic load-induced settlement of foundations reveals that in these studies the loadings were applied to the center of the footing. The existing trend of studying the response of the footing under an eccentric load is mostly applicable for a static load only. The settlement of the foundation under an eccentrically applied static load can be found in [7]-[12]. As reported in the literature, the ultimate load-carrying capacity of the foundation decreases due to an increase in the eccentricity of the applied load.

The study of the foundation under an eccentrically applied load is important because this is the practically prevailing condition in nature as the line of the load application does not always necessarily pass through the centerline of the footing. However, the analysis of these practical conditions is limited to static cases only. Most of the studies aimed at observing the settlement caused by a cyclic load considered applying the load to the center of the footing. In an extended approach, this study observes the footing settlement due to the eccentricity of both static and cyclic loads. A schematic diagram of the considered problem is given in Figure 1. A numerical analysis has been carried out varying the static load, intensity of the cyclic load ($q_{d(max)}$), the embedment ratio (D_f/B) and the eccentricity ratio

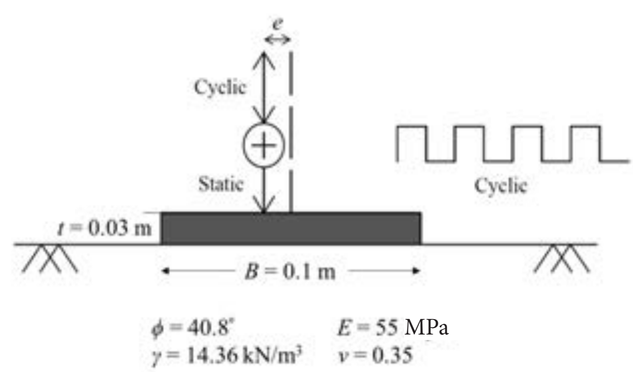

(a)

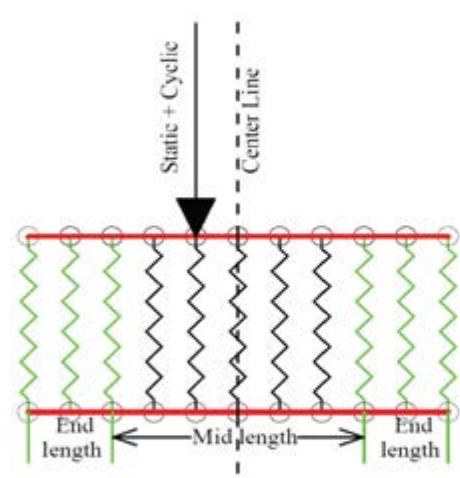

(b)

Figure 1. Footing and loading conditions: (a) schematic diagram, (b) BNWF model.

(e/B). From the parametric analysis, a data set is generated that is further analyzed using a statistical tool, Multivariate Adaptive Regression Splines (MARS). An empirical equation is developed to estimate the total settlement considering all the influencing parameters. Lastly, a sensitivity analysis is performed to determine the parameter significance. The total settlements are presented in non-dimensional form.

2 NUMERICAL APPROACH

The foundation is modelled using the Beam on Nonlinear Winkler Foundation (BNWF) model, which basically consists of three parts (footing, soil and interface). The Open System for Earthquake Engineering Simulation (OpenSEES) [13] is used to create the model. The numerical model is shown in Figure 1. The parameters of the underneath soil are given in Table 1. The soil properties used in Patra et al. [11] are considered in the present analysis, which are mentioned in Figure 1. The dynamic soil properties (E and ν) are selected based on EPRI [14]. The value of E corresponding to the value of ϕ is calculated using the procedure suggested by Harden et al. [15]. First, the value of the relative density is ascertained, which is equal to the value reported in Patra et al. [11]. Then value of E is calculated from Table 5.5 of EPRI [14]. The range of the relative density, which is used for the calculation of E, is taken from Das [16]. The value of ν is selected from Table 5.1 of EPRI [14].

Table 1. Properties of soil.

Soil parameter	Value
Relative density (D_r, %)	69
Angle of internal friction (ϕ, degrees)	40.8
Unit weight of soil (γ, kN/m^3)	14.36
Modulus of elasticity (E, MPa)	55
Poisson's ratio (ν)	0.35

A rigid footing (0.5 m × 0.1 m × 0.03 m) is created in two stages: (a) first, one hundred and one nodes are defined, and (b) the nodes are joined using elastic beam-column elements, which are one dimensional. The one-dimensional elastic beam columns are defined using the area of the cross-section, the moment of inertia and the Young's modulus. The Young's modulus of the footing is taken as 25000 MPa. The nodes have three degrees of freedom (2 translations and 1 rotation). For the BNWF model, it is suggested to consider a minimum of 25 springs [17]. One hundred and one nodes are taken in this study for avoiding the modelling complications of eccentrically loaded foundations. Each footing node is connected to a soil node (DOF = 0). Nonlinear mechanistic springs are used to connect the footing and soil nodes. Each spring consists of an elastic component (to capture far-field behavior) and plastic component (to capture near-field behavior.) A parallel combination of the drag and closure component constitute the gap component of the springs. The closure component is very flexible in tension, which indicates a key property of the soil (weak in tension). A damper is connected parallel to the elastic component. The capacity of the spring is calculated as per Meyerhof [18]. Also, for the eccentric loading condition, the model assumes a contact pressure distribution beneath the footing as per Meyerhof [18], i.e., the contact pressure varies linearly from highest at the toe to the lowest at heel. The vertical and lateral stiffnesses of the springs are calculated using Eq. (1) to Eq. (3), which were given by Gazetas [19].

$$K_V = \frac{GL}{1-\nu}\left[0.73 + 1.54\left(\frac{B}{L}\right)^{0.75}\right] \quad (1)$$

$$K_H = \frac{GL}{2-\nu}\left[2 + 2.5\left(\frac{B}{L}\right)^{0.85}\right] \quad (2)$$

$$K_{H'} = \frac{GL}{2-\nu}\left[2 + 2.5\left(\frac{B}{L}\right)^{0.85}\right] - \frac{GL}{0.75-\nu}\left[0.1\left(1-\frac{B}{L}\right)\right] \quad (3)$$

where K_V is the surface stiffness (vertical translation), K_H is the surface stiffness (horizontal translation towards long side), $K_{H'}$ is the surface stiffness (horizontal translation towards short side), G is the shear modulus of the soil, B is the width of the footing, L is the length of the footing.

For the embedded footing, the embedment factor, used in Gazetas [19] is multiplied by the corresponding surface stiffness. The embedded factors are calculated using Eq. (4)-(6).

$$e_{V'} = \left[1 + 0.095\frac{D_f}{B}\left(1 + 1.3\frac{B}{L}\right)\right]\left[1 + 0.2\left(\frac{2L+2B}{LB}H\right)^{0.67}\right] \quad (4)$$

$$e_H = \left[1 + 0.15\left(\frac{2D_f}{B}\right)^{0.5}\right]\left[1 + 0.52\left(\frac{\left(D_f - \frac{H}{2}\right)16(L+B)H}{BL^2}\right)^{0.4}\right] \quad (5)$$

$$e_{H'} = \left[1 + 0.15\left(\frac{2D_f}{L}\right)^{0.5}\right]\left[1 + 0.52\left(\frac{\left(D_f - \frac{H}{2}\right)16(L+B)H}{LB^2}\right)^{0.4}\right] \quad (6)$$

where e_V is the stiffness embedment factor (vertical translation), e_H is the stiffness embedment factor (horizontal translation towards long side), $e_{H'}$ is the stiffness embedment factor (horizontal translation towards short side), and G is the shear modulus of the soil.

The radiation damping value is taken as 5 %. The distribution of the springs is made according to Harden et al. [15]. According to Harden et al. [15] rounding is observed below the edge of the footing as a result of more compression of the soil at edge rather than at the center. For the cyclic analysis, the distribution of stiffness along the footing dimension is made with the help of two parameters, i.e., the stiffness intensity ratio (R_k) and the end length ratio (R_e), which are given by Eq. (7) and Eq. (8) respectively.

$$R_k = \frac{\textit{end region stiffness}}{\textit{mid region stiffness}} \quad (7)$$

$$R_e = \frac{\textit{end length}}{\textit{total length}} \quad (8)$$

Three different types of springs are considered to capture the soil-structure interaction response. QzSimple2, PySimple2 and TzSimple2 materials have been used to capture the vertical, passive resistance and sliding response, respectively. The QzSimple2 material is used to observe the vertical response of the foundation. The PySimple2 and TzSimple2 materials are horizontal springs, used to capture the passive resistance and sliding capacity, respectively. The passive resistance capacity is calculated as:

$$P_{ult} = \frac{1}{2} \times K_p \times \gamma \times D_f^{\,2} \quad (9)$$

where K_p is the coefficient of passive earth pressure.

In the case of the TzSimple2 material the frictional resistance is calculated as:

$$t_{ult} = W_g \tan\delta \quad (10)$$

where W_g is the vertical force, δ is the soil-concrete interfacial friction angle (0.66 ϕ).

These materials are available in the OpenSEES platform and have been suggested to capture the nonlinear cyclic response of the foundation by Raychowdhury [20]. The expressions of backbone curves for nonlinear plastic response of the springs are similar in nature and can be expressed as:

$$q = q_{ult} - (q_{ult} - q_0)\left[\frac{cz_{50}}{cz_{50} + \left|z^p - z_0^p\right|}\right]^n \quad (11)$$

where q is the load on the plastic component, q_{ult} = the ultimate load, q_0 = the yield load, z_{50} is the displacement corresponding to 50 % of q_{ult}, z_0^p is the displacement corresponding to q_0, and z_p is the displacement corresponding to any point in the nonlinear zone. The parameters c and n are constants. The equation and constants, which are the governing principle of OpenSEES [13] material model, are reported in Raychowdhury [20] by calibrating shallow foundation testing results.

2.1 Load Application

The load is applied in two steps. First, a static load is applied, which is estimated by dividing the Ultimate Bearing Capacity (q_u) of the foundation by a factor of safety (*FS*). The *FS* values are taken as 2, 2.5, 3 and 3.5. For a specific value of *FS*, the allowable static load is kept constant, which also corresponds to the design load on the foundation, which is constant during the cyclic loading. Due to the allowable static load, the footing undergoes an elastic (linear) settlement. Hence, during the application of the cyclic load the nonlinear behavior of the foundation can be observed. The static load is followed by the cyclic load (Figure 1). The eccentricity e is taken as 0, 0.05B, 0.1B and 0.15B in the present study.

The properties of the cyclic load are chosen after a thorough literature review (Raymond and Komos [1]; Das et al. [2]; Sawicki et al. [4]). The cyclic load is applied for a period of 1 million seconds, where each cycle lasts for one second. In other words, 10^6 load cycles are applied to the footing. The time period and the cycles (10^6 cycles with each cycle of 1 second) are chosen following Das et al. [2]. The cyclic load has an intensity ($q_{d(max)}$) that is taken as 5 %, 10 % and 13 % of the q_u for the corresponding condition. The values of q_u for different e/B and D_f/B conditions are listed in Table 2. In OpenSEES, the cyclic loads are defined by providing the details, i.e.,

Table 2. Ultimate bearing capacities obtained from numerical analyses.

D_f/B	Ultimate bearing capacity (q_u, kN/m^2)			
	e/B = 0	e/B = 0.05	e/B = 0.10	e/B = 0.15
0	85.8	74.6	64.3	53.2
0.5	157.9	138.9	121.5	102.6
1	242.9	219.3	194.3	169.5

the intensity, time period and number of load cycles to the numerical algorithm.

2.2 Model Verification

The outcomes (load-displacement curves) obtained from the model when the load passes through the center of footing are verified, which are already presented in Sasmal and Behera [21]. The comparison is shown in Figure 2. From Figure 2, it is observed that the present result is in good agreement with the results obtained by Mohr-Coulomb model, for the same soil and footing parameters. In this paper, the model is verified for the eccentric loading conditions. The static response, i.e., the load-settlement response of the footing is shown in Figure 3. The reduction in q_u and the settlement of the footing can be clearly observed, for which the reason is already established. The model results (Ultimate Bearing Capacity, q_u) are compared with [18] and presented in Figure 4(a). The q_u values for e/B = 0 case ($q_{u(e/B=0)}$) are compared with Patra et al. [11] and presented in Table 3. It should be noted that the experimental procedure of Patra et al. [11] was based on the raining of sand in consecutive layers prior to load testing, where as in the present study the capacities of the springs are calculated using the expressions of Meyerhof [18]. The reduction factors (*RFs*) obtained in the present study are compared with Patra et al. [11] in Figure 4(b). The values of *RF* are listed in Table 3. The reduction factor is calculated using Eq. (12) as per Patra et al. [11]. In the $D_f = 0$ case, the difference is attributed to the fact that the soil is taken as free field in the present numerical analysis and the absence of passive resistance (in the surface condition). But with an increase in D_f, the passive resistance is experienced by the footing and the

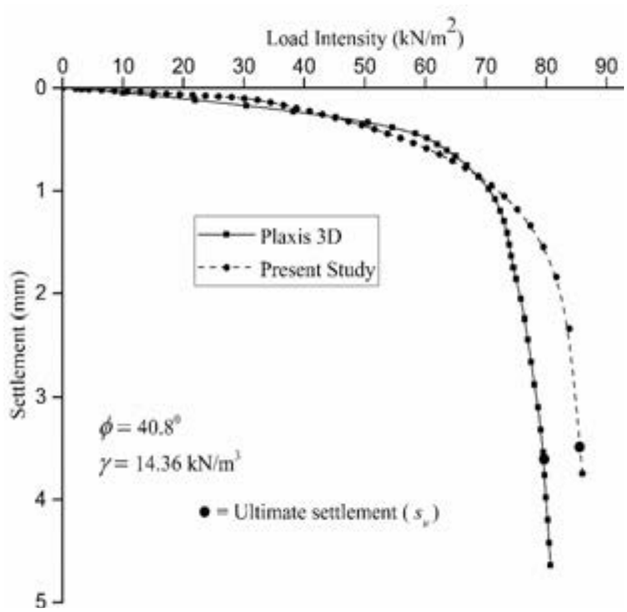

Figure 2. Comparison of static-load settlement response between present study and Mohr-Coulomb model (Sasmal and Behera, 2018).

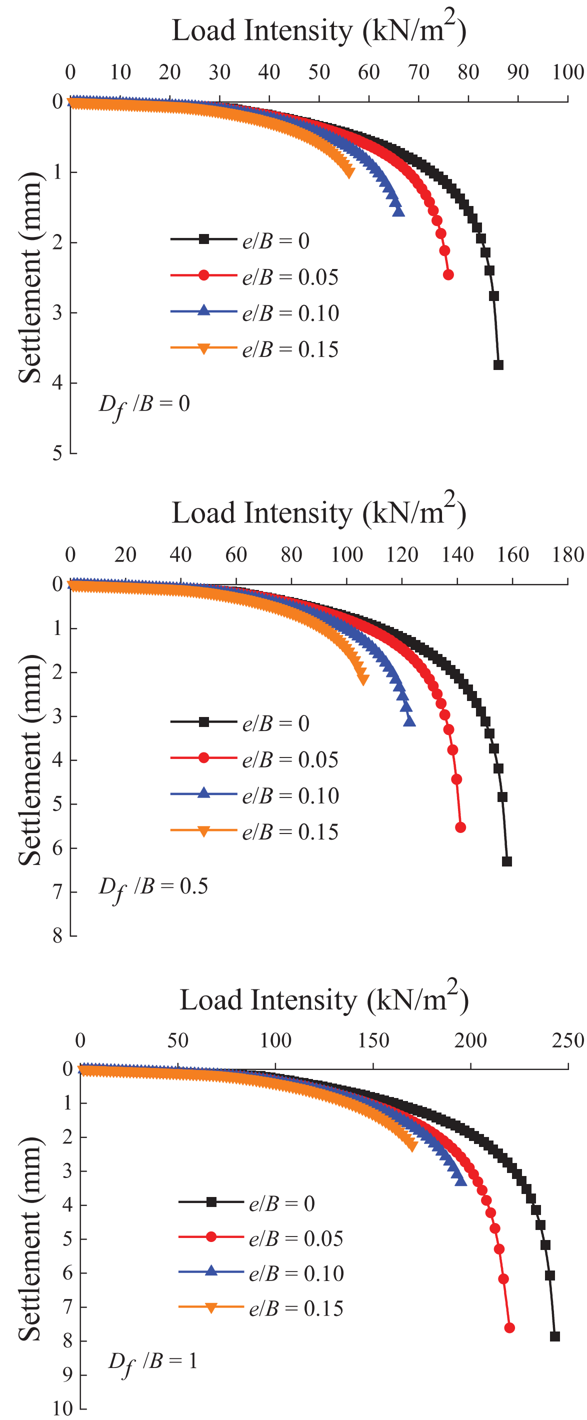

Figure 3. Static response of the foundation.

Table 3. Comparison of $q_{u(e/B=0)}$ and RF.

D_f/B	$q_{u(e/B=0)}$ (kN/m^2)		RF					
			e/B = 0.05		e/B = 0.1		e/B = 0.15	
	Present study	Petra et al. (2012)	Present study	Petra et al. (2012)	Present study	Petra et al. (2012)	Present study	Petra et al. (2012)
0	85.8	166.77	0.87	0.8	0.75	0.659	0.62	0.518
0.5	157.9	264.87	0.88	0.856	0.77	0.737	0.65	0.622
1	242.9	353.16	0.903	0.889	0.80	0.789	0.698	0.694

stiffness is modified due to the embedment factor, due to which a similar soil-footing condition is simulated as that of Patra et al. [11]. Also, there may be some amount of scale effect associated with model test results of Patra et al. [11]. From Figure 4, reasonably good agreement between the results from the present model and existing experimental results can be observed in the static case.

$$Reduction\ \ Factor\ (RF) = \frac{q_{u(D_f\ /\ B, e\ /\ B)}}{q_{u(D_f\ /\ B, e\ /\ B=0)}} \qquad (12)$$

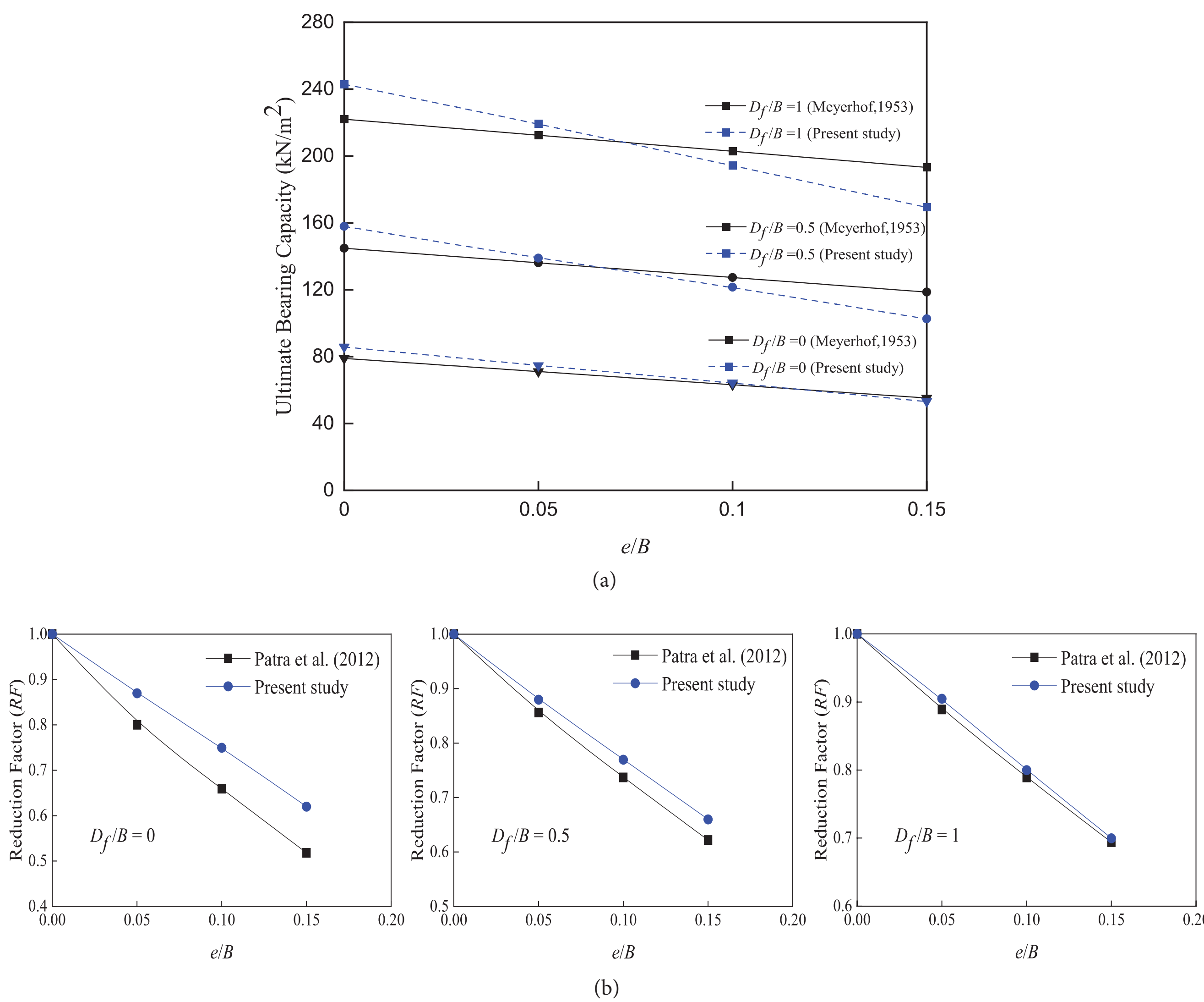

Figure 4. Comparison of model results in static case (a) Comparison with Meyerhof (1953), (b) Comparison with Patra et al. (2012).

3 RESULTS AND DISCUSSION

The total settlements (static+cyclic) at the center of the footing, due to the influence of different parameters, are presented in Figure 5. In Figure 5, the settlement is

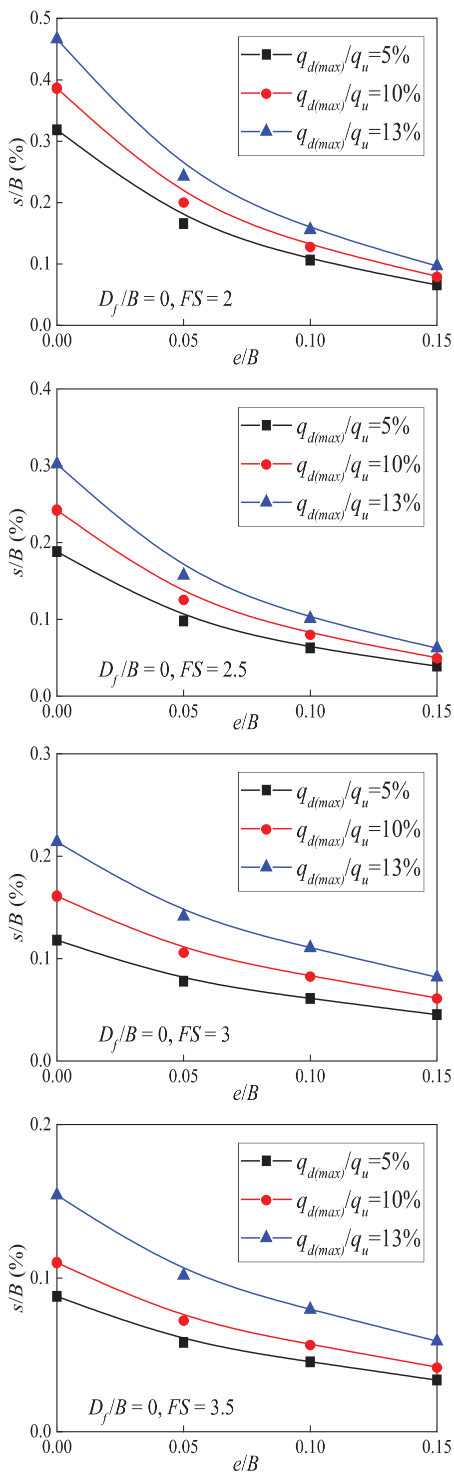

Figure 5a. Effect of load eccentricity on the settlement of surface footing.

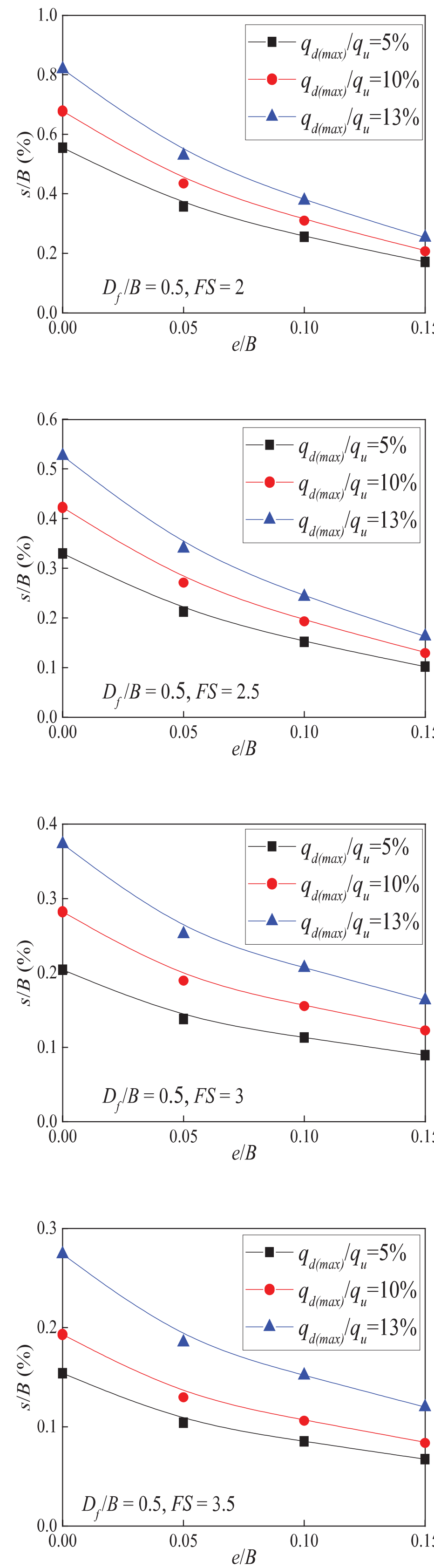

Figure 5b. Effect of load eccentricity on the settlement of embedded footing (D_f/B = 0.5).

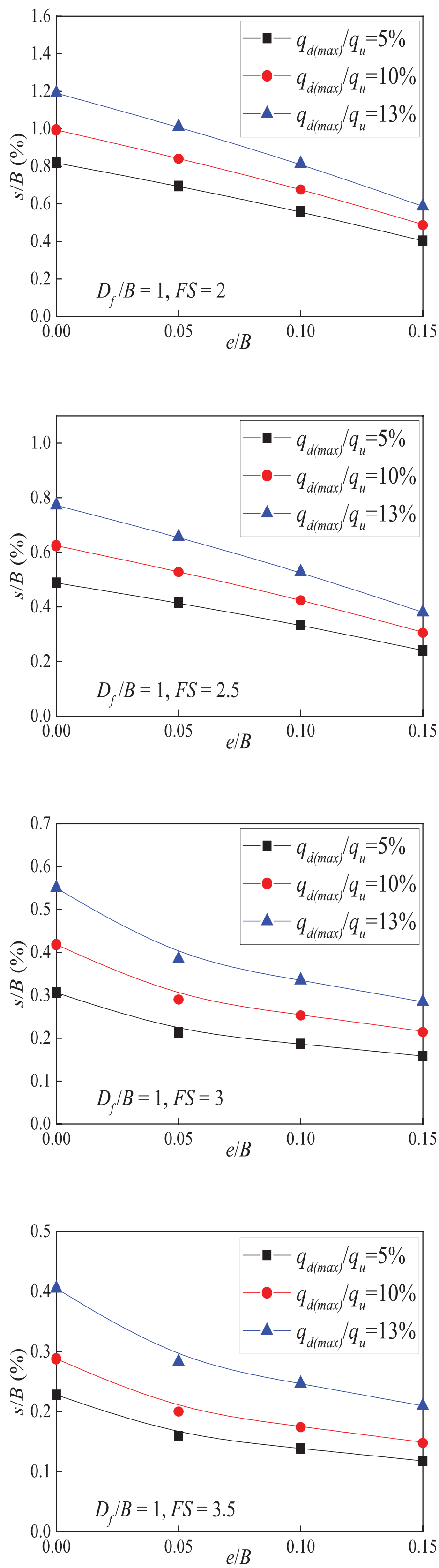

Figure 5c. Effect of load eccentricity on the settlement of embedded footing (D_f/B = 1).

normalized by dividing the width of the footing in each case. The effect of each parameter is described below.

It can be observed from Figure 5 that, keeping all other parameters constant, an increase in the *FS* results in a decrease of the settlement of the footing. This phenomenon is because the factor of safety is inversely related to the allowable static load. As the settlement is the combined response (static+cyclic), a reduction in static load will result in a reduction in the settlement. It is obvious that an increase in $q_{d(max)}$ will result in an increase in the total settlement. However, it is hard to understand the influential weight of the static or cyclic load, for which the statistical analysis presented in this paper will be helpful.

With an increase in the embedment ratio (D_f/B) of the footing, the bearing capacity of the foundation will increase. With this, the allowable static load will increase. The parameter $q_{d(max)}$ will also increase with an increase in q_u. As both the static and cyclic loads attain higher values, the total settlement of the footing increases. It should be noted that the amount of settlement will increase with an increase in D_f/B, but the settlement (s) normalized with corresponding ultimate settlement (s_u) will not show a similar trend, which is attributed to the contribution of the passive resistance due to the embedment. Due to load eccentricity, q_u of the foundation will reduce as a response to a reduction in the bearing area accompanied by rotation of the footing. q_u directly influences the static and cyclic loads. Hence, the settlement will decrease with an increase in the eccentricity. It is important to note that the reduction is more for a higher intensity of cyclic load, irrespective of the amount of allowable static load and the depth of the embedment of the footing.

With a mere observation of the reduction of settlement with *e/B*, the importance of the considered parameters cannot be ascertained. Hence, there is a need for a statistical analysis. An empirical expression is developed, which is the first of its kind to estimate the footing settlement under eccentrically applied static and cyclic loads. A sensitivity analysis is performed on this developed equation for observing the parameter's significance. The detailed procedures are described below.

3.1 Multivariate Adaptive Regression Splines (MARS)

The method developed by [22] is one of the most effective statistical tools to establish a connection between the dependent variable and the independent predictor. MARS has been used in the field of civil engineering in different studies. Samui and Kim [23], using the technique, developed a model equation to calculate the pile load capacity. Muduli et al. [24] predicted the lateral load-carrying capacity of the pile foundation in clay using the MARS technique. Khuntia et al. [25] developed a MARS equation for predicting the compaction parameters for cohesionless soil. Mohanty et al. [26] developed a MARS model to estimate the pullout capacity of ground anchors. A MARS model for the stability of underground excavation was reported by Goh et al. [27]. Lokuge et al. [28] extended the concept of MARS in determining the design strength of geopolymer concrete. Kaveh et al. [29] predicted the properties of self-compacting concrete using MARS. Zheng et al. [30] proposed a MARS model to estimate the uplift behavior of underground structures. Zhang et al. [31] analyzed braced excavation in clay and proposed a semi-empirical expression for wall deflection. Ghanizadeh and Rahrovan [32] created a MARS model for the prediction of the unconfined compressive strength of soil blended with reclaimed asphalt pavement. Liu et al. [33] considered the technique for a reliability analysis of slopes. When the MARS model is concerned, the parameters are generally normalized in the range [0, 1]. The same has been followed in the present analysis. A normalization is made using Eq. (13).

$$X_{normalized} = \frac{X_i - X_{\min imum}}{X_{\max imum} - X_{\min imum}} \qquad (13)$$

The MARS technique is based on dividing the domain into different subsets and then developing the regression expression for each subset. In general, the MARS model can be expressed as:

$$y_{predicted} = \alpha_0 + \sum_{m=1}^{M} \alpha_m B_m(x) \qquad (14)$$

where $B_m(x)$ is the basis function with the coefficient α_m, α_m = coefficient of m^{th} basis function, x = input variable and α_0 = a constant. M = number of basis functions.

MARS uses truncated spline functions (Samui and Kurup, [34]). These functions take the following forms:

$$b_q^-(x^* - t^*) = \left[-(x^* - t^*)\right]_+^q = \begin{cases} (t^* - x^*)^q, if\ x^* < t^* \\ 0, Otherwise \end{cases} \qquad (15)$$

$$b_q^+(x^* - t^*) = \left[+(x^* - t^*)\right]_+^q = \begin{cases} (x^* - t^*)^q, if\ x^* > t^* \\ 0, Otherwise \end{cases} \qquad (16)$$

Where, $b_q^-(x^*\text{-}t^*)$ and $b_q^+(x^*\text{-}t^*)$ are spline functions, t^* is a knot location (ending of one region and beginning of another), and q is the power.

The technique is based on two stages: (a) a forward pass and (b) a pruning pass. The process starts with an intercept, subsequently adding the basis functions. The backward/pruning pass is aimed at developing a well-generalized model by avoiding overfitting. The overfitting is prevented using a Generalized Cross-Validation (*GCV*).

GCV can be calculated using the expression presented in [30], which is given by:

$$GCV(M) = \frac{1}{n}\sum_{i=1}^{n}(y_i - y_p)^2 / \left[1 - \frac{C(M)}{n}\right]^2 \qquad (17)$$

$$C(M) = M + dM \qquad (18)$$

where n is the number of observations, y_i is the i^{th} output, y_p is the predicted value, d is the penalty factor.

In the present analysis, the MARS model is developed for the non-dimensional settlement (s/s_u %) using the "earth" package ([35],[36]), available in R-studio. One hundred and eight data sets are considered for training; the remaining being the testing data set.

The details of the model selection are given in Figure 6(a). In this figure, *Rsq* is the R^2. *GRSq* defined as:

$$GRSq = 1 - \frac{GCV}{GCV*} \qquad (19)$$

where *GCV** is the *GCV* of intercept-only model.

In Figure 6(a) the selected model is represented by a vertical dotted line, which means the model gives 14 terms using all four variables. The residuals for each case are given in Figure 6(b). It can be observed that most of the residuals lie close to zero, indicating a good model. Figure 6(c) shows the cumulative distribution of the residual (absolute values), ranging from 0 to 1. The residual distribution is compared with the normal distribution in a Quantile-Quantile plot (QQ plot), as shown in Figure 6(d). In the case, where the residuals are distributed normally, the values will form a line. The occurrence of most of the points close to the dotted straight line indicates a good model. Hence, Figure 6 justifies the suitability of the present model.

The values of the intercept and the basis functions obtained from the MARS model of second degree are presented in Table 4. In Table 4, the variables $V1$, $V2$, $V3$, and $V4$ represent FS, D_f/B, $q_{d(max)}/q_u$ (%) and e/B, respectively. The final expression to estimate (s/s_u %) is given by:

$$\begin{aligned} s/s_u\,(\%) = I &+ a \times BF1 + b \times BF2 + c \times BF3 + d \times BF4 + \\ & e \times BF5 + f \times BF6 + g \times BF7 + h \times BF8 + \\ & i \times BF9 + j \times BF10 + k \times BF11 + l \times BF12 + \\ & m \times BF13 \end{aligned} \qquad (20)$$

Table 4. Intercept, Basis Functions (*BF*) and coefficients of the MARS model.

Intercept and *BFs*	Coefficient
(Intercept)	$I = 0.829$
$BF1 = \max(0, V1\text{-}0.333)$	$a = 7.004$
$BF2 = \max(0, 0.667\text{-}V1)$	$b = 10.172$
$BF3 = \max(0, V1\text{-}0.667)$	$c = -9.275$
$BF4 = \max(0, 0.5\text{-}V2)$	$d = 1.607$
$BF5 = \max(0, V2\text{-}0.5)$	$e = 7.171$
$BF6 = \max(0, 0.625\text{-}V3)$	$f = -2.048$
$BF7 = \max(0, V3\text{-}0.625)$	$g = 6.782$
$BF8 = \max(0, 0.333\text{-}V4)$	$h = 5.615$
$BF9 = V1 \times \max(0, V2\text{-}0.5)$	$i = -10.285$
$BF10 = V1 \times \max(0, V3\text{-}0.625)$	$j = -4.618$
$BF11 = V2 \times \max(0, V4\text{-}0.333)$	$k = 5.547$
$BF12 = \max(0, V2\text{-}0.5) \times V4$	$l = 7.670$
$BF13 = V3 \times \max(0, V4\text{-}0.333)$	$m = 1.811$

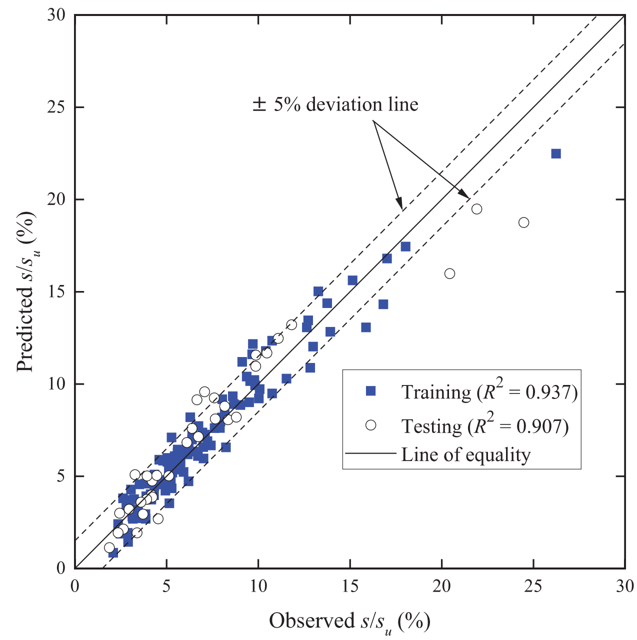

Figure 7. Performance of the MARS model.

Eq. (20) is developed by considering the training data set, which is tested on the testing data set. The outputs from the developed empirical expression are, along with the observed output, compared and shown in Figure 7.

$$R^2 = \frac{E_1 - E_2}{E_1} \qquad (21)$$

$$E_1 = \sum_{i=1}^{n} \left(O_i - O^*\right)^2 \qquad (22)$$

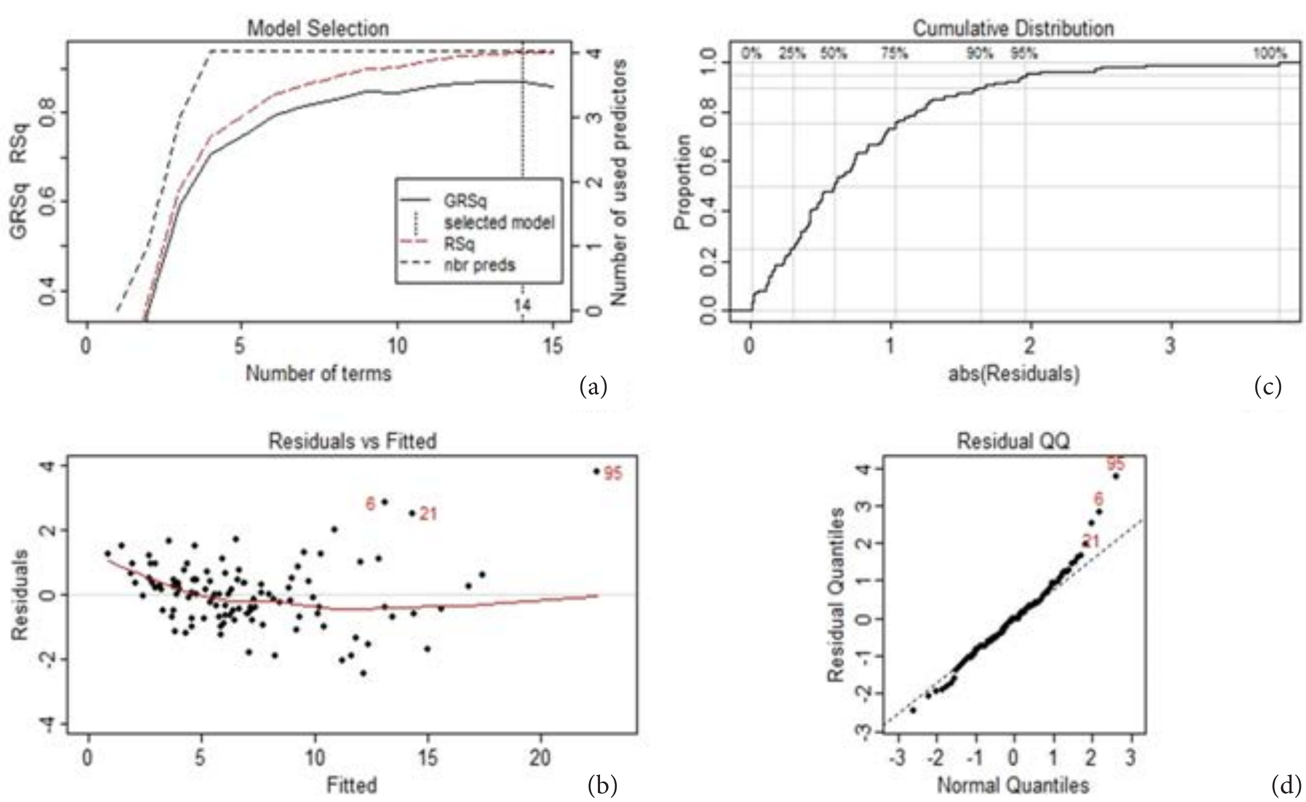

Figure 6. Details of the MARS model,
(a) Model selection details (b) Residual distribution (c) Cumulative residual distribution and (d) Quantile-Quantile plot

$$E_2 = \sum_{i=1}^{n} \left(O_P - O_i \right)^2 \qquad (23)$$

where O_i, O^* and O_p are the observed, average observed and predicted (s/s_u) %, respectively.

The R^2 values for training and testing are 0.937 and 0.907, respectively. From Figure 7, it can be interpreted

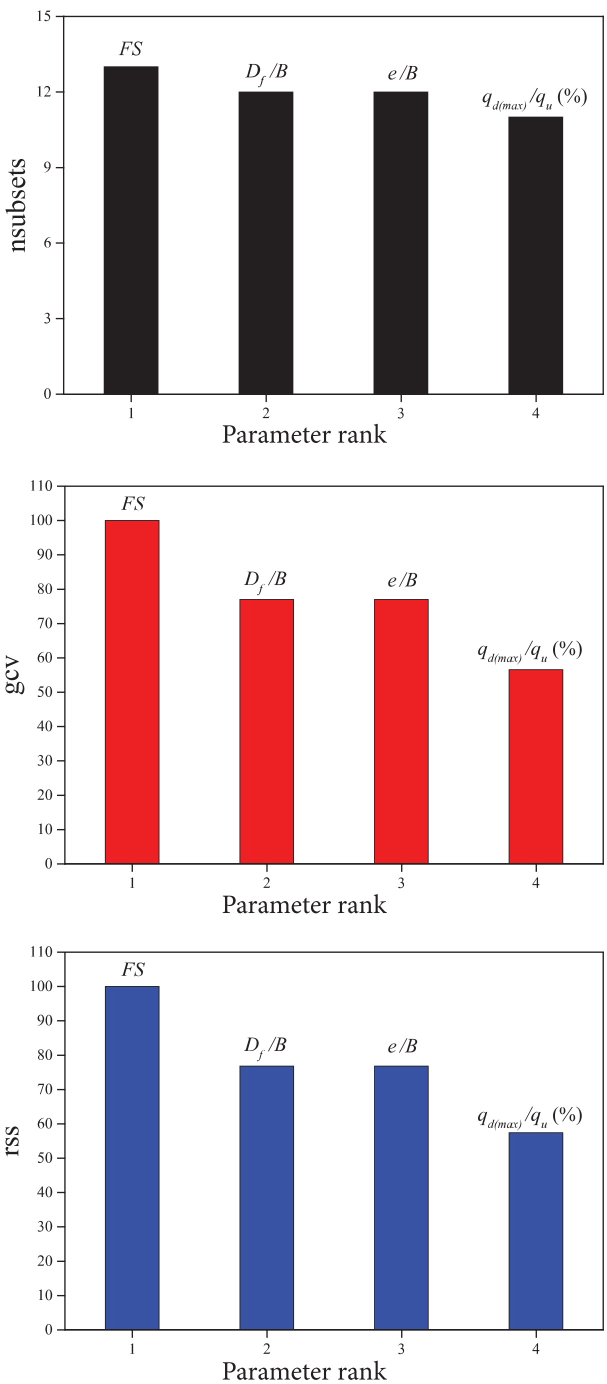

Figure 8. Importance of the input parameters.

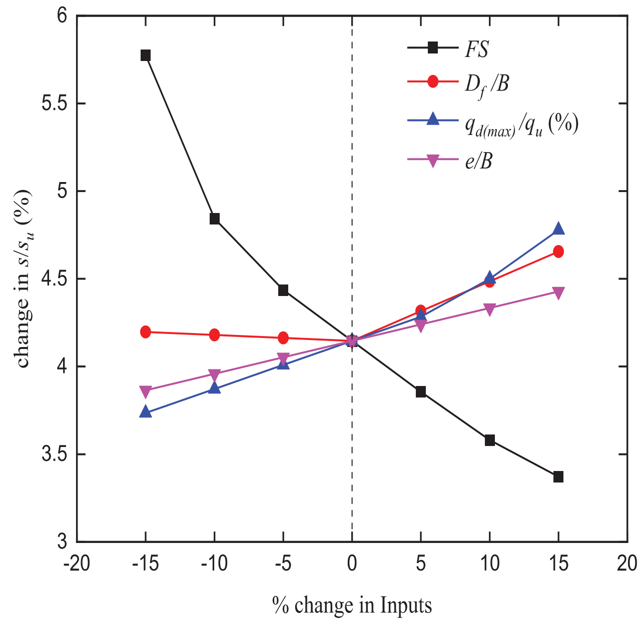

Figure 9. Effect of gradual change in parameters on settlement responses.

that the present MARS model has both reasonable prediction and generalization capability.

3.2 Sensitivity Analysis

The sensitivity of the MARS model can be directly obtained using the "evimp" function available in the "earth" package in R-studio. The sensitivity is determined in terms of *GCV*, residual sum square (*rss*) and the number of subsets (*nsubsets*). The *GCV*, *rss* and *nsubsets* for each parameter are compared and presented in Figure 8. It is then inferred that *FS* is the most important predictor, followed by D_f/B, e/B and $q_{d(max)}/q_u$ (%). Another approach has also been taken to observe the effect of the variation in the predictor variables on the settlement response. The parameters are varied in the range ± 15 % and the change in the output is observed, which is shown in Figure 9. From Figure 9, it is found that the settlement under eccentric static and cyclic loads is controlled by *FS* and *e/B*. So, it can be inferred that the static load and load eccentricity have substantial control over the settlement response of the footing, when a large number of low-intensity cyclic loads are applied. It is also observed that apart from the embedment ratio, all other parameters have a linear effect on the settlement's response. The non-dimensional settlement of the footing is directly proportional to the static load, the intensity of cyclic load and the load eccentricity.

4 CONCLUSIONS

A numerical analysis has been carried out to observe the settlement of an eccentrically static-cyclic loaded strip footing. After the verification of the model, the model outputs are further processed using the Multivariate Adaptive Regression Splines (MARS) technique. A first of its kind empirical expression is developed, based on which a sensitivity analysis has been performed. Based on the numerical and statistical analysis, the derived conclusions are presented below.

a) The effect of load eccentricity is to significantly reduce the amount of static-cyclic settlement (s) of the footing.
b) For a given soil and footing embedment condition, the effect of load eccentricity is more prominent for a higher intensity of cyclic load.
c) The empirical equation in the form of Eq. (20) is proposed to estimate the non-dimensional settlement of the foundation with reasonable accuracy and very good generalization with the R^2 for training and testing being 0.937 and 0.907 respectively.
d) The total settlement under the combined effect of the eccentric static-cyclic load is controlled by two important parameters, the static load on the foundation and the load eccentricity.
e) The non-dimensional settlement (s/s_u %) is directly proportional to the intensity of the cyclic load and eccentricity ratio. It is inversely proportional to the factor of safety. The embedment ratio influences the settlement nonlinearly.

This study is an approach to consider a more practical situation considering load eccentricity. The use of the same concept for different subsoil conditions and seismic loading are future research topics.

REFERENCES

[1] Raymond, G.P., Komos, F.E. 1978. Repeated load testing of a model plane strain footing. Canadian Geotechnical Journal 15(2), 190-201.
[2] Das, B.M., Yen, S.C., Singh, G. 1995. Settlement of shallow foundation on sand due to cyclic loading. Proc. of the International Conference on Recent Advances in Geotechnical Earthquake Engineering and Soil Dynamics 8, 385-388.
[3] Das, B.M., Shin, E.C. 1998. Cyclic Load-Induced Settlement of Foundations on Clay. Proc. of Fourth International Conference on Case Histories in Geotechnical Engineering, 224-227.
[4] Sawicki, A., Swidzinski, W., Zadroga, B. 1998. Settlement of shallow foundation due to cyclic vertical force. Soils and foundations 38(1), 35-43.
[5] Tafreshi, S.M., Mehrjardi, G.T., Ahmadi, M. 2011. Experimental and numerical investigation on circular footing subjected to incremental cyclic loads. International Journal of Civil Engineering 9(4), 265-274.
[6] Fattah, M.Y., Salim, N.M., Alwan, K.K. 2019. Contact pressure distribution under circular shallow foundation subjected to vertical and rocking vibration modes. Journal of Building Engineering 26: 100908. https://doi.org/10.1016/j.jobe.2019.100908 , .
[7] Georgiadis, M., Butterfield, R. 1988. Displacements of footings on sand under eccentric and inclined loads. Canadian Geotechnical Journal 25(2), 199-212.
[8] Saran, S., Agarwal, R.K. 1991. Bearing capacity of eccentrically obliquely loaded footing. Journal of Geotechnical Engineering 117(11), 1669-1690.
[9] Taiebat, H.A., Carter, J.P. 2002. Bearing capacity of strip and circular foundations on undrained clay subjected to eccentric loads. Geotechnique 52(1), 61-64.
[10] Okamura, M., Mihara, A., Takemura, J., Kuwano, J. 2002. Effects of footing size and aspect ratio on the bearing capacity of sand subjected to eccentric loading. Soils and Foundations 42(4), 43-56.
[11] Patra, C.R., Behera, R.N., Sivakugan, N., Das, B.M. 2012. Ultimate bearing capacity of shallow strip foundation under eccentrically inclined load, Part I. International Journal of Geotechnical Engineering 6(3), 343-352.
[12] Patra, C.R., Behera, R.N., Sivakugan, N., Das, B.M. 2013. Estimation of average settlement of shallow strip foundation on granular soil under eccentric loading. International Journal of Geotechnical Engineering 7(2), 218-222.
[13] OpenSEES (Computer software): University of California, Berkeley.
[14] EPRI. 1990. Manual on estimating soil properties for foundation design. Electric Power Research Institute, Palo Alto, California.
[15] Harden, C., Hutchinson, T., Martin, G.R., Kutter, B.L. 2005. Numerical modeling of the nonlinear cyclic response of shallow foundations. Rep. No. 2005/04, Pacific Earthquake Engineering Research Center (PEER), Berkeley, California.
[16] Das, B. M. 2016. Principles of Foundation Engineering, 8th Edition. Cengage learning.
[17] Gajan, S., Hutchinson, T.C., Kutter, B., Raychowdhury, P., Ugalde, J.A., Stewart, J.P. 2008. Numerical models for the analysis and performance-based design of shallow foundations subjected to seismic

loading. Rep. No. 2007/04, Pacific Earthquake Engineering Research Center (PEER), Berkeley, California.
[18] Meyerhof, G.G. 1953. The bearing capacity of foundations under eccentric and inclined loads. Proceedings, Third International Conference on Soil Mechanics and Foundation Engineering, 440-445.
[19] Gazetas, G. 1991. Formulas and charts for impedances of surface and embedded foundations. Journal of geotechnical engineering 117(9), 1363-1381.
[20] Raychowdhury, P. 2008. Nonlinear Winkler-based shallow foundation model for performance assessment of seismically loaded structures. Ph. D Dissertation. University of California, San Diego.
[21] Sasmal, S.K., Behera, R.N. 2018. Prediction of combined static and cyclic load-induced settlement of shallow strip footing on granular soil using artificial neural network. International Journal of Geotechnical Engineering, 1-11, doi: https://doi.org/10.1080/19386362.2018.1557384.
[22] Friedman, J.H. 1991. Multivariate adaptive regression splines. The annals of statistics, 1-67.
[23] Samui, P., Kim, D. 2013. Least square support vector machine and multivariate adaptive regression spline for modeling lateral load capacity of piles. Neural Computing and Applications 23(3-4), 1123-1127.
[24] Muduli, P.K., Das, M.R., Das, S.K., Senapati, S. 2015. Lateral load capacity of piles in clay using genetic programming and multivariate adaptive regression spline. Indian Geotechnical Journal 45(3), 349-359.
[25] Khuntia, S., Mujtaba, H., Patra, C., Farooq, K., Sivakugan, N., Das, B.M. 2015. Prediction of compaction parameters of coarse grained soil using multivariate adaptive regression splines (MARS). International Journal of Geotechnical Engineering 9(1), 79-88.
[26] Mohanty, R., Suman, S., Das, S.K. 2017. Modelling the pull-out capacity of ground anchors using multi-objective feature selection. Arabian Journal for Science and Engineering 42(3), 1231-1241.
[27] Goh, A.T., Zhang, Y., Zhang, R., Zhang, W., Xiao, Y. 2017. Evaluating stability of underground entry-type excavations using multivariate adaptive regression splines and logistic regression. Tunnelling and Underground Space Technology 70, 148-154.
[28] Lokuge, W., Wilson, A., Gunasekara, C., Law, D.W., Setunge, S. 2018. Design of fly ash geopolymer concrete mix proportions using Multivariate Adaptive Regression Spline model. Construction and Building Materials 166, 472-481.
[29] Kaveh, A., Bakhshpoori, T., Hamze-Ziabari, S.M. 2018. M5'and Mars Based Prediction Models for Properties of Self-compacting Concrete Containing Fly Ash. Periodica Polytechnica Civil Engineering 62(2), 281-294.
[30] Zheng, G., Yang, P., Zhou, H., Zeng, C., Yang, X., He, X., Yu, X. 2019. Evaluation of the earthquake induced uplift displacement of tunnels using multivariate adaptive regression splines. Computers and Geotechnics 113 (103099), 1-9.
[31] Zhang, W., Zhang, R., Wang, W., Zhang, F., Goh, A.T.C. 2019. A Multivariate Adaptive Regression Splines model for determining horizontal wall deflection envelope for braced excavations in clays. Tunnelling and Underground Space Technology 84, 461-471.
[32] Ghanizadeh, A.R., Rahrovan, M. 2019. Modeling of unconfined compressive strength of soil-RAP blend stabilized with Portland cement using multivariate adaptive regression spline. Frontiers of Structural and Civil Engineering, 1-13.
[33] Liu, L., Zhang, S., Cheng, Y.M., Liang, L. 2019. Advanced reliability analysis of slopes in spatially variable soils using multivariate adaptive regression splines. Geoscience Frontiers 10(2), 671-682.
[34] Samui, P., Kurup, P. 2012. Multivariate adaptive regression spline and least square support vector machine for prediction of undrained shear strength of clay. International Journal of Applied Metaheuristic Computing (IJAMC) 3(2), 33-42.
[35] Milborrow, S. 2019. Package 'earth', http://www.milbo.users.sonic.net/earth.
36. Milborrow, S. 2020. Notes on earth package,http://www.milbo.org/doc/earth-notes.pdf.

INVESTIGATION OF THE IMPACT BEHAVIOR WHEN USING SINGLE AND DOUBLE LAYERS OF GEOSYNTHETICS ON BURIED PIPE STRUCTURES

RAZISKAVA VPLIVA UPORABE ENEGA ALI DVEH SLOJEV GEOSINTETIKOV NA OBNAŠANJE VKOPANIH CEVOVODOV

Güneş Babagiray
Gazi University,
Department of Civil Engineering,
06570, Ankara, Turkey

Sami Oğuzhan Akbaş
Gazi University,
Department of Civil Engineering,
06570, Ankara, Turkey

Özgür Anil *(corresponding author)*
Gazi University,
Department of Civil Engineering,
06570, Ankara, Turkey
E-mail: oanil@gazi.edu.tr

DOI https://doi.org/10.18690/actageotechslov.18.2.83-104.2022

Keywords

geosynthetics, geocell, geogrid, geotextile, geonet, buried pipeline, impact load, soil reinforcement

Ključne besede

geosintetik, Geocell, Geogrid, Geotextile, Geonet, vkopani cevovod, udarna obtežba, armirana zemljina

Abstract

In this study the behavior of buried pipes under impact loading was investigated by forming protective layers with geosynthetics in various combinations in single and double layers. For this purpose, experiments were performed using a HDPE pipe with a 160 mm outer diameter, which is frequently used in the laboratory. In the experiments, Geocell, Geogrid, Geotextile, and Geonet protective layers at a depth of 120 mm were tested by laying Geosynthetic in single and double layers and then tested under the effects of impact loading by using free-weight dropping test apparatus. In the experimental study, the protective layers' energy absorption capacities were calculated by using acceleration measurements over the pipe and then evaluated together with their costs. In the experiments with a single layer Geosynthetic as a protective layer, Geonet's most successful protection structure was a 72.9 % acceleration-damping capacity. In the experiments with the combination of double-layer reinforcement elements, the most successful performance with 88.0 %, in terms of acceleration damping capacity, was obtained from Geocell and Geonet's combination with a thickness of 1 mm at a depth of 50 mm. When all the experiments with single- and double-layer Geosynthetic protective elements were evaluated as an acceleration damping ratio per unit cost, it was found that the optimum application was achieved when using a single-layer Geogrid.

Izvleček

V tej študiji smo raziskali obnašanje vkopanih cevi pri udarni obtežbi zaščitenimi z enim ali dvema slojema geosintetika. V ta namen so bili izvedeni poskusi z uporabo cevi HDPE z zunanjim premerom 160 mm, ki se pogosto uporablja v laboratoriju. V poskusih smo preizkušali zaščitne plasti Geocell, Geogrid, Geotextile in Geonet na globini 120 mm s polaganjem geosintetika v enem in dveh slojih in nato aplicirali udarno obtežbo z uporabo aparata za spuščanje uteži s prostim padom. V eksperimentalni študiji so bile z meritvami pospeška nad cevjo izračunane zmogljivosti zaščitnih plasti za absorbcijo energije in nato ovrednotene skupaj z njihovimi stroški. V poskusih z enoplastno zaščitno plastjo z Geosintetiko je bila najuspešnejša Geonet zaščitna struktura z 72,9 % zmogljivostjo dušenja pospeškov. V poskusih s kombinacijo dvoslojnih armaturnih elementov je bila najuspešnejša z 88,0 % zmogljivosti dušenja pospeškov dosežena s kombinacijo Geocell in Geonet z debelino 1 mm na globini 50 mm. Ko so bili vsi poskusi z enoslojnimi in dvoslojnimi geosintetičnimi zaščitnimi elementi določeni kot razmerje dušenja pospeškov na enoto stroška, je bilo ugotovljeno, da je bila optimalna uporaba dosežena z uporabo enoslojne Geogrid.

1 INTRODUCTION

The importance of a pipe's "living lines" is evident as the uninterrupted supply of energy and water. Pipelines used for transporting various materials can be subjected to sudden dynamic impact loading due to mass movements such as landslides or rock falls on transition zones. This study aims to examine the behavior of buried pipes under the effect of various impact loads that might occur during their service life in the presence of protection layers. To show that damage caused by sudden dynamic impact loads can be prevented, HDPE (high-density polyethylene) pipes, which are frequently used in infrastructure applications, were tested under an impact load using a free-weight dropping test device together with geosynthetic protective layers.

In this study various combinations of geosynthetics and protective layers were formed on the buried pipe, and then impact loading was applied. In the experiments, the types and application shapes of the geosynthetics were chosen as variables. We tried to determine the effects of impact loads on the buried HDPE pipe with an outer diameter of 160 mm protected by geosynthetics. Geocell, Geogrid, Geotextile, and Geonet with various heights and wall thicknesses were tested by single- and double-layer Geosynthetic laying. The acceleration values, deformation values, load values transferred to the pipe at a certain depth, energy-damping performance against impact loading of the protective layers and the costs were compared.

In the literature, no experimental study in which Geosynthetic's behavior under the effect of impact loading for single and multiple layers are comprehensively examined has been found. It is clear that most previous studies emphasized the static loading. Besides, considering their widespread use for transportation structures, repeated loading tests are also available [1, 2]. Dash, Krishnaswamy and Rajagopal [3] examined the strengthening efficacy of geocell knitted from geogrids strips between the ground under the foundation and the sand above it. The tests were carried out in 1200 mm long, 332 mm wide, and 700 mm high steel tanks under the sand's tightness, geocell cell height and width, the technique of forming the geocell model, geocell laying depth, and geogrid stiffness. The foundation model has 330 × 100 × 25 mm^3 dimensions. The LVDT was attached to both sides of the foundation, and the loading continued until the foundation settlement reached around 50 mm, when there was no failure. Good progress in performance was achieved due to the transfer of foundation loads deeper with the geocell layer. When using Geocell reinforcement, no failure was observed, even for a load of 8 times the final load-carrying capacity of the unreinforced sand and a seating equal to 50 % of the foundation width. The most suitable width of the geocell, where it will prevent all possible failure planes on the ground, was found to be approximately four times the foundation width. The maximum benefit was obtained when the geocell layer is below the foundation, and is 0.1 times the foundation's width.

Laman and Yıldız [4] in their tests with ring-model foundations on sandy ground with geogrid reinforcement, under the variables of foundation inner diameter, geogrid depth, number of the geogrid layer, and layer length. They found that even a single-axis geogrid layer improves the load-carrying capacity by up to three times. An entirely circular foundation and an annular pattern foundation showed similar performance for the same outer diameter. This provided an economical solution for practical applications. The dimensions of the test tank are 700 × 700 × 700 mm^3. In the first test series, the ratio of the inner diameter to the outer diameter was taken as variable, and its effect on the load-carrying capacity was also examined. It was observed that the optimum inner diameter is fixed at 0.3 times the foundation diameter. In the second test series, the first geogrid layer's optimal placement occurred when the ring (from the bottom of the foundation) was below 0.3 times the foundation diameter. In the third series, it we tried to reach the optimum value of the reinforcement layers. As the number of reinforcements increased, the load-carrying capacity also increased. After four reinforcements, the effect on the load-carrying capacity began to disappear. In the fourth test series, it was observed that the load-carrying capacity began to stabilize when the length of the geogrid layer was greater than three times its foundation diameter.

For the test of strengthening the sand layers on soft grounds, Zhou and Wen [5] used a steel tank with dimensions of 3060 × 1180 mm^2 and a height of 2000 mm. Four series of tests were performed. In the first one, a 300 mm sand cushion was covering the soft ground. In the second one, a layer of geogrid was used in the sand cushion. In the third, two geogrid layers and a layer of geocell were used in the last one. The geocell-reinforced sand layer has considerably reduced settlements in the soft ground layer below. In the sand layer, the geocell reinforcement performed relatively better in sitting than the geogrid reinforcement.

To simulate the vehicle load, Moghaddas Tafreshi and Khalaj [6] conducted repeated load modeling on a buried pipe at 1.5–3 times the pipe's diameter. In this experiment, steel tanks with a dimension of 1000 mm × 220 mm × 1000 mm were used. The sand's relative tightness, the number of reinforcement layers, and the pipe's burial depth were chosen as the variables. The results were examined with three different relative tightnesses, four different pipe burial depths, and five geosynthetic layer layouts. The deformations of the pipe remain constant after approximately 400 seconds (120 reps). The pipe deformation and ground-surface settling are reduced on the ground reinforced with geogrid. Besides, geosynthetic strengthening performance on loose ground is more successful than for tight and medium ground. The ground surface sitting and the pipe deformation decrease as the floor's relative tightness increases. By increasing the pipe burial depth, the pipe deformation decreased, and the ground surface deformation increased.

The test tank in the Gürbüz and Mertol [7] study has dimensions of 700.5 × 700.5 mm^2 and a height of 800 mm. The model representing the strip foundation has the dimensions of 70 × 695 mm^2. Th geocell cell heights are 75 and 150 mm. These cells' properties, such as width, height, and the number of layers, and the distance between layers, were studied. The test results showed that with the use of single-layer geocell on the cohesion-free ground, the seating decreased 62 % compared to the unreinforced floor, and the load-carrying capacity improved by about 3 %. The result showed that the optimum distance between the geocell cells is 0.142 times the foundation's width, and the depth of the effect was twice the width of the foundation. Besides, the optimum cell width was around 4.2 times the foundation's width. While the ratio of the geocell laying length to the foundation width is about 8.2, it does not affect the load-carrying capacity.

Moghaddas Tafreshi and Dawson [8] also tested the strip foundations on the floor with and without geocell reinforcement under a combination of static and repetitive loads in the laboratory. The test tank was 750 mm long, 375 mm high, and 150 mm wide. The model foundation is 75 x 148 mm^2 in size. These tests were carried out under the variables such as geocell laying length, geocell height, repeated load-amplitude changes. The presence of reinforcement both delayed and reduced sitting. It also allowed the repeated load to be increased. As the length of the reinforcement element laid at any repeat loading increased, the seating amount decreased. It is stated that this situation can be neglected after the geocell laying length is 3.2 times the foundation width.

Since the traffic loads reduce the pipe systems' functionality and cause economic and social problems, Tavakoli Mehrjardi, Moghaddas Tafreshi, and Dawson [9] analyzed the performance of buried pipes in the ground reinforced with geocell. The filling material is well-graded sand. The embedded PVC pipe has a 160 mm outer diameter and 1100 mm length. Since smaller cell sizes cause worse compression, surface settling was observed in an experiment with geocell with a cell height of 50 mm for different loading conditions. Geocell, which is 100 mm in height, has a better performance by forming a rigid layer as it creates larger bonding boundaries in volume. Compared to the non-reinforced floor, the ground with geocell reinforced reduced the ground surface settlements by 65 % and vertical diametric deformations on the pipe by 35 %.

Corey, Han, Khatri, and Parsons [10] made four static loadings on the steel-reinforced with 610 mm diameter HDPE buried pipe with ground reinforcement with and without geogrid. The laboratory experiments have shown that longitudinal pull deformations on the pipe are reduced by geogrid. Besides, the geogrid layer used at the top has been beneficial with vertical deformations in the pipe. Surface sitting decreased by 11 %, the pipe longitudinal deformations decreased by 25 %, and vertical stresses decreased by 10.

Hegde, Kadabinakatti, and Sitharam [11] made static loading in the laboratory environment by embedded PVC pipes with 75 mm diameter with and without geosynthetic reinforcement. Tests were carried out in the tank by 900 × 900 × 600 mm^3 and 20 mm wall thickness, with 150 mm square plate loading. In all tests the reinforcement laying length was taken as 5.5 times the foundation width. The pipe was buried at two depths: the foundation width and twice the foundation width. It has been shown that the combination of geocell and geogrid can significantly reduce the pipe's burial depth. It was concluded that the combination of geocell and geogrid protected the embedded pipes and, in this way, reduced the deformations in the pipe compared to the ground without reinforcement. In the reinforcement made with the combination of geocell and geogrid at a depth of at least 1.5 the foundation width from the bottom of the foundation, the pressure on the pipe was almost negligible, and the pressure less than 0.1 times the foundation pressure was measured.

Another study using the impact test was carried out by Anıl, Erdem, and Kantar [12]. In this study, steel pipe and steel-concrete composite pipes with 1000 mm length and 220 mm diameter were used. Eight experiments were carried out in total, two of which are direct pipe impact tests, two of which are impact tests on the sand layer, and four of which are protective. The buried pipe is protected against impact loading with a protective layer called geofoam, and the results are examined. In both types of pipes with 50 mm thick geofoam, the acceleration and displacement values were decreased, and the energy-damping values were increased.

As a result of the comprehensive literature review, no studies were conducted to protect the buried pipes against the impact loading reinforced by geosynthetics. For this reason, an experimental study was planned, and the performance of the buried pipes with different types of single- or double-layer geosynthetics was investigated to protect them against the effects of impact loading. The energy-damping performances of the geosynthetic (as the protective layers) and costs against the impact loading were compared by interpreting the acceleration and deformation values obtained from the test study's results.

2 EXPERIMENTAL STUDY

2.1 Test materials

To determine the soil's physical properties and to make a classification according to the USCS system, soil mechanics experiments were conducted on the sand ground. The well-graded sand (*WS*) used in the experiments was characterized by its specific gravity, maximum and minimum void ratios, etc. Its grain size distribution is shown in Table 1 and Figure 1. Direct shear tests conducted on sand specimens that were compacted to a relative density of 40 % resulted in an effective stress friction angle of 32º. This result was obtained at normal stress values between 95 and 500 kPa. Note that all the index and strength and the impact load tests were performed on oven-dried sand samples. The same well-graded sand with properties and grain size distribution were used under the pipe as a cushion layer at 40 % relative density. The cushion layer thickness is a constant 50 mm for all the test experiments [12-17].

The main variables investigated in the test series are the use of the geosynthetics. The geocell, geogrid, geotextile, geonet reinforcement elements were laid in a single layer or combined at 120 mm depth from the tank top face parallel to the pipe axis in the experiments. The protective sand layer was reinforced with geosynthetic materials produced by the Geoplast Company. The geocell, geogrid, geotextile properties, geonet as specified by the manufacturer are given in Tables 2, 3, 4, and 5, respectively. Commercially available, high-density PE100 (HDPE) pipes with 160 mm diameter were used in the experiments. The properties of the pipes, as specified by the manufacturer, are given in Table 6.

Table 1. Properties of the sand used in the experimental studies.

G_s	ρ_{min} (Mg/m^3)	ρ_{max} (Mg/m^3)	e_{min}	e_{max}	D_{10} (mm)	D_{30} (mm)	C_c	C_u
2.949	1.51	1.86	0.57	0.94	0.19	0.7	1.4	9.5

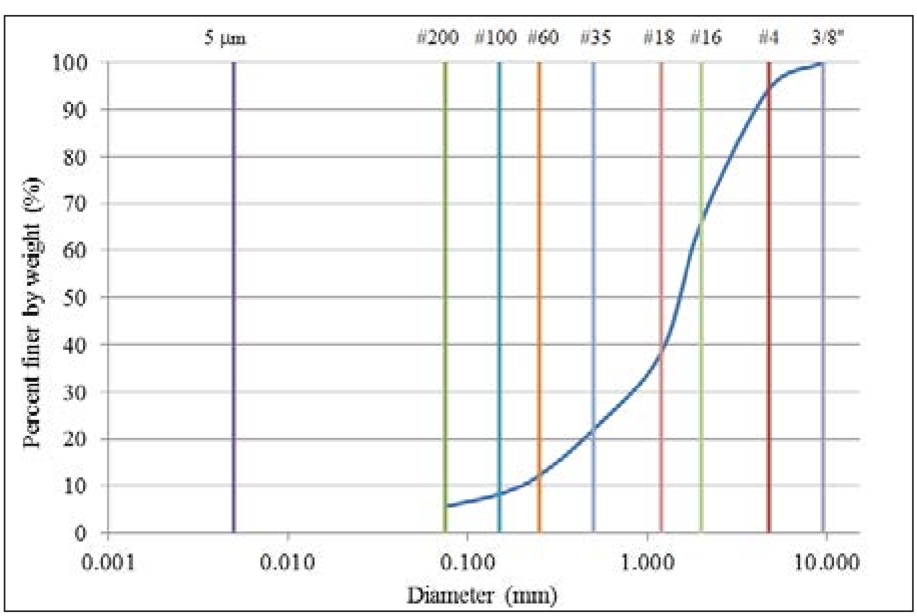

Figure 1. Grain size distribution curve obtained by sieve analysis.

Table 2. Properties of the geocell.

Property	Unit	Value		Method
Material		High-density polyethylene		
Density	g/cm^3	0.935-0.965		EN ISO 1183-1/A
Carbon black	%	1-3		ASTM D 1603
Cell depth	mm	50	100	-----
Tensile strength	kN/m	5-10	10	EN ISO 10319
Welding size	mm	400	330	-----
Cell length × Cell width	mm	250 × 300	210 × 250	-----
Thickness	mm	1.0	1.5	EN ISO 9863-1
Oxidation induction time	dak	>20		ASTM D 3895
Linear thermal expansion	+30 °C	≤90		-----

Table 3. Properties of the geogrid.

Property	Unit	Value		Method
Material		High-density polyethylene		
Density	g/m^2	240	+10 %	EN ISO 9864
Tensile strength (*Dop*/*Vd*)*	kN/m	20/20	+10 %	EN ISO 10319
Elongation at maximum load (*Dop*/*Vd*)	%	<8/<8	+10 %	EN ISO 10319
Aperture size (*Dop*/*Vd*)	mm × mm	40 × 40	+10 %	----
Carbon black	%	20/20		

(* *Dop*: In the direction of production; *Vd*: Vertical direction)

Table 4. Properties of the geotextile.

Property	Unit	Value	Method
Material		Polypropylene	
Density	g/m^2	500	TS EN ISO 9864
Thickness	mm	4	TS EN ISO 9863-1
Rupture strength	kN/m	27-29	TS EN ISO 10319
Elongation at rupture	%	50-80	TS EN ISO 10319
Static puncture strength	N	5500	TS EN ISO 12236
Dynamic puncture strength	mm	3	TS EN ISO 13433
Aperture size	mm	0.08	TS EN ISO 12956

Table 5. Properties of the geonet.

Property	Unit	Value		Method
Material		Polypropylene		
Density	g/m^2	660	10 %	EN ISO 9864
Polymer density	g/cm3	>0.94	10 %	EN ISO 1183
Tensile strength (*Dop*/*Vd*)*	kN/m	13/15	10 %	EN ISO 10319
Carbon black content	%	1-3	10 %	ASTM D 1603
Elongation at maximum load	%	50/40	10 %	EN ISO 10319
Thickness	mm	6.5	10 %	EN ISO 9863-1
Rupture strength	kN/m	32/32	10 %	EN ISO 10319

(* *Dop*: In the direction of production; *Vd*: Vertical direction)

Table 6. Properties of PE100 HDPE pipes.

Property	Unit	Value	Method
Density (23 °C)	g/cm^3	0.950-0.960	ISO 1183
Melting flow rate (MFR) 190 °C - 2.16 kg	g/10 min	0.04-0.07	ISO 1133
Melting flow rate (MFR) 190 °C - 5.00 kg	g/10 min	0.2-0.5	ISO 1133
Elongation	%	> 600	ISO 527-2/1B/50,TS1398
Yield strength	MPa	22-27	ISO 527-2/1B/50,TS1398
Elasticity modulus	MPa	950-1400	ISO 527-2/1B/50,TS1398
Carbon black (190 °C - 5 kg)	%	>2	ISO 6964
Hardness	Shore D	59-60	ISO 868
Thermal resistivity	min.	>20	EN 728 ISO/TR 10837
Vicat softening temperature	°C	126	ISO 306 (Method A)
Crack temperature	°C	< -70	ASTM D-746
Thermal conductivity (20 °C)	W/Mk	0.4	DIN 52612
Thermal conductivity (150 °C)	W/Mk	0.2	DIN 52612
ESCR (at 50 °C), F50	Hour	>10000	ASTM D-1693

2.2 Test setup and instrumentation

In the experimental study, the HDPE pipes' behavior was buried in well-grained sand, which was reinforced with geocell, geogrid, geotextile, geonet, and combinations of them under the influence of sudden dynamic impact loading was investigated. The geosynthetics types and usage patterns were chosen as variables in the study. The authors' designed a free-fall impact apparatus to drop a constant weight of 5.25 kg from a height of 500 mm, making a constant energy impact loading ($5.25 \times 9.81 \times 500/1000 = 25.751$ J) are shown in Figure 2 [12-17]. The base part, on which the apparatus is placed, is made up of a 1000 × 1000 × 70 mm^3 steel

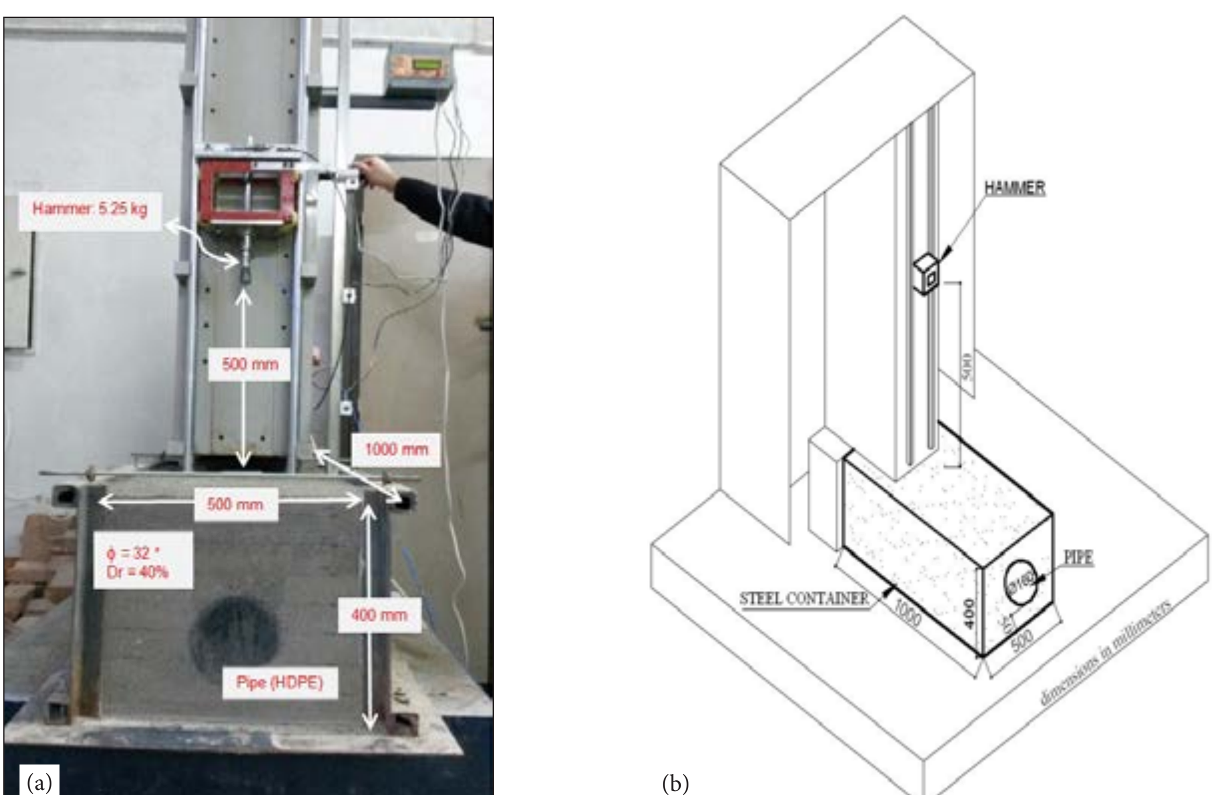

Figure 2. Free-fall impact test mechanism: (a) overview, (b) sketch [16].

plate that stands on a rigid pedestal. In this way, the base part weighs about 500 kg and acts as an absorber. The pipe and the protective layer were systematically placed in a 1000 mm × 500 mm × 400 mm steel container with a Plexiglas front side for observation purposes, situated directly under the free-fall impact apparatus.

The hammer weight, shape, and drop height are constant during all of the experiments. The fixed-weight hammer used in the experiments is made of steel, and it has a 5.250 kg mass Figure 3. The load point, which the hammer is applied, is at 610 mm from the frontal tank face. The spherical hammer's tip is interchangeable, and its weight can be increased to change the dimensions and effects of the regional impact at the drop point. A screwing system is installed, which allows adding weight to the inside and prevents movement of the added weights at the time of the impact to change the hammer's mass. The dropping mechanism of the hammer is manufactured mechanically. Thus, the hammer and holding mechanism can be removed practically and quickly to the height being tested. The hammer is slid with shafts on both sides to make a free fall while remaining on the same axis. The hammer shafts are made of 30 mm chrome. In addition, the upper part is specially designed and allows us to increase the height easily. Cestamide rollers guide it on four sides to minimize the friction forces on the hammer. Cestamide is a polyamide material, and it is manufactured by casting. It has a tight texture and rigidity. It is particularly resistant to impacts, and fatigue loading and its friction coefficient are low.

The applied impact load was measured using a 40-kN capacity dynamic load cell connected to the hammer, and acceleration time histories were measured by ±560 g capacity piezoelectric accelerometers located at two different locations, as shown in Figure 4. Two piezoelectric accelerometers are located on the 1000 mm long HDPE pipe, 250 and 500 mm from the tank's front face. The accelerometer close to the loading plate is called the middle, and the other accelerometer is called the front, and is used as such in the following explanations. Note that the presented data belong to the larger accelerations measured at the middle accelerometer, closer to the impact point. During the experiments, these accelerometers, which are not in contact with the ground and remain in the pipe, are used for general purpose, absolute-motion measurements, shock, and vibration measurements.

Figure 3. Hammer details.

Data obtained from the dynamic loading and acceleration measurements were transferred to the special software using a dynamic data-logger system. This special software was also used during the tests and calibration of the sensors. While selecting this data collector system used in the experiments, the NI 9233-USB-9162 model produced by National Instruments was used by considering the effect of the force and the measuring devices. This data logger is a four-channel dynamic signal catcher made of IEPE sensors that can take accurate measurements. The data-logger device with the technical specifications is shown in Table 7, consisting of two modules. The first module is the data collector, with the measuring

Table 7. Properties of NI 9233-USB-9162 data logger.

Property	Unit	Value
Channel number	Four analog inputs	
Input Current	AC	
Computer Connection	Hi-Speed USB 2.0	
Resolution	bit	24
Dynamic Range	dB	102
Minimum Data Rate	kS/s	2
Maximum Data Rate	kS/s	50
Frequency	MHz	12.8
Precision	ppm max	± 100
Minimum AC Voltage	V	5
Maximum AC Voltage	V	5.8
IEPE Minimum Excitation Current	m.A	2.0
Input Voltage Range	V	± 5
Photograph		

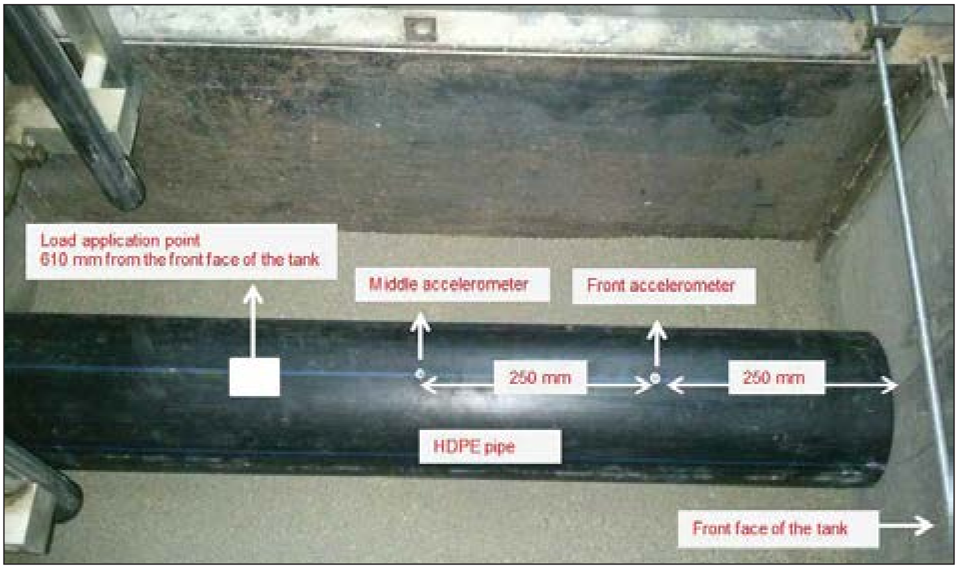

Figure 4. Instrumentation on the pipe [16].

devices connected to this module. This module transmits the signals from the first module to the computer. The modules are independent of each other. Acceleration-time, load-time, and load-displacement relationships were obtained from the measurements, and the energy-absorption capacities of the different pipe-protective layer systems were calculated using load-displacement graphs. In the free weight-dropping experimental setup, the conversion of potential energy into kinetic energy at the time of impact is the main approach. The energy conversion causes stress accumulation, which takes place very quickly on the specimen. The energy lost during the fall is equal to the system's energy according to the law of the conservation of energy.

3 EXPERIMENTAL RESULTS AND DISCUSSION

In the 400 × 500 × 1000 mm^3 test tank, the pipe was placed on dry sand at a height of 50 mm with 40 % relative tightness and a unit volume weight of 16.13 kN/m^3. The base-layer thickness under the pipe is constant in all the experiments. The HDPE pipe is centered and positioned at 250 mm from each face side of the test tank. The same test sand is placed on the pipe with the same tightness. In all experiments, the hammer was dropped from a height of 500 mm onto the sand layer, and measurements were taken from the HDPE pipe with the 160 mm outer diameter. A total of 12 experiments were performed, such as one reference specimen, five specimens with a single layer geosynthetic protective layer, and six specimens with double layer geosynthetic protective layer combinations. Acceleration values obtained from the experimental specimens were evaluated by transferring them to special software in the computer with a dynamic data-logger system. Using the measured values, acceleration-time, load-time, and load-displacement graphs were drawn for each experiment. The energy-absorption capacities were calculated from the area under the load-displacement graphs. Displacement values are calculated by integrating the acceleration values measured on the pipe. Therefore, it should be remembered that the displacement value belongs to the point where the accelerometers are connected. Load-displacement graphs were calculated by integrating the acceleration values measured at the same interval times.

In the reference test specimen, after the 160 mm diameter pipe was placed, no reinforcement element was used up to the tank's top surface. Only the sand was placed for the remaining 190 mm from the top surface of the pipe. In all the tests, geosynthetics have a laying depth of 120 mm. Acceleration-damping ratios were found by dividing the reference experiment maximum acceleration value by the relevant experimental maximum acceleration value. The energy applied to the system by a hammer with a mass of 5.25 kg, dropped from a height of 500 mm, is 25.751 Joules. The energy applied to the system is different from the energy value measured on the pipe, which indicates the energy absorbed by the protective layer. All the results obtained from the experiments are presented in Table 8. The acceleration-time charts obtained from the middle accelerometer are shown in Figure 5. The acceleration-time graphics obtained from the front accelerometers are shown in Figure 6, the load-time graphics are given

Table 8. Results of the experiments.

Test no	Geosynthetics	Maximum measured acceleration (g)	Maximum displacement (mm)	Maximum load (kN)	Reduction in acceleration (%)	Calculated energy on the pipe (J)	Absorbed [b] the energy capacity of the protective layer (J)	Cost of the tests (USD)
1	Without any protective layer	65.95	5.10	10.06	Reference	4.39210	21.36	Reference
2	GEOCELL (h=50, t=1, w=400) [a]	39.90	2.11	10.68	39.5	2.26020	23.49	3.40
3	GEOGRID	25.20	0.58	11.78	61.8	1.09220	24.66	0.85
4	GEOTEXTILE	19.63	0.56	10.93	70.2	0.91170	24.84	1.05
5	GEONET	17.90	0.53	11.10	72.9	0.64100	25.11	1.64
6	GEOCELL (h=100, t=1.5, w=330)	21.04	0.56	11.26	68.1	0.93890	24.81	5.61
7	GEOCELL (h=50, t=1, w=400) / GEOGRID	16.03	0.33	11.49	75.7	0.55078	25.20	4.24
8	GEOGRID / GEOTEXTILE	10.02	0.27	10.79	84.8	0.11290	25.64	1.89
9	GEONET / GEOGRID	10.51	0.28	11.14	84.1	0.12080	25.63	2.48
10	GEONET / GEOTEXTILE	9.12	0.26	11.45	86.2	0.10490	25.65	2.68
11	GEOCELL (h=50, t=1, w=400) / GEOTEXTILE	12.03	0.29	11.27	81.8	0.13679	25.61	4.44
12	GEOCELL (h=50, t=1, w=400) / GEONET	7.89	0.23	11.36	88.0	0.09688	25.65	5.03

[a] h: cell depth of geocell (mm); t: wall thickness of geocell (mm); w: weld interval of geocell (mm).
[b] Absorbed energy is the difference between the applied energy (5.25 × 9.81 × 500/1000 = 25.751 Joule) and the energy calculated at the top of the pipe.

in Figure 7, and the load-displacement graphics are given in Figure 8.

In the calculation of the experimental costs, unit prices of the application year were used. This is important only in terms of giving ideas, although the prices were increased by years, they exhibit the same ratio in terms of cost. Expense items, production, and total cost of the manufacturer's materials are shown in Table 9, based on the unit prices of 2014. The size of all the materials laid from the tank's top surface at a depth of 120 mm is 0.5 m^2. The total cost of geocell experiments, which has high prices compared to other geosynthetics, was also high. It is observed that the total cost of the geogrid material is more economical than other geosynthetic materials.

Within this study's scope, four different geosynthetics are placed as a single layer or double layer, as a protective layer on the buried pipe, and the behavior is investigated under impact loading. A free weight drop test setup designed and produced by the authors was used in the study. In the experiments, the distribution of the acceleration values taken from the two accelerometers on the pipe was in general agreement with the acceleration values taken from the midpoint accelerometer (Figure 9). The evaluations were made with the acceleration values taken from the midpoint accelerometer, which gives the maximum results since it is close to the load application point. The energy-absorption capacities of geosynthetics were evaluated using the midpoint accelerometer and deformations gained from these results. The values of the acceleration and deformations, which give an idea about evaluating the experiment results, showed parallelism in the assessment of performance. The damping capacity is the difference between the energy applied, and the energy calculated on the pipe was achieved by 5.25 × 9.81 × 500/1000 = 25.751 Joule.

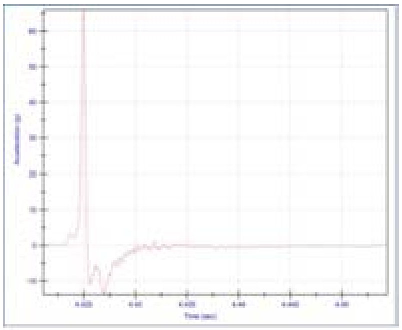
Test 1

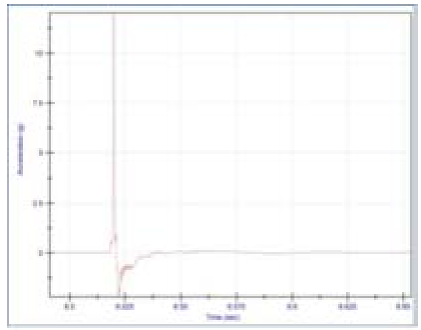
Test 2

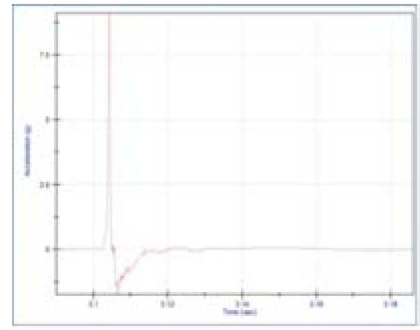
Test 3

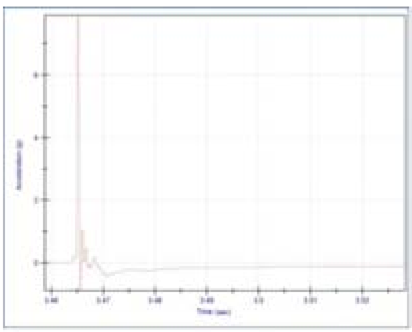
Test 4

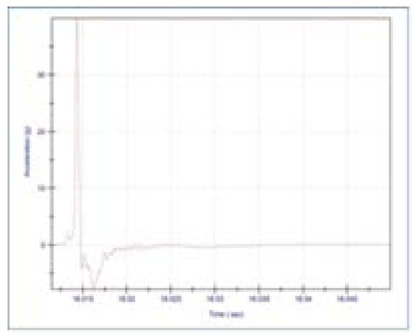
Test 5

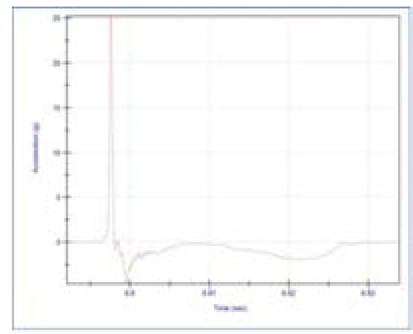
Test 6

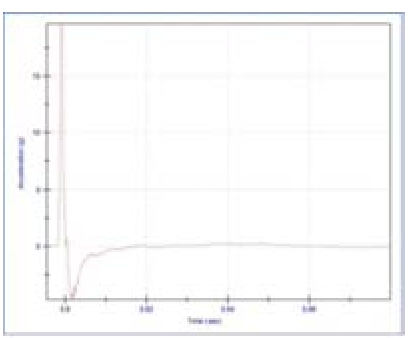
Test 6

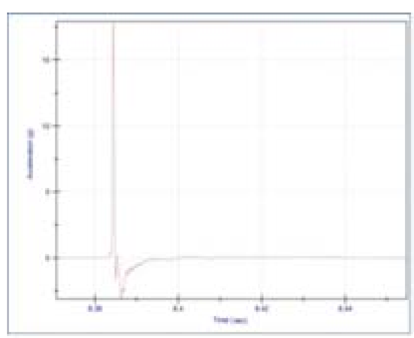
Test 7

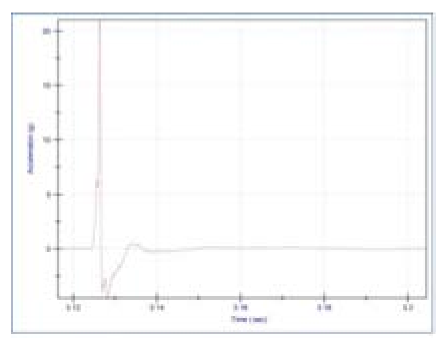
Test 8

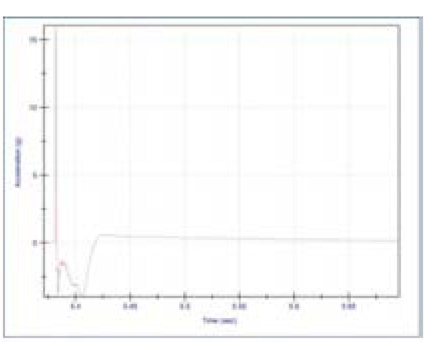
Test 10

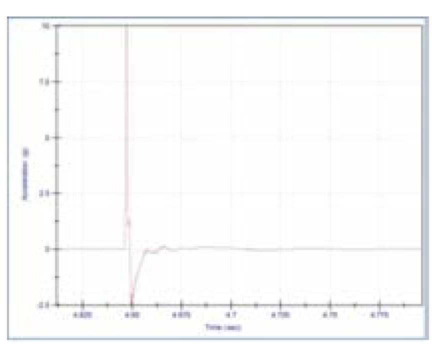
Test 11

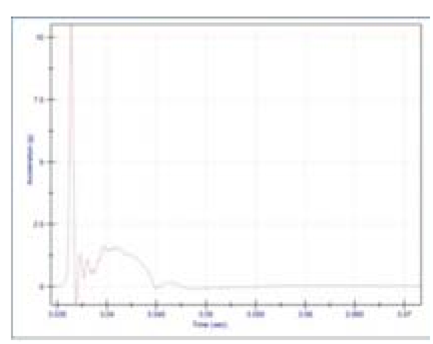
Test 12

Figure 5. Acceleration-time graphs from the middle accelerometer of tests.

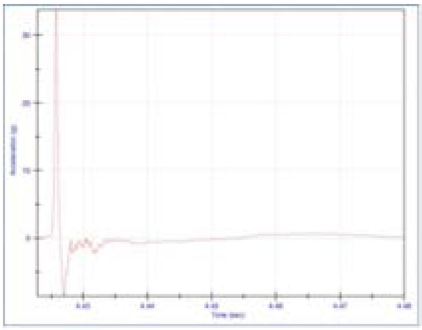
Test 1

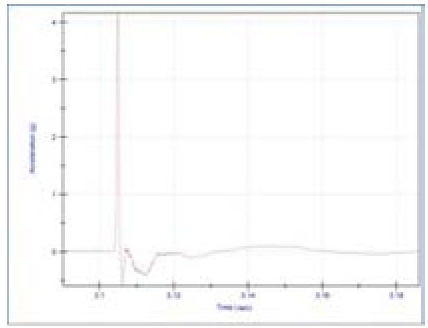
Test 2

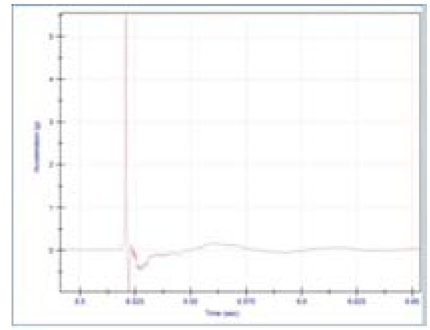
Test 3

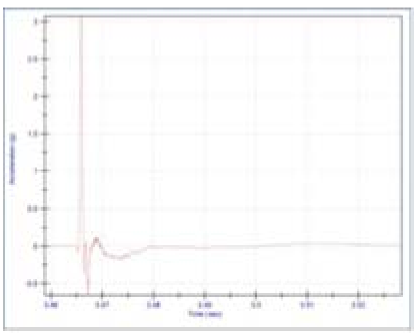
Test 4

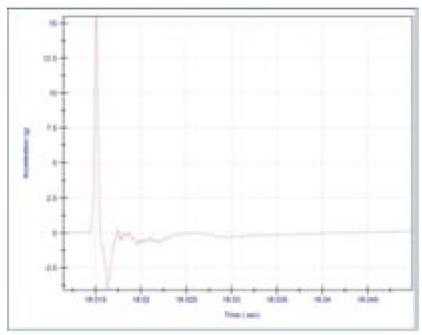
Test 5

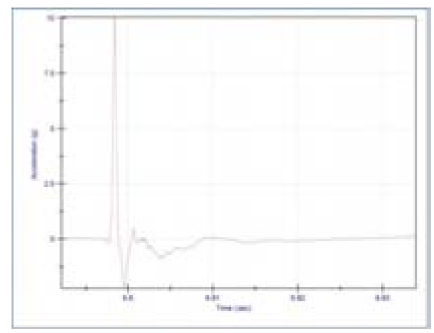
Test 6

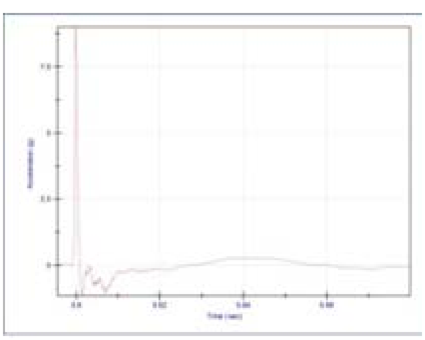
Test 6

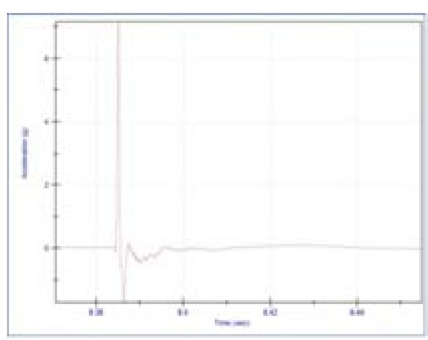
Test 7

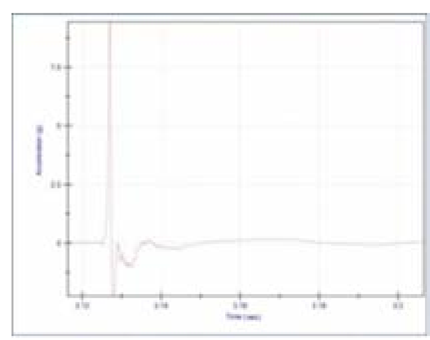
Test 8

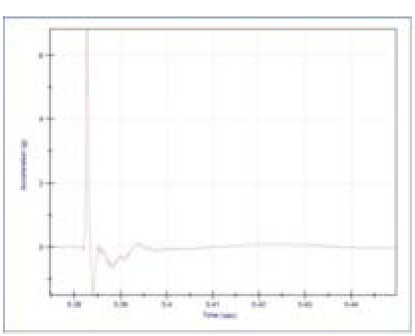
Test 10

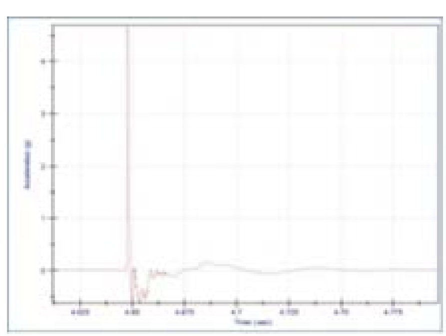
Test 11

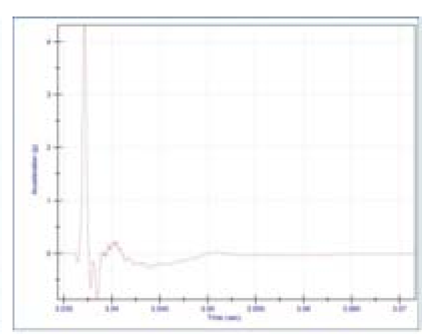
Test 12

Figure 6. Acceleration-time graphs from the front accelerometer of tests.

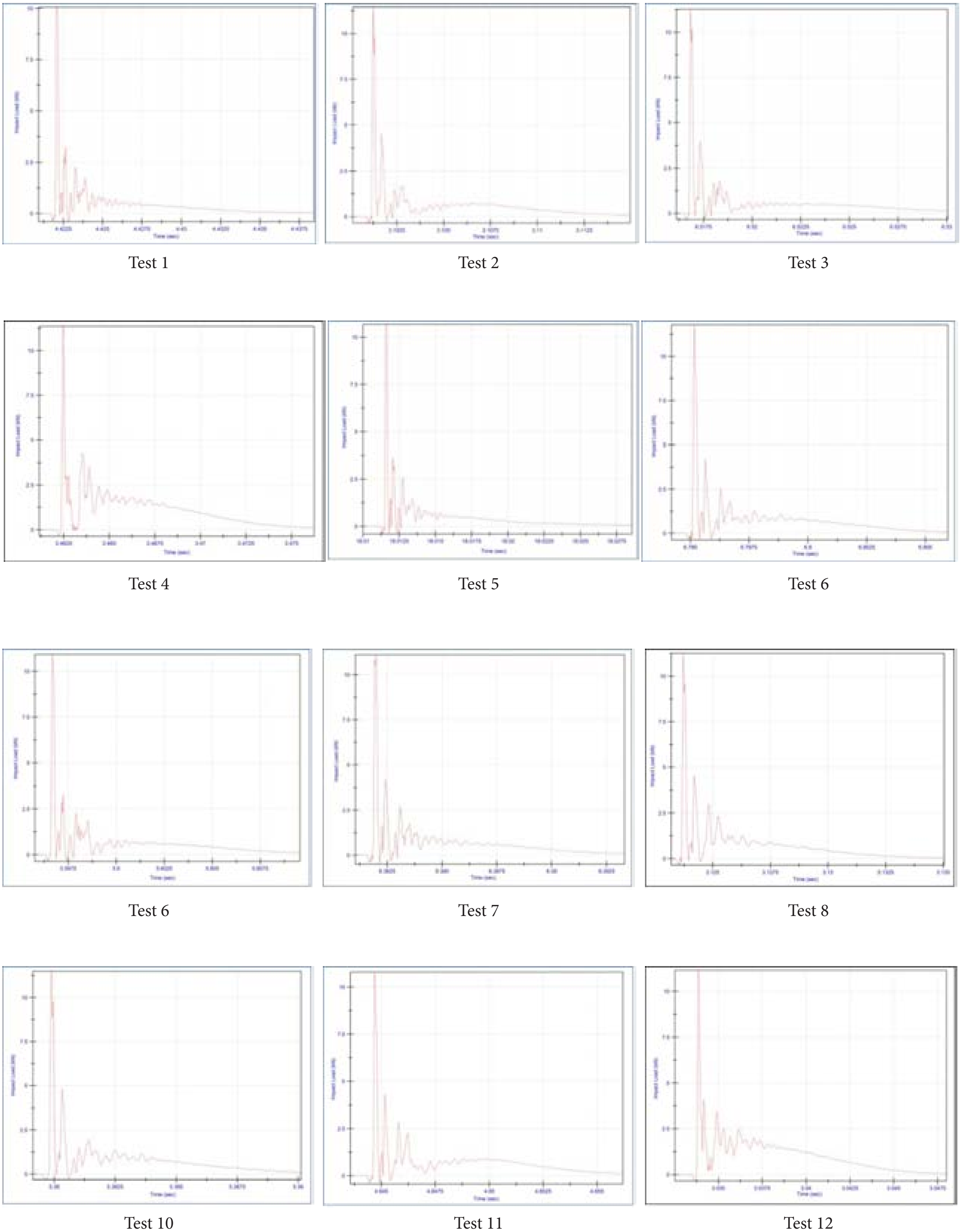

Figure 7. Measured load-time graphs of tests.

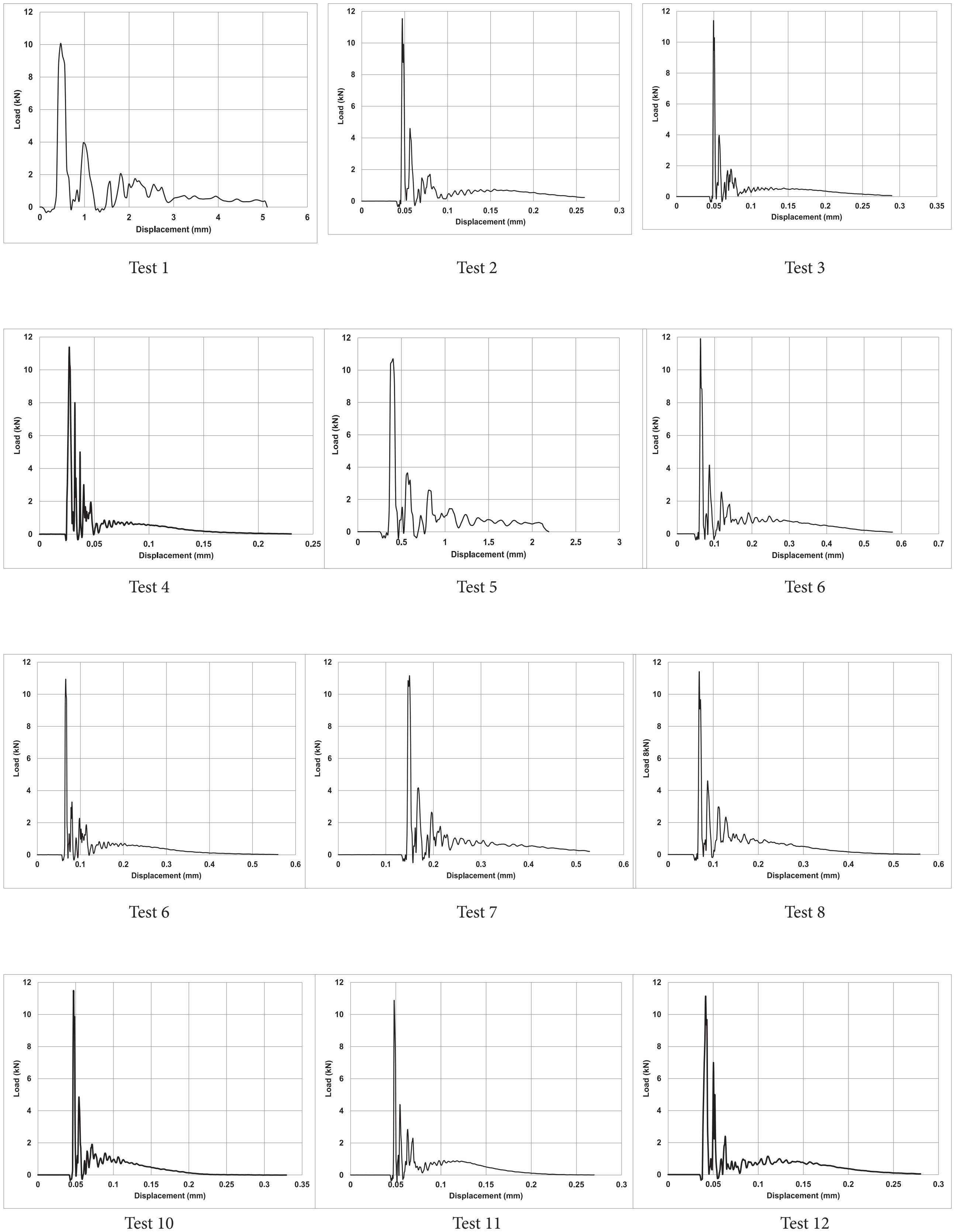

Figure 8. Calculated load-displacement relationships of tests.

Table 9. Expense items and total amounts over unit prices in 2014.

Expense items and total amounts over unit prices in 2014 (USD)					
The definition of business (m^2 cost of geosynthetic spreading work)	Material Prices	Labor Costs	Shipping Costs	General Expenses and Contractor Profit (25 %)	Total Amount
Geogrid	1.05	0.2	0.1	0.34	1.69
Geotextile	1.37	0.2	0.1	0.42	2.09
Geonet	2.31	0.2	0.1	0.66	3.27
Geocell (h = 50, t = 1, w = 400) [a]	1.83	3.5	0.1	1.36	6.79
Geocell (h = 100, t = 1.5, w = 330)	5.37	3.5	0.1	2.25	11.22

[a] *h*: height; *t*: wall thickness; *w*: weld interval; in millimeter.

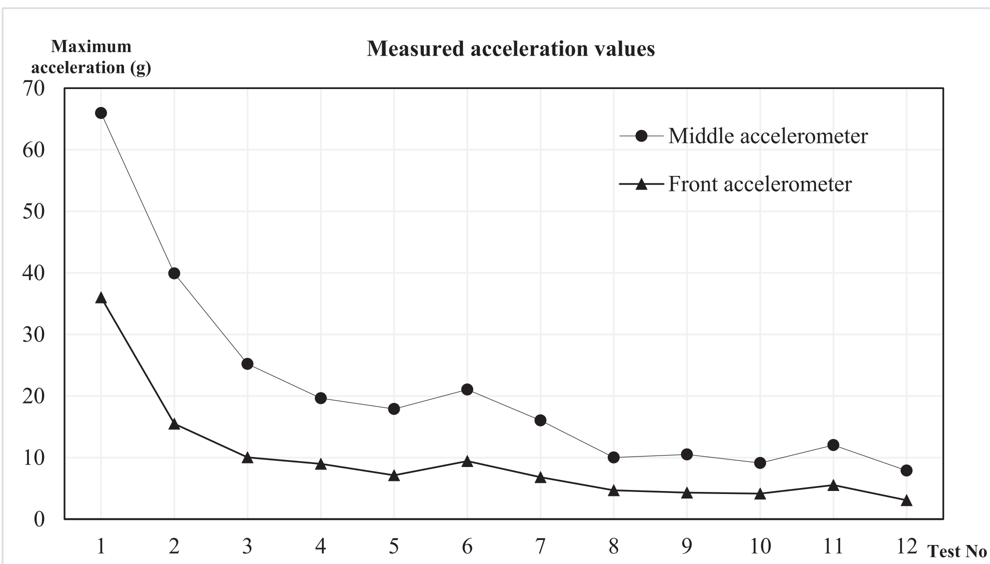

Figure 9. Distribution of acceleration values from accelerometers.

3.1 Reinforcements with a single-layer geosynthetic application

The comparison results from the reference test specimen and the test specimens with single-layer geosynthetic laying at the 120 mm depth from the tank's upper face are presented in this section. Test 2 reinforced with geocell (h = 50 mm, t = 1 mm, w = 400 mm), Test 3 reinforced with geogrid, Test 4 reinforced with geotextile as a protective layer, Test 5 reinforced with geonet, and Test 6 reinforced with geocell (h = 100 mm, t = 1.5 mm, w = 330 mm) are tests where the geosynthetic element is laid in a single layer to be compared with the reference experiment. In these experiments, a detailed illustration of the protective layers' placement is given in Figure 10.

The results showing the decline in the acceleration values are presented comparatively in Figure 11 to compare the acceleration values easily. In experiments carried out using single-layer geosynthetics, the most successful application with 72.9 % acceleration damping, 0.53 mm maximum displacement, and 25.11 Joule energy damping data emerged with the use of geonet. In the experiment where the Geocell (h = 50 mm, t = 1 mm, w = 400 mm) element was used, the maximum displacement was 2.11 mm, and the acceleration damping was 39.5 %. The results are high compared to other experiments used in a single-layer layout. Figure 12 shows the comparison of the calculated experimental costs by considering the types of geosynthetics used only in a single-layer layout. Increasing the cell height and wall thickness of the Geocell protective layer increased the cost and performance. The geogrid layer's acceleration damping capacity, which is 61.8 %, was approximately 1.5 times better than the geocell layer with a cell height of 50 mm. The geocell's energy absorption capacity

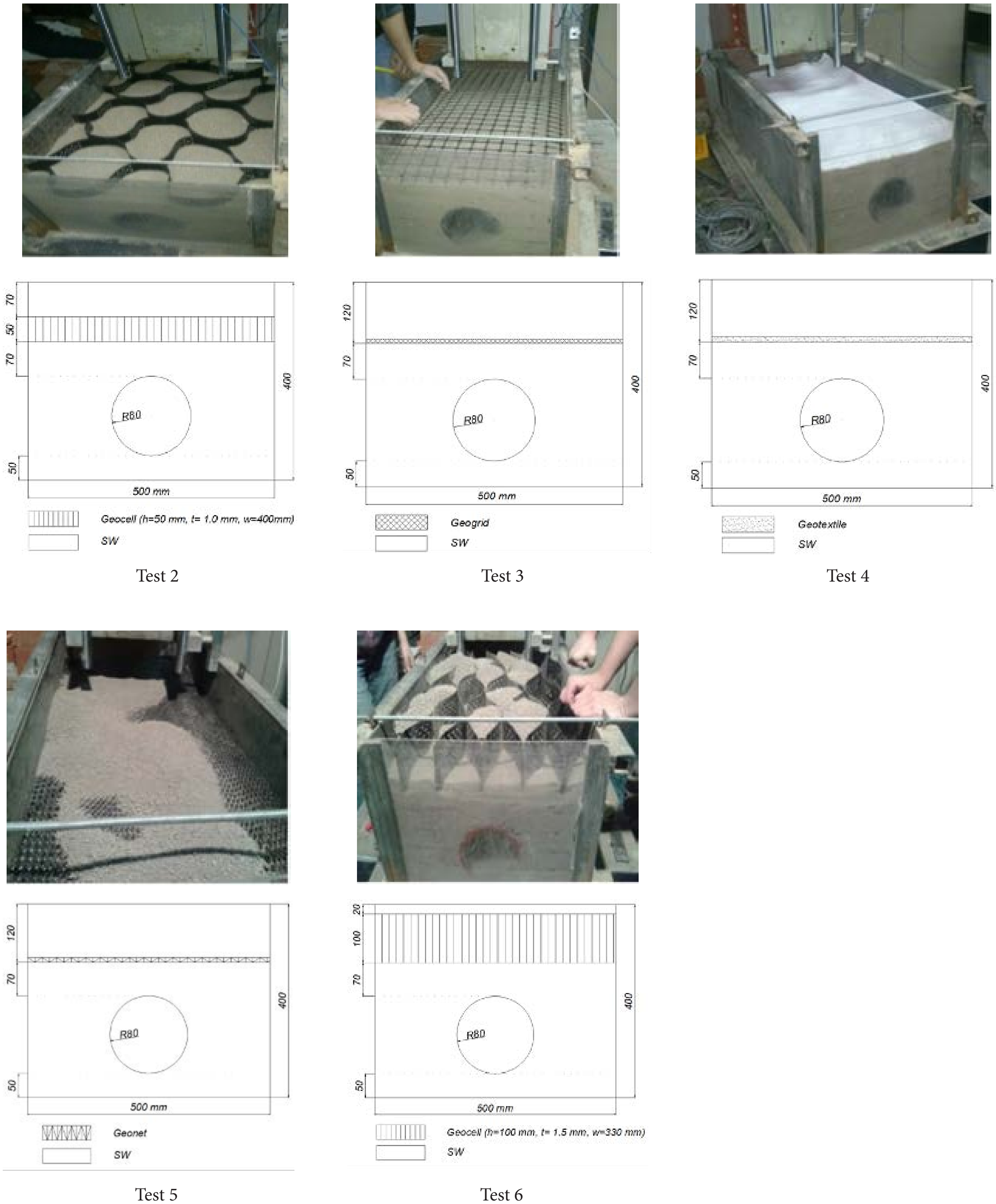

Figure 10. Details of the protective-layer systems that involve single layer.

(h = 100 mm, t = 1.5 mm, w = 330 mm) increased when the cell height and wall thickness was increased, could only pass the geogrid with 68.1 % acceleration damping performance. In terms of economy geonet, which has the most successful results in energy-absorbing and acceleration damping, it was placed in third place. Geotextile

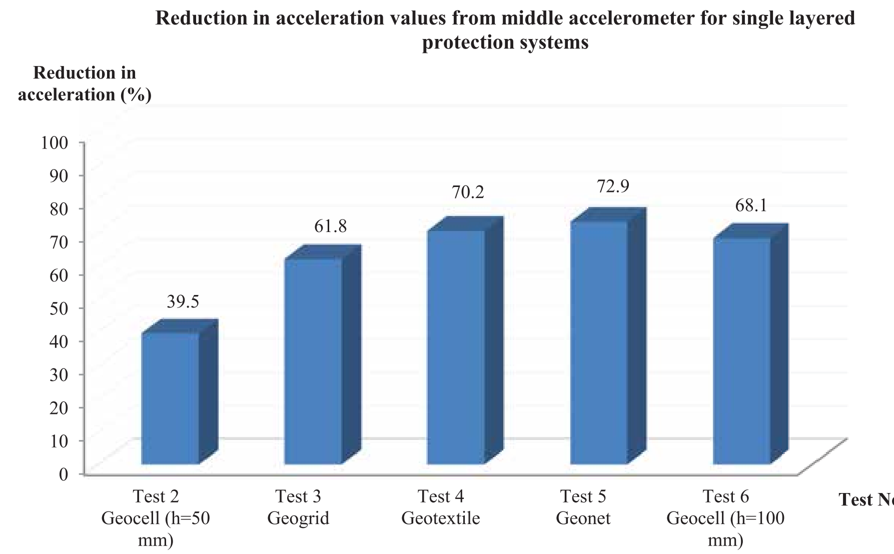

Figure 11. Comparison of acceleration damping performances of single-layer geosynthetic application.

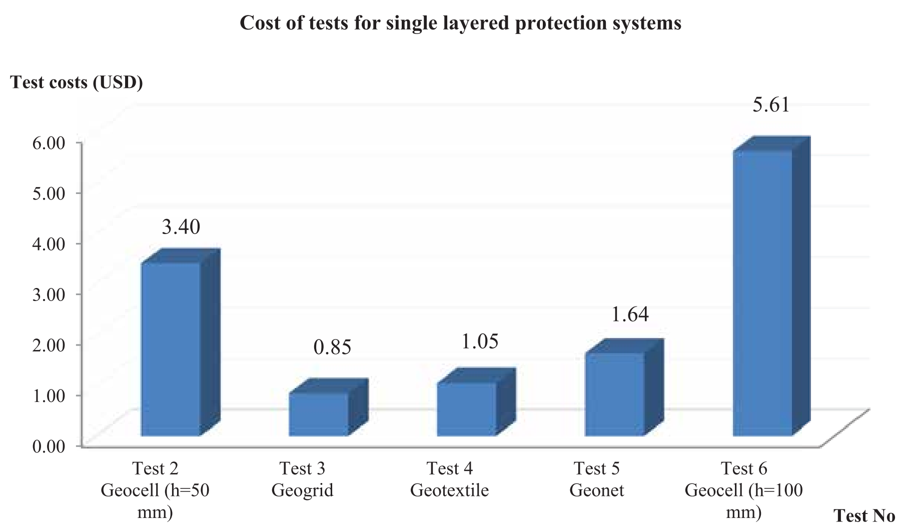

Figure 12. Comparison of test costs considering the geosynthetics used.

and geocell (h = 100 mm, t = 1.5 mm, w = 330 mm) have very close results with maximum acceleration values of 19.63 g, 21.04 g, and maximum displacement of 0.56 mm, respectively. The acceleration damping rate per unit cost of each geosynthetic protective layer is evaluated. Acceleration damping rates per unit cost in experiments using single-layer protective elements are given in Figure 13. It is seen that geogrid provides optimum results.

Within the study's scope, the performance levels of the pipes embedded in the geosynthetic soil environment in the mesh fabric produced from four different types of materials were compared to protect them from the effects caused by sudden dynamic-impact loading.

Although the performance of the geosynthetic layers placed in the ground environment varies according to the type of material, it was observed that all four materials are successful in damping the effects of sudden dynamic impact loading. It was determined that the soil layer, which is reinforced with all four types of materials, gives positive results in damping and reducing the energy, acceleration, and deformation values, depending on the absence of the geosynthetic protective layer. The geonet material exhibits the most successful performance when evaluated in terms of maximum acceleration, displacement, and damped energy values caused by impact loading among four different types of materials examined within the study's scope. One of the effective parameters in this successful performance

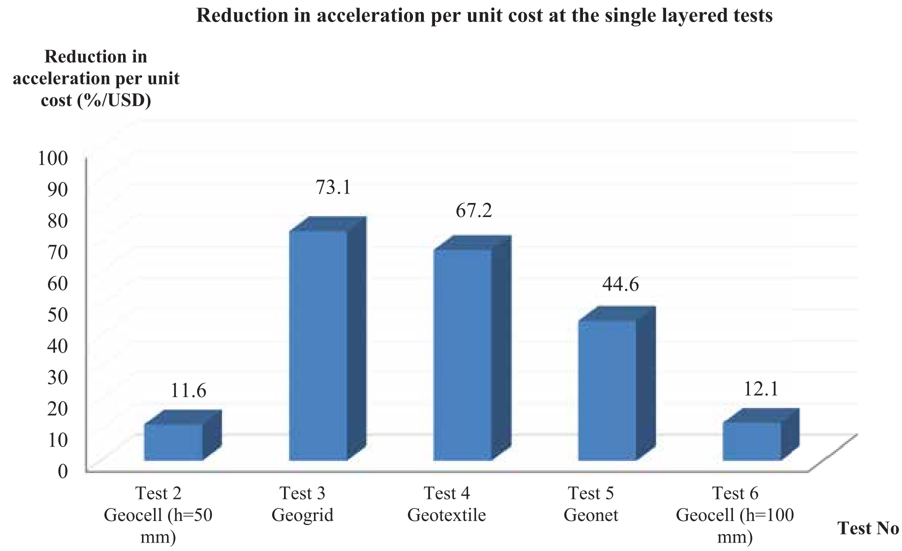

Figure 13. Acceleration-damping ratio per unit cost in single-layer layouts.

achieved by the geonet material is the geometric properties of the mesh structure used in the production of the geosynthetic material. As a result of the dynamic loading applied on the soil layer supported by the geosynthetic protective layer, the soil environment's vertical stress increases. The impact energy transmitted by the falling weight to the soil reaches the geosynthetic layer placed in the soil environment. The soil particles are in the geosynthetic layer mesh in horizontal directions perpendicular to the vertical loading effect. It is thought to play an active role in the damping acceleration, displacement, and energy due to the confinement it creates on it. This developing mechanism has occurred more effectively in geonet-type geosynthetic material than Geocell and Geogrid material. Geocell and geogrid materials have a much larger geometry, and the openings have a wider geometry. This wide mesh netting structure was able to create less efficient confinement on the ground grains. However, the meshes of the geosynthetic mesh produced in Geonet were produced in smaller sizes and with a different knitting logic to form a three-dimensional mesh. It is thought that the sudden stress increase caused by the impact loading due to its geometry is more successfully absorbed by the Geonet material, with the confinement effect of the weave inside the meshes.

3.2 Reinforcement with a double-layer geosynthetic application

Geocell, geogrid, geotextile, and geonet were tested using two geosynthetic elements, with a depth of 120 mm from the tank's upper face. Test 7, Test 8, Test 9, Test 10, Test 11, and Test 12 were made and then compared with the reference test experiment. A double layer of Geocell (h = 50 mm, t = 1 mm, w = 400 mm) was used in all the tests. Tests carried out with the combination of geogrid + geocell for Test 7; the combination of geogrid + geotextile as the protective structure for Test 8; the combination of geonet + geogrid for Test 9; the combination of geonet + geotextile for Test 10; the combination of using geotextile + geocell for Test 11 and the combination of geonet + geocell for Test 12. The location details of the experimental layers of six layers of geosynthetic are given in Figure 14.

The acceleration damping capacities for experiments with double-layer reinforcement elements are presented in Figure 15. The combination of geonet + geocell (Test 12) with 88.0 % acceleration damping capacity was the most successful when reinforced with the double-layer combination at a depth of 120 mm. Among the double layer tests, the acceleration value of the Test 7 experiment was 16.03 g, and the damping capacity was 75.7 %, which had the least acceleration damping capacity. The geonet + geocell combination provided the most cost-effective (Test 12), and the geogrid + geotextile combination (Test 8) provided the most economical strengthening in terms of the experimental costs shown in Figure 16. The "acceleration damping rate per unit cost" of each geosynthetic protective layer was evaluated for double-layer laying experiments and given in Figure 17. In terms of acceleration damping rate per unit cost, it is clear that the optimum application is provided by the combination of geogrid + geotextile in Test 8. As expected, the double-layer geosynthetic protective structures gave better results than a single layer in terms

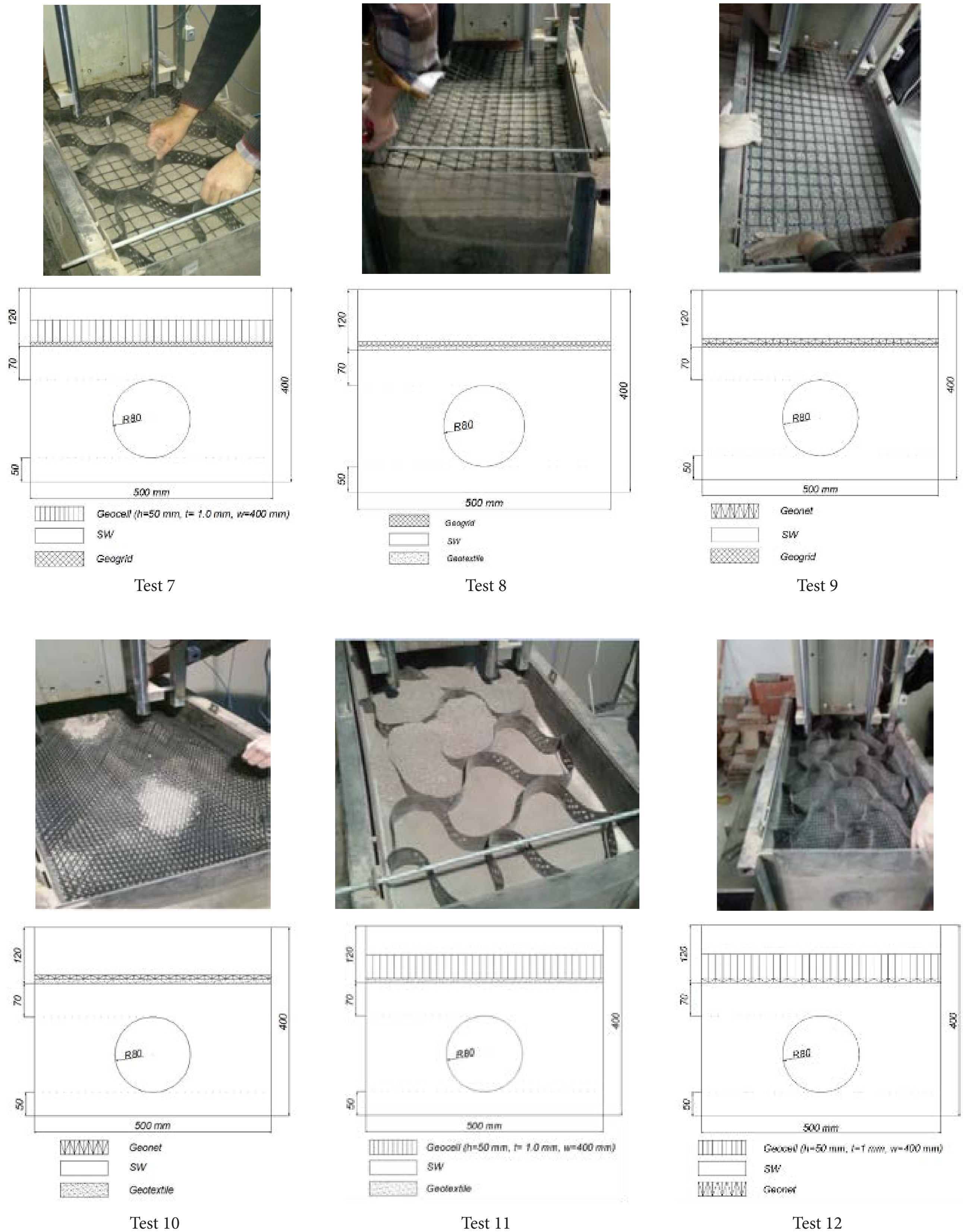

Figure 14. Details of the protective layer systems that involve composite protective layers.

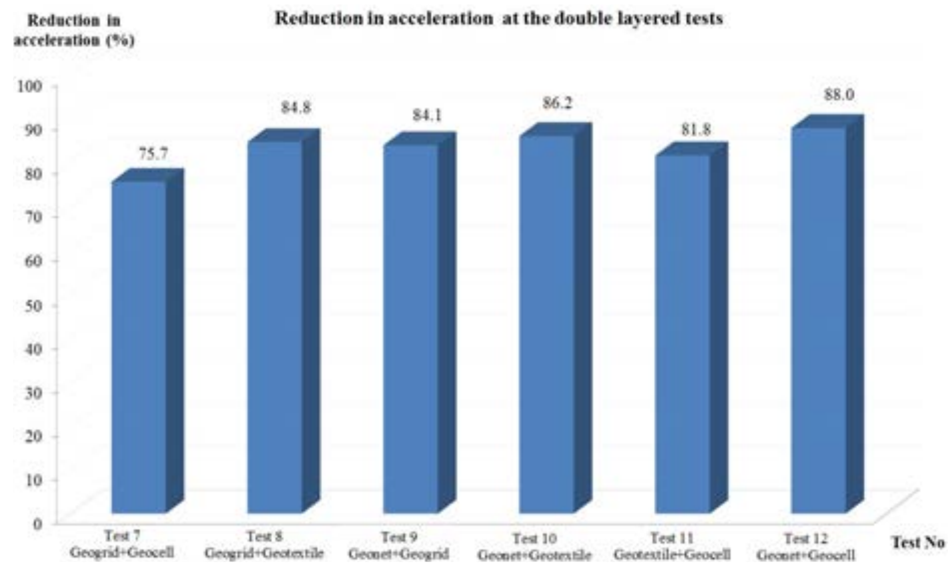

Figure 15. Comparison of acceleration-damping performance of reinforcing with double layer geosynthetic application.

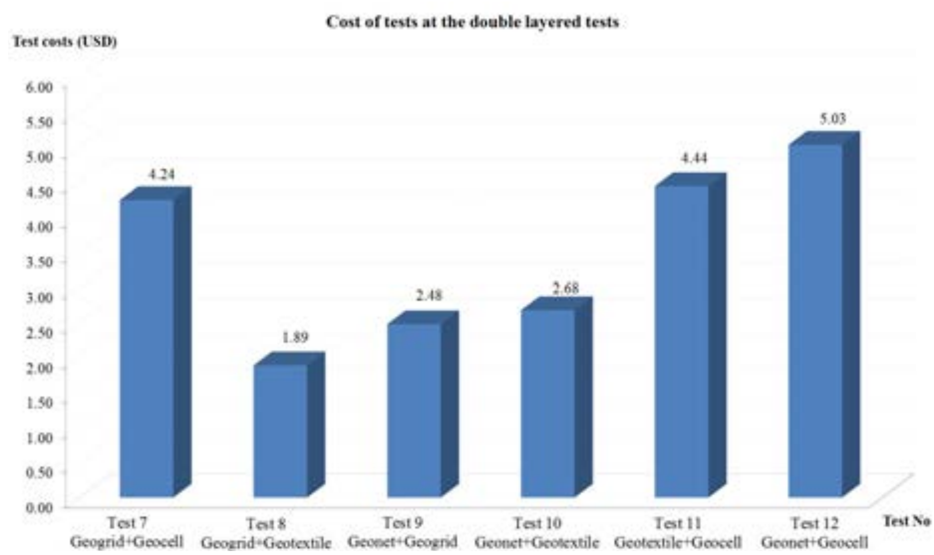

Figure 16. Comparison of test costs considering geosynthetics used for double-layer application.

of performance. However, there was an increase in cost. The "acceleration damping rate per unit cost" in the experiments applied by laying single- and double-layer reinforcement elements at a depth of 120 mm is shown in Figure 18. When all the tests applied in this study are taken into consideration, it is clear that the single-layer geogrid layout provides the optimum application.

It was observed that all two-layer geosynthetic materials were very successful at protecting the buried pipe systems against the effects of sudden dynamic impact loading. It has been determined that two-layer geosynthetic protective layers are effective in all amounts of maximum acceleration, displacement, and damped energy occurring in pipe systems because of impact loading. However, among the two different geosynthetic layered specimens, the most successful performance was seen for geosynthetics in the Geonet and Geocell types. The Geonet material included in this two-layered geosynthetic protective layer is thought to reduce acceleration, displacement effectively, and energy values due to the effective confinement it creates on the soil particles. The Geonet material's production geometry and the structure of the weaving technique showed a

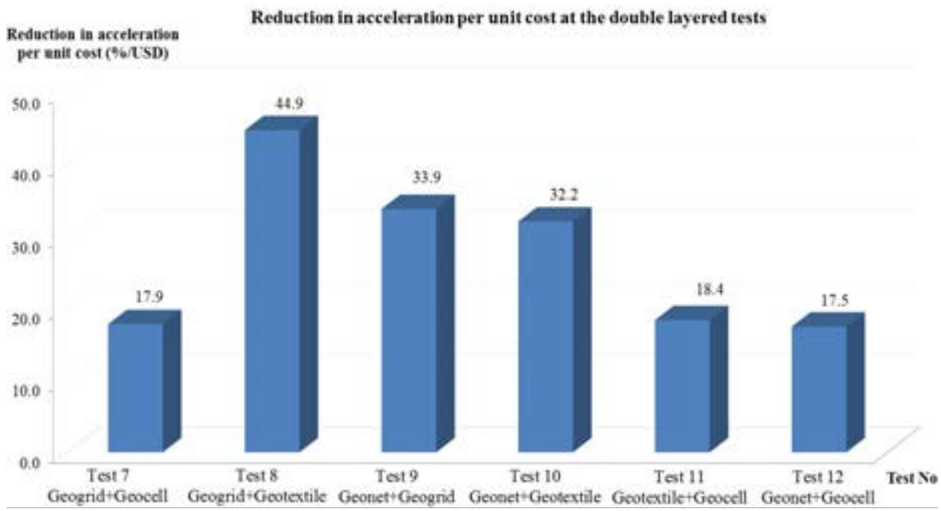

Figure 17. Acceleration-damping ratio per unit cost in double-layer layouts.

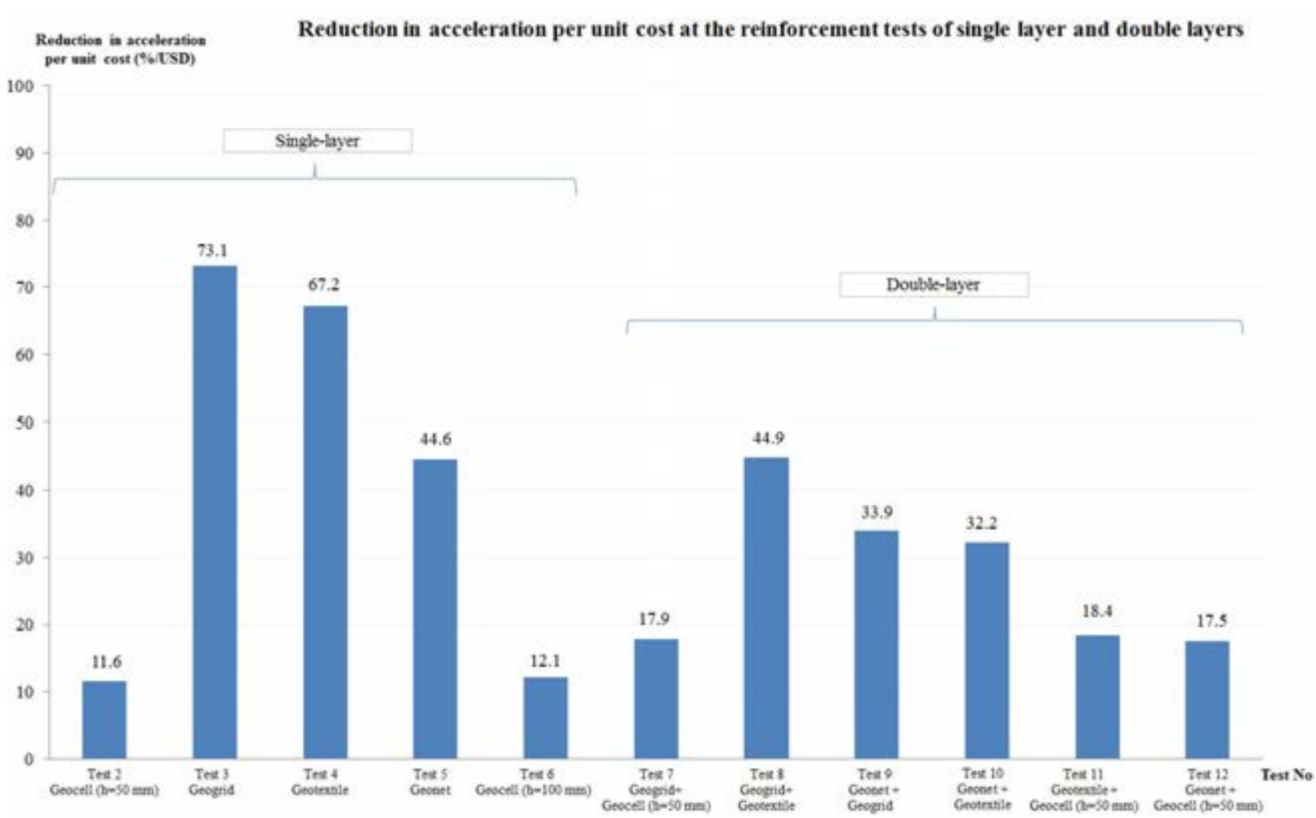

Figure 18. Acceleration-damping ratio per unit cost for single- and double-layer reinforcements.

more effective performance by ensuring that the protective layer of the soil particles was wrapped in the cells of the mesh structure more effectively.

The experiments were designed taking into account the limits of the free weight drop test setup in the laboratory environment and were carried out in sizes allowed by these facilities. In fact, in field applications, in applications where pipe-type structural systems are buried in geotechnical environments, the pipe's route will be passed. In contrast, the geotechnical environment is high strength. After the trench excavation to bury the pipe, the trench walls remain standing for a certain period without collapsing. Generally, they have certain strength to allow the pipe to be placed. Then, after the pipe is placed in the ditch, a uniform sand filling material with the study's properties is filled. In the experimental model carried out in the laboratory environment, the simulation of a similar situation was studied to the extent that the laboratory facilities allowed. The steel container walls are similar to the trench walls of the high-strength soil where the pipe is placed. However, the steel container walls' wave reflection properties at the experimental and high-strength soil trench walls are not very compatible. But it is thought that they can be used to model a higher-strength soil environment and sand-fill environment with different properties. According to the experimental study, it was thought that the model developed for the relative comparison of different types of geosynthetics with different layers and in different shapes as a protective layer would give appropriate and realistic results for the comparisons. The rigidity and material properties of the steel container walls will allow the experimental results to be compared by exhibiting a constant and consistent wave-reflection behavior that will not change in each experiment, such as the soil environment. In order to use the results obtained as a result of this study in practice, it is thought that it would be beneficial to carry out field experiments on larger scales, maybe in real dimensions. In addition, the geosynthetic embedding depth, which cannot be examined within the scope of the study, combining geosynthetics in different combinations, changing the pipe material and depth, changing the properties of the ground used as the filling material, and the experimental examination of different parameters such as filling material are considered necessary to generalize the results obtained from the study and to be used in the application.

4 CONCLUSIONS

Types of geosynthetics and various combinations of them were examined under the influence of impact loads. As a result of the impact loading, the acceleration transferred to the pipe was measured. In addition to the acceleration values, the maximum displacement, maximum load, energy-absorption capabilities of the geosynthetic layer, and costs are also considered in this study. The results of the experiments carried out in the laboratory are summarized below.

- The most successful application with 72.9 % acceleration damping, 0.53 mm maximum displacement, and 25.11 Joule energy damping was the geonet in the experiments performed using single-layer geosynthetic.
- As a result of comparing the cost of experiments by considering only a single-layer geosynthetic layout, the costliest test is the experiment using the geocell (h = 100 mm, t = 1.5 mm, w = 330 mm) material as the protective layer. Geonet, which is the most successful application in energy damping and acceleration damping, ranked third in terms of economy.
- The "acceleration damping rate per unit cost" was calculated to better show the relationship between cost and benefit. When evaluated from this point of view, it was clear that the optimum application is achieved by using geogrid in a single-layer layout.
- When a double-layer reinforcement is made at 120 mm depth from the top face of the tank with the combination of geonet + geocell (h = 50 mm, t = 1 mm, w = 400 mm), the acceleration damping capacity was 88.0 % and showed the most successful performance. The acceleration value of the experiment, in which the geogrid was used together with geocell (h = 50 mm, t = 1 mm, w = 400 mm), was the highest acceleration value, and the system absorbed the least acceleration.
- By considering the unit prices, the combination of geonet + geocell (h = 50 mm, t = 1 mm, w = 400 mm) is the costliest experiment. The combination of geogrid + geotextile provided the most economical strengthening.
- When evaluating the "acceleration damping rate per unit cost" in double-layer layout experiments, the optimum application was achieved with the combination of geogrid + geotextile.
- When the results obtained from all the experiments are evaluated, geonet + geocell (h = 50 mm, t = 1mm, w = 400 mm) the combination was the most successful application with 88.0 % acceleration damping, 0.23 mm maximum displacement, and 25.65 J energy-absorption capacity.
- By evaluating all the laboratory experiments as the acceleration damping rate per unit cost, it was seen that the optimum application was achieved by laying a single-layer geogrid.
- It was observed that the geometric details used during their production and the size of the meshes forming the layer are effective on the performance of the geosynthetic materials examined in the scope of the study in the protection of the pipe systems under the impact loading. Besides, due to the mesh structure used in the production of the geosynthetics and the smaller size of meshes, it was determined that they create more effective confinement in the ground particles and positively affect the performance under impact loading.

REFERENCES

[1] Khalaj, O., Azizian, M., Joz Darabi, N., Moghaddas Tafreshi, S. N., & Jirková, H. 2020. The Role of Expanded Polystyrene and Geocell in Enhancing the Behavior of Buried HDPE Pipes under Trench Loading Using Numerical Analyses. Geosciences, 10(7), 251.

[2] Plácido, R., & Portelinha, F. H. M. 2019. Evaluation of geocomposite compressible layers as induced trench method applied to shallow buried pipelines. Geotextiles and Geomembranes, 47(5), 662-670.

[3] Dash, S. K., Krishnaswamy, N. R., and Rajagopal, K. 2001. Bearing capacity of strip footings supported on geocell-reinforced sand, Geotextiles and Geomembranes, 19, 235–256.

[4] Laman, M., Yıldız, A. 2003. Model studies of ring foundations on geogrid-reinforced sand, Geosynthetics International, 10 (5), 142–152.

[5] Zhou, H., Wen, X. 2008. Model studies on geogrid- or geocell-reinforced sand cushion on soft soil, Geotextiles and Geomembranes, 26, 231–238.

[6] Moghaddas Tafreshi, S.N., Khalaj, O. 2008. Laboratory tests of small-diameter HDPE pipes buried in reinforced sand under repeated-load, Geotextiles and Geomembranes, 26, 145–163.

[7] Gürbüz, A., Mertol, H.C. 2012. Interaction between assembled 3D honeycomb cells produced from high density polyethylene and a cohesionless soil, Journal of Reinforced Plastics and Composites, 31, 828–836.

[8] Moghaddas Tafreshi, S.N., Dawson, A.R. 2012. A comparison of static and cyclic loading responses of foundations on geocell-reinforced sand, Geotextiles and Geomembranes, 32, 55-68.

[9] Tavakoli Mehrjardi, Gh., Moghaddas Tafreshi, S. N., and Dawson, A. R. 2013. Pipe response in a geocell-reinforced trench and compaction considerations, Geosynthetics International, 20 (2), 105–118.

[10] Corey, R., Han, J., Khatri, D.K., and Parsons, R.L. 2014. Laboratory Study on Geosynthetic Protection of Buried Steel-Reinforced HDPE Pipes from Static Loading, Journal of Geotechnical and Geoenvironmental Engineering, 140.

[11] Hegde, A., Kadabinakatti, S., and Sitharam, T.G. 2014. Protection of Buried Pipelines Using a Combination of Geocell and Geogrid Reinforcement: Experimental Studies, Ground Improvement and Geosynthetics, 238.

[12] Anıl, O., Erdem, R.T., ve Kantar, E. 2015. Improving the impact behavior of pipes using geofoam layer for protection, International Journal of Pressure Vessels and Piping, 132 (133), 52-64.

[13] Anıl, Ö., Akbaş, S.O., Gezer, O., Yılmaz, M.C. 2017. Investigation of Impact Behavior of Steel and Composite Pipes with Protective Layer. Structural Concrete, 18 (3) 421-432.

[14] Anıl, Ö., Akbaş, S.O., Gezer, O., Yılmaz, M.C. 2014a. Investigation of Impact Behavior of Steel Pipes with Protective Layer. ICESA 2014, International Civil Engineering & Architecture Symposium for Academicians, Side, Antalya, Turkey.

[15] Anil, Ö., Akbaş, S.O., Gezer, O., Yılmaz M.C. 2014b. Investigation of Impact Behavior of Steel and Composite Pipes with Three Different Protective Layers ", 11th International Congress on Advances in Civil Engineering, İstanbul Technical University, İstanbul, Turkey.v

[16] Babagiray, G., Akbaş, S. O., ve Anıl, O. 2016. Investigation of Impact Behaviour of HDPE Pipes with Geocell Protective Layer, 6th European Geosynthetics Congress (EuroGeo6), Slovenia, 762-773.

[17] Babagiray, G., Akbaş, S.O., Anil, Ö. 2018. Results of full-scale field impact load tests on HDPE pipes with geogrid protective layer. 11th International Conference on Geosynthetics, Coex, Seoul, Korea.

NAVODILA AVTORJEM

Vsebina članka

Članek naj bo napisan v naslednji obliki:

- Naslov, ki primerno opisuje vsebino članka in ne presega 80 znakov.
- Izvleček, ki naj bo skrajšana oblika članka in naj ne presega 250 besed. Izvleček mora vsebovati osnove, jedro in cilje raziskave, uporabljeno metodologijo dela, povzetek izidov in osnovne sklepe.
- Največ 6 ključnih besed, ki bi morale biti napisane takoj po izvlečku.
- Uvod, v katerem naj bo pregled novejšega stanja in zadostne informacije za razumevanje ter pregled izidov dela, predstavljenih v članku.
- Teorija.
- Eksperimentalni del, ki naj vsebuje podatke o postavitvi preiskusa in metode, uporabljene pri pridobitvi izidov.
- Izidi, ki naj bodo jasno prikazani, po potrebi v obliki slik in preglednic.
- Razprava, v kateri naj bodo prikazane povezave in posplošitve, uporabljene za pridobitev izidov. Prikazana naj bo tudi pomembnost izidov in primerjava s poprej objavljenimi deli.
- Sklepi, v katerih naj bo prikazan en ali več sklepov, ki izhajajo iz izidov in razprave.
- Vse navedbe v besedilu morajo biti na koncu zbrane v seznamu literature, in obratno.

Dodatne zahteve

- Vrstice morajo biti zaporedno oštevilčene.
- Predložen članek ne sme imeti več kot 18 strani (brez tabel, legend in literature); velikost črk 12, dvojni razmik med vrsticami. V članek je lahko vključenih največ 10 slik. Isti rezultati so lahko prikazani v tabelah ali na slikah, ne pa na oba načina.
- Potrebno je priložiti imena, naslove in elektronske naslove štirih potencialnih recenzentov članka. Urednik ima izključno pravico do odločitve, ali bo te predloge upošteval.

Enote in okrajšave

V besedilu, preglednicah in slikah uporabljajte le standardne označbe in okrajšave SI. Simbole fizikalnih veličin v besedilu pišite poševno (npr. *v*, *T* itn.). Simbole enot, ki so sestavljene iz črk, pa pokončno (npr. Pa, m itn.). Vse okrajšave naj bodo, ko se prvič pojavijo, izpisane v celoti.

Slike

Slike morajo biti zaporedno oštevilčene in označene, v besedilu in podnaslovu, kot sl. 1, sl. 2 itn. Posnete naj bodo v katerem koli od razširjenih formatov, npr. BMP, JPG, GIF. Za pripravo diagramov in risb priporočamo CDR format (CorelDraw), saj so slike v njem vektorske in jih lahko pri končni obdelavi preprosto povečujemo ali pomanjšujemo.

Pri označevanju osi v diagramih, kadar je le mogoče, uporabite označbe veličin (npr. *v*, *T* itn.). V diagramih z več krivuljami mora biti vsaka krivulja označena. Pomen oznake mora biti razložen v podnapisu slike.

Za vse slike po fotografskih posnetkih je treba priložiti izvirne fotografije ali kakovostno narejen posnetek.

Preglednice

Preglednice morajo biti zaporedno oštevilčene in označene, v besedilu in podnaslovu, kot preglednica 1, preglednica 2 itn. V preglednicah ne uporabljajte izpisanih imen veličin, ampak samo ustrezne simbole. K fizikalnim količinam, npr. *t* (pisano poševno), pripišite enote (pisano pokončno) v novo vrsto brez oklepajev. Vse opombe naj bodo označene z uporabo dvignjene številke[1].

Seznam literature

Navedba v besedilu

Vsaka navedba, na katero se sklicujete v besedilu, mora biti v seznamu literature (in obratno). Neobjavljeni rezultati in osebne komunikacije se ne priporočajo v seznamu literature, navedejo pa se lahko v besedilu, če je nujno potrebno.

Oblika navajanja literature

V besedilu: Navedite reference zaporedno po številkah v oglatih oklepajih v skladu z besedilom. Dejanski avtorji so lahko navedeni, vendar mora obvezno biti podana referenčna številka.

Primer: »..... kot je razvidno [1,2]. Brandl and Blovsky [4], sta pridobila drugačen rezultat…«

V seznamu: Literaturni viri so oštevilčeni po vrstnem redu, kakor se pojavijo v članku. Označimo jih s številkami v oglatih oklepajih.

Sklicevanje na objave v revijah:

[1] Jelušič, P., Žlender, B. 2013. Soil-nail wall stability analysis using ANFIS. Acta Geotechnica Slovenica 10(1), 61-73.

Sklicevanje na knjigo:
[2] Šuklje, L. 1969. Rheological aspects of soil mechanics. Wiley-Interscience, London
Sklicevanje na poglavje v monografiji:
[3] Mitchel, J.K. 1992. Characteristics and mechanisms of clay creep and creep rupture, in N. Guven, R.M. Pollastro (eds.), Clay-Water Interface and Its Rheological Implications, CMS Workshop Lectures, Vol. 4, The clay minerals Society, USA, pp. 212-244..
Sklicevanje na objave v zbornikih konferenc:
[4] Brandl, H., Blovsky, S. 2005. Slope stabilization with socket walls using the observational method. Proc. Int. conf. on Soil Mechanics and Geotechnical Engineering, Bratislava, pp. 2485-2488.
Sklicevanje na spletne objave:
[5] Kot najmanj, je potrebno podati celoten URL. Če so poznani drugi podatki (DOI, imena avtorjev, datumi, sklicevanje na izvorno literaturo), se naj prav tako dodajo.

Podatki o avtorjih

Članku priložite tudi podatke o avtorjih: imena, nazive, popolne poštne naslove, številke telefona in faksa, naslove elektronske pošte. Navedite kontaktno osebo.

Sprejem člankov in avtorske pravice

Uredništvo si pridržuje pravico do odločanja o sprejemu članka za objavo, strokovno oceno mednarodnih recenzentov in morebitnem predlogu za krajšanje ali izpopolnitev ter terminološke in jezikovne korekture. Z objavo preidejo avtorske pravice na revijo ACTA GEOTECHNICA SLOVENICA. Pri morebitnih kasnejših objavah mora biti AGS navedena kot vir.

Vsa nadaljnja pojasnila daje:

Uredništvo
ACTA GEOTECHNICA SLOVENICA
Univerza v Mariboru,
Fakulteta za gradbeništvo, prometno inženirstvo in arhitekturo
Smetanova ulica 17, 2000 Maribor, Slovenija
E-pošta: ags@um.si

INSTRUCTIONS FOR AUTHORS

Format of the paper

The paper should have the following structure:

- A Title, which adequately describes the content of the paper and should not exceed 80 characters;
- An Abstract, which should be viewed as a mini version of the paper and should not exceed 250 words. The Abstract should state the principal objectives and the scope of the investigation and the methodology employed; it should also summarise the results and state the principal conclusions;
- Immediately after the abstract, provide a maximum of 6 keywords;
- An Introduction, which should provide a review of recent literature and sufficient background information to allow the results of the paper to be understood and evaluated;
- A Theoretical section;
- An Experimental section, which should provide details of the experimental set-up and the methods used to obtain the results;
- A Results section, which should clearly and concisely present the data, using figures and tables where appropriate;
- A Discussion section, which should describe the relationships shown and the generalisations made possible by the results and discuss the significance of the results, making comparisons with previously published work;
- Conclusions, which should present one or more conclusions that have been drawn from the results and subsequent discussion;
- A list of References, which comprises all the references cited in the text, and vice versa.

Additional Requirements for Manuscripts

- Use double line-spacing.
- Insert continuous line numbering.
- The submitted text of Research Papers should cover no more than 18 pages (without Tables, Legends, and References, style: font size 12, double line spacing). The number of illustrations should not exceed 10. Results may be shown in tables or figures, but not in both of them.
- Please submit, with the manuscript, the names, addresses and e-mail addresses of four potential referees. Note that the editor retains the sole right to decide whether or not the suggested reviewers are used.

Units and abbreviations

Only standard SI symbols and abbreviations should be used in the text, tables and figures. Symbols for physical quantities in the text should be written in Italics (e.g. v, T, etc.). Symbols for units that consist of letters should

be in plain text (e.g. Pa, m, etc.).
All abbreviations should be spelt out in full on first appearance.

Figures

Figures must be cited in consecutive numerical order in the text and referred to in both the text and the caption as Fig. 1, Fig. 2, etc. Figures may be saved in any common format, e.g. BMP, JPG, GIF. However, the use of CDR format (CorelDraw) is recommended for graphs and line drawings, since vector images can be easily reduced or enlarged during final processing of the paper.

When labelling axes, physical quantities (e.g. v, T, etc.) should be used whenever possible. Multi-curve graphs should have individual curves marked with a symbol; the meaning of the symbol should be explained in the figure caption. Good quality black-and-white photographs or scanned images should be supplied for the illustrations.

Tables

Tables must be cited in consecutive numerical order in the text and referred to in both the text and the caption as Table 1, Table 2, etc. The use of names for quantities in tables should be avoided if possible: corresponding symbols are preferred. In addition to the physical quantity, e.g. t (in Italics), units (normal text), should be added on a new line without brackets.
Any footnotes should be indicated by the use of the superscript[1].

LIST OF references

Citation in text

Please ensure that every reference cited in the text is also present in the reference list (and vice versa). Any references cited in the abstract must be given in full. Unpublished results and personal communications are not recommended in the reference list, but may be mentioned in the text, if necessary.

Reference style

Text: Indicate references by number(s) in square brackets consecutively in line with the text. The actual authors can be referred to, but the reference number(s) must always be given:

Example: "... as demonstrated [1,2]. Brandl and Blovsky [4] obtained a different result ..."

List: Number the references (numbers in square brackets) in the list in the order in which they appear in the text.

Reference to a journal publication:
[1] Jelušič, P., Žlender, B. 2013. Soil-nail wall stability analysis using ANFIS. Acta Geotechnica Slovenica 10(1), 61-73.

Reference to a book:
[2] Šuklje, L. 1969. Rheological aspects of soil mechanics. Wiley-Interscience, London

Reference to a chapter in an edited book:
[3] Mitchel, J.K. 1992. Characteristics and mechanisms of clay creep and creep rupture, in N. Guven, R.M. Pollastro (eds.), Clay-Water Interface and Its Rheological Implications, CMS Workshop Lectures, Vol. 4, The clay minerals Society, USA, pp. 212-244.

Conference proceedings:
[4] Brandl, H., Blovsky, S. 2005. Slope stabilization with socket walls using the observational method. Proc. Int. conf. on Soil Mechanics and Geotechnical Engineering, Bratislava, pp. 2485-2488.

Web references:
[5] As a minimum, the full URL should be given and the date when the reference was last accessed. Any further information, if known (DOI, author names, dates, reference to a source publication, etc.), should also be given.

Author information

The following information about the authors should be enclosed with the paper: names, complete postal addresses, telephone and fax numbers and E-mail addresses. Indicate the name of the corresponding author.

Acceptance of papers and copyright

The Editorial Committee of the Slovenian Geotechnical Review reserves the right to decide whether a paper is acceptable for publication, to obtain peer reviews for the submitted papers, and if necessary, to require changes in the content, length or language.
On publication, copyright for the paper shall pass to the ACTA GEOTECHNICA SLOVENICA. The AGS must be stated as a source in all later publication.

For further information contact:

Editorial Board
ACTA GEOTECHNICA SLOVENICA
University of Maribor,
Faculty of Civil Engineering, Transportation Engineering and Architecture
Smetanova ulica 17, 2000 Maribor, Slovenia
E-mail: ags@um.si

NAMEN REVIJE

Namen revije ACTA GEOTECHNICA SLOVENICA je objavljanje kakovostnih teoretičnih člankov z novih pomembnih področij geomehanike in geotehnike, ki bodo dolgoročno vplivali na temeljne in praktične vidike teh področij.

ACTA GEOTECHNICA SLOVENICA objavlja članke s področij: mehanika zemljin in kamnin, inženirska geologija, okoljska geotehnika, geosintetika, geotehnične konstrukcije, numerične in analitične metode, računalniško modeliranje, optimizacija geotehničnih konstrukcij, terenske in laboratorijske preiskave.

Revija redno izhaja dvakrat letno.

AVTORSKE PRAVICE

ODGOVORNOST

Revija ne prevzame nobene odgovornosti za poškodbe in/ali škodo na osebah in na lastnini na podlagi odgovornosti za izdelke, zaradi malomarnosti ali drugače, ali zaradi uporabe kakršnekoli metode, izdelka, navodil ali zamisli, ki so opisani v njej.

AIMS AND SCOPE

ACTA GEOTECHNICA SLOVENICA aims to play an important role in publishing high-quality, theoretical papers from important and emerging areas that will have a lasting impact on fundamental and practical aspects of geomechanics and geotechnical engineering.

ACTA GEOTECHNICA SLOVENICA publishes papers from the following areas: soil and rock mechanics, engineering geology, environmental geotechnics, geosynthetic, geotechnical structures, numerical and analytical methods, computer modelling, optimization of geotechnical structures, field and laboratory testing.

The journal is published twice a year.

COPYRIGHT

RESPONSIBILITY

No responsibility is assumed by the publisher for any injury and/or damage to persons or property as a matter of product liability, negligence or otherwise, or from any use or operation of any methods, products, instructions or ideas contained in the material herein.

9771854017001

University of Maribor

Faculty of Civil Engineering, Transportation Engineering and Architecture

www.fgpa.um.si

SLOVENSKO GEOTEHNIŠKO DRUŠTVO • SLOVENIAN GEOTECHNICAL SOCIETY

www.sloged.si

University of Ljubljana

Faculty of Civil and Geodetic Engineering

Faculty of Natural Sciences and Engineering

www.fgg.uni-lj.si

www.ntf.uni-lj.si

SLOVENSKO DRUŠTVO ZA PODZEMNE GRADNJE

SLOVENIAN SOCIETY FOR UNDERGROUND STRUCTURES

www.ita-slovenia.si